PRODUCTION OF ^{153}SM-LABELLED MICROPARTICLES AND DOSIMETRIC STUDIES FOR POTENTIAL APPLICATION IN LIVER RADIOEMBOLIZATION

NURUL HASHIKIN BINTI AB. AZIZ

FACULTY OF MEDICINE
UNIVERSITY OF MALAYA
KUALA LUMPUR

2017

PRODUCTION OF ^{153}SM-LABELLED MICROPARTICLES AND DOSIMETRIC STUDIES FOR POTENTIAL APPLICATION IN LIVER RADIOEMBOLIZATION

NURUL HASHIKIN BINTI AB. AZIZ

THESIS SUBMITTED IN FULFILMENT OF THE REQUIREMENTS FOR THE DEGREE OF DOCTOR OF PHILOSOPHY

FACULTY OF MEDICINE
UNIVERSITY OF MALAYA
KUALA LUMPUR

2017

UNIVERSITY OF MALAYA

ORIGINAL LITERARY WORK DECLARATION

Name of Candidate: NURUL HASHIKIN BINTI AB. AZIZ

(I.C/Passport No:

Registration/Matric No: MHA120066

Name of Degree: DOCTOR OF PHILOSOPHY

Title of Project Paper/Research Report/Dissertation/Thesis ("this Work"): PRODUCTION OF ^{153}SM-LABELLED MICROPARTICLES AND DOSIMETRIC STUDIES FOR POTENTIAL APPLICATION IN LIVER RADIOEMBOLIZATION

Field of Study: MEDICAL PHYSICS

I do solemnly and sincerely declare that:

(1) I am the sole author/writer of this Work;
(2) This Work is original;
(3) Any use of any work in which copyright exists was done by way of fair dealing and for permitted purposes and any excerpt or extract from, or reference to or reproduction of any copyright work has been disclosed expressly and sufficiently and the title of the Work and its authorship have been acknowledged in this Work;
(4) I do not have any actual knowledge nor do I ought reasonably to know that the making of this work constitutes an infringement of any copyright work;
(5) I hereby assign all and every rights in the copyright to this Work to the University of Malaya ("UM"), who henceforth shall be owner of the copyright in this Work and that any reproduction or use in any form or by any means whatsoever is prohibited without the written consent of UM having been first had and obtained;
(6) I am fully aware that if in the course of making this Work I have infringed any copyright whether intentionally or otherwise, I may be subject to legal action or any other action as may be determined by UM.

Candidate's Signature Date:

Subscribed and solemnly declared before,

Witness's Signature Date:

Name:

Designation:

ABSTRACT

Yttrium-90 (^{90}Y)-microspheres have been increasingly used for transarterial radioembolization (TARE) of hepatocellular carcinoma (HCC). ^{90}Y (a pure beta emitter) does not show sufficient post-procedural imaging capability. Samarium-153 (^{153}Sm) may serve as a better alternative, due to its promising theranostic (therapy and diagnostic) characteristics. This thesis explored the production of ^{153}Sm-microparticles and dosimetric studies for its application in TARE of HCC. A pilot study was performed to determine the suitable microparticle (diameter: 20-40μm) to be labelled with ^{153}Sm. Two commercially available ion-exchange resins; Fractogel® EMD SO_3^- and Amberlite® IR-120H$^+$, each was labelled with 1g of samarium chloride ($^{152}SmCl_3$) in six different formulations and sent for neutron activation in the TRIGA PUSPATI research reactor. Radionuclide purity of these microparticles were tested via gamma spectrometry, and the optimum formulation for each microparticle was determined following a 48h radiolabelling efficiency study in distilled water and human blood plasma. Amberlite® IR-120H$^+$ was chosen, as it possesses excellent (99.9%) radiolabelling efficiency and did not produced any radionuclide impurity following neutron activation. Physicochemical properties of the chosen microparticle before and after neutron activation was further investigated. Fourier transform infrared (FTIR) spectroscopy showed its unaffected functional group throughout the preparation processes. Energy dispersive x-ray (EDX) spectroscopy confirmed the absence of radionuclide impurity. The microparticles possess irregular surface with increased fragments (<10μm) following neutron activation, as seen via a field emission scanning electron microscope (FESEM). The measured particle density was 2.5g.cm^{-3} with specific radioactivity of 54Bq per microparticle, and settling velocity of 0.03cm.s^{-1}. Monte Carlo (MC) simulations were done using the Geometry and Tracking 4 (Geant4) software toolkit, to study the dosimetric accuracy of the routinely

used Medical Internal Radiation Dose (MIRD) based partition model (PM) for TARE with ^{90}Y-microspheres. It was found that PM markedly underestimated the normal liver dose by up to -78%, due to exclusion of cross-fire irradiation between the tumour and normal liver tissue. The model also overestimated both tumour and lung dose by up to 8 and 12%, respectively. These data can be used to recognise the cases with large dosimetric inaccuracy when PM is being used. Also, a corrected formula for lung dose was suggested for future used. Dosimetric assessment for TARE with ^{153}Sm-microparticles was performed using similar MC method. Various treatment scenarios were simulated by targeting 120Gy to the tumour. The ^{153}Sm-microparticles were able to deliver comparable tumour dose with normal liver and lung dose close to that of ^{90}Y-microspheres, and other organ doses far below 1Gy. Finally, the simulations were repeated with other potential radionuclides; holmium-166 (^{166}Ho), lutetium-177 (^{177}Lu) and rhenium-188 (^{188}Re), and the doses were compared with ^{90}Y and ^{153}Sm. ^{153}Sm-microparticles showed great potential as alternative to ^{90}Y with advantage of post-procedure imaging. It possesses ideal characteristics including; stable for neutron activation, excellent radiolabelling efficiency, absence of radionuclide impurities, stable in suspension, low production cost, and ability to deliver comparable tumour dose, without exceeding the organ dose limit. However, improvements should be made to its physical structure for better intraarterial delivery to the tumour.

ABSTRAK

Sfera-sfera mikro yttrium-90 (^{90}Y) semakin kerap digunakan untuk radioembolisasi rentas arteri (TARE) bagi *hepatocellular carcinoma (HCC)*. ^{90}Y (pembebas beta tulen) tidak menunjukkan kebolehan yang cukup untuk pengimejan selepas prosedur. Samarium-153 (^{153}Sm) berkemungkinan mampu bertindak sebagai alternatif yang lebih baik, kerana kebolehan teranostiknya (terapi dan diagnostik). Tesis in mengkaji pembuatan partikel-partikel mikro ^{153}Sm serta kajian dos untuk penggunaannya dalam TARE untuk HCC. Kajian rintis telah dijalankan bagi mengenalpasti partikel mikro (diameter: 20-40µm) yang sesuai dilabel dengan ^{153}Sm. Dua resin-resin pertukaran ion yang didapati secara komersial; Fractogel® EMD SO_3^- dan Amberlite® IR-120H^+, setiap satu telah dilabel dengan 1g samarium klorida ($^{152}SmCl_3$) dengan enam formulasi berbeza, dan dihantar untuk pengaktifan neutron dalam reaktor penyelidikan TRIGA PUSPATI. Ketulenan radionuklid partikel-partikel mikro ini diperiksa menggunakan spektrometri gamma, dan formulasi optimum untuk setiap partikel mikro dikenalpasti menerusi kajian kecekapan penglabelan radiasi dalam air suling dan plasma darah manusia selama 48jam. Amberlite® IR-120H^+ telah dipilih, kerana kecekapan penglabelan radiasi yang sangat baik (99.9%) dan ketiadaan radionuklid asing selepas pengaktifan neutron. Ciri-ciri fizik dan kimianya (sebelum dan selepas pengaktifan neutron) bagi partikel-partikel mikro yang telah dipilih, seterusnya dikaji. Spektrometri inframerah transformasi Fourier (FTIR) menunjukkan kumpulan berfungsinya tidak terjejas sepanjang proses penyediaan. Spektroskopi sinar-x serakan tenaga (EDX) mengesahkan ketiadaan radionuklid asing. Partikel mikro tersebut mempunyai permukaan yang tidak sekata dengan peningkatan serpihan-serpihan (<10µm) selepas pengaktifan neutron, sebagaimana dilihat melalui mikroskop pelepasan bidang imbasan elektron (FESEM). Ketumpatan partikel yang diukur adalah 2.5g.cm^{-3} dengan radioaktiviti khusus sebanyak 54Bq per partikel, dan halaju pengenapan sebanyak

0.03cm.s^{-1}. Simulasi *Monte Carlo* (MC) dengan kit perisian *Geometry and Tracking 4* (Geant4) telah dijalankan, bagi mengkaji ketepatan dosimetri *partition model* (PM) berasaskan Dos Radiasi Dalaman Perubatan (MIRD) yang diguna secara rutin untuk TARE dengan partikel-partikel ^{90}Y. Didapati, PM kurang anggar dos tisu hati normal sehingga -78%, kerana pengecualian penyinaran *cross-fire* diantara tumor dan tisu hati normal. Ia juga terlebih anggar dos-dos tumor dan paru-paru, masing-masing sehingga 8 dan 12%. Data-data ini boleh digunakan bagi mengenalpasti kes-kes dengan ketidaktepatan dosimetri yang besar apabila PM digunakan. Formula dos paru-paru yang diperbaiki telah dicadangkan bagi penggunaan masa hadapan. Penilaian dos untuk TARE dengan partikel-partikel mikro ^{153}Sm telah dijalankan menggunakan kaedah simulasi MC yang sama. Pelbagai senario rawatan telah disimulasi dengan memberikan 120Gy kepada tumor. Partikel-partikel mikro ^{153}Sm mampu memberikan dos setanding ^{90}Y kepada tumor, dos tisu hati normal dan paru-paru hampir sama dengan dos dari ^{90}Y, dan dos organ lain jauh dari mencapai 1Gy. Akhir sekali, simulasi-simulasi tersebut diulang untuk radionuklid lain yang berpotensi; holmium-166 (^{166}Ho), lutetium-177 (^{177}Lu), dan rhenium-188 (^{188}Re), dan dos-dos ini dibandingkan dengan ^{90}Y dan ^{153}Sm. Partikel-partikel mikro ^{153}Sm menunjukkan potensi sebagai alternatif kepada ^{90}Y dengan kelebihan pengimejan selepas prosedur. Ia mempunyai ciri-ciri unggul termasuklah; stabil untuk pengaktifan neutron, kemampuan penglabelan radiasi yang sangat baik, tiada radionuklid asing, stabil dalam suspensi, kos pengeluaran yang rendah, dan keupayaan untuk memberikan dos yang setanding kepada tumor, tanpa melebihi had dos setiap organ. Namun, penambahbaikan perlu dibuat kepada struktur fizikalnya untuk penghantaran rentas arteri ke tumor yang lebih baik.

ACKNOWLEDGEMENTS

I would like to thank all my supervisors for this opportunity. To Prof. Dr. Basri Johan Jeet, thank you for the wisdom and optimism when I am facing difficulties. To Prof. Dr. Ng Kwan Hoong, thank you for inspiring me, for the regional and international exposures, and for opening doors for me to experience things I may not obtained somewhere else. To Prof. Dr. Chung Lip Yong, thank you for the kind words and support throughout my PhD journey. Last but not least, to Dr. Yeong Chai Hong, massive thank you for always be there for me from the beginning of my journey till now. Thank you for pushing me towards the completion of my study, for being patient when I am being difficult and for not giving up on supervising me. Thank you for all the commitments and support.

Thank you to Prof. Dr. Alan Perkins (Nottingham), Prof. Dr. Anatoly Rosenfeld and Dr. Susanna Guatelli (Wollongong), Dato' Dr. Rehir Dahalan and Datin Zarina (Nuclear Malaysia), and Medical Physics/Nuclear Medicine Unit (UMMC), for the collaborations and for allowing me to do my research in your institutions.

To my colleagues, Susie, Jong, Fione, Hasnah, CK, Safari, Seow, Hanum and Zainor. Thank you for these amazing years. For being there through the hardships, for listening to my problems, for all the guidance and unconditional support throughout these years, and for all the wonderful times we had together. May our friendships last forever.

Most importantly, thank you to my beloved parents for being the reason of me furthering my study. For the endless support and prayers, and for believing in my ability when no one else does. To Iqbal, the love of my life, thank you for allowing me to chase my dreams, for being patient and for our greatest gift, Imtiyaz. And to all my family members, amazing cats and closest friends, thank you for all the love and support.

Alhamdulillah, this is for you Mr. Aziz and Pn. Junaidah.

TABLE OF CONTENTS

LIST OF FIGURES

LIST OF TABLES

LIST OF SYMBOLS AND ABBREVIATIONS

Symbols and Abbreviations

^{24}Na	:	sodium-24
^{65}Zn	:	zinc-65
^{89}Y	:	yttrium-89
^{90}Y	:	yttrium-90
^{90}Sr	:	strontium-90
^{99m}Tc	:	technetium-99m
^{111}In	:	indium-111
^{131}I	:	iodine-131
^{144}Sm	:	samarium-144
^{152}Sm	:	samarium-152
^{153}Eu	:	europium-153
^{153}Sm	:	samarium-153
^{154}Sm	:	samarium-154
^{166}Ho	:	holmium-166
^{176}Lu	:	lutetium-176
^{177}Lu	:	lutetium-177
^{186}Re	:	rhenium-186
^{188}Re	:	rhenium-188
^{188}W	:	tungsten-188
^{198}Au	:	gold-198
^{235}U	:	uranium-235
E_{β^-}	:	energy of beta
E_{γ}	:	energy of gamma

BCLC	:	Barcelona Clinic Liver Cancer
BREP	:	boundary representation
BSA	:	body surface area
CF	:	conversion factor
CLIP	:	Cancer of the Liver Italian Program
CPE	:	charge particle equilibrium
CSG	:	constructive solid geometry
CT	:	computed tomography
DVB	:	divinylbenzene
EBRT	:	external beam radiotherapy
EDTMP	:	ethylenediamine tetramethylenephosphonate
EDX	:	energy dispersive x-ray
EGS	:	electron gamma shower
FDA	:	Food and Drug Administration
FDG	:	fluorodeoxyglucose
FESEM	:	field emission scanning electron microscope
FLUKA	:	Fluktuierende Kaskade
FTIR	:	Fourier transform infrared
Geant4	:	Geometry and Tracking 4
GUI	:	graphic user interface
HCC	:	hepatocellular carcinoma
HPGe	:	high-purity germanium
ICRP	:	International Commission on Radiological Protection
ICRU	:	International Commission on Radiological Units
LEHR	:	low energy high resolution
LET	:	linear energy transfer

LLI	:	lower large intestine
LS	:	lung shunting
MAA	:	macroaggregated albumin
MC	:	Monte Carlo
MCNP	:	Monte Carlo N-particle
MEGP	:	medium energy general purpose
MIRD	:	Medical Internal Radiation Dose
Mo	:	molybdenum
MRI	:	magnetic resonance imaging
NaCl	:	sodium chloride
NaI(Tl)	:	sodium iodide doped with thallium
PENELOPE	:	Penetration and Energy Loss of Positrons and Electrons
PET	:	positron emission tomography
PLLA	:	poly-l-lactic acid
PM	:	partition model
PMT	:	photomultiplier tube
PS	:	performance status
PTS	:	pneumatic transfer system
RR	:	rotary rack
SA/V	:	surface area-to-volume ratio
$SmCl_3$	:	samarium chloride
Sm_2O_3	:	samarium oxide
SNMMI	:	Society of Nuclear Medicine and Molecular Imaging
SPECT	:	single photon emission computed tomography
TACE	:	transarterial chemoembolization
TARE	:	transarterial radioembolization

TI	:	tumour involvement
T/N	:	tumour-to-normal liver uptake ratio
TNM	:	tumour, nodule, metastasis
TOPV	:	total pore volume
ULI	:	upper larger intestine
UMMC	:	University of Malaya Medical Centre
VDK	:	voxel dose kernel

Unit of Measurements

a.m.u	:	atomic mass unit
barn	:	10^{-24} cm^2
Bq	:	Becquerel
Ci	:	Curie
d	:	days
eV	:	electron Volt
g	:	gram
Gy	:	Gray
h	:	hours
J	:	Joule
l	:	litre
m	:	meter
min	:	minutes
P	:	Pascal = 1 $g.cm^{-1}.s^{-1}$
rad	:	radiation absorbed dose = 0.01 Gy
rem	:	Roentgen equivalent man = 0.01 Sv
rpm	:	rotation per minute

s : seconds

Sv : Sievert

y : years

^{o}C : degree Celcius

Frequently used Metric-unit Prefixes

G : giga = 10^{9}

M : mega = 10^{6}

k : kilo = 10^{3}

c : centi = 10^{-2}

m : mili = 10^{-3}

μ : micro = 10^{-6}

Representation of commercial names

Amberlite : Amberlite® IR-120 H^{+}

Fractogel : Fractogel® EMD SO_3^{-}

CHAPTER 1: INTRODUCTION AND OBJECTIVES

1.1 Introduction

Hepatocellular carcinoma (HCC) is the most common type of liver cancer, and the second most common cause of death from cancers worldwide (Ferlay et al., 2015). HCC is often diagnosed at the later stages when other curative approaches are no longer feasible (Sun & Sarna, 2008; Bruix et al., 2001). However, with the continuous improvements in methods and technologies, more HCC patients can now be diagnosed at the earlier stages (Bruix et al., 2016). For advanced unresectable HCC, transarterial radioembolization (TARE), a minimally invasive procedure involving intravascular administration of radioembolic microparticles, can be performed to improve the patient's survival rate (Kwok et al., 2014).

There are currently two commercially available radioembolic agents; classified as glass-based (TheraSphere®, Nordion, Canada) and resin-based (SIR-Spheres®, SIRTex, Australia) microspheres, which are both approved by the United States Food and Drug Administration (FDA) for TARE of liver cancer. TheraSphere® was approved under Humanitarian Device Exemption for radiation treatment, or as neoadjuvant to surgery or transplantation for HCC patients (BTG International, 2013). On the other hand, SIR-Spheres® was approved under Premarket Approval for liver metastases secondary to colorectal cancer (FDA, 2002). They both act as permanent brachytherapy implants localised at the target tumour site until fully decay, delivering all the radiations *in situ*.

A pure beta emitter, yttrium-90 (^{90}Y) (maximum E_{β^-} = 2.28 MeV, yield = 99.98 %) is used as the radioactive source in both TheraSphere® and SIR-Spheres® microspheres. ^{90}Y is typically produced from a strontium-90 (^{90}Sr) generator, which is a nuclear fission

product of uranium-235 (^{235}U) in a nuclear reactor. ^{90}Y is rarely produced via neutron activation due to very low thermal neutron activation cross-section of yttrium-89 (^{89}Y). The various stages involved in the production of ^{90}Y, have resulted in high cost and limited supply of the radionuclide for TARE worldwide. Since ^{90}Y is a pure beta emitter, it is lacking of direct imaging characteristic to verify the actual distribution of the ^{90}Y-microspheres within the treatment volume.

Gamma imaging using macroaggregated albumin (MAA) labelled with technetium-99m (^{99m}Tc) has been used prior to TARE for lung shunting quantification, which provides reasonable information on the microspheres distribution within the tumour, liver and lungs that will aid in the treatment planning decisions. However, this method does not accurately reflect the intrahepatic distribution of the microspheres, due to resolution and partitioning dissimilarities between ^{99m}Tc and ^{90}Y images, as a result of different physical characteristics and number of particles infused (Gupta et al., 2008; Koch & Tatsch, 2008). Although the infused ^{90}Y-labelled microspheres can be followed via Bremsstrahlung x-ray imaging, this technique is rather challenging and requires special imaging procedures and post-processing skills. Furthermore, the images are very low in spatial resolution due to a wide spectrum of scatter energies produced as a result of beta attenuation. High resolution images are crucial as they help in accurately determining the region of extrahepatic microparticles deposition, to prepare for possible complications, i.e. biliary sequelae, radiation pneumonitis, gastroenteritis and acute pancreatitis (Riaz et al., 2014).

Radionuclides which emit both therapeutic beta and diagnostic gamma energies would be ideal for “theranostic” (therapy and diagnostic) application. An ideal theranostic radionuclide should has optimum physical half-life, suitable linear energy transfer (LET) and range in tissues, high ratio of non-penetrating to penetrating radiation, short-lived or

stable daughter nuclide, good and selective concentration with prolonged retention in tumour, and minimum uptake by normal tissues (Yeong et al., 2014; Qaim, 2001). Neutron-activated radionuclides are preferred due to wide availability of nuclear reactors worldwide and the relatively easier production method. In addition, radiation exposures to the personnel can be minimised because non-radioactive nuclide is used during the labelling process. The labelled compound will then be sent for neutron activation with proper shielding in place.

Samarium-153 (^{153}Sm) is a potential alternative radionuclide to ^{90}Y in TARE of HCC. ^{153}Sm has been widely used for palliative pain treatment of bone metastases as well as radiation synovectomy of the knee, however its therapeutic potential has not been fully explored for other applications. The imaging properties of ^{153}Sm has been proven feasible for gastrointestinal scintigraphy (Yeong et al., 2012). The main advantages of ^{153}Sm as a theranostic agent includes optimal physical half-life (1.93 d), relatively high thermal neutron activation cross-section (210 barn), and presence of diagnostic gamma energy (E_γ = 103 keV) which can be easily distinguished by the use of energy windowing. Although the maximum beta energy is about 2.8 times lower than ^{90}Y, this can be compensated by administering higher activity of ^{153}Sm to deliver comparable therapeutic dose to the tumour. The theoretical advantages of ^{153}Sm as compared to ^{90}Y are illustrated in **Figure 1.1**. By using the low energy high resolution (LEHR) collimator attached to a gamma camera, the distribution of ^{153}Sm within the liver can be imaged using similar protocol to that of the ^{99m}Tc.

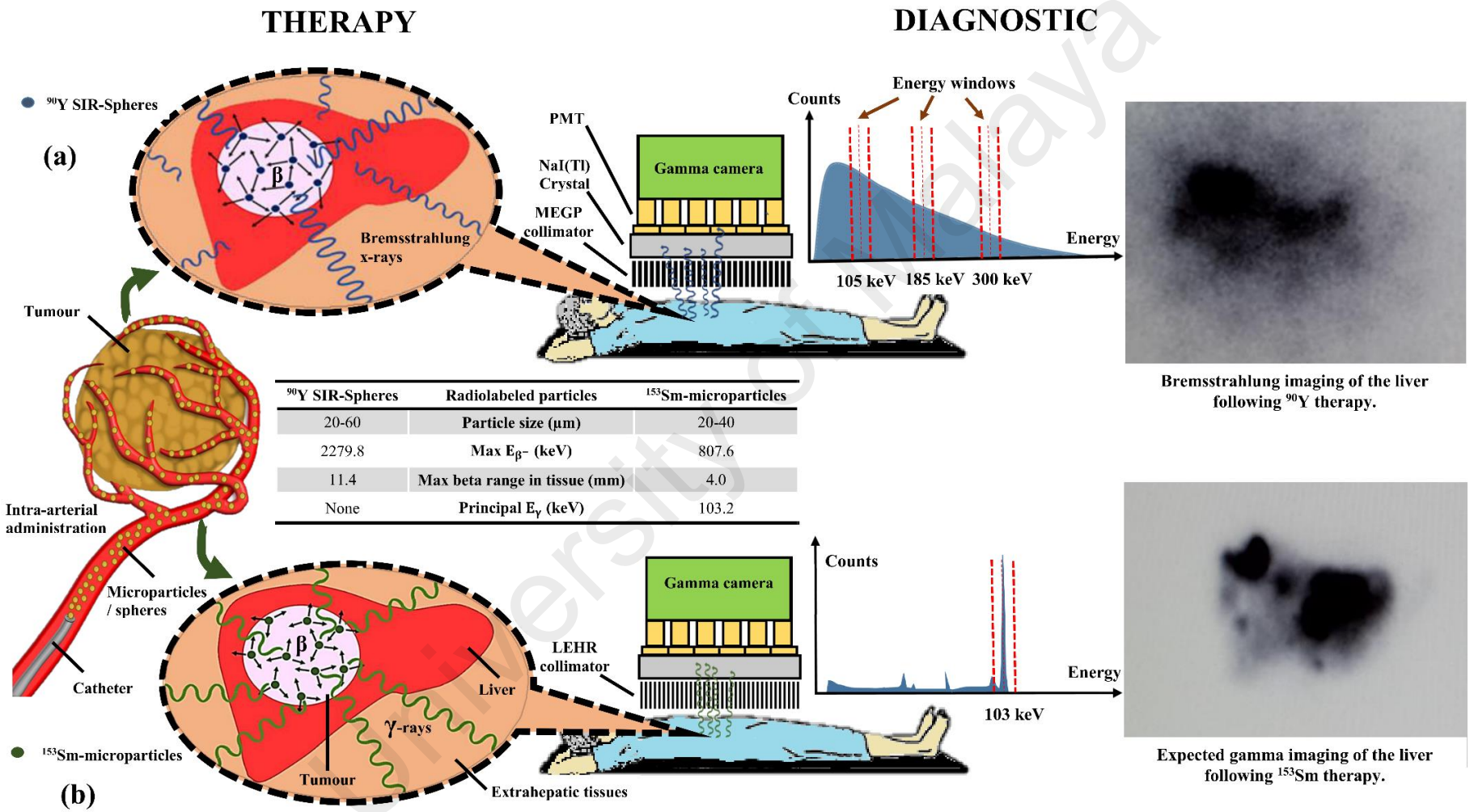

^{90}Y SIR-Spheres	Radiolabeled particles	^{153}Sm-microparticles
20-60	Particle size (μm)	20-40
2279.8	Max E_{β^-} (keV)	807.6
11.4	Max beta range in tissue (mm)	4.0
None	Principal E_γ (keV)	103.2

Figure 1.1: Comparison of TARE with (a) ^{90}Y-microspheres and (b) the proposed ^{153}Sm-microparticles. PMT: photomultiplier tube, NaI(Tl): sodium iodide doped with thallium, MEGP: medium energy general purpose, LEHR: low energy high resolution

1.2 Objectives

The overall aim of this thesis was to investigate the feasibility of ^{153}Sm as an alternative radionuclide to ^{90}Y in TARE of HCC. In achieving this aim, various specific objectives were identified, which include:

i. To determine the suitable ion exchange resin microparticles that can be conveniently labelled with samarium chloride ($^{152}SmCl_3$).
ii. To study the physicochemical properties of the ^{153}Sm-labelled ion exchange resin formulation before and after neutron activation for potential used in TARE.
iii. To evaluate the dosimetric accuracy of the partition model (PM) used in TARE with ^{90}Y-microspheres, by comparing the calculated doses with the doses obtained from Monte Carlo (MC) simulations.
iv. To develop a dosimetric assessment method for TARE with ^{153}Sm-microparticles using the MC simulations.
v. To compare the absorbed doses in TARE with various radionuclide-labelled microparticles; ^{90}Y, ^{153}Sm, holmium-166 (^{166}Ho), lutetium-177 (^{177}Lu) and rhenium-188 (^{188}Re) microparticles using the MC simulations.

1.3 Organization of the Thesis

In this thesis, the potential of ^{153}Sm as alternative to ^{90}Y in TARE of HCC was investigated. The work can be divided into two major parts: (a) production of the ^{153}Sm-microparticles and investigation of its physicochemical properties (Chapters 3 and 4); and (b) radiation dosimetric studies for the application of ^{153}Sm-microparticles in TARE of HCC using MC simulations (Chapters 5, 6 and 7).

In the first part of the study, an alternative radionuclide agent to ^{90}Y-microspheres was explored by investigating the production of resin microparticles labelled with ^{153}Sm (which was produced via neutron activation in TRIGA PUSPATI research reactor). In Chapter 3, a preliminary study was carried out to determine a suitable microparticle from two commercially available options. Both microparticles were labelled with samarium-152 (^{152}Sm) via ion exchange process with $^{152}SmCl_3$ salt, and sent for neutron activation. An investigation on the key characteristics of the microparticles which include, radionuclide purity and radiolabelling efficiency studies were carried out following neutron activation.

In Chapter 4, the chosen ^{153}Sm-microparticles were further characterised for its physicochemical properties before and after neutron activation. The tests include Fourier transform infrared (FTIR) spectroscopy to analyse the functional group of the resin throughout the preparation stages, field emission scanning electron microscope (FESEM) for morphological observation, chemical analysis using energy dispersive x-ray (EDX) spectroscopy, particle size analysis using ImageJ, measurement of particle density, and suspension stability study.

For the second part of the study, a series of Geometry and Tracking 4 (Geant4) MC simulations to systematically investigate the related dosimetry in TARE of HCC were carried out. In Chapter 5, the accuracy of PM, which is frequently used in TARE with ^{90}Y-microspheres were investigated. Based on Medical Internal Radiation Dose (MIRD) scheme, this model assumed a full local dose deposition within the compartments; tumour, normal liver tissue and lungs. However, since ^{90}Y possesses high beta energy (maximum E_{β^-} = 2.28 MeV) that can traverse up to 11 mm in tissue, the assumption of local dose deposition may lead to inaccurate dose estimation. Patient parameters that may

affect the accuracy of the dosimetry method were thoroughly investigated by comparing the doses from the simulations with the doses calculated using PM.

In Chapter 6, a systematic dosimetric assessment on the use of ^{153}Sm-microparticles in TARE of HCC was carried out. Various treatment scenarios were simulated by combining different patient parameters to deliver similar tumour dose of 120 Gy. The corresponding absorbed doses to normal liver tissue, lungs, and other organs were estimated. The maximum scenario allowed for treatment were established by delivering the highest possible activities to each scenario to a point where the maximum absorbed dose limit to the organs were reach. All the data were later compiled into an interactive excel spreadsheet for future clinical use.

The radiation doses comparison between TARE with several other suggested radionuclides (^{166}Ho, ^{177}Lu, ^{188}Re, including ^{90}Y and ^{153}Sm) were carried out using the Geant4 MC simulations. These include the comparison between administered activities required to achieve similar tumour dose, and absorbed doses to normal liver, lungs and other organs. The pros and cons of each alternative radionuclide for TARE were assessed and discussed in Chapter 7.

Finally, in Chapter 8, the potential of TARE with ^{153}Sm-microparticles was discussed and concluded. Methodological limitations from this thesis were highlighted and recommendations for future works were proposed in this chapter.

CHAPTER 2: LITERATURE REVIEW

2.1 Overview of the Human Liver

Liver is one of the vital organs of the human body and also the second largest after skin. It plays an important role in digestion, metabolism, immunity and storage of nutrients within the body.

2.1.1 Anatomy of the Human Liver

The human liver consists of four lobes namely; the right, left, caudate and quadrate lobes. The two largest lobes are the left and right lobes which, are anatomically separated by the falciform ligament. The small caudate lobe extends from the posterior side of the right lobe and wraps around the inferior vena cava. Whilst, the small quadrate lobe is inferior to the caudate lobe and extends from the posterior side of the right lobe and wraps around the gallbladder (Taylor, 2012).

The liver can also be classified based on its functional segments, which the functional right and left side is divided by the Cantlie's line (an imaginary line from the gallbladder fossa to the middle hepatic vein), as shown in **Figure 2.1**. Each functional hemi-liver is composed of two sections: on the right, an anterior section (segments 5 and 8) and a posterior section (segments 6 and 7) separated by the right hepatic vein; and on the left, a lateral section (segments 2 and 3) and a medial section (segment 4) separated by the left hepatic vein and the falciform ligament (Siriwardena et al., 2014).

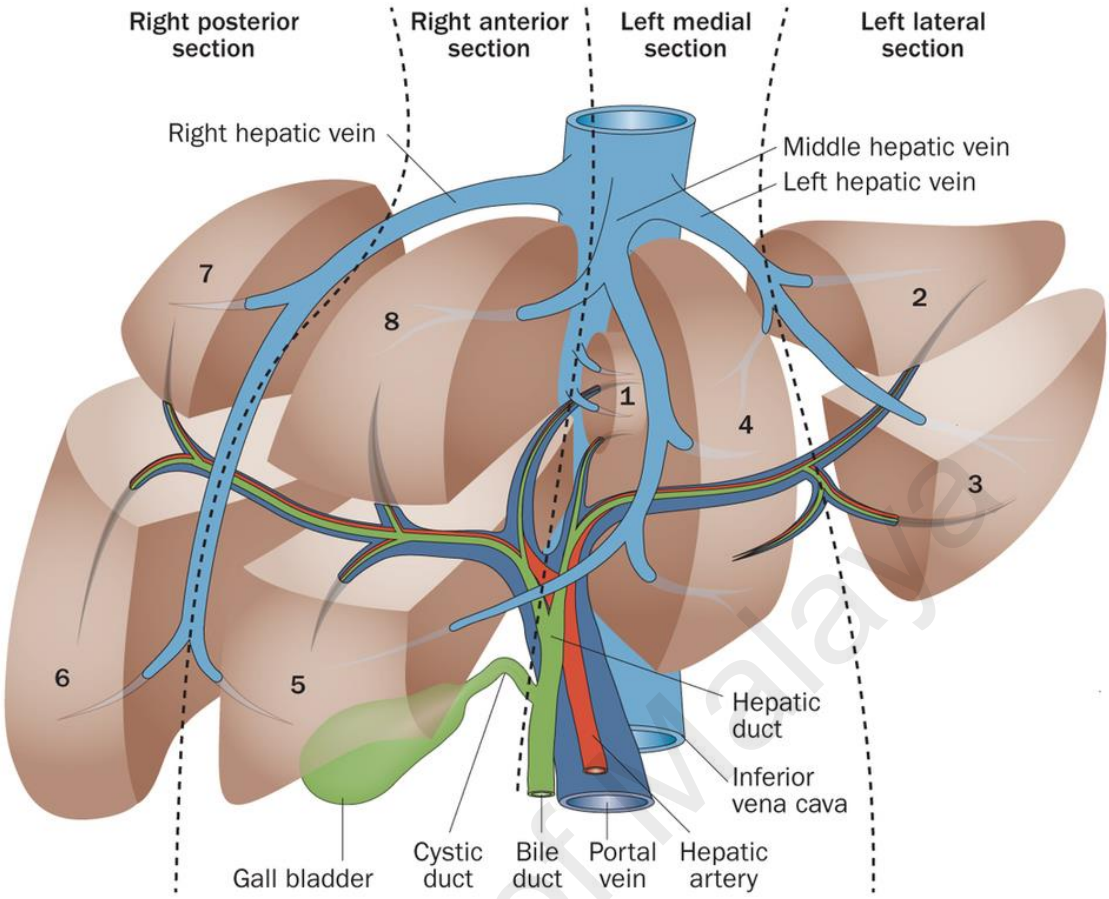

Figure 2.1: Segments of the human liver and current surgical nomenclature of the liver sections (Adapted from Siriwardena et al. (2014)).

The liver is linked with the gastrointestinal system through the bile ducts. The blood supply to the liver is supported mainly by the unique hepatic portal vein system, while the remainder comes from the hepatic artery. Blood travelling to the spleen, stomach, pancreas, gallbladder, and intestines passes through capillaries in these organs and is collected into the hepatic portal vein. The hepatic portal vein then delivers this blood to the tissues of the liver where the contents of the blood are divided up into smaller vessels and processed before being passed throughout the body. Blood leaving the tissues of the liver collects into the hepatic veins, leading them to the vena cava and eventually to the heart (Taylor, 2012).

The liver consist of many smaller hexagonal units called the hepatic lobules, with each containing one large central vein (connected to the hepatic vein) and six portal triads (each consists of branches of the bile duct, hepatic portal vein and hepatic artery), as shown in **Figure 2.2**. The mixed blood from the portal venules and arterioles are channelled into the sinusoids, to be collected by the central vein. Along the sinusoids, lie the main cells of the liver called the hepatocytes. Bile produced by the hepatocytes will be collected through the bile canaliculi and eventually to the bile duct (Pearson Education Inc., 2011).

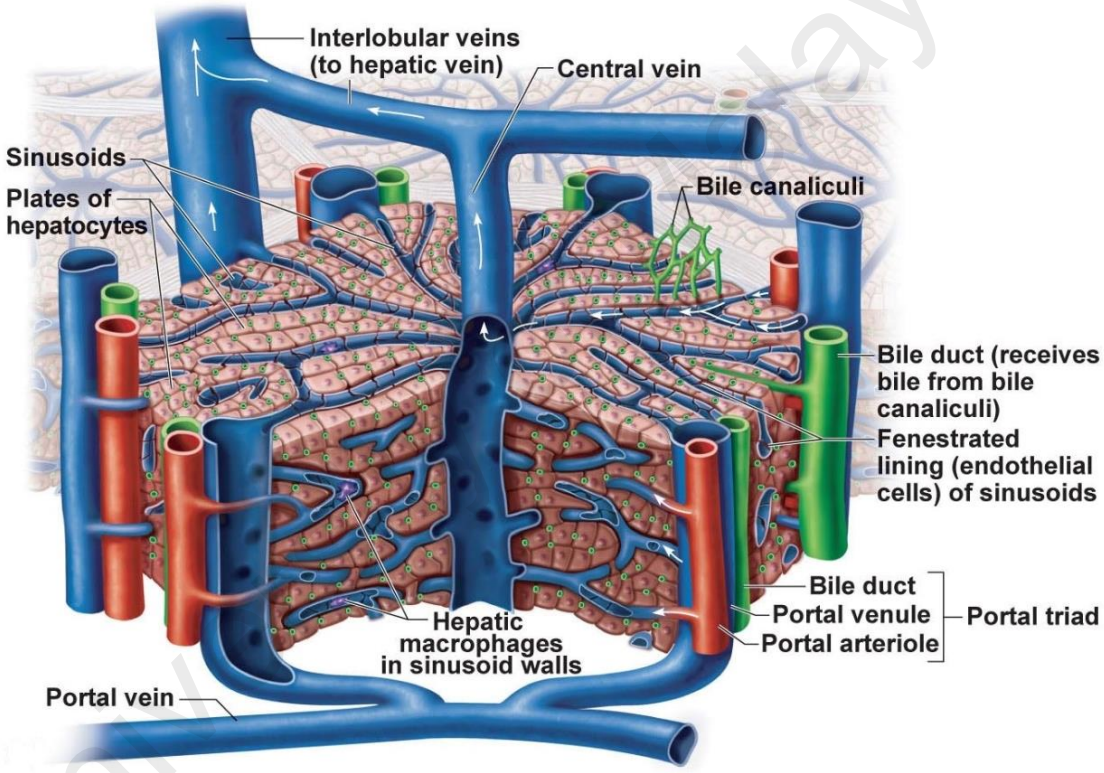

Figure 2.2: The structure of a hepatic lobule. Blood from the portal vein (blue) and artery (red) are mixed at the portal triad, before being channelled into the central vein through the sinusoids. Blood from the central vein will be collected into the hepatic vein which is connected to the vena cava (Adapted from Pearson Education Inc. (2011)).

2.1.2 Physiology of the Human Liver

The liver is one of the vital organs of the body as it performs many crucial functions. Bile is one of the main products of the liver which, is made up of bile salts, cholesterol, bilirubin, electrolytes and water. It helps the small intestine to digest and absorb fats, cholesterol and some vitamins. The bile also helps in the absorption of vitamin K by the body, which the vitamin is needed to produce the blood-clotting (coagulation) factors. Hence, in the case of insufficient production of the bile, the body will absorb less vitamin K and produce less blood-clotting factors, which in turn may results in fatal damage due to excessive bleeding in some patients (Canadian Cancer Society, 2016).

The liver also absorbs and metabolises bilirubin, which is a yellow-red substance formed from haemoglobin when the red blood cells break down. Haemoglobin is a protein found in the red blood cells that carries oxygen and contributes to the red colour of the blood. The iron from the haemoglobin will be stored in the liver or used by the bone marrow for the production of new red blood cells. The liver also acts in the metabolization of protein and carbohydrates. Liver enzymes break down proteins from food so they can be digested and used by the body. Carbohydrates from food break down into glycogen, which is stored in the liver. The liver breaks down glycogen into glucose and releases it into the blood to maintain normal blood sugar levels (Canadian Cancer Society, 2016).

The liver stores vitamins and minerals which include vitamins A, D, E, K and B12. Iron is stored in the liver in the form of ferritin, which is released so the body can make new red blood cells. The liver also stores and releases copper as needed. The liver acts as filters to certain substances from the blood, to prevent build-up which may cause damage to the body. These substances can come from within (such as hormones, e.g. oestrogen, aldosterone and diuretic hormone) or outside (such as alcohol and other drugs, e.g. amphetamines, barbiturates and steroids) the body (Canadian Cancer Society, 2016).

2.2 Hepatocellular Carcinoma (HCC)

The most common type of liver cancer is hepatocellular carcinoma (HCC), which is a primary type of liver cancer that derived from the hepatocytes. Other than HCC, liver cancers could also arise from the other organs as metastases to the liver, such as from colorectal and breast cancer. The unique feature of liver cancers is that there are supplied by the hepatic artery, rather than the main blood supply from the hepatic portal vein. Liver cancers can be diagnosed and confirmed using various modality including, computed tomography (CT), magnetic resonance imaging (MRI), emission imaging in nuclear medicine, tissue biopsy, surgery and clinical biochemistry tests from blood and urine samples. The tumours will be staged or classified based on the origin and spread (presence of metastases) of the tumours.

2.2.1 Staging of HCC

There are various methods of cancer staging for HCC, and one of the most common cancer staging method is the American Joint Committee on Cancer (2002) TNM system. This system only emphasizes on the features and extent of the tumour without taking into account the organ's functionality. TNM is the abbreviation of tumour, nodules, and metastases. The extent of the primary tumour, T is ranked from 1 to 4 with 1 is the single tumour with no vessel involvement and 4 is the tumour which has grown into a nearby organ or into the visceral peritoneum. If the tumour growth is found in any of the adjacent lymph nodes, the N will be ranked as 1, and 0 for tumour not involving any lymph nodes. For cancer which have spread or metastasised to the other parts of the body, the M will be ranked as 1. M will be noted 0 if the tumour is localised.

Due to lack of organ's functionality information with TNM staging, Okuda et al. (1985) developed a staging system for HCC patients based on retrospective review of

patient history. This system allows easier determination of treatments since more valuable prognostic information is given, rather than solely depending on the features and extent of the tumour. Other than this, the Barcelona Clinic Liver Cancer (BCLC) system and the Cancer of the Liver Italian Program (CLIP) system which, both depends on the Child-Pugh score, can also be used for the staging of HCC (American Cancer Society, 2016a).

The BCLC staging system (now preferred as the standard for HCC) can also be used based on the performance status (PS) of the patient, which depends on the number and size of the tumours and patient's condition. The system also depends on the liver function status, which is rated based on the Child-Pugh score (Cancer Research UK, 2016). The five stages of the BCLC system are shown in **Table 2.1**.

Table 2.1: The BCLC staging system with Child-Pugh score (Cancer Research UK, 2016).

Stage	Tumour	Performance Status (PS)	Child-Pugh Score
0	tumour <2 cm,	PS 0: patient feels well	Child-Pugh A: liver is working normally
A	single tumour <5 cm or up to three tumours all <3 cm	PS 0: patient feels well	Child-Pugh A or B: liver is working well
B	multiple tumours	PS 0: patient feels well	Child-Pugh A or B: liver is working well
C	cancer has spread into blood vessels, lymph nodes, or other organs	PS 1 or 2: patient does not feel well	Child-Pugh A or B: liver is still working
D	cancer has spread into blood vessels, lymph nodes, or other organs	PS 3 or 4: patient is unwell, needs help being looked after	Child-Pugh C: severe liver damage

2.2.2 Epidemiology of HCC

According to Ferlay et al. (2015) in the global cancer estimates of GLOBOCAN 2012, liver cancer is the second most common cause of death from cancer worldwide, after lung

cancer. It is the fifth most common cancer in men and ninth in women, with 7.5 % and 3.4 % incidence respectively. South-Eastern Asia is classified as one of the regions of high incidence rate of liver cancer. An estimate of 745,000 deaths from liver cancer worldwide was recorded in 2012, mostly contributed from the very poor prognosis of liver cancer. The most common type of liver malignancy is HCC, which developed from the liver hepatocytes.

Common risk factors of HCC include cirrhosis, alcoholism, and chronic infection with hepatitis B or C virus. In fact, it has been estimated that hepatitis B virus is responsible for 50 – 80 % of HCC cases worldwide, whereas 10 – 25 % of HCC cases are thought to be the outcome of hepatitis C virus infection (Palumbo, 2007; Anthony, 2001). Other risk factors include gender, with men are more susceptible to HCC than women; obesity; anabolic steroid usage especially in bodybuilders or athletes; history of diabetes; and inherited metabolic disease (Movva, 2013).

2.2.3 Available Treatment Options for HCC

The treatment options for HCC can be divided into two categories; non radiation-based and radiation-based treatments.

2.2.3.1 Non Radiation-based Treatments

Non-radiation treatments include surgical resection, liver transplantation, ablation, embolization, chemotherapy and immunotherapy. If the tumour is localised, has well-defined edges, and is not heavily vascularised especially by the main blood vessels, then, surgical resection or partial hepatectomy is highly recommended.

For liver transplantation to be considered, the tumour size should be <5 cm in diameter, or if 2 – 3 tumours are present, the size of each tumour should be <3 cm with no evidence

of macro-vascular involvement or extra-hepatic diseases, and whose liver function cannot support life following resection (Mazzaferro et al., 1996; Bismuth & Chiche, 1993). However, liver transplantation is limited in terms of availability, hence the time required for a patient to receive the donor liver is also uncertain. According to the Morrison et al. (2013), about half of the patients in the United States would have to wait for more than two years for a liver transplant.

For patients with a few small tumours (each with <3 cm) but are not qualified for surgery, and also for patients waiting for a transplant, tumour ablation can be used as an alternative. The most practiced type of ablation is radiofrequency ablation, which is a procedure where a needle probe is inserted through the skin, until the tip of the probe is located in the tumour. During the treatment, a high frequency current is emitted from the tip of the probe, transferring heat that will destroy the tumour cells. Other than that, ethanol ablation using concentrated alcohol, microwave thermotherapy and cryosurgery (used extremely cold gasses to freeze and kill the tumour) can also be used in tumour ablation (American Cancer Society, 2016b).

In certain cases where prominent blood supplies are involved, embolization can be done prior to surgery to reduce the blood supply to the tumour (to avoid patients from losing too much blood during surgery) and also to better define the tumour margin thus, results in better tumour removal with lesser remnants (reduce recurrence rate). Embolization is a nonsurgical, minimally invasive procedure which involves selective occlusion of blood vessels by intentional introduction of embolic particles. Taking into advantage the unique blood supply of the liver tumour from the hepatic artery, the femoral artery is punctured to make way for catheter insertion to the hepatic artery which provides the blood supply to the tumour. When the catheter end position is confirmed under fluoroscopic monitoring, a specific amount of embolic agents were introduced.

Chemotherapy drugs can also be labelled with embolic agents, in a procedure called transarterial chemoembolization or TACE, which embolised the blood supply to the tumour while at the same time delivering the cytotoxic drugs directly to the tumour.

Chemotherapy is a treatment regimen where cytotoxic drugs are given to the patients via either intravenous or oral administration. Cytotoxic drugs are highly toxic to actively dividing and multiplying cells, which are the main characteristics of the cancer cells. Other than that, cell tissues such as skin, hair and nails will also be affected by these drugs. Common side effects of chemotherapy include hair loss, and dry and easily irritated skin. Chemotherapy drugs for HCC include, 5-fluoroauracil, doxorubicin, cisplatin etc. Other than chemotherapy drugs, sorafenib which is a targeted drug taken via oral administration, has been increasingly used in systemic targeted therapy of HCC. Sorafenib works differently from standard chemotherapy drugs, hence causing less severe side effects.

Other alternative for HCC treatment include immunotherapy, which is a treatment where the patient's immune system is induced to fight against the cancer cells, by recognizing them as the target to be destroyed and eventually rejecting them. However, it is still currently under clinical trials and not considered as a standard treatment.

2.2.3.2 Radiation-based Treatments

Radiation treatments for HCC can generally be divided into external and internal beam types; external beam radiotherapy (EBRT) and transarterial radionuclide therapy, respectively. There are four types of treatment intents in EBRT; radical, adjuvant, neo-adjuvant and palliative treatments. Radical therapy is intended for a high rate of local tumour control, especially for early stage tumours. This involves complex planning and a protracted fractionated course of treatment. The dose rate in radical treatment is

normally higher than the other treatment intents. EBRT is commonly used in an adjuvant setting following initial surgery or chemotherapy. The aim of adjuvant treatment is to eradicate loco-regional residual tumour growth. Adjuvant therapy doses are usually slightly less than the doses used for radical treatment, but treatment planning may be just as complicated. In neo-adjuvant treatment, EBRT or chemo-radiotherapy (chemotherapy plus EBRT) may be given prior to surgery either to increase operability by down-staging the disease and/or to treat loco-regional microscopic mass. For terminal stage tumour, palliative treatment is necessary for these patients which is aimed to increase the quality of the patient's life, reduce pain and sometimes can also extend the life expectancy of the patients. Palliative therapy is given over a shorter period of time with larger fraction sizes but a lower overall dose. Patient set up and radiotherapy techniques are often very simple. Treatment may be given as a single or as a short fractionated course. For HCC, EBRT is not often used due to low tolerance of normal liver tissue towards the high dose rate of the beam. EBRT for HCC can be delivered using a linear accelerator or a Cyberknife, in the techniques called stereotactic body radiation therapy or 3-dimensional conformal radiation therapy.

Transarterial radionuclide therapy may be considered for the treatments of HCC, using unsealed radionuclide sources. Therapeutic radionuclides are bounded to a specific carrier which could be of protein structure or synthetic materials, where the deliveries are done similar to embolization procedure. The agents include lipiodol labelled with either iodine-131 (^{131}I) or rhenium-188 (^{188}Re), and resin or glass microspheres labelled with yttrium-90 (^{90}Y). Unlike lipiodol which will eventually degrades via protein denaturing, material based microspheres are non-biodegradable, hence will act as permanent embolic agents in the treatment called transarterial radioembolization (TARE). **Table 2.2** summarised the options available for the treatment of HCC.

Table 2.2: Summary of treatment options for HCC (Saraswat et al., 2014).

Types	Treatment options	Examples of agent/ drug/ source/ radiation used
Non-radiation	Surgical resection	-
	Liver transplantation	-
	Ablation	Radiofrequency, ethanol, microwave, nitrogen or argon gasses
	Embolization/ TACE	Ethiodol, polyvinyl alcohol or gelatine microspheres; labelled with chemotherapy drugs for TACE
	Chemotherapy	5-fluoroauracil, doxorubicin and cisplatin
	Targeted therapy	Sorafenib
	Immunotherapy	Nivolumab
Radiation	EBRT	stereotactic body radiation therapy or 3-dimensional conformal radiation therapy, using linear accelerator or Cyberknife
	Transarterial radionuclide therapy	^{131}I- or ^{188}Re-lipiodol, ^{90}Y-microspheres

2.2.3.3 Recommended Treatment Algorithm for HCC

Although various treatments are available for curative and palliative treatments of HCC, the preferred treatments are based on the BCLC algorithm (Forner et al., 2012). The incorporation of TARE into the algorithm (Han et al., 2011) has been recommended as alternative, as shown in **Figure 2.3**.

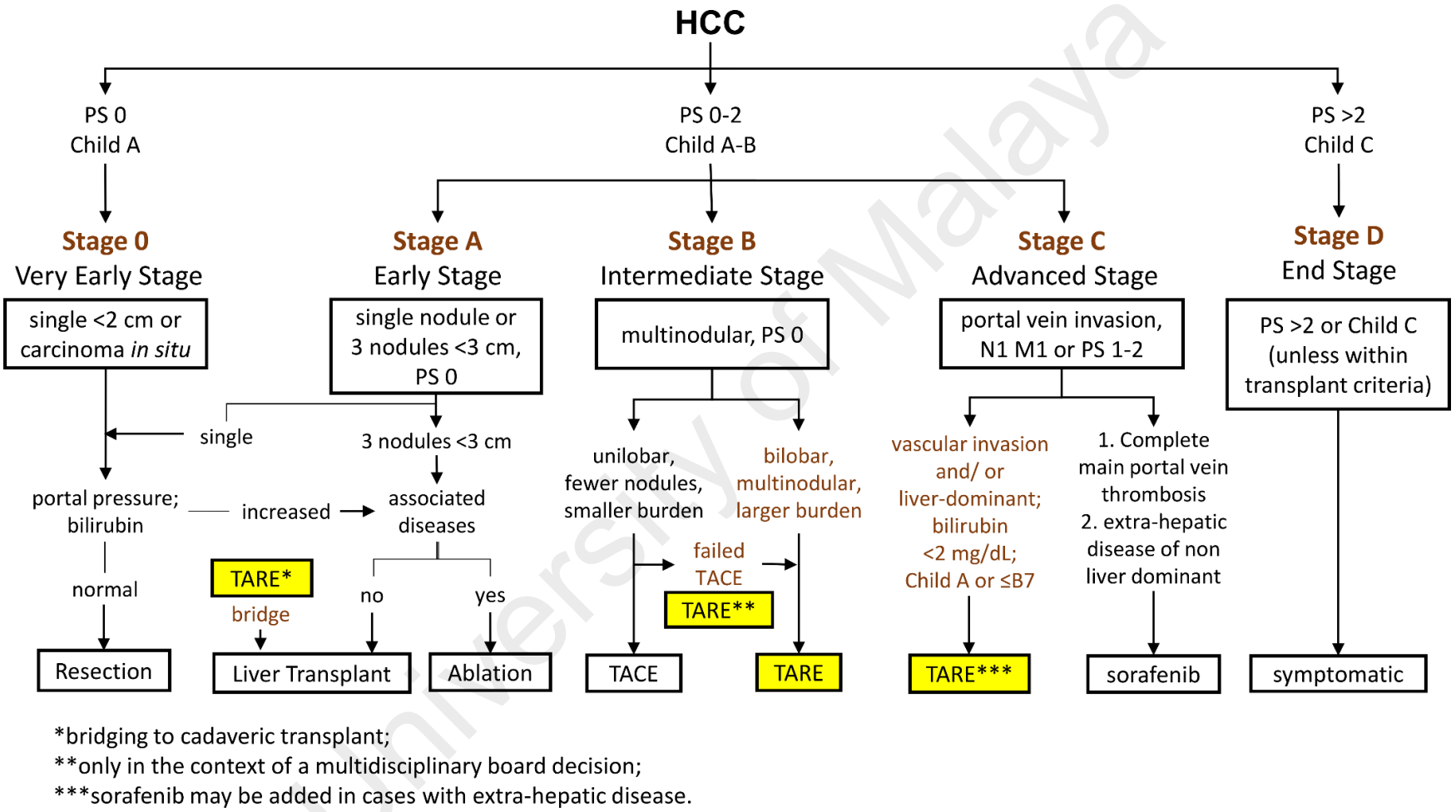

Figure 2.3: Integration of transarterial radioembolization (TARE) into the Barcelona Clinic Liver Cancer (BCLC) algorithm for the treatment of hepatocellular carcinoma (HCC) (Han et al., 2011). PS: performance status; TACE: transarterial chemoembolization.

2.3 Radionuclide Therapy

The requirements for determining the suitable radiopharmaceuticals for theranostic usage may be divided into the physical and biochemical characteristics. Physical characteristics include the half-lives, types and energies of the emissions, methods of production, daughter products, and radionuclide purity (Hoefnagel, 1991), which all depends on the characteristics of the radionuclides. The biochemical aspects include tissue targeting mechanism, retention of the radionuclide in the tumour, *in vivo* stability, and toxicity (Kassis & Adelstein, 2005), all depends on the carrier particles which the radionuclide is labelled to.

2.3.1 Requirements for Suitable Therapeutic Radionuclides

The most important aspect for a suitable radionuclide is the physical half-life, which is readily known based on published radionuclide data. However, following *in vivo* administration, the effective half-life of the radionuclide is the parameter to be considered, as shown in **Equation 2.1**, where T_e, T_p and T_b is the effective, physical, and biological half-life, respectively.

$$T_e = \frac{T_p T_b}{T_p + T_b} \qquad \textbf{2.1}$$

The biological half-life requires the understanding of radiotracer's spatial and temporal *in vivo* distribution, which include radiotracer's delivery, uptake, metabolism, clearance and excretion (Yeong et al., 2014). A good radiopharmaceutical possesses physical half-life in the range of 6 h to 7 d (Qaim, 2001). A very short physical half-life limits the treatment practicality, whilst a long physical half-life is harmful for the people surrounding the patients. This consequently requires the patient to be admitted, which will add to the treatment costs. For biological half-life, depending on the tracers used, if

the tracer is meant to retain within the patient permanently, a long physical half-life should be avoided. Oppositely, the tracer should have a retention properties long enough so that the radiation dose can be delivered to the tumour sufficiently. If biological half-life is too short, the radionuclide will be carried away as radioactive waste with high activity, hence, extensive radioactive waste handling needs to be implemented (Yeong et al., 2014).

For therapy, an ideal radiation type should have high linear energy transfer (LET) e.g. α-particle and β-particle. These type of emissions allow larger ionisations per length of travel, and since they are highly interactive, they will be fully deposited within a smaller range in tissue, usually in millimetre (mm). This is advantageous as only minimal radiation protective measures will be required, since β-radiation cannot penetrate through the patient's body. However, some β-emitting radionuclide decays with a proportion of γ-emission. This type of radiation could be advantageous as it provides the diagnostic capability allowing the determination of the *in vivo* distribution of radiopharmaceutical, given that the energy and intensity is not too high. If the amount of γ-emission is too high, more radiation protective measures need to be taken (Yeong et al., 2014).

Depending on the type of tumour, the energy and intensity of the emitted radiation should be chosen so that the energy and intensity of non-penetrating radiation (i.e. α and β-radiation) is higher as compared to the energy and intensity of penetrating radiation (i.e. γ-radiation, x-rays or Auger electrons), if present. Since energy contributes directly to the resulting absorbed dose, hence a high energy non-penetrating radiation is most preferred, with consideration of the compatibility of the resulting particle range in tissue with the type of tumours to be treated.

A good radiopharmaceutical is those which decay into stable daughter product. For slightly unstable daughter product, the daughter nuclide should at least be short-lived.

This is because, if the daughter nuclide is unstable, it will contribute to the increase in absorbed dose thus, consideration to the portion of dose delivered from the daughter product should be taken, so that it would not affect the treatment plan. Hence, radionuclide with stable daughter product is highly preferred.

A lot of methods of radiopharmaceutical production are available these days. A radionuclide could either be produced by neutron activation in a nuclear reactor, from decay of other radionuclide in a generator, by target activation in a cyclotron, and from naturally or man-made fusion or fission interaction. Amongst all these, the most common method is via neutron activation in a nuclear reactor. However, not all elements can be neutron activated hence the pathway of production needs to be studied first. Therapeutic radionuclides are seldom produced in a cyclotron or generator since very high energy is required to achieve activities in therapeutic ranges, hence are relatively difficult. Thus, these methods are usually used in producing diagnostic radionuclides such as for production of fluorine-18-fluorodeoxyglucose (FDG) using a cyclotron and technetium-99m (^{99m}Tc)-macroaggregated albumin (MAA) via a molybdenum (Mo) generator. However, for some remote facilities sometimes a cyclotron is used for example in the production of rhenium-186 (^{186}Re), but this method may be very costly. Fusion interaction is not easy to be executed since it requires an incredibly high energy and most of the time naturally rare, hence it is the least available and preferred method for radionuclide production. Fission interaction on the other hand are sometimes use such as in the production of strontium-90 (^{90}Sr) which decay into ^{90}Y and ^{131}I which is commonly used in thyroid ablation.

A good radiopharmaceutical should possesses high radionuclide purity so that no other radionuclide will contributes to the absorbed dose and no long-lived radionuclide is present within the formulation. This can be further increased by producing the

radionuclide prior to radiolabelling, since it is possible that other radionuclides may be produced following the neutron activation of the carrier microparticles.

2.3.2 Choices of Carrier Agents / Tracers

The biochemical aspects related to a good tracer as mentioned by Qaim (2001) are, good and selective concentration and prolonged retention in the tumour, and minimum uptake in the normal tissue. Depending on the mechanism of selective uptake of the tumour either by bone deposition, protein binding, metabolic uptake etc., the ratio of the radiopharmaceuticals concentration on the tumour to that of other organs or tissues should be high so that the radiation can be delivered sufficiently while sparing the to the other normal tissues.

If the tracer is made of protein, it should be stable enough during administration and able to maintain *in vivo* long enough for sufficient radiation delivery before being metabolised or excreted (Yeong et al., 2014). Hence for a good radiation delivery, a balanced of optimal biological and physical half-lives should be chosen which results in optimal effective half-life. If the biological half-life is long, a relatively short-lived radionuclide is preferred so that the patient will not receive exceeded dose. Still, this consideration is best made exclusively according to the type of tumour to be treated and the administration and uptake method. However, if the uptake is slow, a radionuclide with relatively long physical half-life should be used so that the radionuclide will not decay completely before they were able to reach the targeted tumour.

Other aspect to be considered is the size of the tracer. For example in TARE with ^{90}Y-microspheres, the particles should be large enough that they will not pass through the tumour vasculature into the other organs i.e. the lungs, but small enough that they will be able to go deep inside the tumour capillaries. Other biochemical characteristics include

low toxicity and biocompatible, optimum specific gravity, suitable pH, and good clearance (except for permanent tracer) (Yeong et al., 2014).

2.4 Transarterial Radioembolization (TARE) with ^{90}Y-microspheres

Different from the typical radionuclide therapy, TARE with ^{90}Y-microspheres does not depends on the systemic circulation and typical physiological uptake. The ^{90}Y-microspheres were administered to the hepatic artery via a catheter through the femoral artery. TARE with ^{90}Y-microspheres allows the delivery of high tumour dose in relative to the dose received by normal liver tissue and other adjacent organs (to as high as 150 Gy), without significant liver toxicity (Sarfaraz et al., 2004), which is not possible for EBRT. There are two commercially available radioembolic agents for TARE; glass-based TheraSphere® (Nordion, Canada) and resin-based SIR-Spheres® (SIRTex, Australia), which both were approved by the United States Food and Drug Administration (FDA) as medical devices. TheraSphere® was approved under Humanitarian Device Exemption for radiation treatment, or as neoadjuvant to surgery or transplantation, for HCC patients (BTG International, 2013). On the other hand, SIR-Spheres® was approved under Premarket Approval for liver metastases secondary to colorectal cancer (FDA, 2002). The characteristics of these two microspheres are shown in **Table 2.3**.

Table 2.3: Physical comparison between TheraSphere® and SIR-Spheres® (Salem & Thurston, 2006; Nordion, 2004; Sirtex, 2004).

Characteristics	TheraSphere®	SIR-spheres®
Isotope	^{90}Y	^{90}Y
Physical half-life (h)	64.2	64.2
Material	Glass	Resin
Particle size (µm)	20 – 30 µm	20 – 60 µm
Activities (GBq) available per vial	3, 5, 7, 10, 15, 20	3
Number of microspheres (million) per vial	1.2, 2, 2.8, 4, 6, 8 respective to above activities	40 – 80
Activity (Bq) per sphere	2,500	50
Shelf-life	7 d	24 h
Embolic effect	Mild	Moderate
Specific gravity	High	Low

2.4.1 SIR-Spheres® versus Therasphere®

Both ^{90}Y-microspheres possess their own advantages and drawbacks. A comparison between these two was highlighted by Salem and Thurston (2006). For SIR-Spheres®, since it is supplied in a fix activity of 3 GBq, this allows the flexibility in manipulating the specific activity for every patient. The lower specific gravity of the resin microspheres provide better suspension of the dose volume which may result in better distribution within the tumour. Finally, since each microsphere only contained a specific activity of 50 Bq, this opens up for the possibility of dose fractionation (Deutsch & Huguet, 2005).

However, the device's shelf-life only lasts for 24 h, which limits the clinical flexibility and patient scheduling. Moreover, the needs for physical decanting of the dose vials could potentially lead to human error in administered activity and also possible handling spills which will require decontamination procedure that might affect the work progress of the institution. SIR-Spheres® possesses a highly embolic property due to high number of

microspheres. This embolic effect may cause hypoxia, thus probably limiting the effect of radiation (Das, 2002; Koukourakis, 2001). The large number of microspheres also cause uncertainty whether any therapeutic effect is a result of radiation or embolic effects.

For TheraSphere®, the v-bottom vial configuration ensures that most of the microspheres are confined to a fixed volume within the sealed vial. Since the activity is determined via dose calibrator which only measures the Bremsstrahlung radiation produced by beta with the vial shielding, hence the measurement accuracy will depends on the volume of the microspheres (the volume of suspended microspheres is limited to only less than 0.5 ml). Due to no physical manipulating required for TheraSphere® dose vial, this automatically reduce the potential dosing error and less exposure time to the staff handling the product. Other than that, the relatively low number of microspheres ensure that more than 95 % successful delivery without reaching stasis or complete plate vessel occlusion, allowing high radiation dose delivered with fewer microspheres. Hence, less embolic administration allows high oxygenation for the tumour, which will improved the radiation dose response (Sato et al., 2006; Liu et al., 2005) and also correlates with low clinical toxicities compared to embolic therapies (Goin et al., 2004; Salem et al., 2004). Finally, unlike SIR-Spheres®, the shelf-life for TheraSphere® is 7 d which allows clinical flexibility of patient treatment and scheduling.

The drawbacks for TheraSphere® is that the high specific activity per microsphere limits the possibility of dose fractionation, since maximum hepatic radiation tolerance might be achieved in just a single treatment. In opposite to SIR-Spheres® resin microspheres, the high specific gravity of glass TheraSphere® microspheres may limit the distribution of the microspheres in the liver. And lastly, the low number of microspheres result in an insufficient tumour coverage for larger tumour.

2.4.2 Lung Shunting (LS)

Before a patient can be considered a candidate for TARE with ^{90}Y-microspheres, a pre-assessment to quantify the lung shunting (LS) will be required. The purpose of this procedure is to determine the presence of extrahepatic deposition of the microspheres to the lungs, which if not being quantify, will contribute to excessive dose to lungs when the treatment is being delivered. According to both TheraSphere® (Nordion, 2004) and SIR-Spheres® package inserts (Sirtex, 2004), the formula for LS is expressed in **Equation 2.2**. LS is calculated through imaging of the liver using ^{99m}Tc-MAA with either planar imaging or single photon emission computed tomography (SPECT). The method of administration for ^{99m}Tc-MAA is identical to ^{90}Y-microspheres as it is assumed that the distribution of MAA depicts the distribution of the microspheres. 4 – 5 mCi of ^{99m}Tc-MAA activity is delivered intra-arterially during this procedure.

$$\text{LS (\%)} = \frac{\text{Total counts in lungs}}{\text{Total counts in liver + Total counts in lungs}} \times 100\ \% \qquad \textbf{2.2}$$

According to Salem and Thurston (2006), there are three potential causes of the overestimation of LS. First, the lead time between ^{99m}Tc-MAA injections in the angiography suite to the time of imaging in nuclear medicine department. If the time taken between the transitions is too long, the proteinaceous ^{99m}Tc-MAA may break down into smaller particles, as a result of protein catabolism. Hence, it is crucial that the patient is transferred for imaging as soon as possible. Second, although the normal manufactured size of ^{99m}Tc-MAA particles are in range of 30 – 90 μm, a small percentage of the particles will fall out of this range. Particles which manufactured smaller than 8 – 10 μm, will shunt to the lungs. Third, free ^{99m}Tc may result in the inaccuracy of the LS estimation.

It should be noted that LS should not exceed 20 % for TARE with ^{90}Y-microspheres to be proceed. For patients with LS exceeding 20 %, alternative treatment option may be considered. The lungs can tolerate 30 Gy per treatment session and 50 Gy cumulatively (Ho et al., 1997). Hence, when LS is present, a calculation of the total pulmonary dose for the entire treatment should be estimated, and treatment will only be delivered if total lung dose do not exceed 50 Gy. For patients with compromised lung function, a conservative dose of 15 Gy per treatment and cumulative 30 Gy may be implemented (Salem & Thurston, 2006).

2.4.3 Determination of Administered Activity

There are three methods available in determining the amount of administered activity for TARE with ^{90}Y-microspheres; the empirical method, the body surface area (BSA) method, and the partition model (PM). Following the activity calculation, the value will be further corrected based on the LS obtained prior to the procedure. LS which is obtained through a series of image projections, affects the calculated activity by reducing the amount, depending on the value of LS as shown in **Table 2.4**. The aim of dose reduction is to ensure that the amount of ^{90}Y reaching the lungs did not exceed the maximum lung dose (30 Gy), so to avoid any complications i.e. radiation pneumonitis.

Table 2.4: Reduction of calculated administered activity based on lung shunting (LS).

LS (%)	Reduction of administered activity (%)
< 10	No reduction
10 – 15	20
15 – 20	40
> 20	No treatment

2.4.3.1 Empirical Method

The empirical method depends solely on the value of the tumour involvement as shown in **Equation 2.3**. For tumour involvements bigger than 50 %, 3 GBq is recommended, follows by 2.5 and 2 GBq for tumour involvements in the range of 25 – 50 % and less than 25 %, respectively. However, the usage of this method has been reduced due to lack of scientific basis.

$$\text{Tumour involvement (\%)} = \left(\frac{\text{Tumour volume}}{\text{Liver volume}} \right) \times 100 \qquad \textbf{2.3}$$

2.4.3.2 Body Surface Area (BSA) Method

The BSA method was formulated based on whole liver infusion. In case if a lobar infusion is intended, the infused activity should be calculated assuming whole liver volume, and later corrected to the correspond volume of the lobe to be infused (Salem & Thurston, 2006). BSA dosimetry depends greatly on the tumour involvement. The administered activity, A (GBq) is expressed as shown in **Equation 2.4**.

$$\text{A (GBq)} = \text{BSA } (\text{m}^2) - 0.2 + \left(\frac{\text{tumour involvement (\%)}}{100} \right) \qquad \textbf{2.4}$$

where, the BSA (m^2) is obtained via an equation by Dubois and Dubois (1916), with known height (m) and weight (kg) of the patients, as shown in **Equation 2.5.**

$$\text{BSA } (\text{m}^2) = 0.20247 \times \text{height}^{0.725}\ (\text{m}) \times \text{weight}^{0.425}\ (\text{kg}) \qquad \textbf{2.5}$$

2.4.3.3 The Partition Model (PM)

Unlike the two former methods, other than the estimation of administered activity, PM also provides the estimation of the absorbed dose to tumour, normal liver tissue and both lungs. It was derived by Ho et al. (1996) based on the Medical Internal Radiation Dose (MIRD) scheme and assuming a complete deposition of energy within a compartment, it depends only on the initial activity in the compartment and the compartment's total mass (Ho et al., 1996). Thus, the absorbed dose, D in a compartment is calculated using **Equation 2.6**, where, A_o is the activity (GBq) in the compartment of mass, m (g).

$$\text{Absorbed dose, D (Gy)} = \frac{49670 \times A_o(\text{GBq})}{m\ (g)} \qquad \textbf{2.6}$$

In order to determine the activity distributed within each organ, the LS and tumour-to-normal liver uptake ratio (T/N) are obtained from the pre-treatment imaging using ^{99m}Tc-MAA. The values are calculated using **Equation 2.2** and **Equation 2.7**, respectively.

$$\text{T/N} = \frac{\text{Total counts in tumour}}{\text{Total counts in liver - Total counts in tumour}} \qquad \textbf{2.7}$$

Thus, the activity uptake in both lungs is calculated using **Equation 2.8**, where, A is the total administered activity (GBq), and A_L is the activity (GBq) taken up by both lungs.

$$A_L = A\left(\frac{LS(\%)}{100}\right)\text{GBq} \qquad \textbf{2.8}$$

The remainder activities that goes to the tumour, A_T and normal liver, A_N are shown in **Equation 2.9**, which correspond to T/N as shown in **Equation 2.10**, where, m_T and m_N are the mass (g) of tumour and normal liver, respectively.

$$A_T + A_N = A - A_L \quad \textbf{2.9}$$

$$\text{T/N} = \frac{A_T / m_T}{A_N / m_N} \quad \textbf{2.10}$$

The desired absorbed dose is adjusted such that, patients with cirrhosis will be given a lower dose or treated under a fractionated regimen. According to Salem and Thurston (2006), for patients with cirrhosis, a range of 80 – 100 Gy is considerable for a single dose. Of patients without presence of cirrhosis, a higher dose of 100 – 150 Gy may be considered. Hence, a range of 80 – 150 Gy is recommended for a single dose. If dose fractionation is considered, a repeated LS assessment should be carried out since LS tend to increase after the treatment with ^{90}Y (Ho et al., 1996).

PM is considered as the most reliable method in determining the activity to be administered due to much detail scientific basis and also the possibility in knowing the resulting absorbed dose to the compartments involved. However, for PM to be considered, the tumour involved should be clearly delineated from the CT and ^{99m}Tc-MAA images. For the tumours with poor defined edges, the BSA method will then be used as an alternative approach.

2.4.4 Clinical Efficacy of TARE with ^{90}Y-microspheres

Over years of commercialization of TARE with ^{90}Y-microspheres, it has been increasingly used by institution all over the world in treating unresectable liver cancers, especially HCC. Kooby et al. (2010) suggested that TACE and TARE provide similar effectiveness and toxicity based on their own institutional experience, each with 6 months medial survival. However, the study only included patients who underwent TARE or TACE as the only treatment. TARE is shown to be more efficient when combined with

other treatments for a more radical intent such as, when used neoadjuvant to chemotherapy (Vente et al., 2009a). As mentioned by Inarrairaegui et al. (2012), TARE with ^{90}Y-microspheres is more efficient to be used in adjuvant therapy and proven able for tumour down staging, to be proceeded with resection, transplantation or ablation. This finding was supported by Sangro et al. (2009), for large or multiple lesions.

TARE is also safe to be used for patients with advanced HCC and those with compromised liver function, as proven by Hilgard et al. (2010). This can be done by modifying the selection criteria and using conservative models for calculating the administered activity (Sangro et al., 2006). Other than HCC, TARE with ^{90}Y-microspheres can also be used as a therapeutic option for patients with intrahepatic cholangiocarcinoma (Ibrahim et al., 2008) and unresectable hepatic metastases from both breast cancer (Coldwell et al., 2007) and colorectal carcinoma (Kennedy et al., 2006). From the technical perspective, when compared between resin and glass ^{90}Y-microspheres, Vente et al. (2009a) found that for HCC cases, TARE with the resin microspheres is significantly more effective than glass microspheres with 89 % and 78 % response, respectively.

According to Goin et al. (2005), the risk of liver toxicities in patients with unresectable HCC treated with TheraSphere® increases with increasing pre-treatment total bilirubin level and liver dose to a maximum of 150 Gy, for a single administration. Most of the toxicities resolved; however, those that did not resolve were attributed to tumour progression or advancing cirrhosis. Of all reported serious adverse events, the most common were elevations and liver enzymes and bilirubin, and upper gastrointestinal ulceration (Dancey et al., 2000). In comparison to EBRT, the normal liver tissues showed more tolerance to internal radiation, according to Lau et al. (1998).

2.4.5 Published Alternative Radionuclide-Labelled Microparticles for TARE

TARE were first initiated by Muller and Rossier (1951), using zinc-65 (^{65}Zn) and gold-198 (^{198}Au) microspheres to treat lung malignancies. Following this study, multiple researchers started to adopt similar principal with other radionuclides and microsphere types for treating unresectable tumours especially for HCC. Preceding the United States FDA approval of TheraSphere®, Hafeli et al. (1999) developed rhenium (mixture of both ^{186}Re and ^{188}Re) glass microspheres and studied the biodistribution and effectiveness of the microspheres in Sprague-Dawley rats. The advantage of Re isotopes over ^{90}Y was that, the neutron activation cross-section is relatively high thus, these Re isotopes are easier and cheaper to be produced since they did not require a neutron flux too high to produce high activity as compare to ^{90}Y. Other than that, the presence of gamma radiation with the decay is also advantageous in determining the *in vivo* distribution. However, Re glass microspheres have not been commercially produced for clinical use since then.

Earlier in that decade, Mumper et al. (1991) developed a biodegradable poly-l-lactic acid (PLLA) microspheres labelled with holmium-166 (^{166}Ho). Unlike glass, PLLA type microspheres have a density near to human blood plasma. Glass microspheres with relatively higher density may result in an inferior *in vivo* distribution as compared to PLLA. Similar to ^{186}Re and ^{188}Re, ^{166}Ho also contains a significant portion of gamma radiation which is beneficial for imaging studies. However, its short physical half-life of only 26.8 h requires ^{166}Ho to be administered in a very high activity to result in the same amount of dose from ^{90}Y or Re isotopes. Plus, its activation cross-section is relatively lower as compare to both ^{186}Re and ^{188}Re. This work was continued by a Utrecht University group (Vente et al., 2010; Nijsen et al., 2001), which progressed to a phase I clinical study (Smits et al., 2012).

Instead of replacing ^{90}Y, Poorbaygi et al. (2011) incorporates lutetium-177 (^{177}Lu) into ^{90}Y loaded glass-based microspheres so that they possess imaging capabilities. Glass microspheres were used instead of PLLA due to the reason that it is highly stable even after long neutron activation period, which is not the case for PLLA microspheres. The advantage of ^{177}Lu over the other radionuclides is that lutetium-176 (^{176}Lu) have a very high cross-section of 2050 barn, hence, it is able to produce high specific activity with shorter activation time. However, its physical half-life of 6.73 d is considered significantly long. Plus, due to the presence of gamma radiation, protective measures need to be taken such that the patient may need to be hospitalised for a longer period of time.

2.5 ^{153}Samarium (^{153}Sm)

2.5.1 Sources of Sm

Samarium (Sm) is the 62nd element in the periodic table which belongs to the transitional or rare earth metal group. It was first discovered by Paul Émile Lecoq de Boisbaudran, a French chemist, and was named after samarskite, which is a mineral from which samarium is extracted (Emsley, 2001). Other than that, samarium can also be obtained from several other minerals which include; gadolinite, cerite, monazite and bastnasite, with the latter two as the most common commercial sources of samarium. These minerals can be found in China, Brazil, USA, Sri Lanka, India and Australia (Emsley, 2001).

2.5.2 Isotopes of Sm

Sm naturally exists in solid form with standard atomic weight of 150.36 a.m.u. Radioisotopes of Sm include a range from samarium-144 (^{144}Sm) to samarium-154

(^{154}Sm), with samarium-152 (^{152}Sm) as the most naturally abundant isotopes (26.7 %) as shown in **Table 2.5**. ^{152}Sm can be activated via neutron activation to produce unstable ^{153}Sm for therapeutic purposes. ^{153}Sm with half-life of 46.3 h, decays into stable europium-153 (^{153}Eu) by emitting beta particles (maximum E_{β^-} = 807.6 keV) with 103.2 keV gamma radiation. The decay scheme of ^{153}Sm is depicted in **Figure 2.4**.

Table 2.5: Isotopes of samarium (Awang et al., 1993).

Isotopes	Natural Abundance (%)	Neutron activation cross-section (10^{-24} cm^2)	Daughter nuclide	Half-life
^{144}Sm	3.1	0.7	^{145}Sm	340 d
^{147}Sm	15.1	57	^{148}Sm	8 x 10^{15} y
^{148}Sm	11.3	4.7	^{149}Sm	Stable
^{149}Sm	13.9	40, 140	^{150}Sm	Stable
^{150}Sm	7.4	104	^{151}Sm	87 y
^{152}Sm	26.7	210	^{153}Sm	46.3 h
^{154}Sm	22.0	5	^{155}Sm	22.4 min

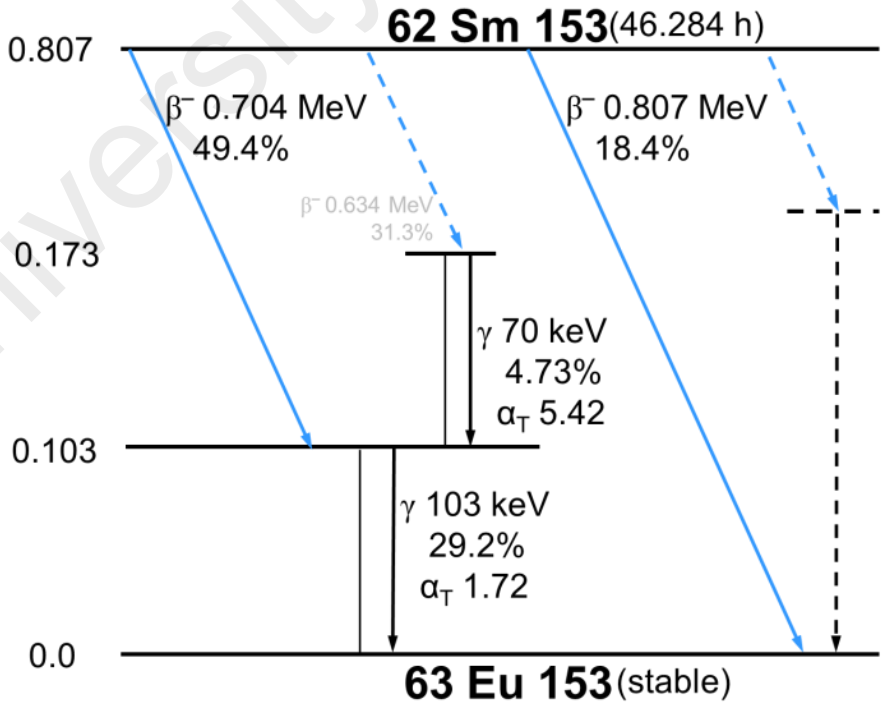

Figure 2.4: A simplified decay scheme of ^{153}Sm (Adapted from nucleonica.net (2013)).

^{152}Sm can be commercially obtained from samarium chloride ($SmCl_3$) and samarium oxide (Sm_2O_3) which appear in solid chunks and powdery form, respectively. Taking advantage of the significantly high thermal neutron activation cross-section of ^{152}Sm (210 barn), a small amount of these materials can produce radioactivity high enough for therapeutic purposes. This could be achieved by manipulating the irradiation time of ^{152}Sm in the nuclear reactor based on estimated target activity. During the activation, a thermal neutron from the reactor core will be captured by the atomic nucleus of ^{152}Sm, in the ^{152}Sm (n, γ) ^{153}Sm reaction, emitting one gamma ray to produce ^{153}Sm.

2.5.3 Medical Applications of ^{153}Sm

^{153}Sm is chosen to be used in this study due to the presence of gamma radiation with optimum energy of 103.2 keV, which is sufficient for biodistribution studies, and the physical half-life of 46.3 h is very ideal for radionuclide therapy. The comparison of physical characteristics for various radionuclides that have been suggested for TARE of HCC are shown in **Table 2.6**.

^{153}Sm has been widely used for bone pain palliation, tagged with ethylenediamine tetramethylenephosphonate (EDTMP), alternatively called lexidronam with commercial name of Quadramet®. It is commonly used to reduce bone pain from metastases from lung, prostate, and breast cancer, and also osteosarcoma. Yeong et al. (2012) prove that ^{153}Sm can be successfully used, as a surrogate for indium-111 (^{111}In) for the purpose imaging in gastrointestinal motility studies. However, it has yet to be practiced clinically.

Table 2.6: Physical properties of selected radionuclides which had been used for TARE of HCC. (LNHB (2014),*IAEA (1974)).

Radionuclide	**^{90}Y**	**^{131}I**	**^{153}Sm**	**^{166}Ho**	**^{177}Lu**	**^{186}Re**	**^{188}Re**
Physical $t_{1/2}$ (h)	64.08	192.48	46.32	26.80	159.6	89.28	17.00
Principal Eγ (keV) [% yield]	None	364.5 [81.7]	103.2 [29.2]	80.6 [6.2]	208.4 [10.4]	137.2 [9.4]	155.0 [15.1]
Max $E_β$ (keV) [% intensity]	2279.8 [99.98]	606 [89.3]	807.6 [19.5]	1854.5 [48.2]	498.3 [79.3]	1069.5 [92.5]	2120.4 [71.7]
Mean β range in soft tissue (mm)	4.0	0.4	0.6	2.5	0.2	1.1	3.1
Max β range in soft tissue (mm)	11.3	2.3	2.5	8.0	1.8	4.5	10.4
Production method	^{89}Y(n,γ)^{90}Y ^{90}Sr/^{90}Y generator	^{130}Te(n,γ,β-)^{131}I	^{152}Sm(n,γ)^{153}Sm	^{165}Ho(n,γ)^{166}Ho	^{176}Yb(n,γ,β-)^{177}Lu ^{176}Lu(n,γ)^{177}Lu	^{185}Re(n,γ)^{186}Re	^{187}Re(n,γ)^{188}Re ^{188}W/^{188}Re generator
Daughter nuclide	^{90}Zr	^{131}Xe	^{153}Eu	^{166}Er	^{177}Hf	^{186}Os (unstable), ^{186}W	^{188}Os
***Thermal neutron activation cross section (barn)**	1.2 ± 0.1	0.2 ± 0.1	210 ± 10.0	61.5 ± 2.0	5.5 ± 1.0 (^{176}Yb) 2050 ± 50 (^{176}Lu)	110 ± 5.0	75 ± 4.0

2.6 Medical Internal Radiation Dose (MIRD)

Since radiation is delivered internally in radionuclide therapy, other neighbouring organs will also receive some fractions of the tumour dose depending of the type and energy of the radionuclide being administered. Unlike in the diagnostic field where a lower dose range is used, much attention needs to be given for the dosimetry in therapeutic radionuclides. Therefore, extensive knowledge related to the dose received by non-target or normal tissue is a crucial aspect to be considered. Consequently, the effectiveness of treatment can be determined by relating dosimetry information to the radiobiological parameters of each related tissue or organ. This can be achieved by estimating the radiation dose using the MIRD Scheme, developed by the MIRD Committee of the Society of Nuclear Medicine and Molecular Imaging (SNMMI) of the United States (SNMMI, 2016).

2.6.1 Absorbed Dose, D

Dosimetry in general is a study to estimate the dose received by a specific tissue after exposure to radiations. The term "dose" can be further subdivided into absorbed, equivalent, and effective doses. Absorbed dose, D can be defined as the amount of energy, E (J) deposited per unit mass, m (kg) of human tissue or other media, as shown in **Equation 2.11**. D is expressed in units of $J.kg^{-1}$ or Gray (Gy), where 1 Gy is equivalent to 100 rad.

$$D = \frac{E}{m} \qquad \textbf{2.11}$$

The absorbed dose, D_t to the target region, t can be presented as **Equation 2.12**.

$$D_t = \sum_s \frac{\tilde{A}_s \Delta \phi_{t \leftarrow s}}{m_t} \qquad \textbf{2.12}$$

where, $\tilde{A}_s$ is the cumulated activity or the total number of disintegrations in the source organ, s; Δ is the energy emitted by the radionuclide per disintegration; $\phi_{t \leftarrow s}$ is the fraction of energy emitted by the radionuclide in source region, s which is absorbed by the target region, t; and m_t is the mass of the target t.

Snyder et al. Snyder et al. (1975), has simplified **Equation 2.12** by introducing S-factors, which is the absorbed dose to a target region per unit cumulated activity in the sources. S-factor values are exclusive for every source-target organ pair and radionuclide, and are calculated by simulating patients' anatomy using standard phantom models, followed by absorb dose calculation using Monte Carlo (MC) simulation (Snyder et al., 1978). Many S-values data has been published since then to provide for more specific cases using female and paediatric models (Cristy & Eckerman, 1987) and also for organ sub-regions (Bouchet et al., 1999; Mardirossian et al., 1999; Stabin, 1994; Watson et al., 1989) and cellular dimensions (Goddu et al., 1994).

The simplified equation incorporating the S-factors is shown in **Equation 2.13**, where S(t←s) is the S-factor of radiation emitted from the source region, s to target region, t. Since S-values are readily available from previous published data, the only unknown variable which needs to be acquired from each patient before absorbed dose estimation can be completed is the cumulated activity, $\tilde{A}_s$.

$$D_t = \sum_s \tilde{A}_s S(t \leftarrow s) \qquad \textbf{2.13}$$

In order to obtain the input for the calculation of cumulated activity, $\tilde{A}_s$ consecutive images of patient's specific body region after the injection of radiopharmaceutical needs to be taken by means of emission planar imaging, SPECT or positron emission tomography (PET). As the images are obtained, region of interest will be drawn on each image in order to get the level of activity per image per time. From these values, a time-activity curve for the particular organ is generated, followed by the integration of the curve to obtain the cumulated activity, $\tilde{A}_s$ received by the region.

2.6.2 Equivalent Dose, H_t

The biological effects of an absorbed dose depends greatly on the type and amount of radiation that delivers the energy. This can be quantify by introducing the equivalent dose, H_t (Sv) (**Equation 2.14**), which is the absorbed dose corrected to the type of radiation that deposits the energy, based on its radiation weighting factor, W_R as shown in **Table 2.7**. 1 Sv is equivalent to 100 rem.

$$H_t = D_t \times W_R \qquad \textbf{2.14}$$

Table 2.7: Radiation weighting factors, W_R. (ICRU, 1998).

Radiation Type and Energy Range	**Radiation Weighting Factor, W_R**
X and γ rays, all energies	1
Electrons, positrons, muons, all energies	1
Neutrons:	
<10 keV	5
10 to 100 keV	10
>100 keV to 2 MeV	20
>2 to 20 MeV	10
>20 MeV	5
Protons (other than recoil), > 2 MeV	2 – 5
α particles, fission fragments, heavy nuclei	20

2.6.3 Effective Dose, *E*

The risks of cancer from an equivalent dose consequently depends on the organs receiving the dose. Some tissues are more sensitive to radiations, hence, will be affected more than those with less sensitivity towards radiation. This can be quantify using the term effective dose, *E* (Sv) as in **Equation 2.15**, which is obtained by correcting the equivalent dose to the tissue weighting factor, W_T of the irradiated organs (**Table 2.8**).

$$E = H_t \times W_T \qquad \textbf{2.15}$$

Table 2.8: Tissue weighting factors, W_T. (ICRP, 2007).

Tissue	**Tissue Weighting Factor, W_T**	**Cumulative, ΣW_T**
Bone marrow (red), colon, lung, stomach, breast, remainder tissues (adrenals, extra-thoracic region, gall bladder, heart, kidneys, lymphatic nodes, muscle, oral mucosa, pancreas, prostate, small intestine, spleen, thymus, uterus/cervix)	0.12	0.72
Gonads	0.08	0.08
Bladder, oesophagus, liver, thyroid	0.04	0.16
Bone surface, brain, salivary glands, skin	0.01	0.04
	Total	1.00

2.7 Radiobiology

2.7.1 Radiation Types and Their Contributions on Absorbed Dose

Radiations can be divided into ionizing and non-ionizing. Ionizing radiations can be further subdivided into two major types, namely the particle and non-particle radiation. Particle radiation includes electrons, β-particles, α-particles, neutrons and protons, while

x-ray and γ-ray are the examples of non-particle radiation. Although both types contribute to significant absorbed dose to soft tissue, the rate of dose deposition differs greatly on the radiation types. This property can be easily explained by introducing the term, linear energy transfer (LET).

The International Commission on Radiological Units, ICRU (2011) defined LET, $L\Delta$ (J m^{-1}) of a material, for charged particles of a given type and energy as in **Equation 2.16**.

$$L\Delta = \frac{dE_{\Delta}}{dl} \qquad \textbf{2.16}$$

where, dE_{Δ} is the mean energy lost by the charged particles due to electronic interactions in traversing a distance dl, minus the mean sum of the kinetic energies in excess of Δ of all the electrons released by the charged particles. As defined by the ICRU, LET is a reference preferably used for charged particle radiation such as β- and α-particles as well as the electrons. However, LET could also be used in expressing mean energy deposition to a medium by uncharged particle or non-particle radiation such as neutrons or γ-rays, except for that the reference of LET is meant for the primary charged particles produced as a result of ionization by the incidence radiation.

Radiation with high LET e.g. α-particles and neutrons, can be called as densely ionizing radiation, whilst low LET radiations are termed as sparsely ionizing radiation, which includes protons, γ-rays and x-rays. For low LET radiation, since only a small portion of the energy is deposited to the traversing medium, most that are not absorbed will pass through the medium with little change in their trajectory. Hence, the range of this type of radiation cannot be defined. Nonetheless, for radiation with high LET, the range is defined as the maximum distance a particle could travel in a given medium. Range is affected by the energy and type of the incidence radiation along with the density

of the medium it travels. In radionuclide therapy, value of particle range is an important parameter to be considered to ensure that the dose is sufficiently received by the target tumour, while at the same time reducing the dose to other non-targeted tissues.

2.7.2 Radiation Effects on Soft Tissues

When radiation hits the soft tissue, the cells in it could either be damaged but able to be repaired, damaged but unable to be repaired and eventually died, or part of the cell deoxyribonucleic acid could be damaged but is still functioning and grows in an abnormal manner which results in cell mutation. The effects of radiation on soft tissue are affected by the type and energy of the incident radiation as well as the cell's radiosensitivity. Radiosensitivity is the relative susceptibility of cells, tissues, organs, or other substances to the damaging action of radiation. Cell radiosensitivity is directly proportional to the rate of cell division and inversely proportional to the degree of cell differentiation. This means that the actively dividing or the immature cells are at high risk for radiation injury. The cells with high metabolic and division rate, non-specialised and well-nourished are most radiosensitive. Radiation has been one of the most effective treatment method for cancers, due to these characteristics. Radiosensitivity is divided into three main categories which are high, moderate and low radiosensitivity. Since tissues in the body are a mix of these different categories, when radiation is being used, multiple considerations need to be taken for tissues located within the path of the delivered radiation.

2.7.3 Radiation Associated Risks

There are two types of risks associated with radiation exposure; deterministic and stochastic effects. Deterministic effects commonly occur following high dose acute exposure (mostly > 0.1 Gy) with a threshold dose limit where below that, the effect is not observed. This feature is common in therapeutic field where high dose rate is used. The

effects usually arise within days; e.g. prodromal syndrome, gastrointestinal syndrome, and central nervous system syndrome, or weeks; e.g. haematopoietic and pulmonary syndromes, following exposure. However, some may arise over period of years or more; e.g. cataracts and hypothyroidism (Edwards & Lloyd, 1998). Due to these effects, all normal tissue are assigned to a specific tolerance dose limit which is the threshold dose to which beyond that the tissue will be at risk of having deterministic effects.

Unlike deterministic effects, stochastic effects are not dependent to the threshold dose limit, but the effects is directly proportional to the radiation dose received. These effects, which can be divided into somatic (any cancer types occur to the exposed person) and genetic (hereditary effects passed to the offspring of the exposed person e.g. childhood cancer, birth defects) effects, usually arise years following the radiation exposure.

2.8 Monte Carlo (MC) Simulation

The MC simulation of particle transport through bulk media, consists of using probability distributions of particle interactions in materials, to simulate the random trajectories of individual particle (Rogers & Bielajew, 1990). One keeps track of physical quantities of interest for a large number of histories to provide the required information about the average quantities. The inherent statistical uncertainty can be controlled to be less than 1 %, often more precise than experimental measurements (Xu, 2014).

MC was not only applicable in medical physics but also in economy, statistics, and engineering. MC in medical physics was pioneered by Berger (1963) where he wrote a book chapter highlighting the condensed history technique of electron transport which is the basis of all current codes for transport at energies above a few tens of keV. Following Berger's code, the Electron Gamma Shower (EGS) (NRC, 2013), Fluktuierende Kaskade

(FLUKA) (Battistoni et al., 2007), Geometry and Tracking 4 (Geant4) (Allison et al., 2006), Monte Carlo N-particle (MCNP) (Brown, 2003) and the Penetration and Energy Loss of Positrons and Electrons (PENELOPE) (Salvat et al., 2006) codes we developed providing improved MC algorithm for more complex problems.

Figure 2.5 show the growth of publications contributed by EGS, MCNP and Geant4 in the medical-related fields. MCNP experienced exponential growth since the introduction of electron transport, but the growth ended at around year 2000. Since then, the usage of both EGS and MCNP codes were observed to be steady, but a significant increase in the growth of Geant4 usage were noticed. MCNP has the most citations in the non-medical literatures, by about 7 times more than EGS. However, EGS is more frequently used in the medical-related fields, since it has been specifically targeted for medical applications (Bielajew, 2013).

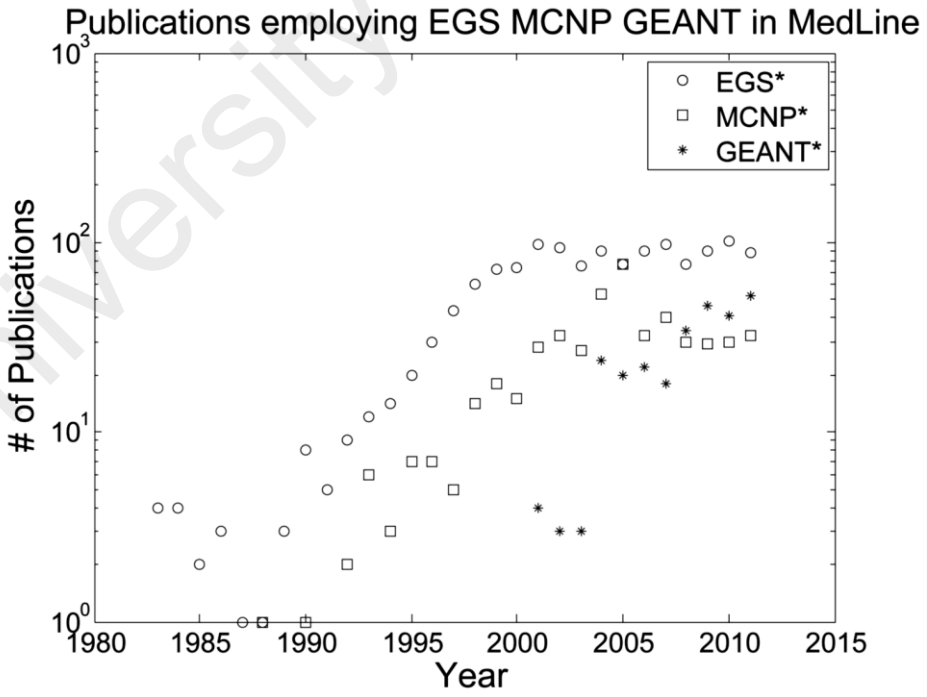

Figure 2.5: Publications using EGSx, MCNPx, and Geantx, as captured on MedLine. (Adapted from Bielajew (2013)).

2.8.1 Anatomical Phantoms

The use of phantoms in radiation dosimetry is important since radiation dose in a living human cannot be directly measured. Phantoms mimicking human anatomical features can be divided into physical or computational types. Physical phantoms consist of solid materials which are radiologically equivalent to human tissues (Xu, 2014). For better representation of human body, anthropomorphic phantoms can be used to measure the dose by placing radiation detectors at the location of interest. However, this approach can be expensive and time-consuming, as a result of needed experimental setups and radiation safety procedures. Also, these phantoms are limited in terms of sizes, which do not fully reflect the diversity of human population. Because of these, computational phantoms incorporated into MC simulations can be used in estimating internal radiation doses. Although experimental measurements are still needed for verification, computational phantoms are still advantageous in versatility, efficiency, precision and safety (Xu, 2014).

Computational phantoms can be constructed using various modelling methods. Two general methods widely used include constructive solid geometry (CSG) and boundary representation (BREP) methods (Stroud, 2006; Leyton, 2001). CSG allows the creation of solid objects using Boolean operations, by combining basic shapes or primitives such as spheres, cylinders, cones and ellipsoids. BREP methods consist of construction of polygon mesh solids using combinations of vertices, edges and faces (Xu, 2014). The example of left lungs modelled using these methods are shown in **Figure 2.6**. Most MC codes can handle CSG shapes including the voxel's form; however BREP shapes is more restricted due to large number of vertices, edges or faces. Over times, the development of computational phantoms have improved from the first generation stylised phantoms (1960s to 2000s), to voxelised phantoms based on tomographic images (1980s to present)

and finally BREP phantoms based on advanced primitives with deformable features (2000s to present) (Xu, 2014).

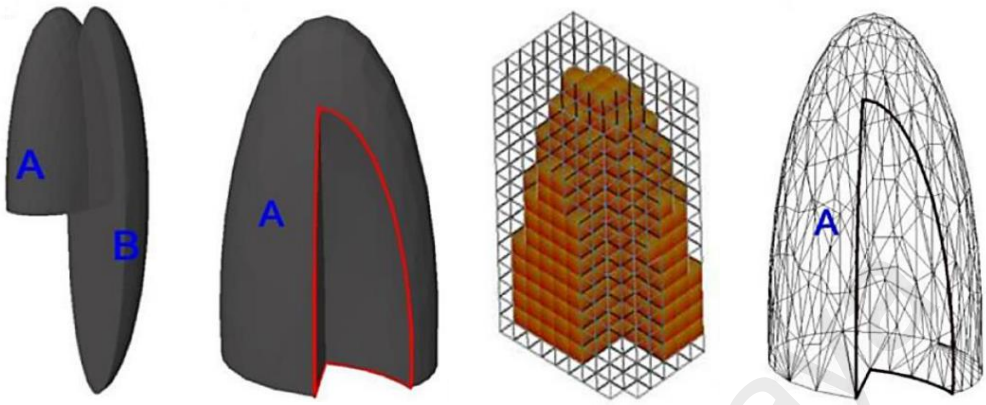

(a) (b) (c) (d)

Figure 2.6: Left lung constructed by different modelling methods. The CSG modelling involving ellipsoids A and B; (a) before and (b) after Boolean operation (subtraction of B from A), and (c) its voxelised representation. (d) The BREP modelling using polygon mesh, of the same lung (Xu, 2014).

2.8.1.1 Stylised Phantoms

The work was pioneered by Fisher and Snyder (Fisher & Snyder, 1967, 1966), from the development of Fisher-Snyder adult phantom using CSG shapes composed of only homogenously distributed soft tissues. Snyder later introduced the MIRD-5 phantom comprising of a skeleton, both lungs and the remainder soft tissues, without other organs specifications (Snyder et al., 1969). The phantom was later revised by incorporating more than 20 organs and additional detailed anatomical features (Snyder et al., 1978). Cristy and Eckerman (1987) reported a new series of phantoms based on previous works, which consist of an adult male and female, a newborn and individuals of ages 1, 5, 10 and 15. Since then, various stylised phantoms with additional features have been introduced including a pregnant phantom (Stabin et al., 1995), gender-specific ADAM and EVA (Kramer et al., 1982), modified age-specific head and brain (Bouchet et al., 1999) and

kidneys (Bouchet et al., 2003) of the MIRD-5 phantom, mathematical cardiac torso or MCAT phantom (Pretorius et al., 1997) etc.

2.8.1.2 Voxelised Phantoms

Unlike stylised phantoms which are based on quadric surface equations, tomographic phantoms consist of a huge number of tiny voxels representing anatomical structures based on tomographic image data sets. However, both phantoms belong to the same class of CGS geometries (Xu, 2014). Tomographic phantoms were constructed by acquiring a set of tomographic images, identifying organs or tissues of interest by assigning every pixel with identification number, specifying the density and chemical composition of organs or tissues and registering the segmented image slices into a three dimensional volume as MC inputs. Pioneered by Pujol and Gibbs (1982), Zubal et al. (1994) created a head-torso model called VoxelMan (famously known as Zubal phantom) from CT images, which was later improved with MRI images of the human brain. The International Commission on Radiological Protection, ICRP (2009) adult Reference Male and Female phantoms were created as an effort to standardise the voxelised phantoms, by adjusting the phantoms height, skeletal mass, and individual organs to reference values.

Nevertheless, there were concerns that the methods used in producing the voxelised phantoms were not ideal (Zaidi & Xu, 2007; Caon, 2004). Firstly, the segmentation of original images into organs and tissues required lengthy and tedious manual process, often consuming months to years to complete. Second, since the voxelised phantoms were based of relatively larger image slice thickness, its anatomical accuracy may be compromised (Xu, 2014). Also, nothing has been done in deciding the most optimum voxel size, and that no standardised guideline for the segmentation of the whole-body voxelised phantoms has been reported, to this date. This leads to uncertainty in comparing the accuracy of different tomographic phantoms. Moreover, voxelised phantoms are

individual specific, hence are not representative of a large population, since the reference phantom requires the phantom to match the 50th percentile values in terms of body height and weight for each gender and age group (Xu, 2014).

2.8.1.3 BREP Phantoms

For BREP phantoms, the steep increase of phantoms of this type has been observed throughout the years. Examples of the phantoms include the NCAT and XCAT phantoms series (Segars et al., 2013; Segars & Tsui, 2010), RPI Adult Male and Adult Female matched with ICRP-89 reference values (Zhang et al., 2009) and the extended weight-specific series for 5th, 25th, 50th, 75th, and 95th weight percentiles (Yong Hum et al., 2010), UF family phantoms (Tianwu & Habib, 2014), FASH and MASH phantoms (Cassola et al., 2010), and IRSN female torso phantom series (Farah et al., 2010). However, the emerging of these phantoms are still restricted by the limits of MC codes design, which only able to handle simple geometries (Xu, 2014). This issue affects the efforts in phantom research such that; the implementation of various anatomically complex phantoms into the codes requires cumbersome manual processes, e.g. mesh-based phantoms must first be converted to voxels, and the limits of MC codes in handling moving targets (i.e. heart or lungs) (Xu, 2014). The evolution of phantom geometries are shown in **Figure 2.7**.

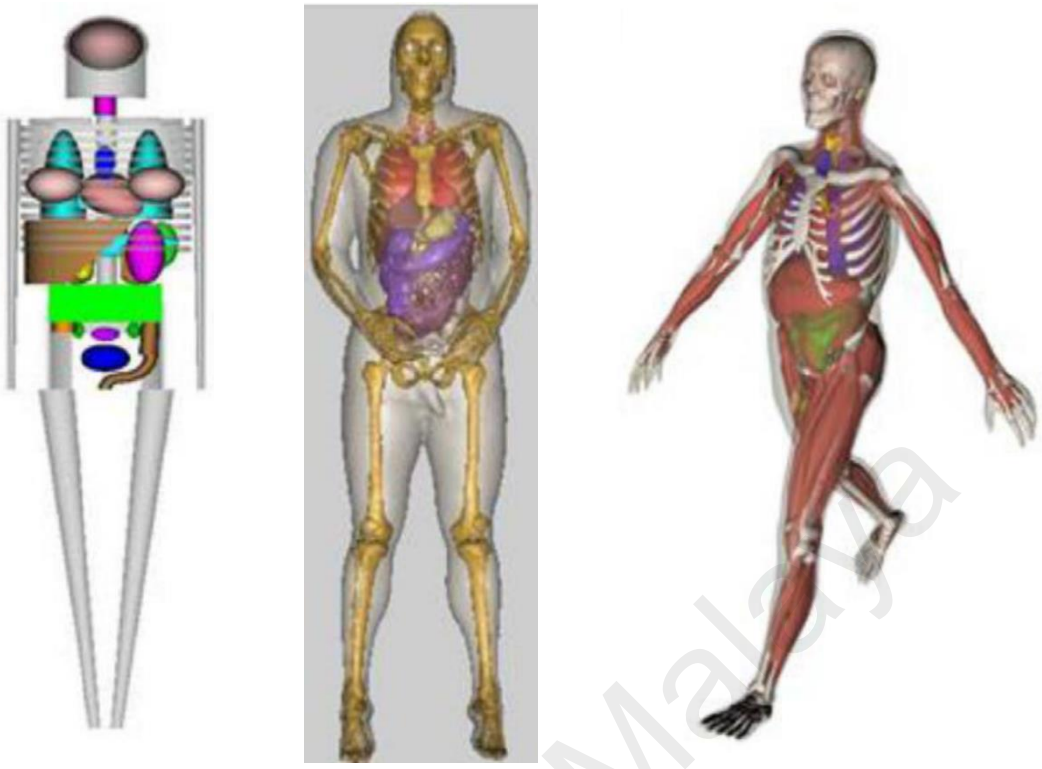

(a) (b) (c)

Figure 2.7: Three phantom generations: (a) Stylised phantom; (b) Voxelised phantom displayed in smooth surface; (c) BREP phantom with deformable features (Xu, 2014).

2.8.2 MC Calculations

According to Kolbert et al. (1997), a personalised MC simulation can be performed by introducing a complete anatomical dataset with known patient geometry, radionuclide type, and concentration locations. Since the medium cross-sections and particle energy are given, the code will either locally deposit the particle, or provide the direction and distance to the next interaction in the corresponding infinite homogenous medium with unit density. The simulation runs until the particle escapes the patient geometry, or the particle energy falls below a preselected threshold, thus the energy is assumed to be locally absorbed (Tsougos et al., 2010).

Due to relatively complex approach of the conventional MC method, the time consumed for this technique is usually very extensive due to the high precision algorithm.

A less time consuming method is the voxel dose kernel (VDK) e.g. as demonstrated by Vente et al. (2009b). By comparing the dose distributions of ^{166}Ho-PLLA microspheres injected into a porcine liver using both MCNP5 and the VDK method, they found that the dose-volume histograms and the isodose representations were almost identical with the average VDK dose, higher by only 0.59 %.

According to Kolbert et al. (1997), dose kernels, K are defined as the absorbed dose per decay at a point, r away from the source. A usual approach is by using MC simulation of a point source in a homogenous media, i.e. water. Then, using convolution methods, the absorbed dose is calculated such that the dose kernel (cGy.Bq^{-1}.s^{-1}) is expressed as in **Equation 2.17** (Furhang et al., 1996), where, n_{dec} is the number of photons per decay and n_{total} is the total number of histories per simulation. For estimation of absorbed dose, a specific dose distribution is required, which may derived from functional images i.e. PET or SPECT images, by convolving these kernels with the activity distribution of the images (Tsougos et al., 2010). Despite the relatively faster calculation, this method does not consider the tissue inhomogeneity, in terms of particle transport.

$$\mathrm{K}(r) = \left(\frac{\text{Dose }(r)}{4\pi r^2}\right)\left(\frac{n_{\text{dec}}}{n_{\text{total}}}\right) \times 1.0602 \times 10^{-8} \qquad \textbf{2.17}$$

CHAPTER 3: DETERMINATION OF A SUITABLE RESIN-BASED MICROPARTICLE FOR TRANSARTERIAL RADIOEMBOLIZATION

3.1 Introduction

Transarterial radioembolization (TARE) is one of the treatment options available for the treatment of hepatocellular carcinoma (HCC). During the procedure, yttrium-90 (^{90}Y)-labelled microspheres were administered directly to the tumour via the aid of a catheter (which is punctured through the femoral artery and ends at the branches of hepatic artery supplying the tumour). In determining the most suitable radioembolic agent for TARE of HCC, one of the most important features to be considered is the embolus size. The diameter of the microparticles should range between 20 – 40 μm, in order to obstruct the blood supply to the tumour. Larger microparticles may be trapped at a larger blood vessel before reaching the tumour, while the smaller microparticles may flow through the tumour capillaries, and leads to the deposition of the microparticles within the lungs (Kim et al., 2015). Microparticles with high resistivity towards heat (i.e. during neutron activation) and body chemicals, near plasma density, biocompatible, and non-degradable are highly preferred.

Ion exchange resins offer the best properties and are most suitable as radioembolic agents. They are useful as carriers for medicinal materials and in slow release applications (Wheaton & Lefevre, 2000), and known to be able to withstand extreme pH in gastric fluid while still retaining its function. Among those that has been commercialised; resin-based and glass-based, the former is being favoured due to its relatively lower density.

In this chapter, the basic properties of two commercially available resin materials were investigated for intended application in TARE of HCC. Both resins were labelled with

samarium chloride ($^{152}SmCl_3$) salt in six different formulations to determine the optimum formulations providing best labelling efficiency. The resins were sent for neutron activation in TRIGA PUSPATI nuclear research reactor (Malaysia Nuclear Agency, Kajang, Selangor) for the production of radioactive samarium-153 (^{153}Sm). Both resins were tested for the presence of radionuclide impurities by analysing them using gamma spectrometry. The prolong retention of both resins were also studied by immersing them in distilled water and human blood plasma for continuous period of 48 h. The suitable resin was eventually chosen for further characterisation for use in TARE of HCC.

3.2 Objectives

This study was carried out to determine the suitable resin types from two commercially available options, which possesses the best properties for use as radioembolic agents labelled with ^{153}Sm. The resin type will be determined after achieving the following objectives:

i. To compare the suitability of both resins for neutron activation, by analysing the presence of radionuclide impurities following the process.

ii. To evaluate the radiolabelling efficiencies of both radiolabelled formulations in distilled water and human blood plasma. A labelling efficiency of >90% was aimed.

3.3 Methodology

3.3.1 Preparation of ^{153}Sm-Amberlite Microparticles

A commercially available styrene-divinylbenzene (DVB) ion exchange resin with sulphonic acid group, Amberlite® IR-120 H^+ was obtained from Fluka GmbH (Buchs, Switzerland). The amber coloured resin was produced as dry beads and is widely known for use in water softening and purification. Its typical properties and chemical structure are shown in **Table 3.1** and **Figure 3.1**, respectively. Samarium (III) chloride hexahydrate ($^{152}SmCl_3 \cdot 6H_2O$; molecular weight 364.81 g.mol^{-1}; isotopic abundance 26.7 %) with assay purity ≥ 99 % was obtained from Aldrich Chemical Co. (Wisconsin, USA).

The Amberlite resin was dried in a laboratory oven at 70°C for 12 h to remove its moisture for better grinding efficiency. In order to meet the desired size for intra-arterial administration to the hepatic artery, the dried resin was ground using a grinding planetary ball mill machine (XQM-(2-6)L, ChangSha LangFeng Metallic Material Ltd., China) at 200 rpm for approximately 5 h. The resin powder was subsequently sieved using a mechanical sieve shaker (AS 200 Analytical Sieve Shaker, Retsch GmbH, Haan, Germany) attached with 20 and 40 µm wire mesh stainless steel test sieves (Endecotts Ltd., London, UK). The resin before and after size reduction are shown in **Figure 3.2**.

Table 3.1: Typical properties of the Amberlite resin (Helfferich, 1964; Dow, 2015).

Matrix	Styrene-divinylbenzene copolymer
Functional group	Sulphonic acid
Ionic form	H^+
Cross-linkage (%)	8
Moisture (%)	53 – 58
Cation exchange capacity (meq.g^{-1})	5.35 (dry)
Total exchange capacity (eq.l^{-1})	1.8 (by wetted bed volume)
Particle size (µm)	620 – 830
Operating pH	0 – 14

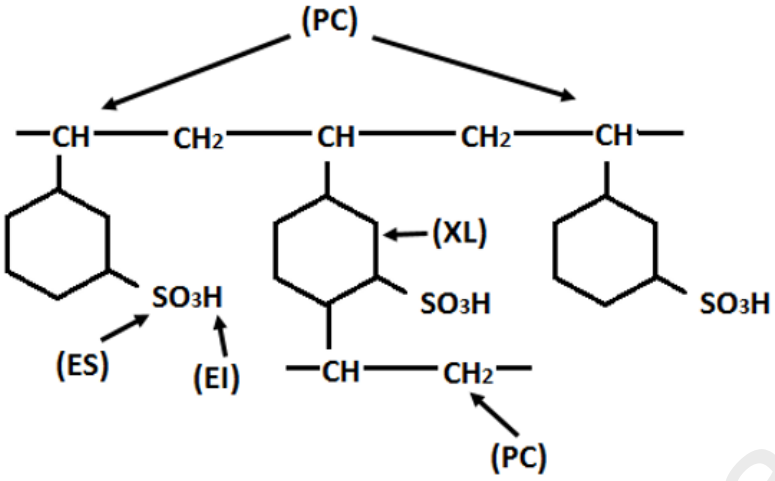

Figure 3.1: Chemical structure of the Amberlite resin. PC: polymer chain; XL: cross-link; ES: exchange site; EI: exchangeable ion.

(a) (b)

Figure 3.2: The Amberlite resin (a) beads (620 – 830 µm) and (b) powder (20 – 40 µm) following size reduction.

1 g of $SmCl_3.6H_2O$ was dissolved in 10 ml distilled water. 5 g of the Amberlite resin powder was poured into the $SmCl_3$ solution and stirred thoroughly for 5 min to allow binding of the Sm^{3+} ions to the resin. The samarium-152 (^{152}Sm)-Amberlite resin was then thoroughly washed with distilled water, using Büchner funnel filtration system, to remove the chlorine ions (Cl^-) and any unbound samarium ions (Sm^{3+}) off the resin. Finally, the formulation was dried in an oven at 70°C for 12 h. The chemical equations for the preparation processes are listed as follows:

Dissolution of Sm salt:

$$SmCl_3.6H_2O_{(s)} + H_2O_{(l)} \rightarrow Sm^{3+}{}_{(aq)} + 3Cl^{-}{}_{(aq)} + 7H_2O_{(l)} \quad \textbf{3.1}$$

Labelling of Sm onto Amberlite resin via ion exchange process:

$$3R-SO_3H_{(s)} + Sm^{3+}{}_{(aq)} + 3Cl^{-}{}_{(aq)} \rightarrow (R-SO_3)_3 Sm_{(s)} + 3HCl_{(aq)} \quad \textbf{3.2}$$

Refinement of Sm-Amberlite microparticles:

$$(R-SO_3)_3 Sm_{(s)} + 3HCl_{(aq)} \xrightarrow[filtration]{+H_2O_{(l)}} (R-SO_3)_3 Sm_{(s)} + H_2O \xrightarrow[dry]{oven} (R-SO_3)_3 Sm_{(s)} \quad \textbf{3.3}$$

where;

$$R = \left[CH_2CH(C_6H_5)\right] \times \left[CH_2CH\left[C_6H_4(CHCH_2)\right]\right]_y \quad \textbf{3.4}$$

3.3.2 Preparation of ^{153}Sm-Fractogel Microparticles

Fractogel® EMD SO_3^- (S) (Merck Millipore, Massachusetts, USA) readily produced in 20 – 40 µm, is made of polymethacrylate with sulphoisobutyl group, suspended in 20 % ethanol and 150 mmol.l-1 sodium chloride (NaCl). The resin appeared as white gel in a milky suspension and is typically used for chromatographic purposes for purification of strong basic and neutral proteins and peptides. The typical properties are shown in **Table 3.2**. The chemical structure and the resin appearance are shown in **Figure 3.3**.

Table 3.2: Typical properties of Fractogel resin (Merck, 2015).

Matrix	Polymethacrylate
Functional group	Sulphoisobutyl
Storage/ preservative	20 % ethanol, 150 mmol.l^{-1} NaCl
Protein binding capacity	150 mg lysozyme per ml of resin
Particle size (µm)	20 – 40
Operating temperature	4°C to room temperature
pH stability range	1 – 13
Linear flow rate	Up to 360 cm.h^{-1}

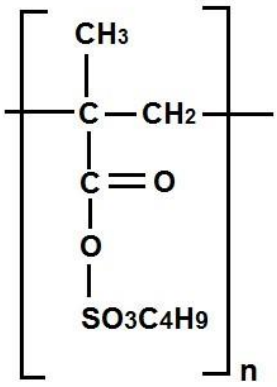

(a)

(b)

Figure 3.3: (a) Chemical structure of the Fractogel resin and (b) the resin supplied in milky turbid suspension.

Using Büchner funnel filtration, the Fractogel resin was thoroughly washed with distilled water to eliminate the ethanol and NaCl solution off the resin. 1 g of $SmCl_3.6H_2O$ was dissolved in 10 ml distilled water. 5 g of washed Fractogel resin was poured into the $SmCl_3$ solution and stirred thoroughly for 5 min to allow binding of the Sm^{3+} ions to the resin. The ^{152}Sm-labelled Fractogel resin was then washed with distilled water to remove any unbound ions (i.e. Na^+, Cl^- and Sm^{3+}). Finally, the formulation was dried in an oven at 70°C for 12 h. The chemical equations for the preparation process are as follows:

Following dissolution of Sm salt as in **Equation 3.1**, the labelling of Sm onto Fractogel resin via ion exchange process:

$$3R-SO_3C_4H_{9(s)} + Sm^{3+}{}_{(aq)} + 3Cl^-{}_{(aq)} \rightarrow \left(R-SO_3\right)_3 Sm_{(s)} + 3C_4H_9Cl_{(aq)} \quad \textbf{3.5}$$

Refinement of Sm-Fractogel microparticles:

$$\left(R-SO_3\right)_3 Sm_{(s)} + 3C_4H_9Cl_{(aq)} \xrightarrow[filtration]{+H_2O_{(l)}} \left(R-SO_3\right)_3 Sm_{(s)} + H_2O \xrightarrow[dry]{oven} \left(R-SO_3\right)_3 Sm_{(s)} \quad \textbf{3.6}$$

where;

$$R = \left(C_4H_5O_2\right)_n \quad \textbf{3.7}$$

3.3.3 Neutron Activation

Both types of ^{152}Sm-labelled microparticles were sent for neutron activation at the Malaysian Nuclear Agency. The TRIGA PUSPATI Reactor (Triga Mark II, General Atomics, California, USA) as shown in **Figure 3.4**, is a pool type, 7 m high aluminium tank surrounded by high density concrete, regularly operates at 750 kW power level. The solid fuel element used is of enriched uranium-235 (^{235}U) (20 % weight), homogenously combined with zirconium-hydride moderator.

Figure 3.4: The top view of the TRIGA PUSPATI Reactor in Malaysia Nuclear Agency, Bangi (Mohamed Takip, 2009), which is a 7 m high pool type reactor surrounded by high density concrete.

One gram of each microparticle was transferred into individual polyethylene vial (3.15 cm height and 1.4 cm diameter), uniquely labelled and the top of the vial was heat sealed to ensure that the sample is safely confined during neutron activation. These vials were further put into separate polyethylene ampoule known as ”rabbit” (10 cm height and 3 cm diameter) as shown in **Figure 3.5**, labelled, and sent for neutron activation.

(a) (b) (c)

Figure 3.5: The microparticles; (a) ^{152}Sm-Amberlite and (b) ^{152}Sm-Fractogel, were sealed in individual polyethylene vial and placed into separate (c) polyethylene ampoule for neutron activation.

Two methods of neutron activation via pneumatic transfer system (PTS) and rotary specimen rack (RR), were studied to investigate their practicality in order to achieve high therapeutic activity (3 GBq) of ^{153}Sm. The protocols for both neutron activation methods are shown in **Table 3.3**.

Table 3.3: Neutron activation protocols to achieve ^{153}Sm activity of 3 GBq. PTS: pneumatic transfer system; RR: rotary rack.

Method	**PTS**	**RR**
Thermal neutron flux, θ_{th} (n.cm^{-2}.s^{-1})	4.813 x 10^{12}	1.494 x 10^{12}
Irradiation time	5 min	6 h
Location in the reactor	Near to the core	Peripheral to the core
Sample entrance and exit	Automatic	Manual

The irradiation time can be estimated using **Equation 3.8**.

$$A_t = \sigma_{act} \varphi N (1 - e^{-\lambda t}) \quad \textbf{3.8}$$

where;

A_t = activity (Bq)

σ_{act} = thermal neutron activation cross-section (barn = 10^{-24} cm^2)

φ = neutron flux (neutron.cm^{-2}.s^{-1})

N = number of parent atoms = (m / w) x θ x (6.023 x 10^{23} atoms.mol^{-1})

m = mass of element in the sample (g)

w = atomic weight of element (g.mol^{-1})

θ = isotopic abundance

λ = decay constant (s^{-1})

t = irradiation time (s)

After activation, the samples were left for 48 h to allow for complete decay of the short-lived contaminant radionuclides (i.e. ^{24}Na, ^{38}Cl). The activities of the samples were then measured using a dose calibrator (CRC 25R, Capintec, New Jersey, USA). The specific activity was calculated by dividing the sample activity with the sample weight.

3.3.4 Gamma Spectrometry

After 48 h, the samples were sent for neutron activation analysis to determine the presence of radionuclide impurities, i.e. the long-lived radionuclides. A coaxial p-type high-purity germanium (HPGe) detector (Canberra Inc., Connecticut, USA) connected to a gamma spectrum analysis system (Genie™ 2000 v.3.2, Canberra Inc., Connecticut, USA) were used (**Figure 3.6**). Each sample was counted for 5 min (live time) at the calibrated distance. Radioactive elements that corresponded to significant energy peaks were identified. The measurements were repeated at 72 h following neutron activation.

(a) (b)

Figure 3.6: Neutron activation analysis system consists of (a) a well-type HPGe detector (Canberra Inc., Connecticut, USA) and (b) a gamma spectrum analysis software system (Genie^{TM} 2000 Ver. 3.2, Canberra Inc., Connecticut, USA).

3.3.4.1 Energy Efficiency Calibration

Prior to the analysis of the samples, an energy efficiency calibration was carried out to determine the detection efficiency with various gamma energies at a distance from the detector, using several standard calibration sources with known energy and activity as shown in **Figure 3.7 (a)**. Since the resin samples were activated to a high therapeutic energy range, the distance of 18 cm (from the source to the detector located at the base of the well chamber) was chosen as the calibrated distance so that the trace samples activity is low enough for analysis following 48 h cooling time. This is to balance the detection yield from exceeding 10 % (for minimal dead time effect) and also to ensure all radionuclides present in the sample can be detected before their fully decay.

Nine pieces of Perspex slabs, each with thickness of 2 cm were used to elevate the samples from the detector. The standard calibration sources were each positioned at the centre of the well chamber at the calibration distance and counted for live time of 5 min. The setup is shown in **Figure 3.7 (c)**.

(a)

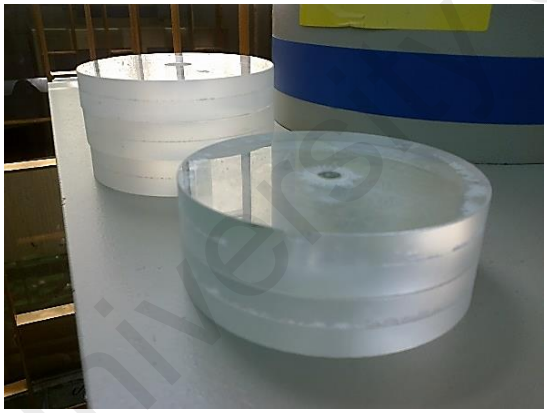

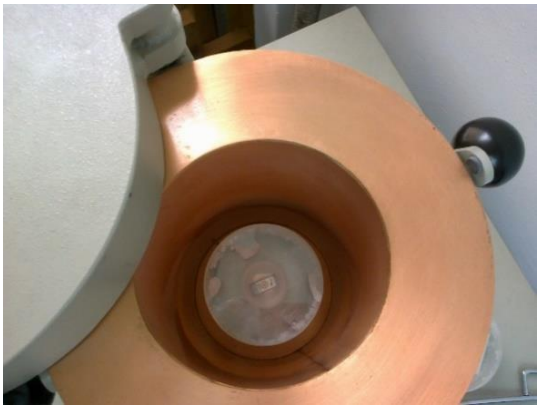

(b) (c)

Figure 3.7: Energy efficiency calibration using (a) standard calibration sources and (b) Perspex slabs each with 2 cm thickness were carried out at (c) 18 cm distance from the detector located at the base of the well chamber.

The software, pre-installed with standard nuclide library will locate the peak centroids of the detected gamma spectrum, and recorded the net area under the peak. The efficiency (counts per disintegration, cpd) of the detection setup for a particular energy was calculated as follow:

$$\text{Efficiency}\ (\text{cpd}) = \frac{\text{Net Area (counts)}}{\text{Live Time (s)} \times \text{Activity (Bq)} \times \text{Yield}} \qquad \textbf{3.9}$$

where, the current activity, A_t of the calibrated source were calculated based on the source label, where the activity on a given date was provided. The yield of the detected energy can be obtained from the decay data of the standard sources, as shown in **Table 3.4**. Following the analysis and efficiency calculations, a graph of efficiency versus energy were plotted and a calibration curve were generated from this data. Based on this curve, the efficiencies of the energy peaks detected from the resin samples will be known, for use in estimating the activity of the sample.

Table 3.4: Physical properties of the standard sources used for efficiency calibration.

#	Radionuclide	Half-life, (y)	E_γ (keV)	Yield per decay (%)	Activity (kBq)
1	^{22}Na	2.6	511.00	180.00	22.61
			1274.50	99.94	
2	^{60}Co	5.27	1173.20	99.86	97.63
			1332.50	99.98	
3	^{109}Cd	1.27	88.00	3.80	1.67
4	^{133}Ba	10.8	53.16	2.20	200.06
			79.61	2.60	
			81.00	34.11	
			276.40	7.15	
			302.85	18.30	
			356.01	61.94	
			383.85	8.91	
5	^{137}Cs	30.17	661.64	85.10	284.14
6	^{152}Eu	13.3	121.78	28.37	221.83
			244.70	7.53	
			344.28	26.57	
			411.12	2.24	
			444.00	3.13	
			778.91	12.97	
			867.38	4.21	
			964.10	14.63	
			1085.84	10.13	
			1089.74	1.73	
			1112.08	13.54	
			1212.95	1.41	
			1299.14	1.63	
			1408.01	20.85	
7	^{241}Am	433	26.00	2.40	359.16
			59.54	36.00	

3.3.5 Radiolabelling Efficiency

Six formulations with different ^{152}Sm: resin ratio was prepared by labelling 1 g of $SmCl_3.6H_2O$ with 1, 2, 3, 4, 5, and 6 g of each resin to determine the optimum formulation with best labelling efficiency. All samples were activated via PTS for 5 min. Following neutron activation, each sample was equally separated into three 10 ml test tubes followed by addition of 10 ml distilled water. The samples were mixed using a roller mixer (Movil-Rod, J.P. Selecta, Barcelona, Spain) at 50 rpm for 1 h. Next, the samples were centrifuged at 1200 rpm for 5 min. 1 ml of supernatant was pipetted from each tube and transferred into gamma assay tubes. These steps were repeated until a total of 8 ml supernatants were obtained from each sample within 48 h. All supernatant samples were assayed using gamma scintillation counter (2470 Wizard2, PerkinElmer Inc., Massachusetts, USA). These steps are shown in **Figure 3.8**.

All steps were repeated in human blood plasma which was obtained from the Department of Transfusion Medicine, University of Malaya Medical Centre (UMMC), Malaysia (UMMC, 2014). Medical ethics approval was not required with reference to Scope 2.1.3, Standard Operating Procedure of UMMC Medical Ethics Committee, since no personal identity information of the donor was acquired for this research (UMMC, 2015a; UMMC, 2015b). Hence, donor consent was also not required due to anonymity of the sample. Labelling efficiency of each formulation was calculated using **Equation 3.10** (Yeong et al., 2011).

$$\text{Retained activity } (\%) = \left[\frac{\left(A_{sus} - A_{sup} \right)}{A_{sus}} \right] \times 100\ \% \qquad \textbf{3.10}$$

where, A_{sus} is the activity of the resin suspension before each extraction of 1 ml supernatant, and A_{sup} is the activity of the 1 ml supernatant.

(a)

(b)

(c)

(d)

(e)

Figure 3.8: Radiolabelling studies of ^{153}Sm-resin in distilled water and blood plasma. (a) Each formulation was divided into three 10 ml test tubes and mixed for 1 h. Following (b) centrifuging process, (c) 1 ml of supernatant from each tube was extracted into (d) gamma assay tubes. A total of 8 ml of supernatant were extracted and (e) sent for gamma counting.

3.4 Results

3.4.1 Determination of Neutron Activation Protocol

Despite the convenience of sample delivery into the nuclear reactor and three times higher neutron flux than the RR method, the automated delivery system of the PTS method only allowed a maximum of 5 min irradiation per sample at one time. The specific activity per gram of the ^{153}Sm-microparticles after 5 min neutron activation via PTS

method was 0.148 ± 0.004 GBq, far lower than the aimed therapeutic activity. Following 6 h neutron activation via the RR method, 3.104 ± 0.029 GBq of ^{153}Sm activity was achieved immediately after activation. Hence, the RR method was shown to be feasible for the production of therapeutic ^{153}Sm.

3.4.2 Gamma Spectrometry

3.4.2.1 Energy Efficiency Calibration

The energy efficiency calibration curve for 18 cm calibration setup is shown in **Figure 3.9** as follows. The efficiency and detected energy are correlated using the equation $y = 0.0002\ e^{-0.002x}$ obtained from the calibration curve. Hence, the efficiency for ^{153}Sm principal gamma energy of 103 keV is 1.63E-04 counts per disintegration.

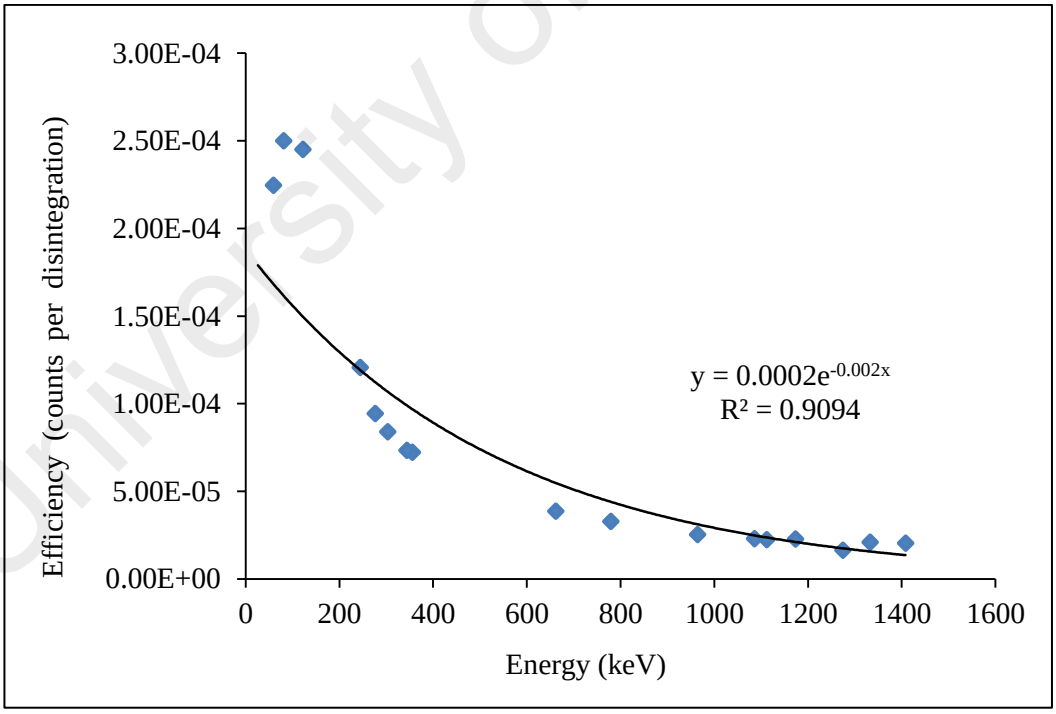

Figure 3.9: Energy efficiency calibration curve for 18 cm source to detector setup.

3.4.2.2 Analysis of Samples

The example of gamma spectrometry analysis report generated by the system is shown in **Figure 3.10**. The most dominant photopeak observed in both samples was the 103.1 ± 0.2 keV peak, which is the principal gamma energy of ^{153}Sm. The other dominant peak was the 69.4 ± 0.2 keV peak, which is the gamma energy with second highest yield (%) associated with ^{153}Sm. Two other significant peaks appeared consistently in all samples were, the 40.7 ± 0.2 and 46.5 ± 0.2 keV peaks, which resulted from the K-shell x-rays of the ^{153}Sm nuclide. In the ^{153}Sm-Fractogel samples, two other peaks were consistently observed, namely the 1368.4 ± 0.2 and 2753.1 ± 0.2 keV peaks. These peaks were recognised to be associated with sodium-24 (^{24}Na). No other significant radionuclide impurities were observed in the ^{153}Sm-Amberlite samples. The results of the gamma spectrometry are shown in **Table 3.5**.

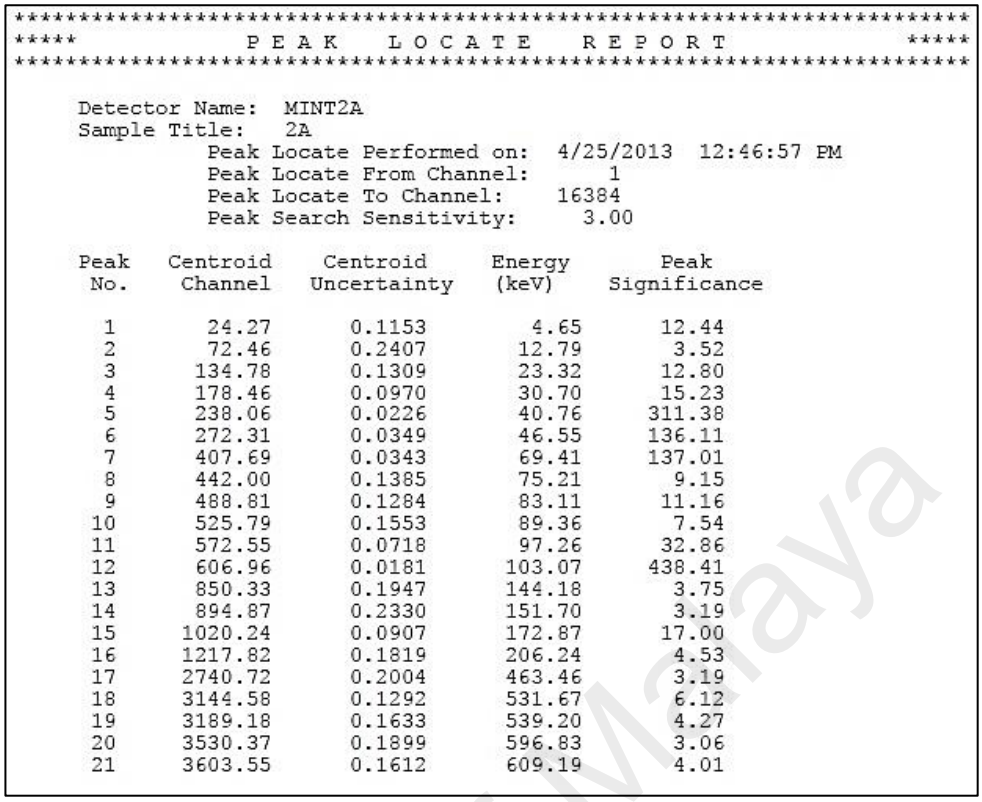

```
*****************************************************************************
*****            P E A K   L O C A T E   R E P O R T                 *****
*****************************************************************************

     Detector Name:  MINT2A
     Sample Title:   2A
               Peak Locate Performed on:  4/25/2013  12:46:57 PM
               Peak Locate From Channel:      1
               Peak Locate To Channel:    16384
               Peak Search Sensitivity:     3.00

     Peak    Centroid     Centroid      Energy       Peak
      No.     Channel    Uncertainty    (keV)     Significance

       1       24.27       0.1153        4.65       12.44
       2       72.46       0.2407       12.79        3.52
       3      134.78       0.1309       23.32       12.80
       4      178.46       0.0970       30.70       15.23
       5      238.06       0.0226       40.76      311.38
       6      272.31       0.0349       46.55      136.11
       7      407.69       0.0343       69.41      137.01
       8      442.00       0.1385       75.21        9.15
       9      488.81       0.1284       83.11       11.16
      10      525.79       0.1553       89.36        7.54
      11      572.55       0.0718       97.26       32.86
      12      606.96       0.0181      103.07      438.41
      13      850.33       0.1947      144.18        3.75
      14      894.87       0.2330      151.70        3.19
      15     1020.24       0.0907      172.87       17.00
      16     1217.82       0.1819      206.24        4.53
      17     2740.72       0.2004      463.46        3.19
      18     3144.58       0.1292      531.67        6.12
      19     3189.18       0.1633      539.20        4.27
      20     3530.37       0.1899      596.83        3.06
      21     3603.55       0.1612      609.19        4.01
```

(a)

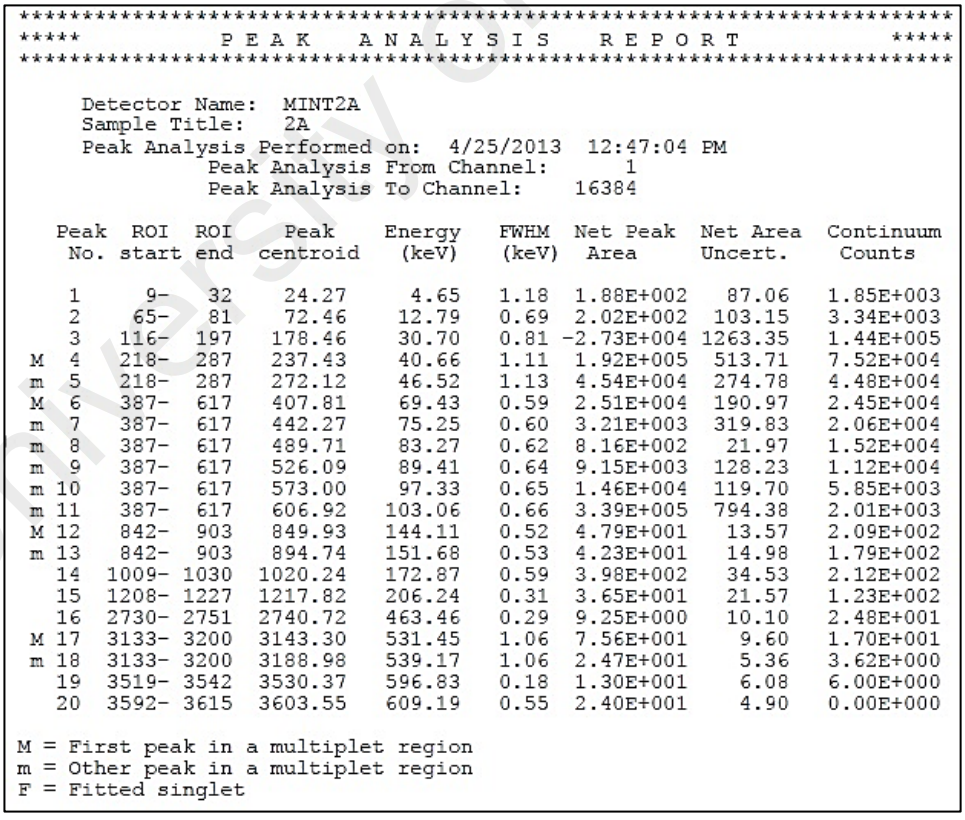

```
*****************************************************************************
*****            P E A K   A N A L Y S I S   R E P O R T             *****
*****************************************************************************

     Detector Name:  MINT2A
     Sample Title:   2A
     Peak Analysis Performed on:  4/25/2013  12:47:04 PM
               Peak Analysis From Channel:      1
               Peak Analysis To Channel:    16384

    Peak  ROI   ROI    Peak     Energy   FWHM  Net Peak   Net Area  Continuum
     No. start  end  centroid    (keV)   (keV)  Area       Uncert.    Counts

     1     9-   32    24.27      4.65   1.18  1.88E+002    87.06   1.85E+003
     2    65-   81    72.46     12.79   0.69  2.02E+002   103.15   3.34E+003
     3   116-  197   178.46     30.70   0.81 -2.73E+004  1263.35   1.44E+005
 M   4   218-  287   237.43     40.66   1.11  1.92E+005   513.71   7.52E+004
 m   5   218-  287   272.12     46.52   1.13  4.54E+004   274.78   4.48E+004
 M   6   387-  617   407.81     69.43   0.59  2.51E+004   190.97   2.45E+004
 m   7   387-  617   442.27     75.25   0.60  3.21E+003   319.83   2.06E+004
 m   8   387-  617   489.71     83.27   0.62  8.16E+002    21.97   1.52E+004
 m   9   387-  617   526.09     89.41   0.64  9.15E+003   128.23   1.12E+004
 m  10   387-  617   573.00     97.33   0.65  1.46E+004   119.70   5.85E+003
 m  11   387-  617   606.92    103.06   0.66  3.39E+005   794.38   2.01E+003
 M  12   842-  903   849.93    144.11   0.52  4.79E+001    13.57   2.09E+002
 m  13   842-  903   894.74    151.68   0.53  4.23E+001    14.98   1.79E+002
    14  1009- 1030  1020.24    172.87   0.59  3.98E+002    34.53   2.12E+002
    15  1208- 1227  1217.82    206.24   0.31  3.65E+001    21.57   1.23E+002
    16  2730- 2751  2740.72    463.46   0.29  9.25E+000    10.10   2.48E+001
 M  17  3133- 3200  3143.30    531.45   1.06  7.56E+001     9.60   1.70E+001
 m  18  3133- 3200  3188.98    539.17   1.06  2.47E+001     5.36   3.62E+000
    19  3519- 3542  3530.37    596.83   0.18  1.30E+001     6.08   6.00E+000
    20  3592- 3615  3603.55    609.19   0.55  2.40E+001     4.90   0.00E+000

M = First peak in a multiplet region
m = Other peak in a multiplet region
F = Fitted singlet
```

(b)

Figure 3.10: Example of a gamma spectrometry analysis result generated from the software system. (a) Peak locate report shows the energy (keV) of the identified peaks, while (b) the peak analysis report shows the details of the region under each peak.

Table 3.5: Gamma spectrometry of ^{153}Sm-resins at 48 and 72 h post-neutron activation. ND: not detectable.

Identified elements	Peak Energy (± 0.2 keV)	^{153}Sm-Fractogel				^{153}Sm-Amberlite			
		48 h		72 h		48 h		72 h	
		Net peak area	Activity (MBq)	Net peak area	Activity (MBq)	Net peak area	Activity (MBq)	Net peak area	Activity (MBq)
^{153}Sm Kα2 xray	40.7	222000 ± 551	23.200	175000 ± 484	18.289	301000 ± 636	31.454	192000 ± 514	20.064
^{153}Sm Kβ xray	46.5	54500 ± 297	8.040	42100 ± 260	6.210	72800 ± 340	10.738	45400 ± 275	6.697
^{153}Sm	69.4	59300 ± 392	23.414	45900 ± 344	18.123	87400 ± 495	34.507	25100 ± 191	9.910
^{153}Sm	103.1	402000 ± 778	27.630	349000 ± 2103	23.987	473000 ± 802	32.508	339000 ± 794	23.300
^{24}Na	1368.4	48.5 ± 8	1.247	21 ± 5	0.540	ND	ND	ND	ND
^{24}Na	2753.1	24 ± 5	0.099	14 ± 4	0.058	ND	ND	ND	ND

3.4.3 Radiolabelling Efficiency

Figure 3.11 shows the comparison of radiolabelling efficiency between two types of ^{153}Sm-microparticles. ^{153}Sm-Amberlite microparticles showed significantly better labelling efficiency in all six formulations with 8.42 ± 0.86 % higher as compared to ^{153}Sm-Fractogel. The lowest labelling efficiency recorded for ^{153}Sm-Amberlite microparticles was 98.48 ± 0.13 %. The efficiencies reached plateau approximately at 1:3 formulation (99.92 ± 0.02 %). For ^{153}Sm-Fractogel microparticles, the lowest recorded efficiency is 89.19 ± 3.1 %. The efficiencies reached plateau at 1:4 formulation (92.27 ± 2.76 %).

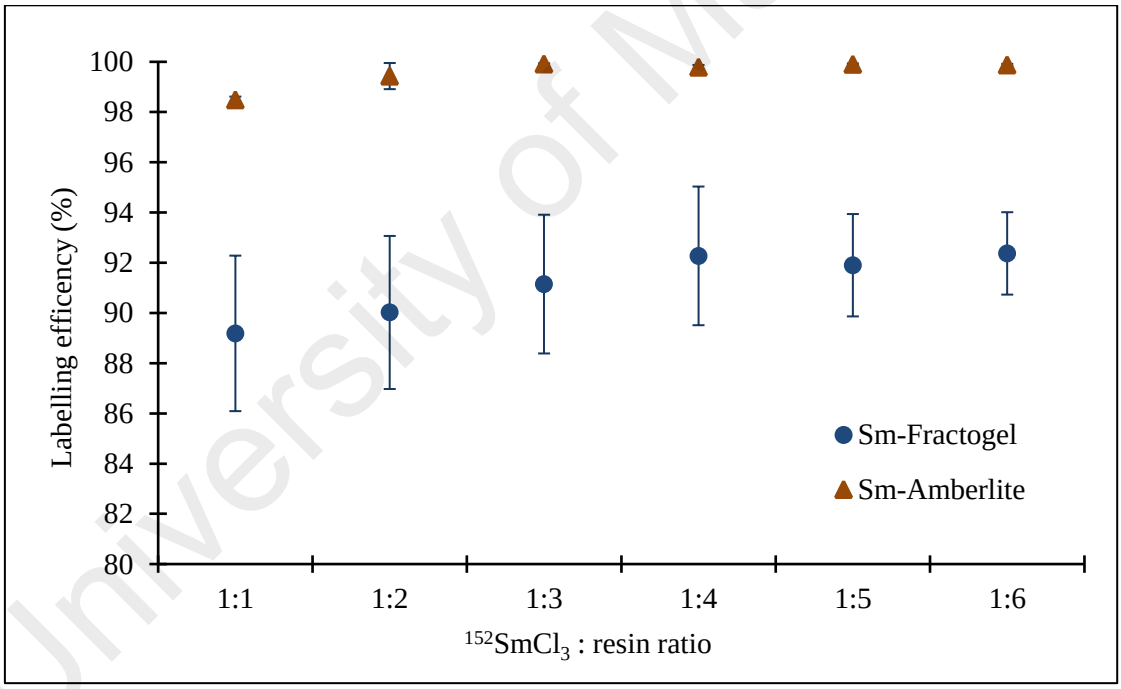

Figure 3.11: Percentage (%) labelling efficiency of two types of ^{153}Sm-resin microparticles with six different ratio of $SmCl_3$: resin.

The most optimum formulations for both ^{153}Sm-microparticles (1:3 and 1:4 for ^{153}Sm-Amberlite and ^{153}Sm-Fractogel, respectively) were compared, and the retention of ^{153}Sm within a time range of 48 h in both distilled water and blood plasma are shown in **Figure 3.12**. ^{153}Sm-Amberlite showed excellent efficiency of > 99 % in distilled water to the

extent of 48 h. Nonetheless, the efficiency dropped to approximately 97 % immediately following suspension in blood plasma, followed by a gradual release to 96 % efficiency at 48 h. ^{153}Sm-Amberlite microparticles showed better retention of ^{153}Sm within 48 h in both distilled water and blood plasma, as compared to ^{153}Sm-Fractogel.

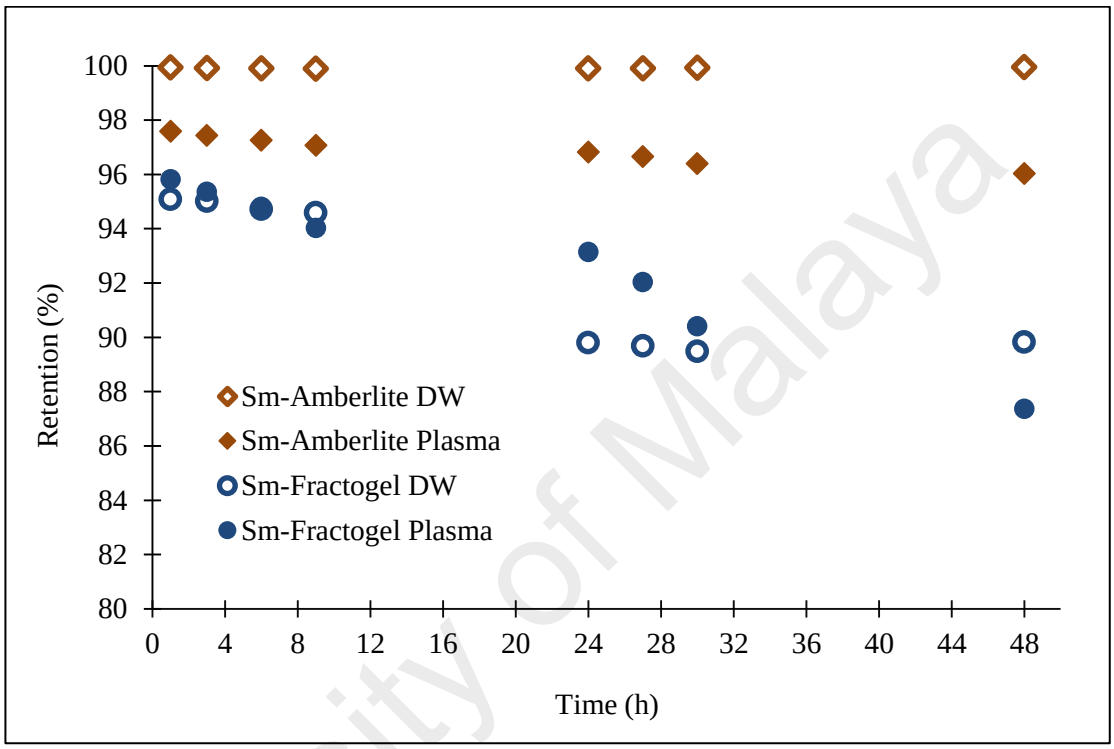

Figure 3.12: Percentage retention of ^{153}Sm in both resins suspended in distilled water (DW) and blood plasma over 48 h.

3.5 Discussions

Ion exchange resins were used in this study due to their commercial availability, safe and relatively easier labelling process. Due to their insoluble characteristic, resins will not be absorbed by the body thus, are very safe for use in medicinal products with limited side effects (Elder, 2005). Ion exchange resins also have high selectivity towards Sm^{3+}, due to the fact that in general the selectivity of ion exchange increases with increase of ion charge (3 extra protons for Sm), and for similar charge ions, the selectivity increases

for ions with higher atomic number (62 for Sm). Also, their non-degradable properties made them suitable for use as permanent implant. The Amberlite resin is made up of cross-linked styrene-DVB copolymer activated with sulphonic acid group. This resin was chosen due to its excellent labelling efficiency as reported in an earlier study (Yeong et al., 2011). The Fractogel resin was used since it is readily available in size range of 20 – 40 µm. This resin is an acrylic ion exchange of polymethacrylate matrix with sulphoisobutyl active group.

There were no impurities present following 48 h post-neutron activation, for the ^{153}Sm-Amberlite samples. This can be explained such that, all elements (^{12}C, ^{1}H, ^{32}S and ^{16}O) present in the resin requires more than one neutron to be activated to radioactive isotopes. Thus, the probability of them being activated is relatively lower than that of ^{152}Sm. Hence, the resin is chemically very stable and suitable for neutron activation. On the other hand, a trace amount of ^{24}Na was found to be present in the ^{153}Sm-Fractogel samples, although both resins comprise of similar group of elements. This may be because, the Fractogel resin was immersed in the NaCl solution in its commercial packing. Although a thorough washing of the resin has been carried out during preparation process, the presence of ^{24}Na may be as a result of the trace amount of Na^{+} bonded to the resin during labelling process, thus was not able to be removed completely. The predicted products of the resins following neutron activation are shown in **Table 3.6**. Although ^{24}Na has a half-life of 15 h, the impurities were still detected following 48 and 72 h, indicating a significant portion of its presence in the samples. However, this may be improved by more thorough and repeated washing of the resin, prior to labelling with ^{152}Sm. ^{24}Na should not be present in the resin during TARE because the energy is very high (1368.4 and 2753.1 keV), hence, may affect the dosimetry estimation made during the treatment planning process.

This study successfully determined the neutron activation protocol for the ^{153}Sm-

microparticles to achieve 3 GBq.g^{-1}, via RR irradiation. The activated sample was kept for 48 h before administration to allow decay of unwanted radioactive impurities and to facilitate transportation of the radioactive source to the hospital. The activity per gram of the resin was estimated to be 1.513 GBq at time of administration (48 h post-activation). Therefore, if administered activity of 3 GBq is to be prescribed, 2 g of ^{153}Sm-microparticles will be required. The administered activities can be adjusted by manipulating the irradiation time or the amount of ^{153}Sm-microparticles in the formulation, according to user's preference.

Table 3.6: Predicted products from neutron activation (NA) of ^{152}Sm-microparticles.

Elements	**NA product**	**Half-life, $t_{1/2}$**	**Next radioisotopes**	**Total neutrons required to produce radioisotopes**
^{1}H	^{2}H	Stable	^{3}H	2
^{12}C	^{13}C	Stable	^{14}C	2
^{16}O	^{17}O	Stable	^{19}O	3
^{32}S	^{33}S	Stable	^{35}S	3
^{23}Na	^{24}Na	15 h		1
^{35}Cl	^{36}Cl	3.0E5 y		1
^{152}Sm	^{153}Sm	46.3 h		1

Neutron activation is the preferred method for radionuclide production, due to increased availability of nuclear reactors worldwide and relatively simple process. Also, it allows lower radiation exposure to the personnel, since the preparation of nuclide labelled embolic agent is being carried out prior to neutron activation. From the cost perspective, our technique requires ^{153}Sm production through neutron activation of relatively low cost ^{152}Sm salt. Since, there are currently 248 nuclear research reactors in active operation in over 56 countries throughout the world (IAEA, 2015), the accessibility of ^{153}Sm provides alternative in reducing the need for expensive global shipping costs.

In comparison, styrene and acrylic-based resins are made up of aromatic and straight chained hydrocarbons, respectively. The active exchange sites of the acrylic resin are part of its physical structure, thus, their physical and chemical stabilities are intertwined (DeSilva, 1999). When an acrylic resin chemically degrades (often at the exchange sites), the physical structure of the resin will be destroyed as well (DeSilva, 1999). This phenomenon is revealed in the radiolabelling efficiency experiment, where the percentage of ^{153}Sm retention in the ^{153}Sm-Fractogel resin dropped at a higher rate as compared to that of the ^{153}Sm-Amberlite resin. The labelling efficiencies and retention of ^{153}Sm were tested in both distilled water and blood plasma because, they will be suspended in distilled water during packaging and injected intra-arterially to the tumour during the treatment.

3.6 Conclusion

We have prepared 20 – 40 µm microparticles using ion exchange resins labelled with ^{153}Sm, which were produced via neutron activation. The ^{153}Sm-microparticles are easy to be labelled and the procedure does not involve unnecessary radiation exposure. The Amberlite resin was chosen as the ideal resin material because of its superior labelling efficiency with strong retention of ^{153}Sm tested over 48 h, no radioactive impurities produced from neutron activation, and the lower production cost (which the Fractogel resin costs about 10 times higher than the Amberlite resin). Further characterisation of the ^{153}Sm-Amberlite microparticles should be carried out for intended use in TARE of HCC.

CHAPTER 4: PHYSICOCHEMICAL CHARACTERISATION OF ^{153}SM-AMBERLITE MICROPARTICLES

4.1 Introduction

From previous chapter, two microparticles have been briefly tested for their suitability as radioembolic agent. The main aspect investigated was the suitability of the microparticles for neutron activation, so that no radionuclide impurities were produced following the process especially those with very long half-life. This is important because presence of radionuclide impurities will affect the dosimetry estimation of the treatment, as well as further exposing the patients with unnecessary radiation. Also, the microparticles ability to retain a maximum amount of samarium-153 (^{153}Sm) following prolong immersion in different media has been investigated. This is to ensure minimal release of ^{153}Sm will occur during the treatment, so that the extrahepatic deposition of ^{153}Sm especially to the lungs can be reduced to avoid further complications.

Thus, the ^{153}Sm-Amberlite microparticles have been chosen as it can be activated with no radionuclide impurities and also able to retain excellent amount of ^{153}Sm with prolong immersion in both distilled water and blood plasma. However, in order for the microparticles to be used as radioembolic agent, it needs to be further tested for its physicochemical suitability. Since the Amberlite resin is commercially produced in large beads, it has to be reduced to the size range of 20 – 40 µm so it can be delivered to the tumour vasculature following administration of the microparticles. Hence, the effect of this process towards the microparticles' physical and chemical structure needs to be evaluated, since a large mechanical force was applied in order to break the beads into smaller fragments. Another important aspect is, the microparticles need to be further

analysed following prolong neutron activation, to make sure that the microparticles still attained the ideal characteristics it has prior to the process.

In this chapter, further characterisations of the selected ^{153}Sm-Amberlite microparticles were carried out to ensure that it is ideal for use as radioembolic agent. This includes the analysis of chemical structures, surface morphology, elemental analysis, particle size distribution analysis, particle density measurements and suspension stability studies.

4.2 Objectives

This study was carried out to further characterise the ^{153}Sm-Amberlite microparticles for its application as radioembolic agent. This will be fulfilled by achieving the following specific objectives:

i. To analyse the chemical structure of the microparticles throughout the preparation stages.
ii. To observe the surface morphology of the microparticles before and after neutron activation.
iii. To analyse the elemental composition of the microparticles before and after neutron activation.
iv. To analyse the particle size of the microparticles before and after neutron activation.
v. To measure the physical density and viscosity of the microparticles following neutron activation.

4.3 Methodology

4.3.1 Fourier Transform Infrared (FTIR) Spectroscopy

Fourier transform infrared (FTIR) spectroscopy (600–4000 cm^{-1} range) on the Amberlite microparticles was carried out using a FTIR spectrometer (Nicolet 6700, Thermo Fisher Scientific Inc., Massachusetts, USA) (**Figure 4.1**) to investigate the chemical structure changes due to mechanical grinding process. The FTIR spectrometer was located at the Biomaterial Research Laboratory, Faculty of Dentistry, University of Malaya. FTIR spectra of fresh Amberlite resin beads, resin microparticles after grinding and sieving processes, resin microparticles after labelling with samarium chloride ($SmCl_3$), and resin microparticles after 6 h continuous neutron activation were compared, and the differences between major peaks were investigated. The FTIR spectrum of $SmCl_3$ salt was also obtained for comparison.

(a) (b)

Figure 4.1: (a) Fourier transform infrared (FTIR) spectrometer (Nicolet 6700, Thermo Fisher Scientific Inc., Massachusetts, USA). (b) A trace amount of the microparticles was placed in the sample holder for analysis.

4.3.2 Field Emission Scanning Electron Microscope (FESEM)

The surface morphology especially the extent of damage of the ^{153}Sm-microparticles before and after neutron activation were investigated, using a field emission scanning electron microscope (FESEM) (Quanta FEG 250, FEI, Oregon, USA) as shown in **Figure 4.2**. The FESEM was located at the Faculty of Dentistry, University of Malaya. The samples that have been neutron activated were monitored using a radiation survey meter (Victoreen® ASM 990, Fluke Biomedical, Everett, WA) to ensure that they have been fully decayed (non-radioactive) before they were used for analysis. This is to prevent unnecessary radiation exposure to the personnel handling the samples and also to avoid any radionuclide contamination. The samples were prepared by using a double-sided adhesive tape mounted on an aluminium stub, followed by dispersion of the microparticles on top of the tape. The excess of the microparticles were removed using a blower, so that they are thinly dispersed and evenly distributed.

Figure 4.2: The field emission scanning electron microscope (FESEM) system (Quanta FEG 250, FEI, Oregon, USA).

4.3.3 Energy Dispersive X-ray (EDX) Spectroscopy

The FESEM system (Quanta FEG 250, FEI, Oregon, USA) as in **Figure 4.2** is also equipped with an energy dispersive x-ray (EDX) spectroscopy, thus samples that were analysed for surface morphology were also analysed using EDX, for validation of the chemical compositions. The findings were used to validate the gamma spectrometry data which has been obtained in the previous chapter, and to confirm the chemical compositions of the microparticles.

4.3.4 Particle Size Analysis using ImageJ

The FESEM images obtained for samples before and after neutron activation were analysed using the particle analysis function in the ImageJ software (version 1.45s, US National Institutes of Health, Maryland, USA). The microscopic scale (μm) on the FESEM images was first compared with the scale provided by the ImageJ box selection in cm. The images were then converted to binary format for analysis. The measurements were set by choosing the Feret's diameter (the longest distance between two points or the "maximum diameter"), as this will be the size of the microparticles. The images were analysed and the results were generated. From this results, distribution histograms were generated and the mean, mode and median of each sample were obtained.

4.3.5 Particle Density Measurement

The particle density, ρ_s (g.cm^{-3}) and total pore volume, TOPV (cm^3.g^{-1}) of the ^{153}Sm-Amberlite microparticles were measured using a helium gas pycnometer (AccuPvc II 1340, Micromeritics Ins. Corp., Georgia, USA) as shown in **Figure 4.3**, at standard room temperature of 25°C. The pycnometer was located at the Department of Chemical Engineering, Faculty of Engineering, University of Malaya. From the measured values, the porosity (%) of the microparticles was calculated using **Equation 4.1**.

$$Porosity\ (\%) = \left[\frac{TOPV}{\left(\left(\frac{1}{\rho_s}\right)+TOPV\right)}\right] \times 100\ \% \qquad \textbf{4.1}$$

Figure 4.3: Helium gas pycnometer (AccuPvc II 1340, Micromeritics Ins. Corp., Georgia, USA)

The particle density value was then incorporated into **Equation 4.2** (ThermoFisherScientific, 2009), to estimate the particle concentration (particles.ml^{-1}) of the microparticles suspended in 0.9 % saline solution.

$$\text{Particle concentration}\left(\text{particles.ml}^{-1}\right) = \frac{6\,\rho_f}{\left[\pi D_p{}^3\left(\rho_f + \left(\frac{\rho_s}{C}\right) - \rho_s\right)\right]} \qquad \textbf{4.2}$$

where;

C = mass fraction (% w/w)

D_p = mean diameter of the particles (cm)

ρ_f = density of the solvent (g.cm^{-3})

ρ_s = particle density (g.cm^{-3})

4.3.6 Viscosity

The viscosity, η_o of 2.5 % w/v microparticles in saline suspension was measured at 37°C, using DV-II Pro EXTRA viscometer attached with TC-502 water bath (Brookfield Engineering Labs Inc., Massachusetts, USA), as shown in **Figure 4.4**. The viscometer was located at the Department of Chemical Engineering, Faculty of Engineering, University of Malaya. Once the water bath has reached 37°C, the sample was poured into the sample holder followed by insertion of the holder into the viscometer. The spindle was then attached to the pivot cup above the viscometer, and was levelled so that the spindle is immersed into the sample. The measurement was carried out for about 3 min to a maximum speed of 150 rpm. The mean viscosity was determined and the value was incorporated into Stokes' Law as shown in **Equation 4.3,** to study the sedimentation rate (settling velocity) of the suspension.

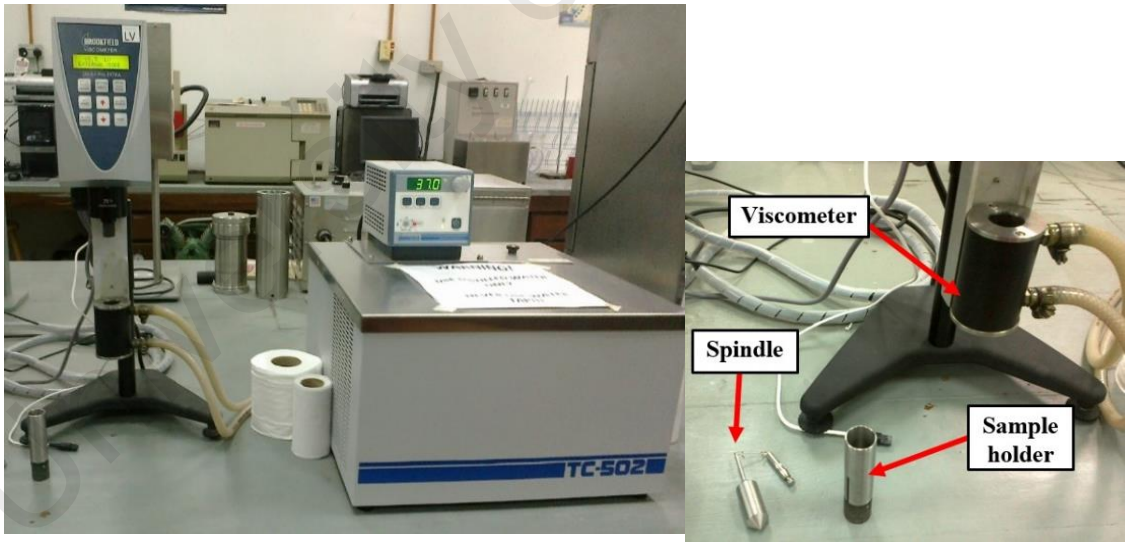

(a) (b)

Figure 4.4: (a) The DV-II Pro EXTRA viscometer attached with TC-502 water bath (Brookfield Engineering Labs Inc., Massachusetts, USA) was set at 37°C. (b) The main functional parts of the viscometer.

$$V_{sed} = \frac{\left[g\ D_p{}^2 \left(\rho_s - \rho_f \right) \right]}{18\eta_o} \qquad \textbf{4.3}$$

where;

V_{sed} = sedimentation rate ($cm.s^{-1}$)

g = gravitational acceleration constant (981 $cm.s^{-2}$)

η_o = dynamic viscosity of the fluid (Pascal, P = $g.cm^{-1}.s^{-1}$)

D_p = mean diameter of the particles (cm)

ρ_f = density of the solvent ($g.cm^{-3}$)

ρ_s = particle density ($g.cm^{-3}$)

4.4 Results

4.4.1 FTIR Spectroscopy

The comparison between the spectra in different production stages alongside $SmCl_3$ spectrum is shown in **Figure 4.5 (a)** – **(e)**. FTIR spectrum of the fresh Amberlite resin beads in **Figure 4.5 (b)** was compared to a FTIR spectrum of the same resin from a previous study (Singare et al., 2011). As compared to the other spectra, the water content within the samples decreased following size reduction, labelling and neutron activation. As shown in **Figure 4.5 (b)** – **(e)**, the functional sulphonic group within the ion exchange resins were still present at each production stage. There were no major differences observed between those peaks.

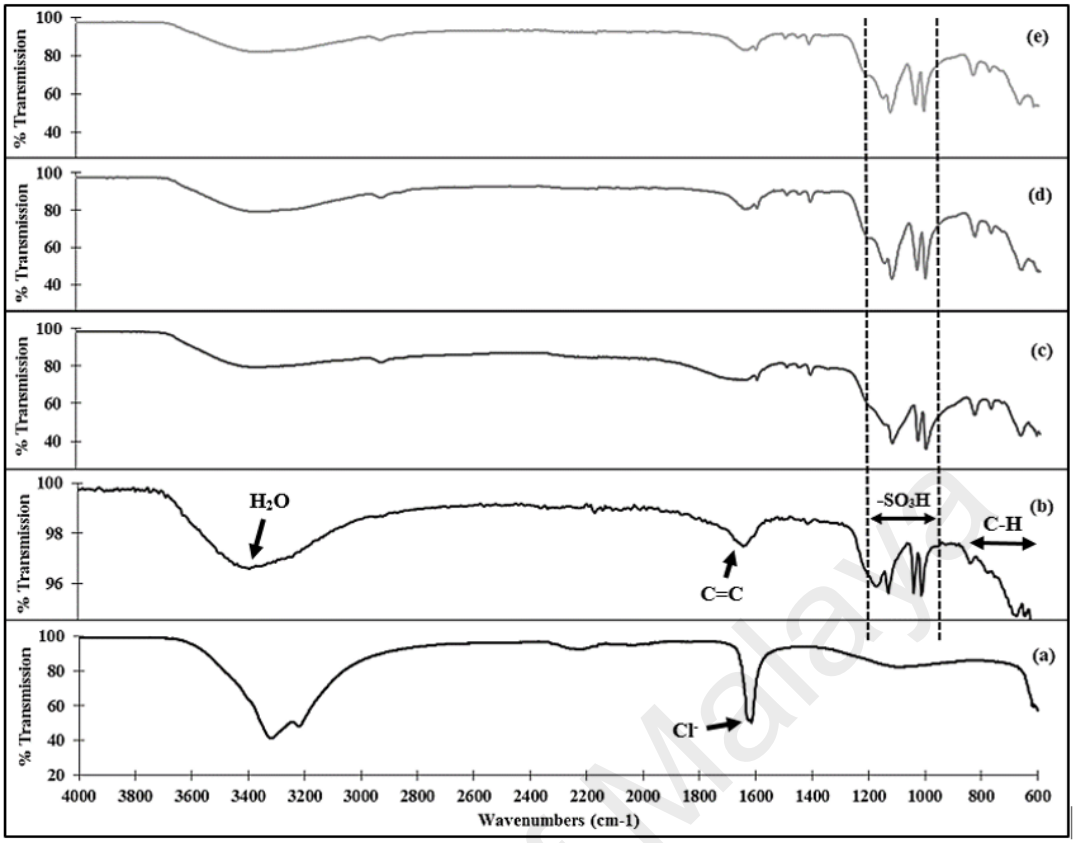

Figure 4.5: FTIR spectra of (a) $SmCl_3.6H_2O$ salt, (b) fresh Amberlite beads, (c) Amberlite ground and sieved to size 20 – 40 µm, (d) Amberlite microparticles labelled with $SmCl_3.6H_2O$ salt, and (e) ^{153}Sm-Amberlite microparticles after 6h neutron activation.

4.4.2 FESEM and EDX Spectroscopy

The FESEM images of the microparticles before and after neutron activation are shown in **Figure 4.6 (a)** and **(b)**. The microparticles were observed to be irregular in shape. Following neutron activation, an increase amount of smaller fragments were observed, however no major changes were seen in the overall shapes of the microparticles. The EDX spectra of the microparticles are shown in **Figure 4.6 (c)** and **(d)**. Both spectra confirmed the composition of the resins which comprised of C, O, Sm, S and H, which the later cannot be detected in the EDX analysis due to its atomic number ($Z < 6$). The elemental weight fraction of each sample indicated about 7 % of Sm was present, hence each 1 g of the ^{153}Sm-Amberlite microparticles consisted of 70 mg ^{153}Sm.

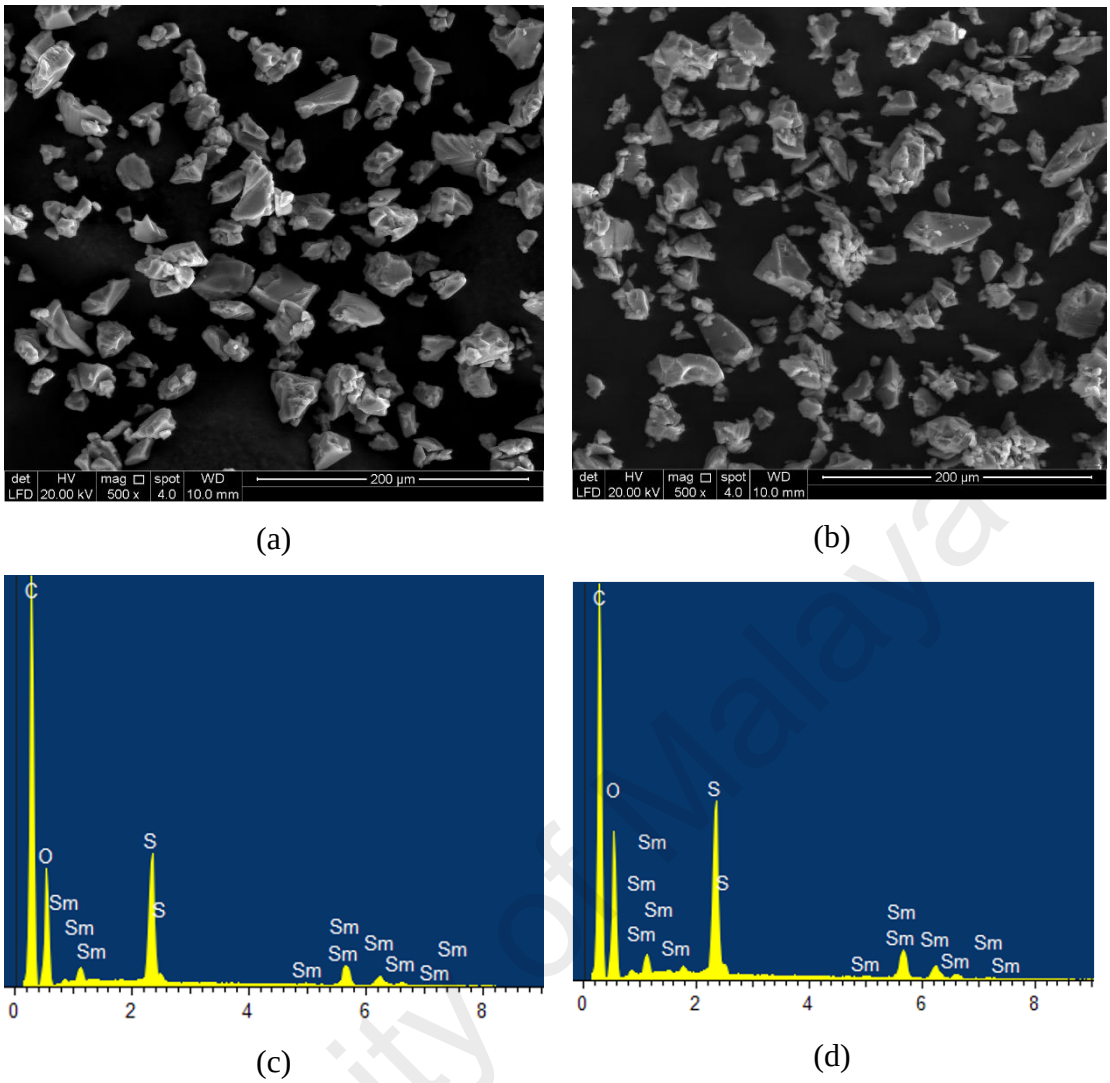

Figure 4.6: FESEM images of the Sm-Amberlite microparticles, (a) before and (b) after 6 h neutron activation with their corresponding EDX spectra (c) and (d), respectively.

4.4.3 Particle Size Analysis using ImageJ

The particle size distributions of both samples are shown in **Figure 4.7 (a)** and **(b)**. Since, the microparticles were non-spherical, the Feret's diameter measurement was used. The mean diameter of the particles before and after 6 h neutron activation were 32.6 ± 2.1 µm and 23.5 ± 2.3 µm, respectively. Before neutron activation, 34.7 ± 2.6 % of the microparticles were in the range of 20 – 40 µm, while 72.1 ± 4.9 % were in the range of 10 – 60 µm. Following 6 h neutron activation, 28.0 ± 1.5 % remained in the 20 – 40 µm

range, while 62.9 ± 6.7 % of the microparticles were in the range of 10 – 60 µm. The differences in size distributions of the microparticles were mainly contributed by the increase amount of fragments (< 10 µm) following neutron activation.

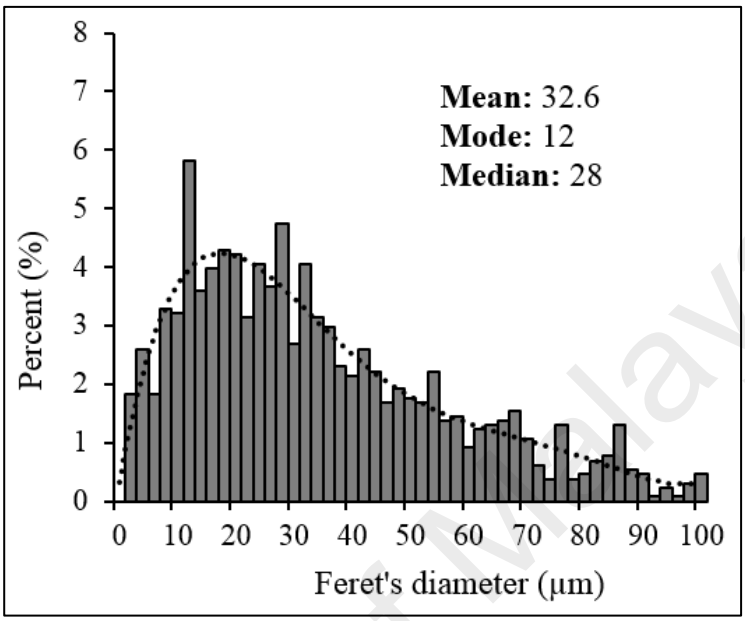

(a)

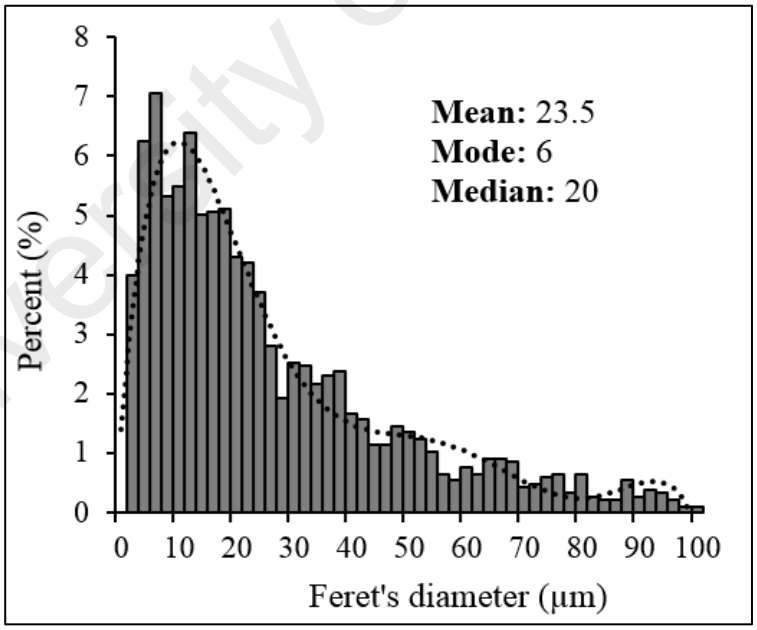

(b)

Figure 4.7: Particle size distribution of Sm-Amberlite microparticles (a) before and (b) after 6 h neutron activation.

4.4.4 Particle Density and Viscosity of the Suspension

The particle density and porosity of the microparticles were 2.538 ± 0.012 g.cm^{-3} and 61 %, respectively. For 1 g of the sample, it was found to consist of approximately 57,561,972 microparticles, which corresponded to specific activity of 53.855 ± 0.503 Bq following 6 h neutron activation. The dynamic viscosities of the suspension at 37°C are shown in **Figure 4.8**. The differences in viscosity at various shear rates were small, hence the mean viscosity (1.43 ± 0.29 cP) was used to estimate the settling velocity of the suspension. The estimated settling velocity for the suspension was 0.033 ± 0.006 cm.s^{-1}. The comparisons between microparticles developed in this study as compared to previous published studies are tabulated in **Table 4.1**.

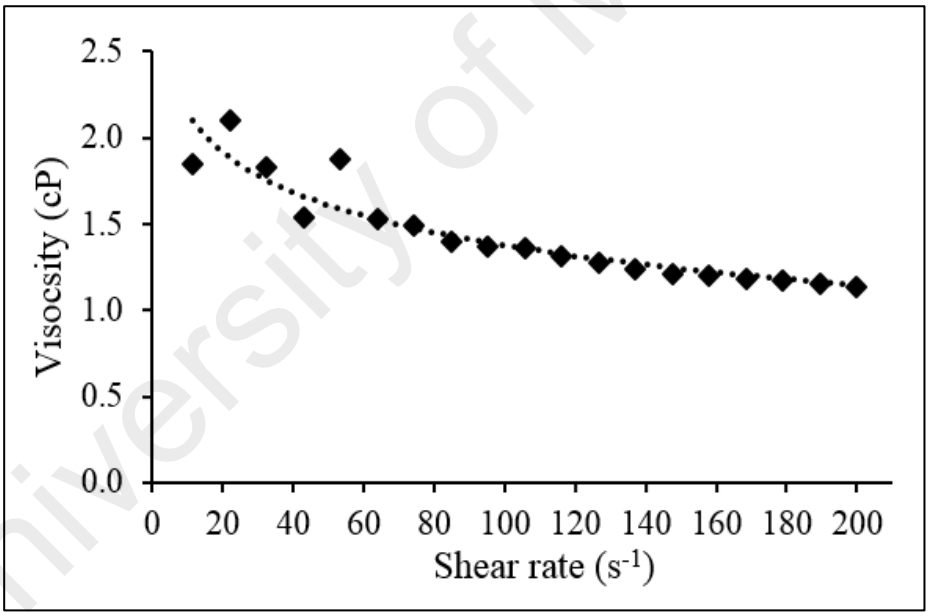

Figure 4.8: The viscosity of 2.5% w/v suspension of ^{153}Sm-Amberlite in saline at 37°C with various shear rate.

Table 4.1: Physical characteristics of previously produced radionuclide labelled microparticles for transarterial radioembolization (TARE) (LNHB, 2014; Hruby et al., 2011; Poorbaygi et al., 2011; Hafeli et al., 1999; Mumper et al., 1991) as compared to this study. *NP: not provided; E_{β}-: energy of beta emission; Eγ: energy of gamma emission, PLLA: poly-l-lactic acid.

Manufacturer	**TheraSphere**	**SIR-Spheres**	**This study**	**Mumper et al. 1991**	**Hruby et al. 2011**	**Poorbaygi et al. 2011**	**Hafeli et al. 1999**
Radionuclide	^{90}Y	^{90}Y	^{153}Sm	^{166}Ho	^{177}Lu	^{90}Y(^{177}Lu)	^{186}Re/ ^{188}Re
Physical half-life, $T_{1/2}$ (h)	64.08	64.08	46.32	26.80	159.6	64.08 (159.6)	89.28/ 17.00
Maximum E_{β}- (keV) [% yield]	2279.8 [99.98]	2279.8 [99.98]	807.6 [19.5]	1854.5 [48.2]	498.3 [79.3]	2279.8 [99.98]	2120.4 [71.7]
Principal Eγ (keV) [% yield]	None	None	103.2 [29.2]	80.6 [6.6]	208.4 [10.4]	208.4 [10.4]	155.0 [15.2]
Matrix material	Glass	Resin	Resin	PLLA	Polymer	Glass	Glass
Size (μm)	20-30	20-60	20-40	10-45	20-40	20-40	25-32
Density (g cm^{-3})	3.2	1.6	2.5	1.4	NP	3.3	2.9
Activities (GBq) available per vial or per g	3, 5, 7, 10, 15, 20	3	3.1	25.9	NP	NP	NP
Number of particles (million) per vial or per g	1.2, 2, 2.8, 4, 6, 8 respectively	40 - 80	57.6	132	NP	NP	NP
Activity (Bq) per particles	2,500	50	54	196	NP	NP	NP

4.5 Discussions

The FTIR spectroscopy showed that harsh physical force applied on the resin beads during grinding process did not destroy the chemical structure of the resin especially its functional group. The FTIR spectra before and after neutron activation also indicated that high temperature during oven drying (70°C) and neutron activation (>100°C) did not affect the chemical structure of the resins and its functional properties.

Following neutron activation, an increase in the number of smaller fragments were observed. The tendency to break could be influenced by the physical structure of the resin which is very jagged following size reduction. In order to overcome this problem, spherical microparticles will be ideal since a spherical structure can withstand larger mechanical force due to a more compact structure. For the pre-irradiated microparticles, although a separation to obtain microparticles of 20 – 40 μm had been done via sieve analysis, the presence of microparticles outside of this range were still observed. This can be explained by two reasons, one is since the microparticles did not have a uniform structure, those with large Feret's diameter might still pass through the 40 μm sieve from its shorter edge. The second reason could be due to flocculation of smaller microparticles or overlapping of microparticles captured by the FESEM. Thus, during image analysis, these microparticles were measured as one microparticle with very large diameter.

For the smaller range microparticles, the reason could be due to inadequate sieving as a result of difficulty of separating very fine microparticles and due to jagged physical structure, hence it requires longer time to be separated as compared to spherical particles. This can be improved by increasing the sieving time to ensure that the smaller microparticles can be removed or by using ultrasonic micro sieves to reduce time. The other reason could be due to image noise produced during the image analysis. Regardless, the microparticles in the range of 10 – 60 μm were still higher than 60 % following

neutron activation. Even though there were only 28 % microparticles in the initial desired range of 20 – 40 µm, further improvements can be made with more spherical particles for improved particle strength and sieving efficiency, hence a more uniform microparticles distribution can be achieved within the desired range.

The viscosity of the suspension should be indistinguishable from normal saline, and relatively lower than blood viscosity (3 cP). The suspension was prepared in dilute form as it is during intra-arterial administration to prevent blockage of the microcatheter. The settling velocity is relatively low due to reduced mean diameter following neutron activation, and should be better than that of glass microparticles, since the settling velocity is largely dependent on the diameter and particle density. Hence, the suspension is relatively stable. A lower settling rate and higher stability can be further achieved by using slightly higher viscosity solvent such as 5 % dextrose solution, which is practiced by our institution for the administration of SIR-Spheres®.

As compared to the other studies, the main advantages of the microparticles developed in this study are the ability to produce zero radionuclide impurities and also very high labelling efficiency following prolong neutron activation, as shown in the previous chapter. Despite some breakage of the physical structure, the microparticles were still able to retain ^{153}Sm for long period of 48 h and labelling efficiency higher than 95 % was achieved. Unlike glass microparticles with high density, resin is a much better choice since it possesses lower settling rate hence, will aid in easy microparticles delivery. The microparticles were able to provide great functionality despite long irradiation period which is not possible for poly-l-lactic acid (PLLA) or other biodegradable polymer (Hafeli et al., 2001).

In terms of the radionuclides used in previous studies, the production of rhenium (Re) via neutron activation of the ReO_2 (Hafeli et al., 1999) is not recommended, as this will

produce both rhenium-186 (^{186}Re) and rhenium-188 (^{188}Re), with the former decaying to an unstable daughter nuclide with long physical half-life. Also, for practicality, having half-lives of about 1 d or less might be a disadvantage for ^{188}Re and holmium-166 (^{166}Ho). On the other hand, lutetium-177 (^{177}Lu) with half-life of 6.65 d will require patients to be hospitalised, hence contributing to added cost. In terms of the therapeutic beta energy, ^{166}Ho and ^{188}Re provide high maximum beta energies, close to that of yttrium-90 (^{90}Y). However, since the major aim is to overcome the issue with post-procedure imaging, the energy of the gamma radiation is important in this respect. In this case, the gamma energy of ^{166}Ho (80.6 keV) is considered to be relatively low thus, high resolution images might still not able to be achieved. ^{177}Lu, on the other hand, possesses the highest gamma energy (208.4 keV) amongst these radionuclides, although its therapeutic beta energy is very low. Another important aspect for radionuclides produced via neutron activation is the thermal neutron activation cross-section, σ_{act} (barn) of the target nuclide. Lutetium-176 (^{176}Lu) possesses the highest value of 2050 barn (IAEA, 1974), while both ^{165}Ho and ^{187}Re possess low cross-section values of less than 100 barn.

We have shown that styrene-divinylbenzene (DVB) copolymer ion exchange resin has a stable chemical structure and function, and is suitable for use in TARE despite the irregular shapes of the microparticles. An effort to improve the surface of the microparticles has been done, by investigating the possibility for spheroidisation to produce spherical microparticles which will possess higher mechanical strength and improved flow during intra-arterial administration. The Amberlite resin has been sent to Aveka Inc. (Woodbury, MN) which offers particles spheroidisation by melt-spraying technology. However from the report provided, it was found that even though the thermogravimetric analysis of the resin shows that it degrades at around 300^{o}C, when the temperature was raised to 200^{o}C, the resin material did not melt. Instead, they turned into dark brown and appeared to begin degrading. Hence, it was concluded that the material

was not suitable for melt processing, and will not be able to be spheroidised. For future work, we are looking into the production of an improved ^{153}Sm-microparticles which possess a spherical shape but retaining all the excellent qualities explained in the current and previous chapters, before it can be further used for animal studies.

We were able to achieve 3 GBq of ^{153}Sm activity with corresponding number of microparticles similar to that of ^{90}Y SIR-Spheres®. However, it should be noted that similar activity of ^{153}Sm and ^{90}Y will not result in similar therapeutic response, because the energies of the beta emissions are different between these two radioisotopes. Hence, further studies to determine ^{153}Sm activity equivalent to 3 GBq of ^{90}Y, need to be carried out.

Due to the presence of gamma energy from ^{153}Sm, radiation exposure received by neighbouring organs and patient's surrounding need to be considered and a tolerable dose limit needs to be determined. As compared to iodine-131 (^{131}I) treatment with 3.5 times higher gamma energy and 4 times longer half-life than that of ^{153}Sm, protective measures required following TARE with ^{153}Sm-microparticles are predicted to be of relatively lesser concern. A dosimetry study for TARE with ^{166}Ho-microspheres reported that only 1.1 % of the overall absorbed dose were contributed by the gamma emission (Turner et al., 1994). Although the contribution by ^{153}Sm should be higher due to slightly higher gamma energy and two times longer half-life, the risk is still expected to be minimal as compared to the benefits from dose delivered to the tumour. However, patient's hospitalisation and crucial radiation monitoring need to be carried out, before the patient can be released following the ^{153}Sm treatment. Internal radiation dosimetry on this matter can be done using Monte Carlo (MC) simulations.

4.6 Conclusion

A theranostic 20 – 40 μm resin microparticles have been prepared using ion exchange resin (styrene-DVB with sulphonic acid group), labelled with ^{153}Sm produced via neutron activation. The ^{153}Sm-Amberlite microparticles are easy to be labelled and the procedure does not involve unnecessary radiation exposure. They were able to withstand prolonged irradiation, at the same time possessed excellent labelling efficiency with strong retention of ^{153}Sm tested over 48 h, no radioactive impurities produced from neutron activation, low settling velocity and stable in suspension, and the lower production cost than that of ^{90}Y SIR-Spheres®. The ^{153}Sm-Amberlite microparticles have the potential to be used as an alternative to ^{90}Y-microspheres, with added advantage of gamma radiation for imaging of activity distribution following TARE. Dosimetric studies to estimate the total ^{153}Sm activity needed to deliver equivalent tumour dose and therapeutic response from 3 GBq ^{90}Y shall be carried out.

CHAPTER 5: SYSTEMATIC EVALUATION OF CURRENT DOSIMETRY METHOD USED IN HEPATIC RADIOEMBOLIZATION USING GEANT4 MONTE CARLO SIMULATION

5.1 Introduction

Transarterial radioembolization (TARE) of hepatocellular carcinoma (HCC) is being done by administering radioembolic agents (resin or glass) labelled with yttrium-90 (^{90}Y) directly to the tumour in the liver, via the aid of a catheter to the hepatic artery. Since ^{90}Y and samarium-153 (^{153}Sm) have different physical characteristics (energy and yield of beta and gamma radiations, and half-lives), similar activity of each radionuclide will not deliver the same amount of absorbed dose. Hence, the total amount of ^{153}Sm activity required to deliver the absorbed dose equal to that of ^{90}Y needs to be determined, in order for similar therapeutic ability to be achieved.

TARE with ^{90}Y-microspheres is typically delivered so to achieve absorbed dose to tumour of 100 - 120 Gy (Garin et al., 2015; Dezarn et al., 2011; Kennedy et al., 2007; Salem & Thurston, 2006), which balances between safety and effectiveness (Kennedy et al., 2007; Salem & Thurston, 2006). In order to lower the risk of radiation pneumonitis, the extrahepatic shunting of the microspheres especially to the lungs is assessed, prior to the treatment, using technetium-99m (^{99m}Tc)-macroaggregated albumin (MAA) (Sirtex, 2015). The lung shunting (LS) should be lower than 20 %, to limit the absorbed dose to lungs from exceeding the maximum dose of 30 Gy per treatment session, and 50 Gy cumulatively (Garin et al., 2015; Ho et al., 1997). Moreover, in order to preserve enough liver functions following the treatment, a maximum normal liver dose of 70 Gy is recommended (Sirtex, 2015; Lau et al., 2012).

In estimating the absorbed dose received from the administered activity of ^{90}Y, the partition model (PM) method is currently being used, however, the method assumes a local dose deposition and disregards the effect of cross-fire irradiation (Garin et al., 2015; Sirtex, 2015; Ho et al., 1996). This approximation introduced uncertainties on the estimated dose: firstly, it is well-known that tumour vascularity has the tendency to be distributed at the periphery of the tumour (Kennedy et al., 2004; Campbell et al., 2001, 2000; Fox et al., 1991), hence, it is reasonable to assume that most of the ^{90}Y-microspheres will be concentrated around the tumour edges rather than its centre. Secondly, since ^{90}Y beta particles have a relatively long maximum range of approximately 11 mm in tissue, some of the beta particles originated from the tumour, especially those located at the tumour edges, will reach the normal liver and deposit energy. Thus, the cross-fire irradiation, especially at the tumour and normal liver boundary may contribute to a significant fraction of the absorbed dose.

The absorbed doses estimated using PM has been previously compared with dose measured using intraoperative beta probing (Ho et al., 1996). Although correlations were found between the measured and calculated data, the discrepancies were still large with mean dose differences of 14.8 ± 14.0 and 15.1 ± 27.2 % for tumour and normal liver, respectively. Also, the highly invasive approach is considered impractical and contradictive to TARE, which is minimally invasive. Several publications have recommended the use of Monte Carlo (MC) simulations in estimating the absorbed dose in TARE of HCC (Garin et al., 2015; Kao et al., 2011; Gulec et al., 2010; Flamen et al., 2008; Kennedy et al., 2004; Sarfaraz et al., 2004). It is expected that the MC method is more accurate in estimating the dose delivered to the tumour and the surrounding healthy tissues as compared to PM, because the energy deposition in a medium is calculated without adopting any geometrical assumption or any simplified model in terms of particle

transportation. Geometry and Tracking 4 (Geant4) (Allison et al., 2006; Agostinelli et al., 2003) MC package has been increasingly used for estimation of absorbed dose in nuclear medicine, with its accuracy validated through experimental measurements using physical phantoms (Ziaur et al., 2012; Meo et al., 2008).

In this chapter, the accuracy of the absorbed doses estimated by PM, as a result of exclusion of cross-fire irradiation, especially between the tumour and normal liver tissue was investigated, for TARE with ^{90}Y-microspheres. Geant4 MC simulations were carried out and the resulting absorbed doses were compared with the doses calculated using PM. The factors that may affect the accuracy of PM estimations were determined and discussed in this study. The findings will be useful to estimate a more accurate absorbed dose received by the compartments; tumour, normal liver tissue, and both lungs, from the administration of ^{90}Y-microspheres, so that the correct amount of ^{153}Sm can be delivered in order to achieve similar absorbed doses, which the latter will be explained in the next chapter.

5.2 Objectives

This study was carried out to investigate the accuracy of PM in estimating the absorbed doses to tumour, normal liver tissue and lungs in TARE with ^{90}Y-microspheres, as a results of the exclusion of cross-fire irradiation between the compartments. This will be determined by achieving these specific objectives which includes:

i. To compare the absorbed dose to tumour, normal liver, and both lungs obtained from the PM calculations with the Geant4 simulations.
ii. To determine the combinations of patient parameters; tumour involvement, lung shunting (LS) and tumour-to-normal liver uptake ratio (T/N), that contribute to larger absorbed dose difference between the PM calculations and the Geant4 simulations.

5.3 Methodology

5.3.1 The Partition Model (PM)

PM is used to estimate the absorbed dose to tumour, normal liver tissue and both lungs for TARE of HCC with ^{90}Y-microspheres. It was derived by Ho et al. (1996) and it assumes that the radioactive microspheres are distributed only in the three compartments, with no redistribution during the treatment. The model was derived from the decay data of ^{90}Y and, assuming a complete deposition of energy within a compartment, it depends only on the initial activity in the compartment and the compartment's total mass (Ho et al., 1996). Thus, the absorbed dose, D in a compartment is calculated using **Equation 5.1**, where, A_o is the activity (GBq) in the compartment of mass, m (expressed in grams).

$$\text{Absorbed dose, D (Gy)} = \frac{49670 \times A_o(\text{GBq})}{m\ (g)} \qquad \textbf{5.1}$$

In order to determine the activity distributed within each organ, the LS and T/N are obtained from the pre-treatment imaging using ^{99m}Tc-MAA. The values are calculated using **Equation 5.2** and **Equation 5.3**.

$$\text{LS (\%)} = \frac{\text{Total counts in lungs}}{\text{Total counts in liver + Total counts in lungs}} \times 100\ \% \qquad \textbf{5.2}$$

$$\text{T/N} = \frac{\text{Total counts in tumour}}{\text{Total counts in liver - Total counts in tumour}} \qquad \textbf{5.3}$$

Thus, the activity uptake in both lungs is calculated using **Equation 5.4**, where, A is the total administered activity (GBq), and A_L is the activity (GBq) taken up by both lungs.

$$A_L = A\left(\frac{LSF(\%)}{100}\right)\text{GBq} \qquad \textbf{5.4}$$

The remainder activities that goes to the tumour, A_T and normal liver, A_N are shown in **Equation 5.5**, which correspond to T/N as shown in **Equation 5.6**, where, m_T and m_N are the mass (g) of tumour and normal liver, respectively.

$$A_T + A_N = A - A_L \qquad \textbf{5.5}$$

$$\text{T/N} = \frac{A_T / m_T}{A_N / m_N} \qquad \textbf{5.6}$$

5.3.2 The Geant4 Monte Carlo Application

5.3.2.1 Computational Phantom

This study was carried out using Geant4 version 9.6.p03 (Allison et al., 2006; Agostinelli et al., 2003). As in the Geant4 advanced example *human_phantom*, a mathematical adult phantom was modelled according to the Medical Internal Radiation Dose (MIRD) Pamphlet 5 consisting of complete anatomical organs (Snyder et al., 1978), with either female or male genitalia (which the former are shown in **Figure 5.1**). The 70 kg MIRD-5 phantom comprises of three types of tissues namely the bone, lung and soft tissue (densities of 1.4862, 0.2958 and 0.9869g.cm^{-3}, respectively). However, for this study, the only organs of interest are the liver and both lungs, hence the gender of the phantom and all the other organs were not of primary interest. The masses of each lung and liver are 500 and 1809 g, respectively.

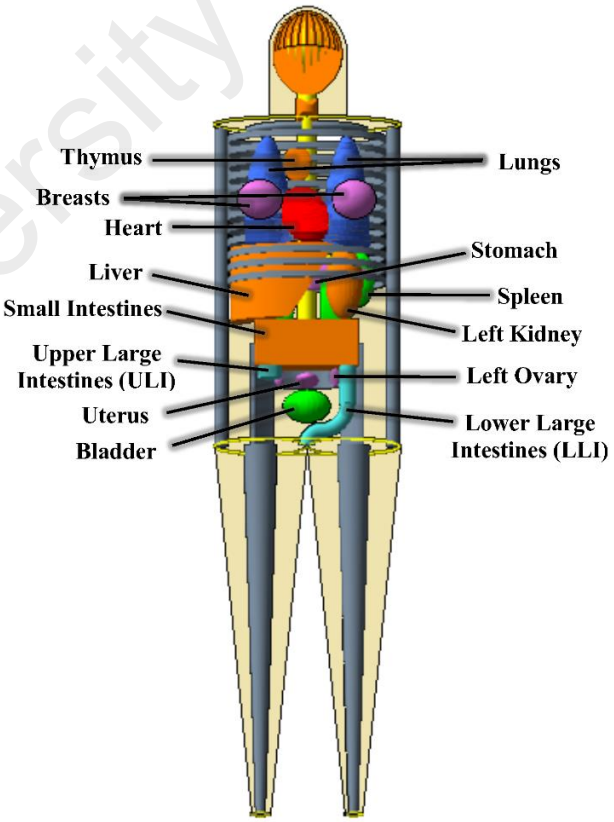

Figure 5.1: MIRD pamphlet 5 adult female human phantom (Snyder et al., 1978), as constructed and visualised using Geant4.

In this study, a single tumour with similar shape as the mathematical MIRD-5 liver, located at the centre of the liver and varying in mass was considered (**Figure 5.2**). The tumour mass was indirectly defined by the tumour involvement (%) calculated using **Equation 5.7**.

$$\text{Tumour involvement (\%)} = \frac{\text{Mass of tumour}}{\text{Mass of liver}} \times 100\ \% \qquad \textbf{5.7}$$

The use of a non-spherical tumour was justified by two considerations: first, geometrical limitations allowed only spheres of radius up to 4.3 cm to be confined within the liver, which corresponded to a tumour mass of 329 g or a maximum tumour involvement of only 18 %. Secondly, the dose calculated by PM is largely dependent on the tumour mass, and due to assumption that all emissions will be absorbed within the tumour, the shape of the tumour should not affect the absorbed dose estimated by PM. Nonetheless, additional simulations with spherical tumour of 10 % tumour involvement was also carried out for comparison. The surface area-to-volume ratios (SA/V) for the tumours used in this study are shown in **Table 5.1**. The surface area of the liver was 1724.0 ± 5.3 cm^2.

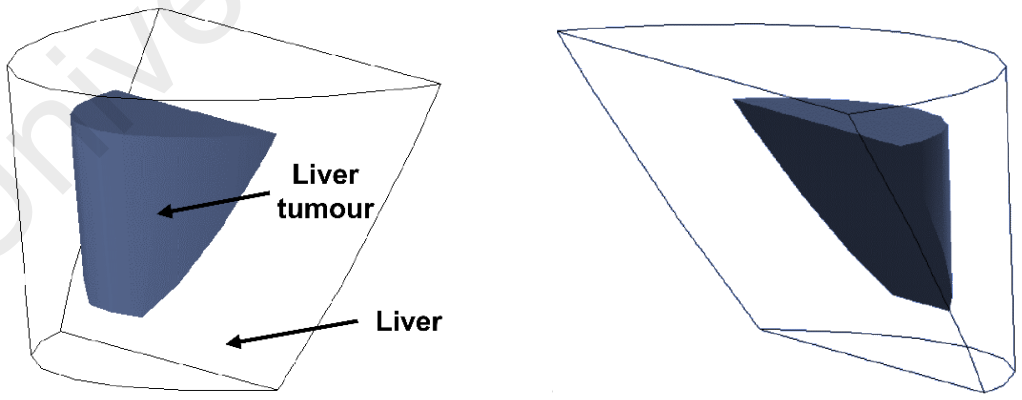

(a) (b)

Figure 5.2: (a) Antero-superior and (b) postero-superior view of the tumour model for 10 % tumour involvement.

Table 5.1: Surface area-to-volume ratios (SA/ V) (cm^{-1}) for the tumour model used in our study.

Tumour mass (g)	Tumour involvements (%)	Surface area (cm^2)	Volume (cm^3)	SA /V (cm^{-1})
180.9	**10 (sphere)**	156.1	183.3	0.85
180.9	**10**	577.8 ± 3.4	183.3	3.15
542.7	**30**	944.5 ± 4.3	549.9	1.72
904.5	**50**	1222.6 ± 2.3	916.5	1.33
1266.3	**70**	1426.9 ± 1.8	1283.1	1.11

5.3.2.2 Details on the Geant4 Code

The Low Energy Electromagnetic Package (Chauvie et al., 2004), based on the Livermore Evaluated Data Libraries, was adopted to model the electromagnetic interactions of photons and electrons. The threshold of production of secondary particles was fixed to 1 mm. The Geant4 Radioactive Decay component was used to model the decay of ^{90}Y. The Geant4 General Particle Source was used to model the radionuclide in the tumour. ^{90}Y point sources were homogenously distributed within each compartment with activity uptake based on the selected T/N and LS, with randomised direction of emissions. The tumour, normal liver, right lung and left lung were each set as a sensitive volume. The output was set as mean energy (MeV) deposited to each volume.

5.3.3 Effects of Various Patient Parameters on Absorbed Dose

The effects of various patient parameters; tumour involvement (10, 30, 50, 70 %), T/N (1, 2.5, 5, 7.5, 10) and LS (0, 5, 10, 15, 20 %; with no activity reduction for 15 and 20 %), on the accuracy of absorbed dose estimated using PM were investigated. Using Geant4, 10^8 disintegrations (corresponded to 300 Bq of ^{90}Y) were generated for each parameter combination and repeated three times to obtain a standard deviation of less than

1 %. The mean energy (MeV) deposited within each compartment (tumour, normal liver and both lungs) was converted to joules, J and divided by the mass to obtain the absorbed dose (Gy) to each compartment. The absorbed doses were divided by the activity deposited to each compartment to obtain the corresponding absorbed dose per activity ($mGy.MBq^{-1}$). The results were compared with the corresponding PM estimations to quantify the deviations between the two methods.

The implications of the dosimetric differences were studied by targeting either the maximum absorbed dose (by administering the highest possible activity estimated using PM) to the normal liver tissue or lungs of 70 or 30 Gy, respectively, for each parameter combination. The same activities were applied to the absorbed dose per activity values calculated from the simulations, to obtain the actual absorbed doses received by each compartment. Finally, the absorbed doses obtained from the two methods (PM versus Geant4) were compared, and the parameter combinations that may contribute to lungs or normal liver overdose were determined.

5.4 Results

5.4.1 Comparison of Absorbed Dose to Lungs

The absorbed dose per activity uptake to both lungs for all T/N and LS (except for 0 %) generated by PM and Geant4 were 49.67 ± 0.00 and 43.84 ± 0.01 $mGy.MBq^{-1}$, respectively. Tumour involvement (%) was not a factor that affects the absorbed dose to the lungs since the lungs size are fixed to a mass of 1 kg throughout the study. This correspond to the absorbed dose difference of 11.74 ± 0.03 % with respect to PM.

5.4.2 Comparison of Absorbed Dose to Tumour

The absorbed dose per activity uptake to tumour with various tumour involvements and T/N are shown in **Table 5.2**. LS does not affect the absorbed dose to the tumour. As seen in the table, the absorbed dose to tumour by PM are not affected by the T/N, rather they only depends on the tumour involvement. On the other hand, our simulations shown that T/N indeed affect the absorbed dose to the tumour. The absorbed dose for spherical tumour of 10 % tumour involvement showed close agreement of within 3.2 %, with its non-spherical counterpart. **Figure 5.3** shows the relative difference between the absorbed dose to tumour generated by the two methods with various tumour involvements and T/N, with respect to PM. For tumour, the relative differences are observed to be larger for lower tumour involvement and higher T/N, with maximum absorbed dose overestimation of up to 8 % by PM. The relative difference for spherical tumour of 10 % tumour involvement was indistinguishable with the non-spherical tumour of 30 % tumour involvement used in this study.

Table 5.2: Absorbed dose per activity uptake to tumour calculated using the partition model and Geant4 simulations. TI: tumour involvement; S: sphere; T/N: tumour-to-normal liver uptake ratio.

TI (%)	Absorbed dose per activity uptake to tumour (mGy.MBq^{-1})					
	Partition Model (all T/N)	Geant4				
		T/N				
		1	2.5	5	7.5	10
10	274.57	275.13	259.97	254.92	253.28	252.41
10 (S)	274.57	275.16	265.33	262.15	261.03	260.54
30	91.52	91.70	88.45	87.37	87.00	86.82
50	54.91	55.02	53.40	52.87	52.69	52.60
70	39.22	39.27	38.27	37.93	37.82	37.76

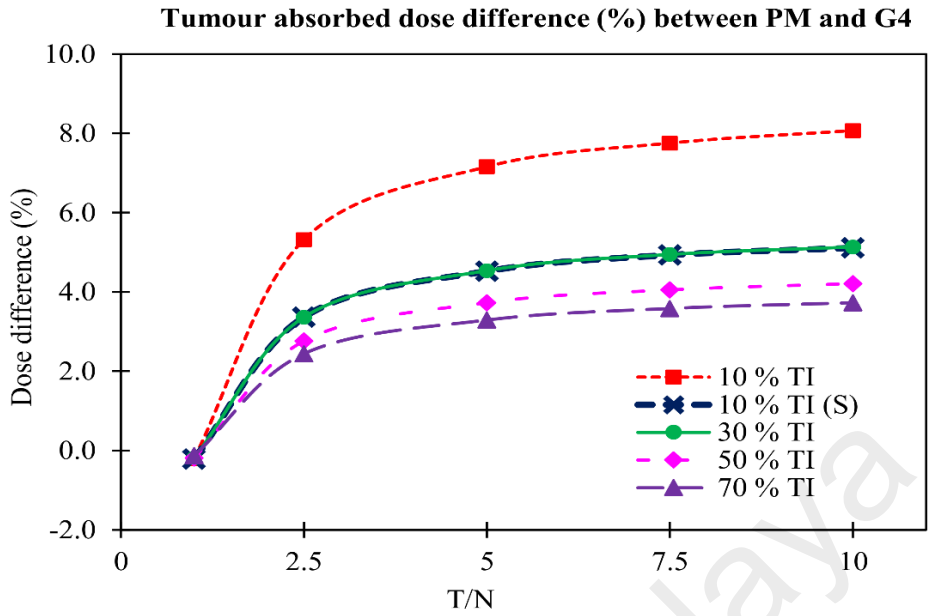

Figure 5.3: Tumour absorbed dose difference (%) between the partition model (PM) and Geant4 (G4) for various tumour involvements (TI) (including 10 % sphere (S)) and tumour-to-normal liver uptake ratio (T/N), normalised to PM.

5.4.3 Comparison of Absorbed Dose to Normal Liver

The absorbed dose per activity uptake to normal liver with various tumour involvements and T/N are shown in **Table 5.3**, respectively. LS does not affect the absorbed dose to the normal liver. As seen in the table, the absorbed dose to normal liver by PM are not affected by the T/N, rather they only depends on the tumour involvement. On the other hand, our simulations shown that T/N indeed affect the absorbed dose to the normal liver. The normal liver absorbed dose for spherical tumour of 10 % tumour involvement showed close agreement of within -3.3 %, with its non-spherical counterpart. **Figure 5.4** shows the relative differences between normal liver absorbed dose generated by the two methods with various tumour involvements and T/N, with respect to PM. For normal liver, the relative differences for T/N of less than 2 were larger for higher tumour involvement and lower T/N. However as the T/N goes beyond 2, the relative differences drastically shift to negative values with larger differences observed for higher tumour

involvement and T/N, up to a maximum difference of -78 %. From **Figure 5.4**, it was found that at T/N of approximately 2, the relative differences for all tumour involvements are equal with values of about 3 %, with respect to PM.

Table 5.3: Absorbed dose per activity uptake to normal liver calculated using the partition model and Geant4 simulations. TI: tumour involvement; S: sphere; T/N: tumour-to-normal liver uptake ratio.

TI (%)	Absorbed dose per activity uptake to normal liver ($mGy.MBq^{-1}$)					
	Partition Model (all T/N)	Geant4				
		T/N				
		1	2.5	5	7.5	10
10	30.51	29.28	29.75	30.53	31.31	32.09
10 (S)	30.51	29.28	29.58	30.08	30.59	31.08
30	39.22	37.18	38.67	41.17	43.66	46.15
50	54.91	50.87	54.92	61.65	68.37	75.10
70	91.52	80.27	94.00	116.92	139.75	162.71

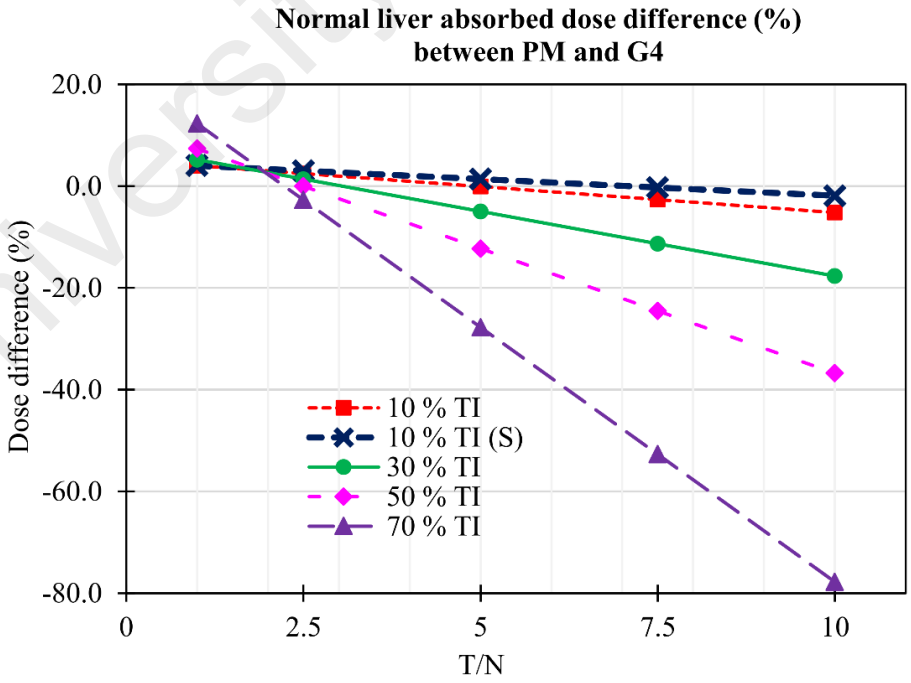

Figure 5.4: Normal liver absorbed dose difference (%) between the partition model (PM) and Geant4 (G4) for various tumour involvements (TI) (including 10 % sphere (S)) and tumour-to-normal liver uptake ratio (T/N), normalised to PM.

5.4.4 Implications on Absorbed Dose

Amongst 125 simulated cases (including 25 cases for spherical tumour of 10 % tumour involvement), 31 cases where the actual absorbed dose to normal liver (obtained via Geant4 simulations) exceeded the maximum limit (70 Gy) were determined, and are listed in **Table 5.4**. Since PM overestimated all absorbed dose to lungs by 11.7 %, hence the actual dose to lungs estimated by Geant4 never exceeded the maximum limit of 30 Gy. All cases in **Table 5.4** involved LS values of equal or lower than 10 % with most T/N of equal or larger than 5 (only 2 cases with T/N of 2.5). The mean administered activity was 8.18 ± 3.61 GBq, with minimum and maximum activity of 4.21 and 18.61 GBq, respectively.

The absorbed dose to tumour as estimated by PM were in the range of 175 to 700 Gy, however Geant4 estimated a significantly lower ranges of tumour dose. Out of the 31 cases, only 4 cases were estimated by PM to reach the maximum dose to lungs (hence, the absorbed dose to normal liver should be lower than 70 Gy), but the maximum limit to normal liver was still exceeded. Two cases with absorbed dose to normal liver of larger than 100 Gy were recorded by the liver with 70 % tumour involvement. Only 3 cases were recorded by the spherical tumour model, half as compared to the non-spherical model with similar mass used in this study.

Table 5.4: Cases with absorbed dose to normal liver (via Geant4 simulations) exceeded the maximum limit of 70 Gy. TI: tumour involvement; S: spherical tumour; LS: lung shunting; T/N: tumour-to-normal liver uptake ratio; A: activity; NL: normal liver.

No.	TI (%)	LS (%)	T/N	A (GBq)	Absorbed dose (Gy)					
					Partition Model			Geant4		
					Lungs	Tumour	NL	Lungs	Tumour	NL
1	10	0	7.5	4.21	0.0	525.0	70.0	0.0	484.3	71.8
2	10	0	10	4.84	0.0	700.0	70.0	0.0	643.5	73.6
3	10	5	7.5	4.43	11.0	525.0	70.0	9.7	484.3	71.8
4	10	5	10	5.10	12.7	700.0	70.0	11.2	643.5	73.6
5	10	10	7.5	4.67	23.2	525.0	70.0	20.5	484.3	71.8
6	10	10	10	5.38	26.7	700.0	70.0	23.6	643.5	73.6
7	10 (S)	0	10	4.84	0.0	700.0	70.0	0.0	664.2	71.3
8	10 (S)	5	10	5.10	12.7	700.0	70.0	11.2	664.2	71.3
9	10 (S)	10	10	5.38	26.7	700.0	70.0	23.6	664.2	71.3
10	30	0	5	5.61	0.0	350.0	70.0	0.0	334.1	73.5
11	30	0	7.5	7.52	0.0	525.0	70.0	0.0	499.1	77.9
12	30	0	10	9.43	0.0	700.0	70.0	0.0	664.1	82.4
13	30	5	5	5.90	14.7	350.0	70.0	12.9	334.1	73.5
14	30	5	7.5	7.92	19.7	525.0	70.0	17.4	499.1	77.9
15	30	5	10	9.93	24.7	700.0	70.0	21.8	664.1	82.4
16	30	10	5	6.04	30.0	339.2	67.8	26.5	323.8	71.2
17	50	0	5	7.65	0.0	350.0	70.0	0.0	336.9	78.6
18	50	0	7.5	10.84	0.0	525.0	70.0	0.0	503.7	87.2
19	50	0	10	14.02	0.0	700.0	70.0	0.0	670.5	95.7
20	50	5	5	8.05	20.0	350.0	70.0	17.6	337.0	78.6
21	50	5	7.5	11.41	28.3	525.0	70.0	25.0	503.7	87.2
22	50	5	10	12.08	30.0	572.9	57.3	26.5	548.8	78.3
23	70	0	2.5	5.23	0.0	175.0	70.0	0.0	170.7	71.9
24	70	0	5	9.69	0.0	350.0	70.0	0.0	338.5	89.4
25	70	0	7.5	14.15	0.0	525.0	70.0	0.0	506.2	106.9
26	70	0	10	18.61	0.0	700.0	70.0	0.0	673.9	124.4
27	70	5	2.5	5.50	13.7	175.0	70.0	12.1	170.7	71.9
28	70	5	5	10.20	25.3	350.0	70.0	22.4	338.5	89.4
29	70	5	7.5	12.08	30.0	425.8	56.8	26.5	410.6	86.7
30	70	5	10	12.08	30.0	431.6	43.2	26.5	415.5	76.7
31	70	10	2.5	5.81	28.8	175.0	70.0	25.5	170.7	71.9

5.5 Discussions

PM was derived by Ho et al. (1996) from the decay data of ^{90}Y, where 0.037 MBq taken up by 1 g of soft tissue will results in absorbed dose of 183.78 cGy. Following simplification, this has resulted in the constant value of 49670, which is used in the main formula (**Equation 5.1**) for absorbed dose estimation (Ho et al., 1996). However, the major error to this is that the same constant was used to estimate the absorbed dose to lungs, where the constant derived from energy deposited in lung tissue (which composed mostly of air) should be used instead. This by default has already resulted in an inaccurate estimation of dose to lungs which has been demonstrated in this study, with PM constantly overestimates the lung dose by 11.7 %. Using this finding, **Equation 5.1** can be corrected exclusively for estimation of the absorbed dose to lungs, by multiplying 0.883 to 49670, thus, **Equation 5.8** is as follows:

$$\mathrm{D_L\ (Gy)} = \frac{43859 \times A_L\,(\mathrm{GBq})}{m_L\,(g)} \qquad \textbf{5.8}$$

where, m_L is the mass of both lungs. Other than this, the effect of cross-fire at the lung boundary and even from deep in the lungs (since beta has longer range in air) have also contribute to the overestimation, since some beta particles managed to escape from the lungs. From our study, we did not find any significant contribution of the absorbed dose to lungs from the radiations in the liver as a result of the phantom geometry used in the study, where liver and lungs separation distant is larger than the beta range of ^{90}Y (11 mm).

As mentioned in the methodology section, the spherical tumour model was limited to a maximum of 18 % tumour involvement hence the model was not used in this study. As provided, the surface area of the trapezoidal tumour model used in this study is higher

than the spherical model of similar mass, hence it is expected that relatively more beta particles would escape from the trapezoidal model, which consequently would affect the results. From the comparison made with both models of 10 % tumour involvement, it was found that the absorbed doses to tumour and normal liver for the trapezoidal model were smaller and larger by ~3 %, respectively, as compared to the spherical model, as a result of more cross-dose to the normal liver. For tumour involvement of larger than 10 %, it is expected that the tumour dose difference between the spherical and the trapezoidal model to be much smaller as a result of relatively closer SA/V between the tumour models and since larger mass are less affected by the difference in energy deposition. However, for the absorbed dose to the normal liver, the difference would be the opposite as it is expected that the difference would increase with increase tumour involvement, as a result of decreased in normal liver mass. Nonetheless, since PM assumed all radiations to be fully absorbed by the compartment, hence, they are only dependent on the compartment's mass. Hence, as the tumour varies with size and shape, the dose estimations by PM could varies greatly with these respect, which will affect the accuracy of the absorbed dose to both tumour and normal liver, when PM is being used.

Further, as shown in the results, the absorbed dose to both tumour and normal liver obtained by Geant4 are also dependent on the T/N which was ignored by PM, as a result of exclusion of cross-fire irradiation between the compartments. For the tumour model used in this study, it was found that PM overestimates the absorbed dose to the tumour to a maximum of 8 % especially for lower tumour involvement and higher T/N. Larger overestimation by PM for lower tumour involvement was due to higher tumour SA/V. Hence, for these tumours, the probability of the beta particles leaving is higher than being self-absorbed, which leads to a larger overestimation by PM. Larger overestimation for higher T/N was due to higher total number of beta particles leaving the tumour as compare

to the lower T/N (**Figure 5.5**). For lower T/N, the fraction of beta particles leaving the tumour is being compensated by the particles entering the tumour from the normal liver. As a result, the tumour absorbed dose for lower T/N is higher and closer to the tumour dose estimated by PM. The tumour dose difference for T/N of 1 were negligible due to charge particle equilibrium (CPE) at the tumour and normal liver boundary.

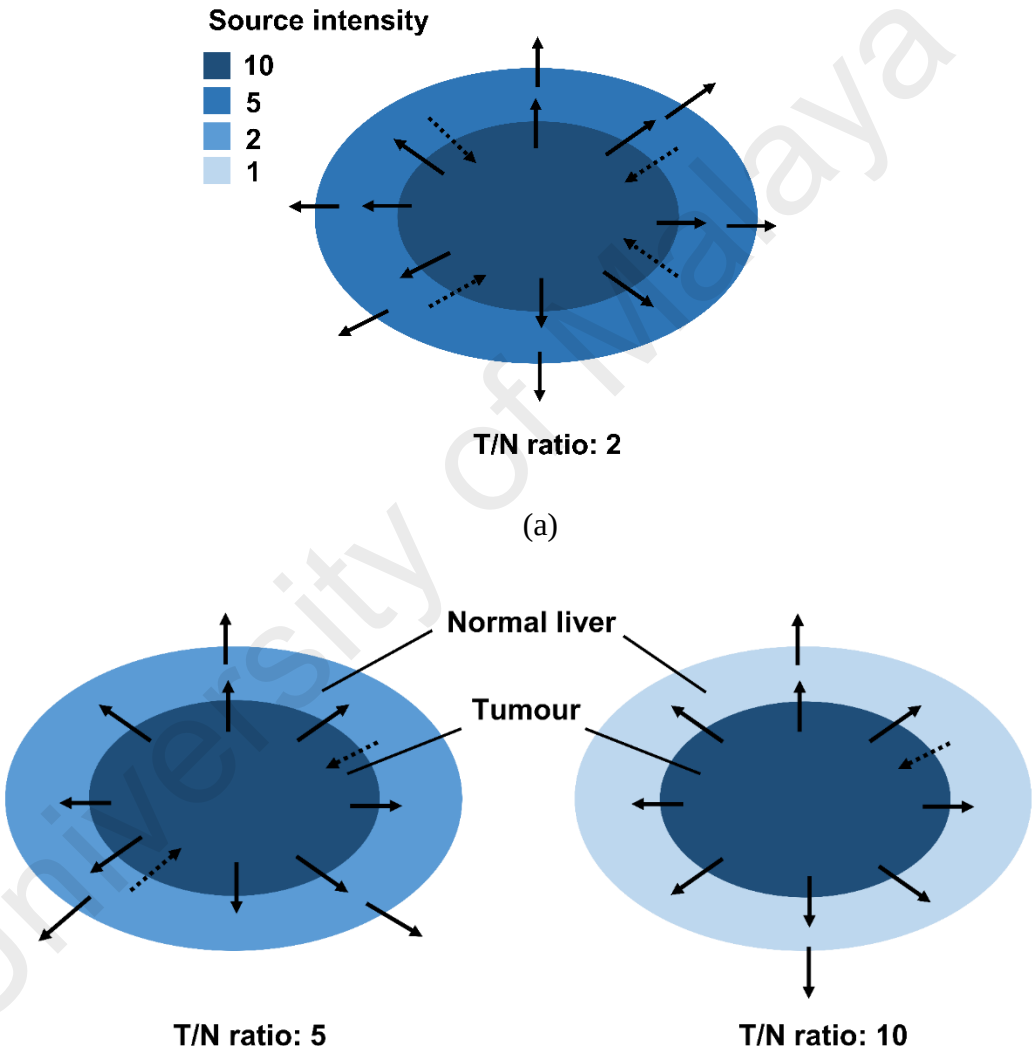

Figure 5.5: Cross-fire events occurring at the compartment boundaries which affect the absorbed dose to both tumour and normal liver, as a result of difference in the tumour-to-normal liver uptake ratio (T/N).

The difference between the absorbed dose to normal liver estimated by the two methods were found to be rather complex. It was found that PM overestimates the dose to normal liver for T/N of < 2 by up to 12.3 %. This happens due to higher radionuclide concentration in the normal liver (low T/N) as shown in **Figure 5.5 (a)**; the total number of particles leaving the normal liver from both tumour and extrahepatic boundaries surpassed the number of particles entering the normal liver from the tumour boundary. This effect is more dominant for higher tumour involvement (hence smaller normal liver volume) due to higher normal liver SA/V. For T/N of >2, it was found that PM underestimates the normal liver dose. This is due to lower radionuclide concentration in the normal liver (high T/N), hence the dose to the normal liver is being affected by the particles entering the normal liver from the tumour boundary, resulting in higher normal liver dose than estimated by PM. Again, the difference is more dominant for smaller normal liver volume (higher tumour involvement) due to higher SA/V.

The transition that occurs at T/N of ~2 can be explained due to CPE. When T/N increases and approaching 2, the particles leaving the normal liver is slowly compensated by the increased number of particles entering from the tumour boundary. As the T/N increases beyond 2, the amount of particles entering the normal liver from the tumour boundary finally overtakes the total number of particles leaving the normal liver from both tumour and extrahepatic boundaries, hence the absorbed dose to normal liver is higher than estimated by PM as shown in **Figure 5.5 (b)** and **(c)**. The effects of T/N towards the dose difference with respect to PM is summarised in **Table 5.5**.

Table 5.5: Net events occurring at the tumour and normal liver boundaries with various tumour-to-normal liver uptake ratio (T/N) and the effects on the absorbed dose estimated by the partition model (PM). CPE: charge particle equilibrium.

T/N	Net events		Absorbed dose estimated by PM	
	Tumour	Normal liver	Tumour	Normal liver
1	CPE	Particles leaving	Equal	Overestimation
1.5	Particles leaving	Particles leaving	Overestimation	Slight overestimation
2	Particles leaving	CPE	Overestimation	Equal
5	Particles leaving	Particles entering	Overestimation	Underestimation
10	Particles leaving	Particles entering	Overestimation	Large underestimation

Even though the maximum dose difference for tumour between the two methods were only of up to 8 % and as shown in **Table 5.5**; where all dose to tumour were being overestimated by PM, this under dosing may lead to less treatment efficiency if radical approach is being aimed, especially for smaller tumours. For normal liver, it is a concern for patients with higher tumour involvement and T/N, as it is found that surprisingly high underestimation of normal liver dose of up to -78 % by PM, which may cause normal liver overdose even when 70 Gy to normal liver was not aimed, as shown in **Table 5.4** (case no. 16, 22, 29 and 30). Since it is crucial to reserve the liver function, having slightly increase dose could lead to detrimental effects, especially for larger tumour involvement where the reserve normal liver volume is very small. Furthermore, although the administered activities used to achieve either maximum dose to normal liver or lungs were considered to be very high as compared to maximum of 3 GBq recommended for SIR-Spheres® (Sirtex, 2004), they are still highly possible if TheraSphere® is being used. However, this will still be possible for SIR-Spheres® if a whole liver volume of lower than 1809 g is being used, hence requires less activity to achieve similar doses.

It has been demonstrated that PM can be inaccurate in estimating the absorbed dose to tumour, normal liver and both lungs, as a result of the exclusion of cross-fire irradiation between these compartments. However, in terms of safety, PM is still sufficient in estimating the doses to both tumour and lungs, since there is no upper limit to the tumour dose and that maximum dose to lungs of 30 Gy were never exceeded. Nonetheless, it would be recommended that the estimation of the absorbed dose to lungs to be based on the corrected formula (**Equation 5.8**). For normal liver dose, cautions should be taken in estimating the dose especially for cases with higher tumour involvement and T/N, and lower LS, by possibly administering lower activity or separating the treatment in several fractions to favour the normal liver tissue.

This study was done using simple model of the standard MIRD-5 human phantom so to easily understand the pattern of the physical factors that may affect the absorbed dose estimations, by manipulating the patient parameters accordingly. Since every patient's tumour is unique (in terms of size, shape and location), the used of tomographic data may be useful to further estimates the dose to these compartments, with the incorporation of heterogeneity of source distribution which was not considered in our study. However, this method requires more time in terms of code development and simulation runs hence, may not be practical for clinical use. As alternative, voxel dose kernel (VDK) (simulating radiation transport in water and applying the dose distribution map into tomographic images) can be used. However, this method does not take into account the tissue inhomogeneity correction, especially since there is major density difference between the liver and lungs, thus improvements into this matter should be further investigated.

5.6 Conclusion

In conclusion, PM leads to inaccurate dose estimations, due to the exclusion of cross-fire irradiation, especially between the tumour and normal liver. The inaccuracy is especially concerning for cases with higher tumour involvement and T/N, and lower LS, as they contribute to major underestimation of the absorbed dose to normal liver tissue. As for the dose to lungs, the absorbed dose equation by PM should be re-evaluated, since the transport of beta particles varies greatly in lungs (which comprised mostly of air) and soft tissue, which will surely affect the resulting dose as demonstrated in this study. Hence, the corrected equation can be implemented exclusively for lungs, for better accuracy of the estimation of lung dose.

CHAPTER 6: DOSIMETRIC ASSESSMENT ON ^{153}SM-MICROPARTICLES FOR LIVER RADIOEMBOLIZATION

6.1 Introduction

From Chapter 3, we have proven that it is feasible to achieve 3 GBq of samarium-153 (^{153}Sm) activity with corresponding number of microparticles similar to that of yttrium-90 (^{90}Y) SIR-Spheres. However, since ^{153}Sm and ^{90}Y have different physical characteristics (decay yield and energies, and half-life), similar activity of each radionuclide will not result in similar therapeutic dose. Hence, it is crucial to determine the amount of ^{153}Sm activity equivalent to that of ^{90}Y, in order to deliver similar therapeutic dose. Also, due to the presence of gamma energy from ^{153}Sm, radiation exposure received by neighbouring organs need to be considered and a tolerable dose limit needs to be determined.

As compared to iodine-131 (^{131}I) treatment with 3.5 times higher gamma energy and 4 times longer half-life than that of ^{153}Sm, protective measures required following transarterial radioembolization (TARE) with ^{153}Sm are predicted to be of relatively lesser concern. A dosimetry study for TARE with holmium-166 (^{166}Ho)-microspheres reported that only 1.1 % of the overall absorbed dose were contributed by the gamma emission (Turner et al., 1994). Although the contribution by ^{153}Sm should be higher due to slightly higher gamma energy and two times longer half-life as compared to ^{166}Ho, the risk is still expected to be minimal as compared to the benefits from dose delivered to the tumour. However, patient's hospitalisation and crucial radiation monitoring need to be carried out, before the patient can be released following the ^{153}Sm treatment. Although the radiation data for ^{153}Sm-ethylenediamine tetramethylenephosphonate (EDTMP) for bone metastasis has been long established (Vanzi et al., 2009), the data for permanently

administered ^{153}Sm is still yet to be assessed, especially since TARE with ^{153}Sm-microparticles will require higher therapeutic activity than ^{153}Sm-EDTMP, with no excretion or physiological release.

Unlike radiation doses contributed from external beam radiation, it is highly impossible to directly measure radiation doses to organs from internal sources (Stabin, 1996). Ho et al. (1996) have previously measured the absorbed doses using intraoperative beta probing following TARE with ^{90}Y-microspheres. Although correlations were found between the measured and calculated data, the discrepancies were still large with mean dose differences of 14.8 ± 14.0 % and 15.1 ± 27.2 % for tumour and normal liver, respectively. Furthermore, the highly invasive approach is considered impractical and contradictory to the minimally invasive TARE procedure. Internal radiation dosimetry using Monte Carlo (MC) simulations can be done in order to estimate the radiation dose received by organs in the proximity of the liver, as a result from gamma exposure throughout the treatment. It is important that the dose to these organs to be within the safe exposure limit, based on the maximum tolerance limit of each tissue.

In this chapter, the absorbed doses following TARE with ^{153}Sm-microparticles were assessed. Various patient scenarios were simulated by combining three main patient parameters; tumour involvement (10, 30, 50, and 70 %), lung shunting (LS) (0, 5, 10, 15, and 20 %) and tumour-to-normal liver uptake ratio (T/N) (1, 2.5, 5, 7.5, and 10). The tumour was aimed to receive 120 Gy, hence the ^{153}Sm activity needed to deliver the tumour dose for each scenario was also estimated. The doses to normal liver tissue, lungs, and other organs were recorded, and the maximum limit for the treatment will be established based on the maximum activity allowed for administration without exceeding normal tissue tolerance limit.

6.2 Objectives

The simulations were carried out to assess the organs' absorbed doses following TARE with ^{153}Sm-microparticles, when the tumour was aimed to receive 120 Gy. The assessment will be completed by achieving these objectives:

i. To estimate the administered activities of ^{153}Sm required to achieve a target tumour dose of 120 Gy for various scenarios.
ii. To estimate the absorbed dose to normal liver tissue, lungs and other organs, when 120 Gy of tumour dose is delivered.
iii. To determine the maximum scenario allowed for treatment by comparing the absorbed doses with each organ tolerance dose limit.

6.3 Methodology

6.3.1 Computational Phantom

In this study a mathematical hermaphrodite adult phantom (**Figure 6.1**) was adopted according to the Medical Internal Radiation Dose (MIRD) Pamphlet 5 consisting of complete anatomical organs (Snyder et al., 1978), with both female (ovaries and uterus) and male (testicles) reproductive organs. Female breasts were also incorporated into the phantom by adopting the breasts from Cristy and Eckerman (1987). The list of masses for the organs of interest is shown in **Table 6.1**. The 70 kg MIRD-5 phantom comprises of three types of tissues namely the bone, lung and soft tissue (densities of 1.4862, 0.2958 and 0.9869g.cm^{-3}, respectively) with chemical compositions as shown in **Table 6.2**.

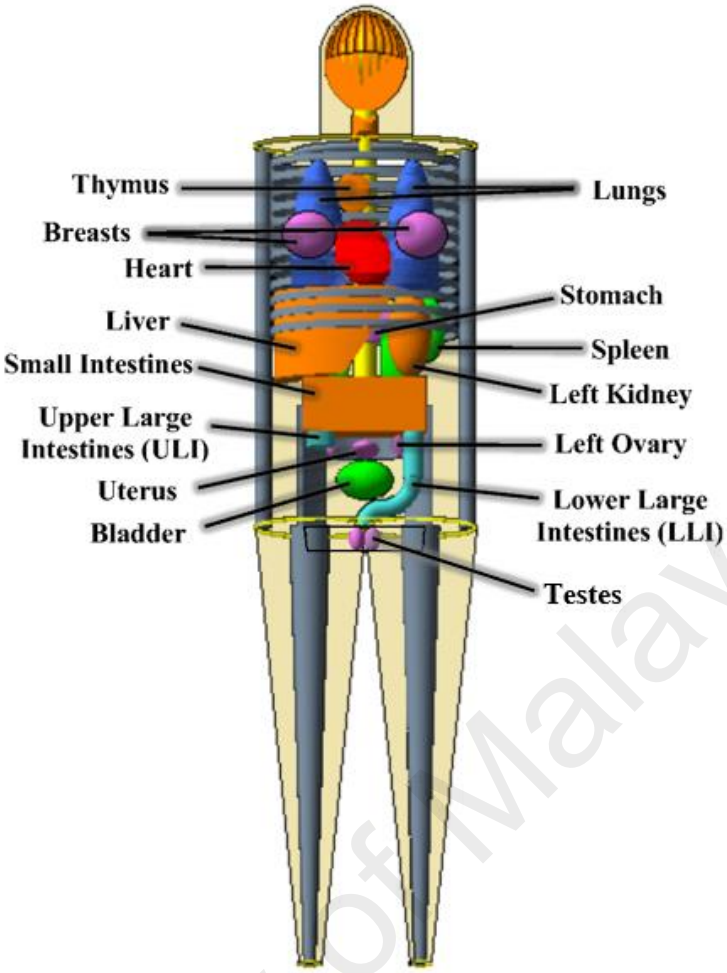

Figure 6.1: MIRD pamphlet 5 adult hermaphrodite human phantom (Snyder et al., 1978), as constructed and visualised using Geant4.

Table 6.1: Masses of MIRD-5 organs. (Snyder et al., 1978)

Organ	Mass (g)	Organ	Mass (g)
Brain	1451.00	**Both Kidneys**	284.20
Thyroid	19.63	**Liver**	1809.00
Thymus	24.80	***Small Intestine**	1040.00
Heart	595.20	***Upper Large Intestines**	429.25
Both Lungs	1000.00	***Lower Large Intestines**	294.37
Both Breasts	388.00	**Both Ovaries**	8.27
Spleen	173.60	**Uterus**	65.40
***Stomach**	396.90	**Urinary Bladder**	45.13
Pancreas	60.27	**Both Testicles**	37.08
Both Adrenals	15.50		

*with contents

Table 6.2: Elemental composition (% by weight) of MIRD-5 tissues (ICRP, 1975; Tipton et al., 1966)

Element	Skeletal tissue	Lung tissue	Soft tissue
H	7.04	10.21	10.47
C	22.79	10.01	23.02
N	3.87	2.80	2.34
O	48.56	75.96	63.21
Na	0.32	0.19	0.13
Mg	0.11	7.40E-03	1.50E-02
P	6.94	8.10E-02	0.24
S	0.17	0.23	0.22
Cl	0.14	0.27	0.14
K	0.15	0.20	0.21
Ca	9.91	7.00E-03	0.00
Fe	8.00E-03	3.70E-02	6.30E-03
Zn	4.80E-03	1.10E-03	3.20E-03
Rb	0.00	3.70E-04	5.70E-04
Sr	3.2E-03	5.90E-06	3.40E-05
Zr	0.00	0.00	8.00E-04
Pb	1.10E-03	4.10E-05	1.60E-05

6.3.2 Distribution of ^{153}Sm Activity Following TARE

Following the administration of ^{153}Sm-microparticles into the tumour, a smaller fraction of the microparticles will be taken up by the normal liver tissue and both lungs. The amount of this extra-tumour uptakes were dependent on the LS and T/N values, which can be calculated based on the partition model (PM) (Ho et al., 1996), used in TARE with ^{90}Y-microspheres. It was derived by Ho et al. and it assumes that the radioactive microparticles are distributed only in the three compartments (tumour, normal liver, and lung), with no redistribution during the treatment. In order to determine the activity distributed within each compartment, the LS and T/N are obtained from the pre-treatment imaging using technetium-99m (^{99m}Tc)-macroaggregated albumin (MAA). The

values are calculated using **Equation 6.1** and **Equation 6.2**.

$$\text{LS (\%)} = \frac{\text{Total counts in lungs}}{\text{Total counts in liver + Total counts in lungs}} \times 100\ \% \qquad \textbf{6.1}$$

$$\text{T/N} = \frac{\text{Total counts in tumour}}{\text{Total counts in liver - Total counts in tumour}} \qquad \textbf{6.2}$$

Thus, the activity uptake in both lungs is calculated using **Equation 6.3**, where, A is the total administered activity (GBq), and A_L is the activity (GBq) taken up by both lungs.

$$A_L = A\left(\frac{LSF(\%)}{100}\right)\text{GBq} \qquad \textbf{6.3}$$

The remainder activities that goes to the tumour, A_T and normal liver, A_N are shown in **Equation 6.4**, which correspond to T/N as shown in **Equation 6.5**, where, m_T and m_N are the mass (g) of tumour and normal liver, respectively.

$$A_T + A_N = A - A_L \qquad \textbf{6.4}$$

$$\text{T/N} = \frac{A_T / m_T}{A_N / m_N} \qquad \textbf{6.5}$$

6.3.3 Geant4 Monte Carlo Simulations

This study was carried out using the Geometry and Tracking 4 (Geant4) version 9.6.p03 (Allison et al., 2006; Agostinelli et al., 2003). The computational phantom was provided in the Geant4 advanced example *human_phantom*. A single tumour with similar shape as the mathematical MIRD-5 liver, located at the centre of the liver and varying in mass was considered (**Figure 6.2**). The tumour mass was indirectly defined by the tumour

involvement (%) calculated using **Equation 6.6**.

$$\text{Tumour involvement (\%)} = \frac{\text{Mass of tumour}}{\text{Mass of liver}} \times 100\ \% \qquad \textbf{6.6}$$

The non-spherical tumour was used due to the geometrical limitations which allowed only spheres of radius up to 4.3 cm to be confined within the liver, which corresponded to a tumour mass of 329 g or a maximum tumour involvement of only 18 %.

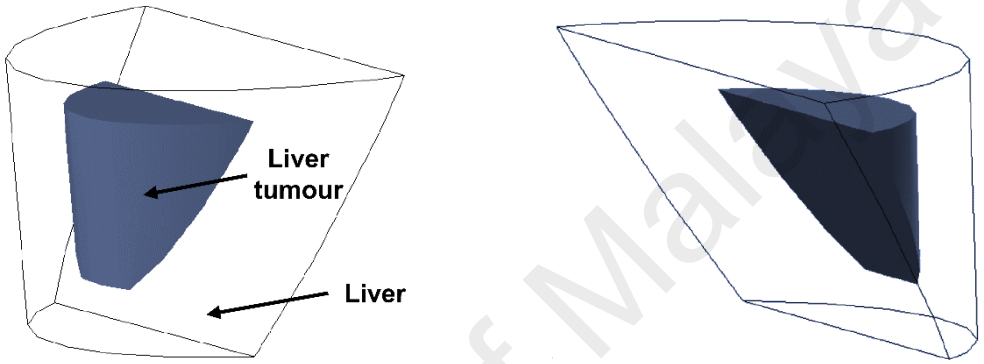

(a) (b)

Figure 6.2: (a) Antero-superior and (b) postero-superior view of the tumour model for 10 % tumour involvement.

The Low Energy Electromagnetic Package (Chauvie et al., 2004), based on the Livermore Evaluated Data Libraries, was adopted to model the electromagnetic interactions of photons and electrons. The threshold of production of secondary particles was fixed to 1 mm. The Geant4 Radioactive Decay and General Particle Source components were used to model the decay of ^{153}Sm and its distribution in the main compartments (tumour, normal liver tissue and lungs), respectively. ^{153}Sm point sources were homogenously distributed within each compartment with activity uptake based on the selected T/N and LS, with randomised direction of emissions. The tumour, normal liver, each lung and other organs of interest were each set as a sensitive volume. The simulation output was set as mean energy (MeV) deposited to each volume.

Various patient scenarios consisting of combinations of different tumour involvement (10, 30, 50, 70 %), T/N (1, 2.5, 5, 7.5, 10) and LS (0, 5, 10, 15, 20 %; with no activity reduction for 15 and 20 %) were simulated. 10^7 disintegrations corresponded to 41.6 Bq of ^{153}Sm (as calculated using **Equation 6.7**), were generated for each parameter combination and repeated three times to obtain a standard deviation of less than 1 %.

$$A\ (Bq) = \lambda N \qquad \textbf{6.7}$$

where,

A = activity (Bq)

λ = radionuclide's decay constant (s^{-1}) = ln 2/ $t_{1/2}$

N = number of disintegrations

The mean energy (MeV) deposited within each compartment/organ was converted to joules, J and divided by the mass to obtain the absorbed dose (Gy) to each compartment/organ. The dose per activity ($Gy.GBq^{-1}$) of the tumour (obtained by dividing tumour dose with 41.6 Bq) for each scenario was used to estimate the total administered activity of ^{153}Sm required to achieve tumouricidal dose of 120 Gy. Using the tumour absorbed dose per activity data for ^{90}Y from **Table 5.2** (refer p. 103), the actual administered activity required to achieve tumour dose of 120 Gy for ^{90}Y were estimated, and compared with the corresponding ^{153}Sm activities.

The absorbed doses for all compartments/organs were normalised to the tumour absorbed dose to obtain the corresponding normalised absorbed dose for each compartment/organ. The normalised value was used to obtain the corresponding absorbed dose to each organ when 120 Gy of tumour dose is being delivered. Finally, the compartments/organs absorbed doses which exceeded the tissue maximum tolerance limit were determined, and the maximum limit allowed for the treatment was established.

6.3.4 Compilation of Simulated Data into Dose Calculation Spreadsheet

For future accessibility, all the data obtained from the simulations were compiled into a systematic dose calculation spreadsheet. The required input information include the patient's tumour involvement, LS, T/N and desired dose to the tumour. The features that are available in the spreadsheet can be divided into two; estimation of administered activity based on desired input information, and the estimated organ's absorbed doses which will be further divided into three parts namely the absorbed dose to source organs (normal liver tissue, right and left lungs), other organs and gonads.

All data were tabulated based on the combination of the three main parameters; tumour involvement, LS and T/N. The values in each parameter were labelled and presented by a number, based on **Table 6.3**. For administered activity estimation, the tumour dose per activity ($Gy.GBq^{-1}$) were listed in a sheet named A_o, while for absorbed doses to source organs, other organs and gonads, the normalised absorbed doses were tabulated in separate sheets named D_n, D_o, and D_g, respectively.

Table 6.3: Name label equivalent to the values for each parameter.
LS: lung shunting; T/N: tumour-to-normal liver uptake ratio.

Label	Tumour involvement (%)	LS	T/N
1	10	0	1.0
2	30	5	2.5
3	50	10	5.0
4	70	15	7.5
5	-	20	10.0

A spreadsheet representing the main interface were created, consisting of all the information, both input and output. Using SUMPRODUCT function as in the example shown in **Equation 6.8** to estimate the administered activity, the desired data were linked and each result was shown in a specific cell in the interface sheet.

= SUMPRODUCT((Ao!A2:A101=G5)*(Ao!B2:B101=G6)

(Ao!C2:C101=G7)(M5/Ao!D2:D101)) **6.8**

The first three round brackets represented the desired parameter combination where, 'Ao!A2:A101=G5' represented the tumour involvement input values from Sheet Ao, listed in Column A from Row 2 to 101 which, the selected value is shown in Cell G5 on the interface sheet. Cells G6 and G7 represents the input values of LS and T/N, respectively. The fourth round bracket represent the formula for the calculation in the cell that contained the SUMPRODUCT formula, in this case the estimation of the administered activity where, 'M5/Ao!D2:D101' represented the desired tumour dose in Cell M5 in the interface sheet divided by the tumour dose per activity values listed in Column D, Row 2 to 101 in Sheet Ao.

The dose calculation spreadsheet was used to determine the maximum treatment limit allowed for TARE with the ^{153}Sm-microparticles. The maximum absorbed doses to tumour for all scenarios were estimated so that the maximum absorbed doses to normal liver or lungs of 70 and 30 Gy, respectively, were not exceeded.

6.4 Results

6.4.1 ^{153}Sm Administered Activity to Achieve 120 Gy Tumour Dose

The comparison between total administered activities for ^{153}Sm and ^{90}Y to achieve tumour dose of 120 Gy, for various patient parameter combinations/ scenarios are tabulated in **Table 6.4**. The multiplication factor/conversion factor (CF) to obtain the ^{153}Sm activity that corresponds to ^{90}Y activity to achieve similar tumour dose, were found to be in the range of 4.42 to 4.6.

Table 6.4: Administered activity required for ^{153}Sm as compared to ^{90}Y to achieve tumour dose of 120 Gy for various patient scenarios. TI: tumour involvement; LS: lung shunting; T/N: tumour-to-normal liver uptake ratio; CF: conversion factor.

TI (%)	LS (%)	Administered Activity (GBq)									
		T/N 1		T/N 2.5		T/N 5		T/N 7.5		T/N 10	
		^{153}Sm	^{90}Y	^{153}Sm	^{90}Y	^{153}Sm	^{90}Y	^{153}Sm	^{90}Y	^{153}Sm	^{90}Y
10	0	19.83	4.36	9.47	2.12	5.84	1.32	4.61	1.04	3.99	0.90
	5	20.88	4.59	9.97	2.24	6.15	1.39	4.86	1.10	4.20	0.95
	10	22.03	4.85	10.53	2.36	6.49	1.46	5.12	1.16	4.43	1.00
	15	23.32	5.13	11.14	2.50	6.87	1.55	5.42	1.23	4.69	1.06
	20	24.79	5.45	11.84	2.65	7.30	1.65	5.76	1.30	4.99	1.13
Mean CF		4.55 ± 0.00		4.46 ± 0.01		4.43 ± 0.01		4.42 ± 0.01		4.42 ± 0.01	
30	0	19.94	4.36	11.85	2.62	9.07	2.01	8.12	1.81	7.65	1.70
	5	20.98	4.59	12.48	2.76	9.54	2.12	8.55	1.90	8.05	1.79
	10	22.16	4.85	13.16	2.91	10.07	2.24	9.02	2.01	8.50	1.89
	15	23.45	5.13	13.93	3.09	10.66	2.37	9.56	2.13	9.00	2.01
	20	24.92	5.45	14.80	3.28	11.32	2.52	10.15	2.26	9.56	2.13
Mean CF		4.57 ± 0.00		4.52 ± 0.01		4.50 ± 0.01		4.49 ± 0.01		4.49 ± 0.01	
50	0	20.03	4.36	14.25	3.15	12.28	2.72	11.62	2.58	11.29	2.51
	5	21.07	4.59	15.00	3.31	12.92	2.87	12.23	2.72	11.88	2.64
	10	22.23	4.85	15.83	3.50	13.64	3.03	12.91	2.87	12.54	2.79
	15	23.53	5.13	16.76	3.70	14.45	3.20	13.67	3.04	13.27	2.95
	20	25.00	5.45	17.80	3.93	15.34	3.40	14.52	3.23	14.10	3.14
Mean CF		4.59 ± 0.00		4.53 ± 0.00		4.51 ± 0.01		4.50 ± 0.00		4.50 ± 0.00	
70	0	20.11	4.36	16.66	3.67	15.50	3.43	15.11	3.35	14.92	3.31
	5	21.15	4.59	17.54	3.87	16.31	3.62	15.90	3.53	15.70	3.49
	10	22.32	4.85	18.50	4.08	17.21	3.82	16.78	3.73	16.56	3.68
	15	23.63	5.14	19.59	4.32	18.22	4.04	17.77	3.95	17.53	3.90
	20	25.10	5.46	20.81	4.59	19.35	4.29	18.87	4.19	18.63	4.14
Mean CF		4.60 ± 0.01		4.53 ± 0.00		4.51 ± 0.01		4.50 ± 0.00		4.50 ± 0.00	

6.4.2 Absorbed Dose to Source Organs

Following TARE, most of the microparticles will be distributed in the tumour while a smaller portion (based on T/N) will be taken up by the normal liver tissue. Due to the presence of direct arteriovenous shunting bypassing the capillary bed (Chen et al., 1999)

of the tumour to the lungs, some of the microparticles will also be deposited into the lungs, hence determined the values of the LS.

6.4.2.1 Normal Liver Tissue

The absorbed doses to normal liver for various tumour involvements, LS and T/N are shown in **Figure 6.3**. The normal liver doses were observed to be independent of the tumour involvement and LS, but were greatly dependent on the T/N. The normal liver doses for all scenarios were in the range of 13.15 to 115.60 Gy. Based on the maximum dose limit to normal liver of 70 Gy (Sirtex, 2015; Lau et al., 2012) (red dotted lines), only doses for T/N of 1 exceeded the value, when tumour dose of 120 Gy is being delivered.

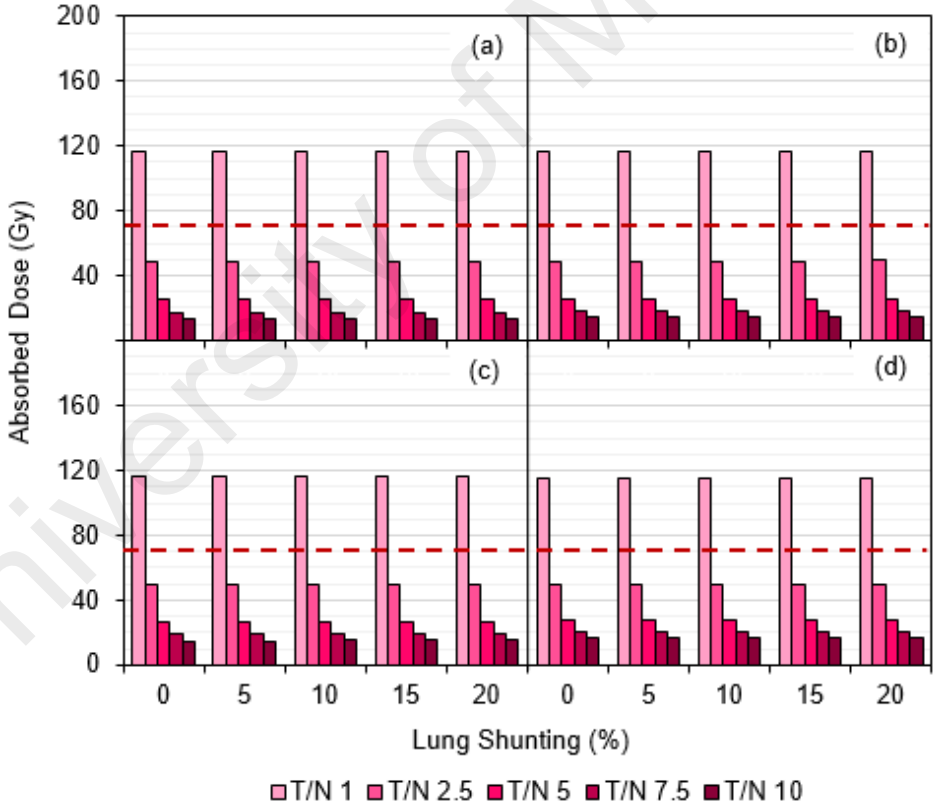

Figure 6.3: Absorbed dose to normal liver for various tumour involvements of (a) 10, (b) 30, (c) 50, and (d) 70 %, lung shunting (LS) and tumour-to-normal liver uptake ratio (T/N), when 120 Gy is delivered to the tumour. The red dotted lines indicate maximum dose limit to normal liver of 70 Gy.

6.4.2.2 Lungs

The absorbed doses to left and right lungs for various tumour involvements, LS and T/N are shown in **Figure 6.4** and **Figure 6.5**, respectively. The dose to both lungs were observed to be dependent by all three factors; tumour involvement, LS, and T/N. The doses to left and right lungs for all scenarios were in the range of 0.02 to 51.21 Gy, and 0.19 to 51.93 Gy, respectively, with right lung recorded slightly higher doses by a factor in the range of 1.01 to 8.22. The scenarios that exceeded the lung dose limit of 30 Gy (Garin et al., 2015; Ho et al., 1997) (for 120 Gy of tumour dose) were 15 % LS with T/N of 1 (for all tumour involvements), and 20 % LS with various T/N; 1 (for all tumour involvements), 2.5 (30, 50 and 70 % tumour involvements), 5 (50 and 70 % tumour involvements), 7.5 and 10 (both for 70 % tumour involvement).

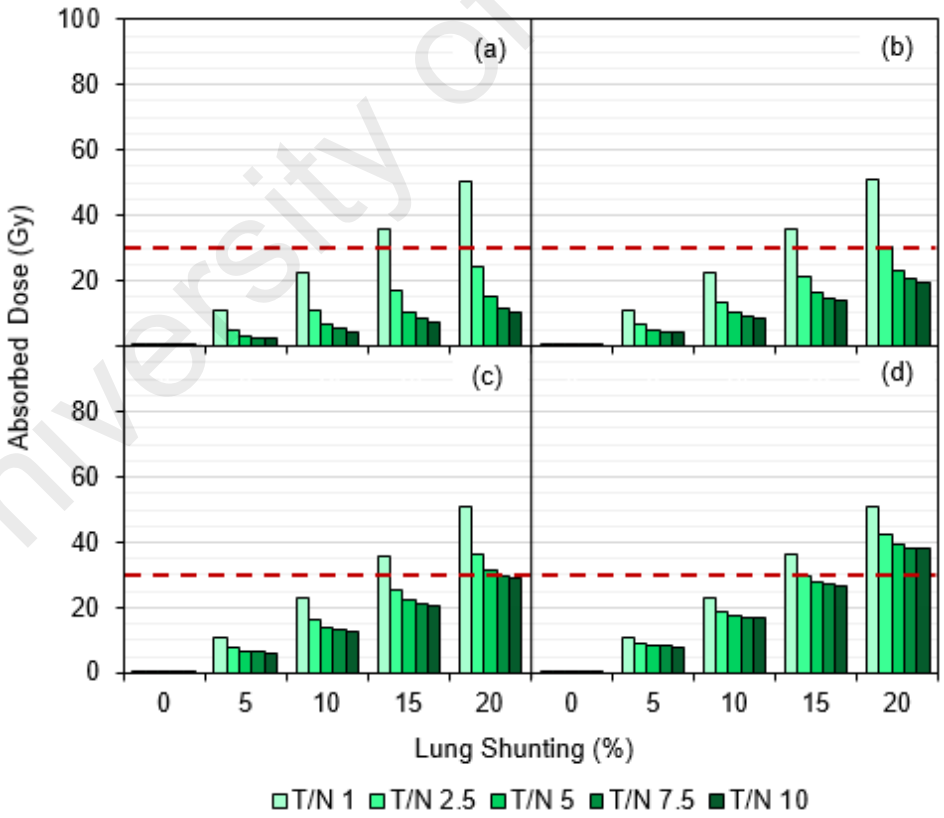

Figure 6.4: Absorbed dose to left lung for various tumour involvements of (a) 10, (b) 30, (c) 50, and (d) 70 %, lung shunting (LS) and tumour-to-normal liver uptake ratio (T/N), when 120 Gy is delivered to the tumour. The red dotted lines indicate maximum dose limit to lungs of 30 Gy.

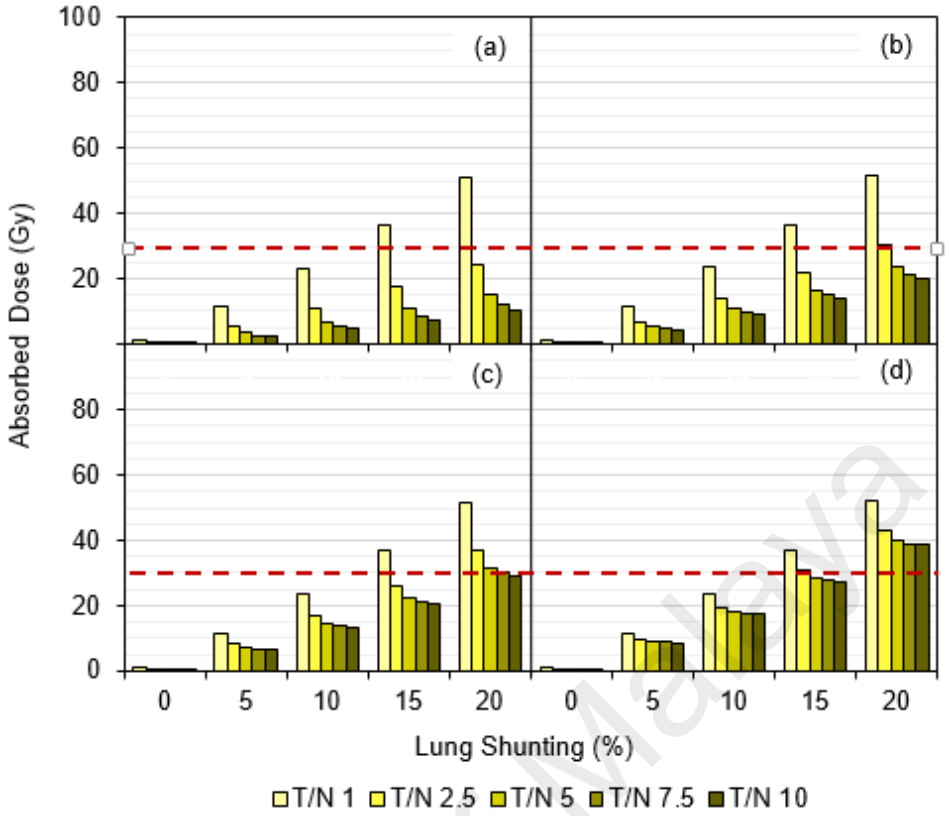

Figure 6.5: Absorbed dose to right lung for various tumour involvements of (a) 10, (b) 30, (c) 50, and (d) 70 %, lung shunting (LS) and tumour-to-normal liver uptake ratio (T/N), when 120 Gy is delivered to the tumour. The red dotted lines indicate maximum dose limit to lungs of 30 Gy.

6.4.3 Absorbed Dose to Other Organs

From the simulations, the overall absorbed doses to all organs were observed to be increased with higher tumour involvement and LS values, as a result of the increase in the total administered activity to achieve the tumour dose of 120 Gy. Conversely, the organs absorbed doses were reduced as the T/N increased, as a result of lesser administered activity required to achieve 120 Gy of tumour dose. All organ doses were found to be well below 1 Gy.

6.4.3.1 Brain

The normalised absorbed dose for brain with various tumour involvements, LS and T/N are shown in **Table 6.5** Absorbed doses to brain for all scenarios (for tumour dose of 120 Gy) were in the range of 0.02 to 0.39 cGy, which correspond to effective dose of 0.002 to 0.040 mSv.

Table 6.5: Normalised absorbed dose for brain with various tumour involvements (TI), lung shunting (LS) and tumour-to-normal liver uptake ratio (T/N).

TI (%)	LS (%)	Normalised absorbed dose for Brain				
		T/N 1	T/N 2.5	T/N 5	T/N 7.5	T/N 10
10	0	7.88E-06	3.94E-06	2.50E-06	1.94E-06	1.68E-06
	5	1.27E-05	6.32E-06	3.97E-06	3.11E-06	2.76E-06
	10	1.86E-05	8.79E-06	5.66E-06	4.47E-06	3.93E-06
	15	2.47E-05	1.22E-05	7.42E-06	5.89E-06	5.07E-06
	20	3.10E-05	1.53E-05	9.59E-06	7.15E-06	6.51E-06
30	0	8.23E-06	4.93E-06	3.70E-06	3.48E-06	3.21E-06
	5	1.34E-05	8.14E-06	6.21E-06	5.20E-06	5.04E-06
	10	1.87E-05	1.13E-05	8.46E-06	7.90E-06	7.38E-06
	15	2.53E-05	1.52E-05	1.14E-05	1.03E-05	9.63E-06
	20	3.20E-05	1.90E-05	1.51E-05	1.33E-05	1.30E-05
50	0	8.68E-06	5.88E-06	4.93E-06	4.86E-06	4.56E-06
	5	1.35E-05	9.57E-06	8.39E-06	7.73E-06	7.63E-06
	10	1.92E-05	1.36E-05	1.14E-05	1.11E-05	1.10E-05
	15	2.54E-05	1.79E-05	1.57E-05	1.45E-05	1.38E-05
	20	3.22E-05	2.28E-05	2.00E-05	1.85E-05	1.82E-05
70	0	8.73E-06	6.94E-06	6.42E-06	6.33E-06	6.14E-06
	5	1.36E-05	1.09E-05	1.06E-05	1.01E-05	9.95E-06
	10	1.97E-05	1.49E-05	1.54E-05	1.40E-05	1.39E-05
	15	2.64E-05	2.18E-05	1.93E-05	1.92E-05	1.87E-05
	20	3.24E-05	2.73E-05	2.54E-05	2.42E-05	2.42E-05

6.4.3.2 Thyroid

The normalised absorbed dose for thyroid with various tumour involvements, LS and T/N are shown in **Table 6.6**. Absorbed doses to thyroid for all scenarios (for tumour dose of 120 Gy) were in the range of 0.22 to 5.93 cGy, which correspond to effective dose of 0.09 to 2.37 mSv.

Table 6.6: Normalised absorbed dose for thyroid with various tumour involvements (TI), lung shunting (LS) and tumour-to-normal liver uptake ratio (T/N).

TI (%)	LS (%)	Normalised absorbed dose for Thyroid				
		T/N 1	T/N 2.5	T/N 5	T/N 7.5	T/N 10
10	0	9.38E-05	5.28E-05	2.86E-05	2.11E-05	1.82E-05
	5	1.71E-04	8.62E-05	5.47E-05	4.07E-05	3.61E-05
	10	2.64E-04	1.26E-04	8.54E-05	6.39E-05	5.70E-05
	15	3.58E-04	1.74E-04	1.03E-04	8.53E-05	7.75E-05
	20	4.82E-04	2.51E-04	1.49E-04	1.18E-04	1.04E-04
30	0	9.76E-05	5.72E-05	3.85E-05	3.82E-05	3.55E-05
	5	1.74E-04	1.05E-04	8.33E-05	7.07E-05	6.64E-05
	10	2.65E-04	1.74E-04	1.28E-04	1.08E-04	1.03E-04
	15	3.75E-04	2.32E-04	1.66E-04	1.50E-04	1.43E-04
	20	4.82E-04	3.00E-04	2.16E-04	2.09E-04	1.79E-04
50	0	1.02E-04	6.32E-05	5.74E-05	5.57E-05	5.32E-05
	5	1.92E-04	1.22E-04	1.18E-04	1.08E-04	1.07E-04
	10	2.79E-04	1.92E-04	1.63E-04	1.51E-04	1.46E-04
	15	3.83E-04	2.63E-04	2.27E-04	2.20E-04	2.19E-04
	20	4.89E-04	3.50E-04	3.02E-04	2.93E-04	2.78E-04
70	0	1.05E-04	8.44E-05	7.81E-05	7.70E-05	6.41E-05
	5	1.92E-04	1.56E-04	1.37E-04	1.31E-04	1.28E-04
	10	2.83E-04	2.19E-04	2.09E-04	2.04E-04	1.96E-04
	15	3.90E-04	3.03E-04	3.02E-04	2.78E-04	2.74E-04
	20	4.95E-04	4.35E-04	4.02E-04	3.90E-04	3.74E-04

6.4.3.3 Thymus

The normalised absorbed dose for thymus with various tumour involvements, LS and T/N are shown in **Table 6.7**. Absorbed doses to thymus for all scenarios (for tumour dose of 120 Gy) were in the range of 1.68 to 31.82 cGy, which correspond to effective dose of 2.02 to 38.18 mSv.

Table 6.7: Normalised absorbed dose for thymus with various tumour involvements (TI), lung shunting (LS) and tumour-to-normal liver uptake ratio (T/N).

TI (%)	LS (%)	Normalised absorbed dose for Thymus				
		T/N 1	T/N 2.5	T/N 5	T/N 7.5	T/N 10
10	0	7.28E-04	3.61E-04	2.15E-04	1.66E-04	1.40E-04
	5	1.11E-03	5.15E-04	3.23E-04	2.57E-04	2.18E-04
	10	1.55E-03	7.30E-04	4.46E-04	3.59E-04	3.06E-04
	15	2.03E-03	9.65E-04	5.84E-04	4.59E-04	4.13E-04
	20	2.57E-03	1.24E-03	7.62E-04	6.09E-04	5.07E-04
30	0	7.34E-04	4.17E-04	3.23E-04	2.78E-04	2.53E-04
	5	1.12E-03	6.57E-04	4.86E-04	4.43E-04	4.26E-04
	10	1.57E-03	9.19E-04	6.88E-04	6.18E-04	5.57E-04
	15	2.03E-03	1.21E-03	9.35E-04	8.13E-04	7.60E-04
	20	2.59E-03	1.53E-03	1.15E-03	1.04E-03	9.62E-04
50	0	7.34E-04	5.10E-04	4.33E-04	4.25E-04	4.00E-04
	5	1.12E-03	8.00E-04	6.92E-04	6.61E-04	6.06E-04
	10	1.58E-03	1.06E-03	9.53E-04	9.14E-04	8.61E-04
	15	2.06E-03	1.44E-03	1.24E-03	1.18E-03	1.13E-03
	20	2.62E-03	1.84E-03	1.58E-03	1.50E-03	1.45E-03
70	0	7.52E-04	6.02E-04	5.67E-04	5.42E-04	5.44E-04
	5	1.13E-03	9.41E-04	8.68E-04	8.50E-04	8.22E-04
	10	1.61E-03	1.31E-03	1.20E-03	1.20E-03	1.16E-03
	15	2.07E-03	1.70E-03	1.58E-03	1.56E-03	1.52E-03
	20	2.65E-03	2.17E-03	1.99E-03	1.93E-03	1.92E-03

6.4.3.4 Heart

The normalised absorbed dose for heart with various tumour involvements, LS and T/N are shown in **Table 6.8**. Absorbed doses to heart for all scenarios (for tumour dose of 120 Gy) were in the range of 10.54 to 101.48 cGy, which correspond to effective dose of 12.65 to 121.78 mSv.

Table 6.8: Normalised absorbed dose for heart with various tumour involvements (TI), lung shunting (LS) and tumour-to-normal liver uptake ratio (T/N).

TI (%)	LS (%)	Normalised absorbed dose for Heart				
		T/N 1	T/N 2.5	T/N 5	T/N 7.5	T/N 10
10	0	5.20E-03	2.37E-03	1.38E-03	1.05E-03	8.78E-04
	5	5.85E-03	2.69E-03	1.58E-03	1.20E-03	1.01E-03
	10	6.57E-03	3.04E-03	1.79E-03	1.37E-03	1.16E-03
	15	7.42E-03	3.43E-03	2.04E-03	1.56E-03	1.33E-03
	20	8.34E-03	3.87E-03	2.31E-03	1.78E-03	1.52E-03
30	0	5.22E-03	2.82E-03	1.99E-03	1.72E-03	1.58E-03
	5	5.87E-03	3.23E-03	2.30E-03	1.99E-03	1.84E-03
	10	6.63E-03	3.66E-03	2.64E-03	2.29E-03	2.12E-03
	15	7.43E-03	4.14E-03	3.01E-03	2.63E-03	2.44E-03
	20	8.35E-03	4.69E-03	3.44E-03	3.01E-03	2.80E-03
50	0	5.24E-03	3.46E-03	2.87E-03	2.66E-03	2.57E-03
	5	5.90E-03	3.94E-03	3.27E-03	3.06E-03	2.94E-03
	10	6.64E-03	4.48E-03	3.74E-03	3.48E-03	3.36E-03
	15	7.49E-03	5.08E-03	4.24E-03	3.97E-03	3.82E-03
	20	8.45E-03	5.74E-03	4.81E-03	4.50E-03	4.37E-03
70	0	5.26E-03	4.17E-03	3.79E-03	3.67E-03	3.61E-03
	5	5.94E-03	4.73E-03	4.33E-03	4.19E-03	4.10E-03
	10	6.70E-03	5.34E-03	4.91E-03	4.74E-03	4.67E-03
	15	7.50E-03	6.04E-03	5.54E-03	5.37E-03	5.29E-03
	20	8.46E-03	6.82E-03	6.27E-03	6.07E-03	5.99E-03

6.4.3.5 Breasts

The normalised absorbed dose for left and right breasts with various tumour involvements, LS and T/N are shown in **Table 6.9** and **Table 6.10**, respectively. The absorbed doses to both breasts for all scenarios (for tumour dose of 120 Gy) were in the ranges of 0.91 to 21.50 cGy, and 4.75 to 39.90 cGy for left and right breasts, respectively. These corresponded to effective doses in ranges of 1.09 to 25.80 mSv and 5.70 to 47.88 mSv, to left and right breasts, respectively.

Table 6.9: Normalised absorbed dose for left breast with various tumour involvements (TI), lung shunting (LS) and tumour-to-normal liver uptake ratio (T/N).

TI (%)	LS (%)	Normalised absorbed dose for Left Breast				
		T/N 1	T/N 2.5	T/N 5	T/N 7.5	T/N 10
10	0	4.58E-04	2.07E-04	1.21E-04	8.99E-05	7.58E-05
	5	7.32E-04	3.39E-04	2.02E-04	1.53E-04	1.29E-04
	10	1.03E-03	4.85E-04	2.88E-04	2.21E-04	1.93E-04
	15	1.36E-03	6.46E-04	3.91E-04	3.02E-04	2.57E-04
	20	1.75E-03	8.26E-04	5.02E-04	3.93E-04	3.33E-04
30	0	4.59E-04	2.44E-04	1.69E-04	1.44E-04	1.32E-04
	5	7.42E-04	4.06E-04	2.95E-04	2.50E-04	2.38E-04
	10	1.04E-03	5.97E-04	4.30E-04	3.82E-04	3.52E-04
	15	1.39E-03	7.91E-04	5.80E-04	5.18E-04	4.76E-04
	20	1.76E-03	1.01E-03	7.52E-04	6.75E-04	6.26E-04
50	0	4.67E-04	3.01E-04	2.42E-04	2.24E-04	2.12E-04
	5	7.43E-04	4.98E-04	4.11E-04	3.82E-04	3.67E-04
	10	1.05E-03	7.04E-04	5.92E-04	5.64E-04	5.37E-04
	15	1.39E-03	9.63E-04	8.04E-04	7.55E-04	7.35E-04
	20	1.78E-03	1.23E-03	1.04E-03	9.76E-04	9.46E-04
70	0	4.69E-04	3.60E-04	3.29E-04	3.12E-04	3.12E-04
	5	7.49E-04	5.89E-04	5.35E-04	5.21E-04	5.06E-04
	10	1.05E-03	8.46E-04	7.76E-04	7.57E-04	7.39E-04
	15	1.39E-03	1.12E-03	1.04E-03	1.01E-03	9.97E-04
	20	1.79E-03	1.44E-03	1.32E-03	1.29E-03	1.26E-03

Table 6.10: Normalised absorbed dose for right breast with various tumour involvements (TI), lung shunting (LS) and tumour-to-normal liver uptake ratio (T/N).

TI (%)	LS (%)	Normalised absorbed dose for Right Breast				
		T/N 1	T/N 2.5	T/N 5	T/N 7.5	T/N 10
10	0	1.97E-03	9.47E-04	5.81E-04	4.59E-04	3.96E-04
	5	2.27E-03	1.07E-03	6.63E-04	5.20E-04	4.53E-04
	10	2.55E-03	1.23E-03	7.53E-04	5.91E-04	5.11E-04
	15	2.90E-03	1.39E-03	8.47E-04	6.67E-04	5.77E-04
	20	3.28E-03	1.56E-03	9.62E-04	7.62E-04	6.53E-04
30	0	2.00E-03	1.16E-03	8.83E-04	7.86E-04	7.37E-04
	5	2.27E-03	1.32E-03	1.00E-03	8.92E-04	8.50E-04
	10	2.57E-03	1.51E-03	1.14E-03	1.01E-03	9.55E-04
	15	2.91E-03	1.71E-03	1.30E-03	1.16E-03	1.08E-03
	20	3.28E-03	1.95E-03	1.47E-03	1.32E-03	1.24E-03
50	0	2.00E-03	1.41E-03	1.21E-03	1.15E-03	1.10E-03
	5	2.28E-03	1.60E-03	1.38E-03	1.30E-03	1.27E-03
	10	2.58E-03	1.83E-03	1.57E-03	1.48E-03	1.44E-03
	15	2.92E-03	2.07E-03	1.76E-03	1.68E-03	1.62E-03
	20	3.31E-03	2.35E-03	2.03E-03	1.89E-03	1.85E-03
70	0	2.02E-03	1.67E-03	1.56E-03	1.52E-03	1.51E-03
	5	2.28E-03	1.89E-03	1.75E-03	1.72E-03	1.70E-03
	10	2.58E-03	2.13E-03	2.01E-03	1.96E-03	1.91E-03
	15	2.95E-03	2.45E-03	2.27E-03	2.23E-03	2.18E-03
	20	3.33E-03	2.74E-03	2.56E-03	2.48E-03	2.45E-03

6.4.3.6 Spleen

The normalised absorbed dose for spleen with various tumour involvements, LS and T/N are shown in **Table 6.11**. Absorbed doses to spleen for all scenarios (for tumour dose of 120 Gy) were in the range of 2.60 to 28.06 cGy, which correspond to effective dose of 3.12 to 33.67 mSv.

Table 6.11: Normalised absorbed dose for spleen with various tumour involvements (TI), lung shunting (LS) and tumour-to-normal liver uptake ratio (T/N).

TI (%)	LS (%)	Normalised absorbed dose for Spleen				
		T/N 1	T/N 2.5	T/N 5	T/N 7.5	T/N 10
10	0	1.24E-03	5.76E-04	3.34E-04	2.60E-04	2.17E-04
	5	1.46E-03	6.73E-04	4.03E-04	3.07E-04	2.60E-04
	10	1.70E-03	7.94E-04	4.72E-04	3.68E-04	3.13E-04
	15	1.98E-03	9.37E-04	5.57E-04	4.28E-04	3.64E-04
	20	2.31E-03	1.08E-03	6.51E-04	4.98E-04	4.30E-04
30	0	1.26E-03	6.88E-04	4.91E-04	4.21E-04	3.95E-04
	5	1.47E-03	8.16E-04	5.94E-04	5.21E-04	4.82E-04
	10	1.72E-03	9.67E-04	7.11E-04	6.17E-04	5.70E-04
	15	1.99E-03	1.13E-03	8.32E-04	7.37E-04	6.82E-04
	20	2.32E-03	1.33E-03	9.86E-04	8.59E-04	8.06E-04
50	0	1.27E-03	8.58E-04	7.02E-04	6.61E-04	6.38E-04
	5	1.48E-03	1.01E-03	8.44E-04	7.85E-04	7.66E-04
	10	1.72E-03	1.19E-03	9.99E-04	9.38E-04	9.08E-04
	15	2.00E-03	1.38E-03	1.17E-03	1.10E-03	1.06E-03
	20	2.32E-03	1.61E-03	1.37E-03	1.28E-03	1.22E-03
70	0	1.27E-03	1.01E-03	9.13E-04	8.91E-04	8.60E-04
	5	1.50E-03	1.18E-03	1.10E-03	1.06E-03	1.03E-03
	10	1.72E-03	1.40E-03	1.28E-03	1.25E-03	1.22E-03
	15	2.02E-03	1.64E-03	1.49E-03	1.46E-03	1.44E-03
	20	2.34E-03	1.89E-03	1.75E-03	1.70E-03	1.66E-03

6.4.3.7 Stomach

The normalised absorbed dose for stomach with various tumour involvements, LS and T/N are shown in **Table 6.12**. Absorbed doses to stomach for all scenarios (for tumour dose of 120 Gy) were in the range of 6.32 to 49.21 cGy, which correspond to effective dose of 7.58 to 59.05 mSv.

Table 6.12: Normalised absorbed dose for stomach with various tumour involvements (TI), lung shunting (LS) and tumour-to-normal liver uptake ratio (T/N).

TI (%)	LS (%)	Normalised absorbed dose for Stomach				
		T/N 1	T/N 2.5	T/N 5	T/N 7.5	T/N 10
10	0	3.29E-03	1.48E-03	8.50E-04	6.34E-04	5.26E-04
	5	3.46E-03	1.56E-03	8.95E-04	6.72E-04	5.58E-04
	10	3.63E-03	1.64E-03	9.47E-04	7.11E-04	5.94E-04
	15	3.82E-03	1.73E-03	1.01E-03	7.52E-04	6.31E-04
	20	4.04E-03	1.84E-03	1.07E-03	8.07E-04	6.76E-04
30	0	3.31E-03	1.75E-03	1.20E-03	1.02E-03	9.27E-04
	5	3.48E-03	1.84E-03	1.27E-03	1.08E-03	9.89E-04
	10	3.64E-03	1.94E-03	1.35E-03	1.16E-03	1.06E-03
	15	3.84E-03	2.06E-03	1.44E-03	1.24E-03	1.13E-03
	20	4.05E-03	2.18E-03	1.54E-03	1.33E-03	1.21E-03
50	0	3.33E-03	2.16E-03	1.74E-03	1.62E-03	1.54E-03
	5	3.49E-03	2.26E-03	1.85E-03	1.70E-03	1.64E-03
	10	3.65E-03	2.38E-03	1.95E-03	1.81E-03	1.74E-03
	15	3.86E-03	2.54E-03	2.06E-03	1.93E-03	1.84E-03
	20	4.09E-03	2.69E-03	2.21E-03	2.05E-03	1.97E-03
70	0	3.35E-03	2.58E-03	2.32E-03	2.22E-03	2.19E-03
	5	3.52E-03	2.71E-03	2.45E-03	2.37E-03	2.31E-03
	10	3.70E-03	2.86E-03	2.58E-03	2.50E-03	2.44E-03
	15	3.87E-03	3.03E-03	2.72E-03	2.64E-03	2.59E-03
	20	4.10E-03	3.19E-03	2.90E-03	2.80E-03	2.73E-03

6.4.3.8 Pancreas

The normalised absorbed dose for pancreas with various tumour involvements, LS and T/N are shown in **Table 6.13**. Absorbed doses to pancreas for all scenarios (for tumour dose of 120 Gy) were in the range of 15.75 to 104.07 cGy, which correspond to effective dose of 18.90 to 124.88 mSv.

Table 6.13: Normalised absorbed dose for pancreas with various tumour involvements (TI), lung shunting (LS) and tumour-to-normal liver uptake ratio (T/N).

TI (%)	LS (%)	Normalised absorbed dose for Pancreas				
		T/N 1	T/N 2.5	T/N 5	T/N 7.5	T/N 10
10	0	7.49E-03	3.47E-03	2.02E-03	1.56E-03	1.31E-03
	5	7.71E-03	3.55E-03	2.08E-03	1.61E-03	1.36E-03
	10	7.92E-03	3.67E-03	2.17E-03	1.66E-03	1.40E-03
	15	8.27E-03	3.83E-03	2.25E-03	1.73E-03	1.46E-03
	20	8.56E-03	3.99E-03	2.35E-03	1.79E-03	1.52E-03
30	0	7.54E-03	4.20E-03	3.00E-03	2.63E-03	2.43E-03
	5	7.81E-03	4.32E-03	3.12E-03	2.73E-03	2.51E-03
	10	8.01E-03	4.43E-03	3.24E-03	2.82E-03	2.60E-03
	15	8.28E-03	4.62E-03	3.35E-03	2.95E-03	2.71E-03
	20	8.64E-03	4.81E-03	3.49E-03	3.05E-03	2.85E-03
50	0	7.62E-03	5.15E-03	4.34E-03	4.08E-03	3.97E-03
	5	7.81E-03	5.36E-03	4.52E-03	4.23E-03	4.10E-03
	10	8.07E-03	5.51E-03	4.68E-03	4.36E-03	4.20E-03
	15	8.36E-03	5.71E-03	4.84E-03	4.58E-03	4.38E-03
	20	8.67E-03	5.96E-03	5.05E-03	4.70E-03	4.54E-03
70	0	7.65E-03	6.10E-03	5.62E-03	5.44E-03	5.35E-03
	5	7.88E-03	6.29E-03	5.83E-03	5.61E-03	5.51E-03
	10	8.08E-03	6.50E-03	5.95E-03	5.76E-03	5.73E-03
	15	8.37E-03	6.75E-03	6.15E-03	6.03E-03	5.89E-03
	20	8.67E-03	7.07E-03	6.39E-03	6.27E-03	6.11E-03

6.4.3.9 Adrenal Glands

The normalised absorbed dose for left and right adrenals with various tumour involvements, LS and T/N are shown in **Table 6.14** and **Table 6.15**, respectively. The absorbed doses to both adrenals for all scenarios (for tumour dose of 120 Gy) were in the ranges of 4.31 to 40.28 cGy, and 25.14 to 145.20 cGy, respectively. These corresponded to effective doses in ranges of 5.17 to 48.34 mSv, and 30.17 to 174.24 mSv to left and right adrenals, respectively.

Table 6.14: Normalised absorbed dose for left adrenal with various tumour involvements (TI), lung shunting (LS) and tumour-to-normal liver uptake ratio (T/N).

TI (%)	LS (%)	Normalised absorbed dose for Left Adrenal				
		T/N 1	T/N 2.5	T/N 5	T/N 7.5	T/N 10
10	0	1.98E-03	9.49E-04	5.64E-04	4.14E-04	3.59E-04
	5	2.21E-03	1.03E-03	6.38E-04	4.89E-04	4.18E-04
	10	2.49E-03	1.20E-03	7.10E-04	5.49E-04	4.71E-04
	15	2.80E-03	1.34E-03	7.95E-04	6.26E-04	5.29E-04
	20	3.15E-03	1.48E-03	9.34E-04	7.11E-04	6.17E-04
30	0	1.98E-03	1.08E-03	8.36E-04	7.30E-04	6.52E-04
	5	2.31E-03	1.28E-03	9.44E-04	8.29E-04	7.65E-04
	10	2.50E-03	1.46E-03	1.06E-03	9.36E-04	8.67E-04
	15	2.89E-03	1.66E-03	1.22E-03	1.13E-03	1.02E-03
	20	3.23E-03	1.86E-03	1.35E-03	1.24E-03	1.18E-03
50	0	2.04E-03	1.34E-03	1.18E-03	1.12E-03	1.08E-03
	5	2.34E-03	1.54E-03	1.38E-03	1.26E-03	1.24E-03
	10	2.57E-03	1.86E-03	1.43E-03	1.43E-03	1.42E-03
	15	2.91E-03	2.02E-03	1.75E-03	1.57E-03	1.54E-03
	20	3.25E-03	2.32E-03	1.99E-03	1.84E-03	1.84E-03
70	0	2.09E-03	1.62E-03	1.49E-03	1.44E-03	1.44E-03
	5	2.34E-03	1.89E-03	1.75E-03	1.64E-03	1.60E-03
	10	2.63E-03	2.10E-03	1.92E-03	1.90E-03	1.83E-03
	15	2.97E-03	2.39E-03	2.25E-03	2.18E-03	2.09E-03
	20	3.36E-03	2.62E-03	2.52E-03	2.32E-03	2.32E-03

Table 6.15: Normalised absorbed dose for right adrenal with various tumour involvements (TI), lung shunting (LS) and tumour-to-normal liver uptake ratio (T/N).

TI (%)	LS (%)	Normalised absorbed dose for Right Adrenal				
		T/N 1	T/N 2.5	T/N 5	T/N 7.5	T/N 10
10	0	1.07E-02	5.12E-03	3.12E-03	2.51E-03	2.10E-03
	5	1.09E-02	5.23E-03	3.26E-03	2.52E-03	2.16E-03
	10	1.11E-02	5.37E-03	3.29E-03	2.55E-03	2.24E-03
	15	1.14E-02	5.51E-03	3.33E-03	2.66E-03	2.26E-03
	20	1.20E-02	5.64E-03	3.48E-03	2.75E-03	2.35E-03
30	0	1.07E-02	6.30E-03	4.76E-03	4.24E-03	3.88E-03
	5	1.09E-02	6.34E-03	4.76E-03	4.25E-03	4.08E-03
	10	1.12E-02	6.57E-03	4.92E-03	4.37E-03	4.15E-03
	15	1.16E-02	6.68E-03	5.11E-03	4.51E-03	4.17E-03
	20	1.21E-02	6.93E-03	5.20E-03	4.66E-03	4.47E-03
50	0	1.08E-02	7.66E-03	6.51E-03	6.16E-03	5.81E-03
	5	1.10E-02	7.81E-03	6.57E-03	6.25E-03	6.14E-03
	10	1.13E-02	8.09E-03	6.81E-03	6.47E-03	6.33E-03
	15	1.16E-02	8.26E-03	7.12E-03	6.78E-03	6.54E-03
	20	1.21E-02	8.40E-03	7.24E-03	6.88E-03	6.58E-03
70	0	1.10E-02	8.79E-03	8.20E-03	7.93E-03	7.82E-03
	5	1.11E-02	8.88E-03	8.38E-03	8.04E-03	8.02E-03
	10	1.13E-02	9.23E-03	8.69E-03	8.40E-03	8.30E-03
	15	1.17E-02	9.72E-03	8.94E-03	8.65E-03	8.57E-03
	20	1.21E-02	1.00E-02	9.12E-03	8.91E-03	8.70E-03

6.4.3.10 Kidneys

The normalised absorbed dose for left and right kidneys with various tumour involvements, LS and T/N are shown in **Table 6.16** and **Table 6.17**, respectively. The absorbed doses to both kidneys for all scenarios (for tumour dose of 120 Gy) were in the ranges of 3.36 to 22.20 cGy, and 27.62 to 135.05 cGy, respectively. These corresponded to effective doses in ranges of 4.03 to 26.64 mSv, and 33.14 to 162.06 mSv to the left and right kidney, respectively.

Table 6.16: Normalised absorbed dose for left kidney with various tumour involvements (TI), lung shunting (LS) and tumour-to-normal liver uptake ratio (T/N).

TI (%)	LS (%)	Normalised absorbed dose for Left Kidney				
		T/N 1	T/N 2.5	T/N 5	T/N 7.5	T/N 10
10	0	1.52E-03	7.06E-04	4.20E-04	3.29E-04	2.80E-04
	5	1.57E-03	7.28E-04	4.47E-04	3.45E-04	2.93E-04
	10	1.64E-03	7.77E-04	4.59E-04	3.61E-04	3.09E-04
	15	1.73E-03	8.20E-04	4.90E-04	3.75E-04	3.25E-04
	20	1.84E-03	8.42E-04	5.10E-04	4.02E-04	3.37E-04
30	0	1.53E-03	8.71E-04	6.37E-04	5.58E-04	5.23E-04
	5	1.58E-03	9.06E-04	6.64E-04	5.84E-04	5.51E-04
	10	1.66E-03	9.53E-04	6.97E-04	6.25E-04	5.76E-04
	15	1.73E-03	9.88E-04	7.37E-04	6.50E-04	6.04E-04
	20	1.85E-03	1.05E-03	7.88E-04	6.87E-04	6.41E-04
50	0	1.53E-03	1.07E-03	8.96E-04	8.49E-04	8.21E-04
	5	1.59E-03	1.11E-03	9.43E-04	8.88E-04	8.71E-04
	10	1.69E-03	1.16E-03	9.92E-04	9.35E-04	9.03E-04
	15	1.74E-03	1.22E-03	1.04E-03	9.65E-04	9.62E-04
	20	1.85E-03	1.29E-03	1.09E-03	1.03E-03	1.00E-03
70	0	1.53E-03	1.24E-03	1.16E-03	1.11E-03	1.09E-03
	5	1.60E-03	1.29E-03	1.20E-03	1.17E-03	1.14E-03
	10	1.69E-03	1.37E-03	1.25E-03	1.22E-03	1.19E-03
	15	1.75E-03	1.46E-03	1.31E-03	1.29E-03	1.27E-03
	20	1.85E-03	1.50E-03	1.39E-03	1.36E-03	1.33E-03

Table 6.17: Normalised absorbed dose for right kidney with various tumour involvements (TI), lung shunting (LS) and tumour-to-normal liver uptake ratio (T/N).

TI (%)	LS (%)	Normalised absorbed dose for Right Kidney				
		T/N 1	T/N 2.5	T/N 5	T/N 7.5	T/N 10
10	0	1.08E-02	5.27E-03	3.29E-03	2.64E-03	2.30E-03
	5	1.09E-02	5.29E-03	3.32E-03	2.65E-03	2.31E-03
	10	1.10E-02	5.34E-03	3.34E-03	2.65E-03	2.33E-03
	15	1.10E-02	5.35E-03	3.37E-03	2.69E-03	2.35E-03
	20	1.11E-02	5.41E-03	3.40E-03	2.72E-03	2.36E-03
30	0	1.09E-02	6.63E-03	5.18E-03	4.66E-03	4.43E-03
	5	1.09E-02	6.71E-03	5.19E-03	4.69E-03	4.45E-03
	10	1.10E-02	6.71E-03	5.23E-03	4.73E-03	4.47E-03
	15	1.11E-02	6.76E-03	5.27E-03	4.77E-03	4.50E-03
	20	1.12E-02	6.81E-03	5.29E-03	4.80E-03	4.53E-03
50	0	1.09E-02	8.02E-03	6.99E-03	6.66E-03	6.48E-03
	5	1.10E-02	8.04E-03	7.03E-03	6.68E-03	6.50E-03
	10	1.11E-02	8.11E-03	7.07E-03	6.76E-03	6.58E-03
	15	1.12E-02	8.17E-03	7.13E-03	6.77E-03	6.64E-03
	20	1.12E-02	8.18E-03	7.17E-03	6.87E-03	6.68E-03
70	0	1.09E-02	9.15E-03	8.54E-03	8.35E-03	8.24E-03
	5	1.11E-02	9.22E-03	8.60E-03	8.42E-03	8.32E-03
	10	1.11E-02	9.26E-03	8.67E-03	8.42E-03	8.34E-03
	15	1.12E-02	9.36E-03	8.69E-03	8.53E-03	8.39E-03
	20	1.13E-02	9.42E-03	8.78E-03	8.62E-03	8.49E-03

6.4.3.11 Small Intestine

The normalised absorbed dose for small intestine with various tumour involvements, LS and T/N are shown in **Table 6.18**. The absorbed doses to small intestine for all scenarios (for tumour dose of 120 Gy) were in the range of 6.14 to 36.16 cGy, which correspond to effective dose of 7.37 to 43.39 mSv.

Table 6.18: Normalised absorbed dose for small intestine with various tumour involvements (TI), lung shunting (LS) and tumour-to-normal liver uptake ratio (T/N).

TI (%)	LS (%)	Normalised absorbed dose for Small Intestine				
		T/N 1	T/N 2.5	T/N 5	T/N 7.5	T/N 10
10	0	2.92E-03	1.35E-03	7.95E-04	6.06E-04	5.11E-04
	5	2.94E-03	1.35E-03	7.99E-04	6.12E-04	5.15E-04
	10	2.96E-03	1.36E-03	8.01E-04	6.15E-04	5.17E-04
	15	2.96E-03	1.37E-03	8.06E-04	6.15E-04	5.20E-04
	20	2.99E-03	1.37E-03	8.14E-04	6.21E-04	5.23E-04
30	0	2.95E-03	1.65E-03	1.21E-03	1.05E-03	9.81E-04
	5	2.96E-03	1.66E-03	1.21E-03	1.06E-03	9.87E-04
	10	2.96E-03	1.66E-03	1.22E-03	1.07E-03	9.92E-04
	15	2.98E-03	1.68E-03	1.22E-03	1.07E-03	9.98E-04
	20	3.00E-03	1.68E-03	1.23E-03	1.08E-03	1.00E-03
50	0	2.96E-03	2.01E-03	1.69E-03	1.58E-03	1.52E-03
	5	2.96E-03	2.01E-03	1.70E-03	1.58E-03	1.53E-03
	10	2.98E-03	2.03E-03	1.70E-03	1.58E-03	1.54E-03
	15	2.99E-03	2.03E-03	1.71E-03	1.60E-03	1.54E-03
	20	3.03E-03	2.04E-03	1.71E-03	1.60E-03	1.54E-03
70	0	2.97E-03	2.36E-03	2.15E-03	2.09E-03	2.05E-03
	5	2.99E-03	2.37E-03	2.16E-03	2.10E-03	2.06E-03
	10	2.99E-03	2.38E-03	2.18E-03	2.11E-03	2.06E-03
	15	3.00E-03	2.39E-03	2.18E-03	2.12E-03	2.08E-03
	20	3.01E-03	2.40E-03	2.20E-03	2.12E-03	2.09E-03

6.4.3.12 Large Intestines

The normalised absorbed dose for upper large intestine (ULI) and lower large intestine (LLI) with various tumour involvements, LS and T/N are shown in **Table 6.19** and **Table 6.20**, respectively. The absorbed doses to ULI for all scenarios (for tumour dose of 120 Gy) were in the range of 10.94 to 65.56 cGy, which correspond to effective dose of 13.13 to 78.67 mSv. For LLI, the absorbed doses for all scenarios (for tumour dose of 120 Gy) were in the range of 0.61 to 3.68 cGy, corresponded to effective dose of 0.73 to 4.42 mSv.

Table 6.19: Normalised absorbed dose for upper large intestine (ULI) with various tumour involvements (TI), lung shunting (LS) and tumour-to-normal liver uptake ratio (T/N).

TI (%)	LS (%)	Normalised absorbed dose for ULI				
		T/N 1	T/N 2.5	T/N 5	T/N 7.5	T/N 10
10	0	5.34E-03	2.45E-03	1.42E-03	1.09E-03	9.12E-04
	5	5.35E-03	2.45E-03	1.44E-03	1.09E-03	9.18E-04
	10	5.36E-03	2.45E-03	1.44E-03	1.09E-03	9.18E-04
	15	5.36E-03	2.46E-03	1.44E-03	1.09E-03	9.20E-04
	20	5.39E-03	2.47E-03	1.45E-03	1.10E-03	9.29E-04
30	0	5.35E-03	2.99E-03	2.17E-03	1.89E-03	1.76E-03
	5	5.37E-03	2.99E-03	2.18E-03	1.91E-03	1.77E-03
	10	5.38E-03	3.01E-03	2.18E-03	1.91E-03	1.77E-03
	15	5.40E-03	3.01E-03	2.21E-03	1.92E-03	1.78E-03
	20	5.42E-03	3.03E-03	2.21E-03	1.92E-03	1.78E-03
50	0	5.38E-03	3.65E-03	3.05E-03	2.87E-03	2.75E-03
	5	5.39E-03	3.66E-03	3.06E-03	2.87E-03	2.76E-03
	10	5.41E-03	3.67E-03	3.09E-03	2.89E-03	2.78E-03
	15	5.43E-03	3.69E-03	3.09E-03	2.89E-03	2.78E-03
	20	5.44E-03	3.70E-03	3.09E-03	2.91E-03	2.79E-03
70	0	5.42E-03	4.33E-03	3.95E-03	3.83E-03	3.77E-03
	5	5.42E-03	4.34E-03	3.98E-03	3.83E-03	3.80E-03
	10	5.45E-03	4.34E-03	3.98E-03	3.85E-03	3.80E-03
	15	5.46E-03	4.36E-03	3.98E-03	3.88E-03	3.81E-03
	20	5.46E-03	4.39E-03	4.01E-03	3.88E-03	3.83E-03

Table 6.20: Normalised absorbed dose for lower large intestine (LLI) with various tumour involvements (TI), lung shunting (LS) and tumour-to-normal liver uptake ratio (T/N).

TI (%)	LS (%)	Normalised absorbed dose for LLI				
		T/N 1	T/N 2.5	T/N 5	T/N 7.5	T/N 10
10	0	2.87E-04	1.33E-04	7.88E-05	6.05E-05	5.09E-05
	5	2.90E-04	1.35E-04	7.92E-05	6.14E-05	5.18E-05
	10	2.96E-04	1.37E-04	8.14E-05	6.16E-05	5.21E-05
	15	2.99E-04	1.39E-04	8.18E-05	6.35E-05	5.39E-05
	20	3.00E-04	1.40E-04	8.27E-05	6.45E-05	5.43E-05
30	0	2.87E-04	1.60E-04	1.20E-04	1.04E-04	9.56E-05
	5	2.91E-04	1.65E-04	1.21E-04	1.06E-04	9.64E-05
	10	2.97E-04	1.66E-04	1.21E-04	1.07E-04	9.97E-05
	15	2.99E-04	1.67E-04	1.23E-04	1.07E-04	1.01E-04
	20	3.03E-04	1.68E-04	1.26E-04	1.10E-04	1.03E-04
50	0	2.90E-04	1.97E-04	1.67E-04	1.55E-04	1.52E-04
	5	2.91E-04	1.99E-04	1.71E-04	1.58E-04	1.53E-04
	10	2.98E-04	2.06E-04	1.71E-04	1.61E-04	1.53E-04
	15	3.00E-04	2.08E-04	1.73E-04	1.63E-04	1.56E-04
	20	3.04E-04	2.13E-04	1.80E-04	1.66E-04	1.60E-04
70	0	2.93E-04	2.31E-04	2.15E-04	2.06E-04	2.03E-04
	5	2.93E-04	2.36E-04	2.17E-04	2.11E-04	2.09E-04
	10	2.99E-04	2.40E-04	2.21E-04	2.12E-04	2.11E-04
	15	3.00E-04	2.42E-04	2.24E-04	2.19E-04	2.12E-04
	20	3.07E-04	2.44E-04	2.30E-04	2.21E-04	2.15E-04

6.4.3.13 Urinary Bladder

The normalised absorbed dose for urinary bladder with various tumour involvements, LS and T/N are shown in **Table 6.21**. The absorbed doses to urinary bladder for all scenarios (for tumour dose of 120 Gy) were in the range of 0.43 to 2.66 cGy, which correspond to effective dose of 0.17 to 1.06 mSv.

Table 6.21: Normalised absorbed dose for urinary bladder with various tumour involvements (TI), lung shunting (LS) and tumour-to-normal liver uptake ratio (T/N).

TI (%)	LS (%)	Normalised absorbed dose for Urinary Bladder				
		T/N 1	T/N 2.5	T/N 5	T/N 7.5	T/N 10
10	0	1.93E-04	9.00E-05	5.40E-05	4.14E-05	3.56E-05
	5	1.99E-04	9.14E-05	5.44E-05	4.27E-05	3.56E-05
	10	2.00E-04	9.32E-05	5.70E-05	4.39E-05	3.68E-05
	15	2.03E-04	9.45E-05	5.77E-05	4.42E-05	3.68E-05
	20	2.05E-04	9.67E-05	6.03E-05	4.51E-05	3.79E-05
30	0	1.95E-04	1.11E-04	8.28E-05	7.06E-05	6.44E-05
	5	2.01E-04	1.11E-04	8.70E-05	7.07E-05	6.71E-05
	10	2.05E-04	1.14E-04	8.71E-05	7.48E-05	6.72E-05
	15	2.06E-04	1.15E-04	9.03E-05	7.60E-05	6.73E-05
	20	2.10E-04	1.18E-04	9.28E-05	7.66E-05	6.99E-05
50	0	1.96E-04	1.36E-04	1.15E-04	1.11E-04	1.01E-04
	5	2.04E-04	1.37E-04	1.18E-04	1.11E-04	1.03E-04
	10	2.10E-04	1.38E-04	1.19E-04	1.13E-04	1.05E-04
	15	2.11E-04	1.39E-04	1.21E-04	1.13E-04	1.09E-04
	20	2.11E-04	1.40E-04	1.22E-04	1.16E-04	1.09E-04
70	0	1.98E-04	1.60E-04	1.47E-04	1.45E-04	1.33E-04
	5	2.05E-04	1.64E-04	1.52E-04	1.45E-04	1.33E-04
	10	2.10E-04	1.67E-04	1.54E-04	1.52E-04	1.46E-04
	15	2.11E-04	1.74E-04	1.55E-04	1.54E-04	1.49E-04
	20	2.22E-04	1.78E-04	1.57E-04	1.55E-04	1.51E-04

6.4.3.14 Uterus

The normalised absorbed dose for uterus with various tumour involvements, LS and T/N are shown in **Table 6.22**. The absorbed doses to uterus for all scenarios (for tumour dose of 120 Gy) were in the range of 1.28 to 7.62 cGy, which correspond to effective dose of 1.54 to 9.14 mSv.

Table 6.22: Normalised absorbed dose for uterus with various tumour involvements (TI), lung shunting (LS) and tumour-to-normal liver uptake ratio (T/N).

TI (%)	LS (%)	Normalised absorbed dose for Uterus				
		T/N 1	T/N 2.5	T/N 5	T/N 7.5	T/N 10
10	0	6.00E-04	2.76E-04	1.64E-04	1.25E-04	1.07E-04
	5	6.05E-04	2.77E-04	1.66E-04	1.27E-04	1.07E-04
	10	6.06E-04	2.79E-04	1.66E-04	1.29E-04	1.07E-04
	15	6.13E-04	2.85E-04	1.69E-04	1.30E-04	1.07E-04
	20	6.23E-04	2.88E-04	1.71E-04	1.30E-04	1.10E-04
30	0	6.03E-04	3.35E-04	2.45E-04	2.19E-04	2.06E-04
	5	6.09E-04	3.43E-04	2.52E-04	2.21E-04	2.12E-04
	10	6.09E-04	3.46E-04	2.57E-04	2.26E-04	2.12E-04
	15	6.16E-04	3.49E-04	2.57E-04	2.27E-04	2.14E-04
	20	6.24E-04	3.53E-04	2.58E-04	2.31E-04	2.17E-04
50	0	6.04E-04	4.20E-04	3.49E-04	3.29E-04	3.16E-04
	5	6.10E-04	4.23E-04	3.56E-04	3.34E-04	3.17E-04
	10	6.12E-04	4.23E-04	3.61E-04	3.34E-04	3.19E-04
	15	6.22E-04	4.24E-04	3.64E-04	3.41E-04	3.25E-04
	20	6.29E-04	4.30E-04	3.69E-04	3.44E-04	3.29E-04
70	0	6.04E-04	4.84E-04	4.53E-04	4.29E-04	4.26E-04
	5	6.15E-04	4.91E-04	4.58E-04	4.36E-04	4.31E-04
	10	6.20E-04	4.92E-04	4.59E-04	4.44E-04	4.42E-04
	15	6.25E-04	5.05E-04	4.64E-04	4.56E-04	4.42E-04
	20	6.35E-04	5.07E-04	4.65E-04	4.57E-04	4.43E-04

6.4.4 Absorbed Dose to Gonads

6.4.4.1 Ovaries

The normalised absorbed dose for left and right ovaries with various tumour involvements, LS and T/N are shown in **Table 6.23** and **Table 6.24**, respectively. The absorbed doses to both ovaries for all scenarios (for tumour dose of 120 Gy) were in the ranges of 0.81 to 5.36 cGy, and 2.11 to 13.62 cGy for left and right ovaries, respectively. These corresponded to effective doses in ranges of 0.65 to 4.29 mSv and 1.69 to 10.90 mSv, to left and right ovaries, respectively.

Table 6.23: Normalised absorbed dose for left ovary with various tumour involvements (TI), lung shunting (LS) and tumour-to-normal liver uptake ratio (T/N).

TI (%)	LS (%)	Normalised absorbed dose for Left Ovary				
		T/N 1	T/N 2.5	T/N 5	T/N 7.5	T/N 10
10	0	3.66E-04	1.76E-04	9.67E-05	8.21E-05	6.74E-05
	5	3.66E-04	1.80E-04	1.01E-04	8.39E-05	6.78E-05
	10	3.76E-04	1.84E-04	1.05E-04	8.68E-05	6.88E-05
	15	3.76E-04	1.86E-04	1.06E-04	8.75E-05	7.05E-05
	20	4.25E-04	1.88E-04	1.08E-04	8.97E-05	8.13E-05
30	0	3.71E-04	2.06E-04	1.47E-04	1.35E-04	1.18E-04
	5	3.88E-04	2.07E-04	1.59E-04	1.42E-04	1.31E-04
	10	3.98E-04	2.26E-04	1.62E-04	1.44E-04	1.34E-04
	15	4.01E-04	2.27E-04	1.64E-04	1.45E-04	1.41E-04
	20	4.31E-04	2.34E-04	1.65E-04	1.59E-04	1.42E-04
50	0	3.85E-04	2.46E-04	2.31E-04	2.13E-04	1.96E-04
	5	3.88E-04	2.78E-04	2.33E-04	2.16E-04	2.10E-04
	10	4.18E-04	2.98E-04	2.35E-04	2.23E-04	2.11E-04
	15	4.23E-04	2.99E-04	2.56E-04	2.31E-04	2.16E-04
	20	4.33E-04	3.18E-04	2.58E-04	2.34E-04	2.17E-04
70	0	3.93E-04	3.07E-04	2.98E-04	2.76E-04	2.51E-04
	5	3.94E-04	3.19E-04	2.99E-04	2.82E-04	2.61E-04
	10	4.20E-04	3.19E-04	3.01E-04	2.87E-04	2.75E-04
	15	4.25E-04	3.40E-04	3.06E-04	2.92E-04	2.77E-04
	20	4.46E-04	3.81E-04	3.42E-04	2.95E-04	2.91E-04

Table 6.24: Normalised absorbed dose for right ovary with various tumour involvements (TI), lung shunting (LS) and tumour-to-normal liver uptake ratio (T/N).

TI (%)	LS (%)	Normalised absorbed dose for Right Ovary				
		T/N 1	T/N 2.5	T/N 5	T/N 7.5	T/N 10
10	0	9.72E-04	4.51E-04	2.66E-04	2.04E-04	1.75E-04
	5	1.02E-03	4.57E-04	2.69E-04	2.10E-04	1.83E-04
	10	1.04E-03	4.64E-04	2.76E-04	2.14E-04	1.92E-04
	15	1.04E-03	4.76E-04	2.76E-04	2.20E-04	1.93E-04
	20	1.04E-03	4.79E-04	2.94E-04	2.24E-04	1.96E-04
30	0	9.75E-04	5.81E-04	4.19E-04	3.84E-04	3.64E-04
	5	1.03E-03	5.85E-04	4.27E-04	3.91E-04	3.65E-04
	10	1.04E-03	6.10E-04	4.45E-04	3.93E-04	3.68E-04
	15	1.04E-03	6.18E-04	4.48E-04	3.96E-04	3.86E-04
	20	1.05E-03	6.32E-04	4.51E-04	4.02E-04	3.91E-04
50	0	9.98E-04	7.18E-04	5.84E-04	5.56E-04	5.38E-04
	5	1.03E-03	7.29E-04	6.27E-04	5.63E-04	5.39E-04
	10	1.05E-03	7.34E-04	6.28E-04	5.67E-04	5.59E-04
	15	1.08E-03	7.52E-04	6.52E-04	5.79E-04	5.62E-04
	20	1.11E-03	7.58E-04	6.99E-04	5.99E-04	5.80E-04
70	0	1.01E-03	8.06E-04	7.90E-04	7.26E-04	7.06E-04
	5	1.04E-03	8.06E-04	7.91E-04	7.33E-04	7.14E-04
	10	1.08E-03	8.52E-04	7.94E-04	7.39E-04	7.16E-04
	15	1.11E-03	8.65E-04	8.21E-04	7.73E-04	7.36E-04
	20	1.13E-03	8.92E-04	8.28E-04	7.83E-04	7.43E-04

6.4.4.2 Testicles

The normalised absorbed dose for left and right testicles with various tumour involvements, LS and T/N are shown in **Table 6.25** and **Table 6.26**, respectively. The absorbed doses to both testicles for all scenarios (for tumour dose of 120 Gy) were in the ranges of 0.04 to 0.35 cGy, and 0.05 to 0.44 cGy for left and right testicles, respectively. These corresponded to effective doses in ranges of 0.03 to 0.28 mSv and 0.04 to 0.35 mSv, to left and right testicles, respectively.

Table 6.25: Normalised absorbed dose for left testicle with various tumour involvements (TI), lung shunting (LS) and tumour-to-normal liver uptake ratio (T/N).

TI (%)	LS (%)	Normalised absorbed dose for Left Testicle				
		T/N 1	T/N 2.5	T/N 5	T/N 7.5	T/N 10
10	0	1.63E-05	8.76E-06	5.16E-06	3.98E-06	3.41E-06
	5	2.06E-05	1.10E-05	6.55E-06	4.86E-06	3.54E-06
	10	2.27E-05	1.16E-05	6.68E-06	5.05E-06	3.90E-06
	15	2.37E-05	1.18E-05	6.87E-06	5.09E-06	3.99E-06
	20	2.76E-05	1.23E-05	7.56E-06	5.59E-06	4.24E-06
30	0	1.70E-05	1.08E-05	8.82E-06	7.54E-06	6.41E-06
	5	2.24E-05	1.27E-05	9.43E-06	7.71E-06	6.65E-06
	10	2.28E-05	1.31E-05	9.95E-06	7.71E-06	7.00E-06
	15	2.47E-05	1.33E-05	1.05E-05	8.10E-06	7.03E-06
	20	2.83E-05	1.37E-05	1.09E-05	8.52E-06	7.70E-06
50	0	1.97E-05	1.51E-05	1.25E-05	1.12E-05	9.25E-06
	5	2.25E-05	1.52E-05	1.26E-05	1.13E-05	1.00E-05
	10	2.32E-05	1.56E-05	1.29E-05	1.16E-05	1.03E-05
	15	2.65E-05	1.62E-05	1.43E-05	1.25E-05	1.05E-05
	20	2.88E-05	1.70E-05	1.47E-05	1.40E-05	1.24E-05
70	0	2.02E-05	1.59E-05	1.56E-05	1.53E-05	1.36E-05
	5	2.27E-05	1.83E-05	1.67E-05	1.55E-05	1.44E-05
	10	2.34E-05	1.95E-05	1.71E-05	1.60E-05	1.45E-05
	15	2.70E-05	2.29E-05	1.78E-05	1.65E-05	1.56E-05
	20	2.92E-05	2.31E-05	1.90E-05	1.83E-05	1.72E-05

Table 6.26: Normalised absorbed dose for right testicle with various tumour involvements (TI), lung shunting (LS) and tumour-to-normal liver uptake ratio (T/N).

TI (%)	LS (%)	Normalised absorbed dose for Right Testicle				
		T/N 1	T/N 2.5	T/N 5	T/N 7.5	T/N 10
10	0	2.36E-05	1.12E-05	6.98E-06	5.71E-06	4.27E-06
	5	2.71E-05	1.30E-05	7.40E-06	5.75E-06	4.55E-06
	10	3.02E-05	1.38E-05	8.19E-06	6.11E-06	4.55E-06
	15	3.10E-05	1.46E-05	8.39E-06	6.36E-06	4.79E-06
	20	3.36E-05	1.55E-05	9.02E-06	6.61E-06	5.51E-06
30	0	2.37E-05	1.29E-05	1.14E-05	9.58E-06	7.44E-06
	5	2.79E-05	1.58E-05	1.15E-05	9.85E-06	8.24E-06
	10	3.05E-05	1.69E-05	1.17E-05	1.05E-05	8.44E-06
	15	3.11E-05	1.69E-05	1.23E-05	1.08E-05	9.98E-06
	20	3.38E-05	1.73E-05	1.28E-05	1.18E-05	1.09E-05
50	0	2.47E-05	1.83E-05	1.45E-05	1.34E-05	1.24E-05
	5	2.94E-05	1.85E-05	1.47E-05	1.36E-05	1.28E-05
	10	3.10E-05	1.91E-05	1.48E-05	1.47E-05	1.28E-05
	15	3.15E-05	2.00E-05	1.65E-05	1.49E-05	1.35E-05
	20	3.42E-05	2.03E-05	1.77E-05	1.57E-05	1.43E-05
70	0	2.61E-05	2.10E-05	1.79E-05	1.68E-05	1.56E-05
	5	2.95E-05	2.35E-05	1.91E-05	1.72E-05	1.66E-05
	10	3.11E-05	2.56E-05	2.13E-05	1.88E-05	1.80E-05
	15	3.24E-05	2.58E-05	2.18E-05	2.01E-05	1.84E-05
	20	3.65E-05	2.64E-05	2.32E-05	2.04E-05	1.98E-05

6.4.5 Development of Treatment Dose Calculation Spreadsheet

The interface of the dose calculation spreadsheet is shown in **Figure 6.6**. In part (a) the parameters consist of drop down menu with discrete values; tumour involvement (10, 30, 50, and 70 %), LS (0, 5, 10, 15, 20 %) and T/N (1, 2.5, 5, 7.5, 10). For part (b), the desired tumour dose is chosen in a text fill box, thus the administered activity and the organ's absorbed doses (in part (c)) will be obtained spontaneously. The spreadsheet.xlsx program is included in the compact disc located in the Appendix.

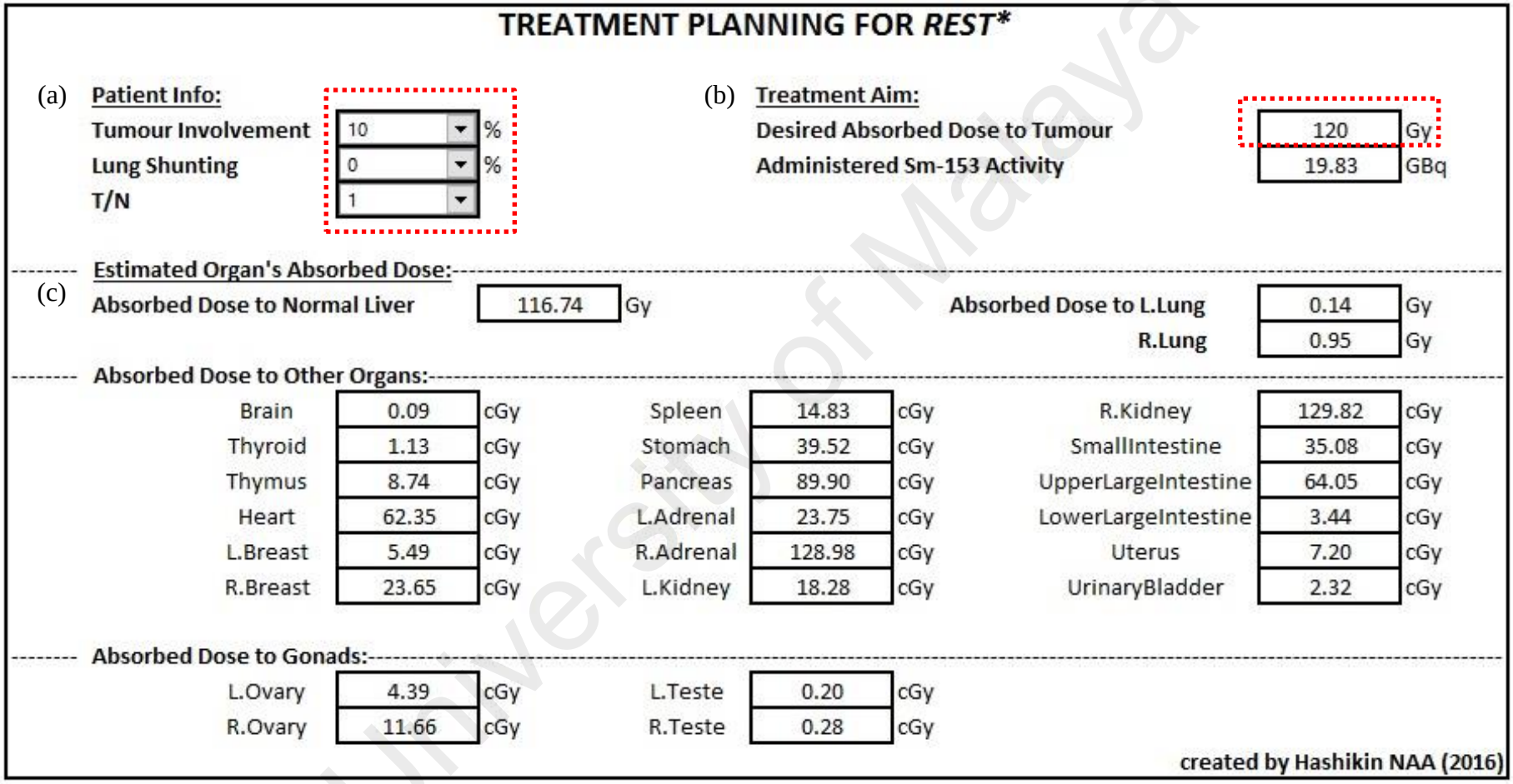

Figure 6.6: The user interface of the dose calculation spreadsheet for TARE with ^{153}Sm-microparticles; (a) patient information input, (b) targeted tumour dose input and its corresponding administered activity, and (c) the corresponding organ absorbed dose. Red dotted boxes indicate changeable values. REST: 'radioembolization samarium therapy'.

6.4.6 The Determination of Treatment Limit

The maximum tumour dose allowed to be delivered without exceeding either 70 Gy to normal liver or 30 Gy to lungs for all scenarios with tumour involvements of 10, 30, 50 and 70 %, are shown in **Table 6.27**, **Table 6.28**, **Table 6.29**, and **Table 6.30**, respectively.

Table 6.27: Estimated maximum absorbed dose allowed for treatment for 10 % tumour involvement (TI). LS: lung shunting; T/N: tumour-to-normal liver uptake ratio; A: activity.

TI (%)	LS (%)	T/N	A (GBq)	Absorbed dose (Gy)			
				Tumour	Normal Liver	Left Lung	Right Lung
10	0	1	11.9	72.0	**70.0**	0.1	0.6
10	0	2.5	13.5	171.4	**70.0**	0.1	0.6
10	0	5	16.2	332.7	**70.0**	0.1	0.8
10	0	7.5	18.8	488.5	**70.0**	0.1	0.9
10	0	10	21.3	638.9	**70.0**	0.1	1.0
10	5	1	12.5	71.9	**70.0**	6.5	6.9
10	5	2.5	14.2	171.4	**70.0**	7.3	7.9
10	5	5	17.0	332.3	**70.0**	8.8	9.4
10	5	7.5	19.7	487.9	**70.0**	10.1	10.9
10	5	10	22.4	638.9	**70.0**	11.5	12.4
10	10	1	13.2	71.9	**70.0**	13.5	14.0
10	10	2.5	15.0	171.3	**70.0**	15.4	15.9
10	10	5	18.0	332.1	**70.0**	18.4	19.0
10	10	7.5	20.8	487.9	**70.0**	21.3	22.0
10	10	10	23.6	638.1	**70.0**	24.1	25.0
10	15	1	14.0	71.9	**70.0**	21.4	21.9
10	15	2.5	15.9	171.3	**70.0**	24.3	24.9
10	15	5	19.0	332.1	**70.0**	29.1	29.8
10	15	7.5	19.2	424.7	61.0	29.3	**30.0**
10	15	10	19.2	490.3	53.8	29.3	**30.0**
10	20	1	14.5	70.2	68.4	29.6	**30.0**
10	20	2.5	14.5	147.0	60.1	29.6	**30.0**
10	20	5	14.5	238.4	50.3	29.6	**30.0**
10	20	7.5	14.5	302.3	43.4	29.6	**30.0**
10	20	10	14.5	348.0	38.2	29.5	**30.0**

Table 6.28: Estimated maximum absorbed dose allowed for treatment for 30 % tumour involvement (TI). LS: lung shunting; T/N: tumour-to-normal liver uptake ratio; A: activity.

TI (%)	LS (%)	T/N	A (GBq)	Absorbed dose (Gy)			
				Tumour	Normal Liver	Left Lung	Right Lung
30	0	1	12.0	72.0	**70.0**	0.1	0.6
30	0	2.5	16.9	171.1	**70.0**	0.1	0.8
30	0	5	24.6	325.5	**70.0**	0.1	1.1
30	0	7.5	31.7	468.2	**70.0**	0.2	1.4
30	0	10	38.3	600.1	**70.0**	0.2	1.7
30	5	1	12.6	71.9	**70.0**	6.5	7.0
30	5	2.5	17.8	171.1	**70.0**	9.2	9.8
30	5	5	25.9	325.4	**70.0**	13.3	14.3
30	5	7.5	33.3	467.9	**70.0**	17.1	18.3
30	5	10	40.2	599.4	**70.0**	20.7	22.1
30	10	1	13.3	71.9	**70.0**	13.6	14.1
30	10	2.5	18.8	171.1	**70.0**	19.2	19.8
30	10	5	27.3	325.2	**70.0**	27.9	28.9
30	10	7.5	28.4	377.1	56.5	29.0	**30.0**
30	10	10	28.4	400.5	46.8	29.0	**30.0**
30	15	1	14.1	71.9	**70.0**	21.5	22.0
30	15	2.5	19.2	165.4	67.7	29.4	**30.0**
30	15	5	19.2	216.1	46.5	29.4	**30.0**
30	15	7.5	19.2	240.9	36.1	29.4	**30.0**
30	15	10	19.2	255.9	29.9	29.3	**30.0**
30	20	1	14.5	69.8	67.9	29.5	**30.0**
30	20	2.5	14.5	117.6	48.2	29.6	**30.0**
30	20	5	14.5	153.7	33.1	29.5	**30.0**
30	20	7.5	14.5	171.7	25.8	29.6	**30.0**
30	20	10	14.5	182.1	21.3	29.6	**30.0**

Table 6.29: Estimated maximum absorbed dose allowed for treatment for 50 % tumour involvement (TI). LS: lung shunting; T/N: tumour-to-normal liver uptake ratio; A: activity.

TI (%)	LS (%)	T/N	A (GBq)	Absorbed dose (Gy)			
				Tumour	Normal Liver	Left Lung	Right Lung
50	0	1	12.1	72.2	**70.0**	0.1	0.6
50	0	2.5	20.2	170.3	**70.0**	0.1	1.0
50	0	5	32.5	317.3	**70.0**	0.2	1.5
50	0	7.5	43.3	446.6	**70.0**	0.3	2.0
50	0	10	52.8	561.6	**70.0**	0.3	2.4
50	5	1	12.7	72.2	**70.0**	6.5	7.0
50	5	2.5	21.3	170.2	**70.0**	10.9	11.7
50	5	5	34.2	317.1	**70.0**	17.6	18.9
50	5	7.5	45.5	446.4	**70.0**	23.4	25.1
50	5	10	54.4	549.5	68.5	28.0	**30.0**
50	10	1	13.4	72.2	**70.0**	13.7	14.2
50	10	2.5	22.4	170.2	**70.0**	23.0	23.8
50	10	5	28.4	249.8	55.2	29.0	**30.0**
50	10	7.5	28.4	263.7	41.4	29.0	**30.0**
50	10	10	28.4	271.3	33.9	28.9	**30.0**
50	15	1	14.2	72.2	**70.0**	21.7	22.1
50	15	2.5	19.2	137.3	56.5	29.4	**30.0**
50	15	5	19.2	159.3	35.2	29.4	**30.0**
50	15	7.5	19.2	168.5	26.5	29.3	**30.0**
50	15	10	19.2	173.6	21.7	29.3	**30.0**
50	20	1	14.5	69.6	67.5	29.5	**30.0**
50	20	2.5	14.5	97.7	40.2	29.5	**30.0**
50	20	5	14.5	113.4	25.1	29.6	**30.0**
50	20	7.5	14.5	119.8	18.8	29.6	**30.0**
50	20	10	14.5	123.4	15.4	29.6	**30.0**

Table 6.30: Estimated maximum absorbed dose allowed for treatment for 70 % tumour involvement (TI). LS: lung shunting; T/N: tumour-to-normal liver uptake ratio; A: activity.

TI (%)	LS (%)	T/N	A (GBq)	Absorbed dose (Gy)			
				Tumour	Normal Liver	Left Lung	Right Lung
70	0	1	12.2	72.7	**70.0**	0.1	0.6
70	0	2.5	23.5	169.0	**70.0**	0.2	1.1
70	0	5	39.5	305.6	**70.0**	0.3	1.9
70	0	7.5	52.8	419.8	**70.0**	0.3	2.5
70	0	10	64.0	514.5	**70.0**	0.4	3.0
70	5	1	12.8	72.7	**70.0**	6.6	7.1
70	5	2.5	24.7	168.9	**70.0**	12.7	13.7
70	5	5	41.5	305.5	**70.0**	21.3	23.0
70	5	7.5	54.3	409.4	68.4	27.8	**30.0**
70	5	10	54.2	414.2	56.4	27.9	**30.0**
70	10	1	13.5	72.7	**70.0**	13.8	14.3
70	10	2.5	26.0	168.8	**70.0**	26.6	27.6
70	10	5	28.4	197.9	45.4	29.0	**30.0**
70	10	7.5	28.3	202.5	33.8	29.0	**30.0**
70	10	10	28.3	205.2	28.0	28.9	**30.0**
70	15	1	14.3	72.7	**70.0**	21.9	22.4
70	15	2.5	19.2	117.4	48.7	29.3	**30.0**
70	15	5	19.2	126.2	28.9	29.3	**30.0**
70	15	7.5	19.2	129.4	21.7	29.3	**30.0**
70	15	10	19.2	131.4	17.9	29.4	**30.0**
70	20	1	14.5	69.3	66.8	29.6	**30.0**
70	20	2.5	14.5	83.4	34.6	29.5	**30.0**
70	20	5	14.5	89.9	20.6	29.6	**30.0**
70	20	7.5	14.5	92.2	15.4	29.5	**30.0**
70	20	10	14.5	93.3	12.8	29.5	**30.0**

For all tumour involvements, the scenarios with T/N of 1 are limited to maximum tumour absorbed dose in the range of 69.3 to 72.7 Gy, which correspond to administered activities of 11.29 to 14.5 GBq. For LS of 20 %, all scenarios were limited by the right lung absorbed dose (30 Gy), consistently resulting in maximum administered activity of 14.5 GBq. Normal liver dose limit was achieved mostly by scenarios with lower LS and T/N, while the lung dose limit was easily achieved by scenarios with higher LS and T/N. The highest limit for treatment belongs to scenario with 10 % tumour involvement, T/N of 10 and LS of both 0 and 5 %, which allow the administration of tumour dose of up to 638.9 Gy. Conversely, the lowest limit to treatment was of 70 % tumour involvement, LS of 20 % and T/N of 1, with only 69.3 Gy possible to be delivered to the tumour. Collectively, lower tumour involvement and LS, and higher T/N were able to achieve larger tumour dose, without exceeding the normal liver and lung dose limits.

6.5 Discussions

In this study, Geant4 was used due to its flexibility in terms of geometry set up and physics environment. Although OLINDA/EXM has been widely used in nuclear medicine for estimation of absorbed dose during diagnostic procedures, it was not used in this study due to unavailability for models related to TARE which is more closely related in principle to brachytherapy rather than nuclear medicine due to permanent administration of the ^{153}Sm-microparticles. The mathematical phantom was chosen due to its simplicity hence allowing for geometrical manipulation and shorter simulation time than voxelised phantoms. Also since the phantom was built based on a standard reference values, hence it is more representative of the whole population rather than the patient-specific voxelised phantoms.

We have found that for ^{153}Sm to deliver similar tumour dose to that of ^{90}Y, ^{153}Sm administered activities need to be given in the range of 4.42 to 4.60 times higher than ^{90}Y. This was mainly due to the difference in the physical characteristics between the two radionuclides. Higher ^{153}Sm activities need to be administered to compensate for its shorter half-life (46.3 versus 64.1 h of ^{90}Y), and lower maximum beta energy (0.81 versus 2.28 Mev of ^{90}Y) and yield (19.5 versus 99.98 %).

The partition model dosimetry for dose and activity calculations in TARE with ^{90}Y-microspheres can be easily derived from the MIRD equation based on the assumption of full dose deposition within the source organs/compartments, since only beta radiation is involved. However, for gamma dosimetry, more complex problems arise as a result of the dependency of energy deposition by penetrative radiation towards the gamma energies, the distance between the source and target, and also the volume and chemical composition of the tissues involved. Hence, it is impossible to obtain a simplified equation such as **Equation 5.1** (refer p. 98) as used in the partition model, since the constant values (49670 for ^{90}Y) will be different for every scenario when ^{153}Sm is being used.

However, based on MIRD scheme, an estimation of absorbed dose for each source and target organs pair can be obtained using **Equation 6.9**.

$$D_k = \Sigma_h \tilde{A}_h S(r_k \leftarrow r_h) \qquad \textbf{6.9}$$

where,

D_k = absorbed dose to target organ, k.

$\tilde{A}_h$ = cumulated activity in source organ, h.

$S(r_k \leftarrow r_h)$ = mean dose per unit cumulated activity between the target and source organ pair.

However, since the dose estimation involved several organs, each with different source and target organ combination, and thus has made the dose estimation a tedious task.

Hence, the advantage of our study is that the data from the simulations has been compiled into a dose calculation spreadsheet, which can be directly used to estimate the organs absorbed doses.

Our findings showed that TARE with ^{153}Sm-microparticles is safe and that the treatment is not limited by the absorbed dose received by the organs other than the liver and lungs. This is because, all organ doses were found to be far below 1 Gy (for tumour dose of 120 Gy) or only less than 1 % as compared to the absorbed dose given to the tumour. This was supported by Turner et al. (1994) dosimetric study for TARE with ^{166}Ho-microspheres, which reported that only 1.1 % of the overall absorbed dose were contributed by the gamma emission. Hence the limit to treatment were only determined by the maximum absorbed dose limit to normal liver tissue and lungs, as being done in the study.

From the estimation of the maximum limit for TARE with ^{153}Sm-microparticles, it was found that lower tumour involvement and LS, and larger T/N allowed the administration of higher ^{153}Sm activities, hence a recommended therapeutic dose of 120 Gy can be easily delivered without overdosing the normal liver and lungs. However, for the remainder scenarios, especially for T/N of 1, higher tumour involvement and LS, a series of fractionated treatment may be considered, thus allowing time for the normal tissue to regenerate from the biological effects of radiation, at the same time higher therapeutic dose to the tumour can be delivered. Nonetheless, this should first be investigated for its effectiveness in radiobiological studies involving animal subjects, before it can be clinically implemented.

A dose calculation spreadsheet has been successfully built for ease in future clinical use. The features are user friendly with all the information included in a single interface for better visualization. However, since the simulations were only carried out in a discrete

manner, the spreadsheet will not be directly available for certain scenarios. Future work to obtain a trend curve (connecting the values for every parameters) for every organ and scenarios should be carried out, however this effort may be relatively complex as collectively hundreds of scenarios could be derived as a result of combinations of the tumour involvement, LS and T/N. A recommendation would be to interpolate the absorbed dose between the discrete values, however the accuracy of this method has yet to be validated, which we are currently looking into.

6.6 Conclusion

A dosimetric study for TARE with ^{153}Sm-microparticles has been thoroughly investigated by estimating the radiation dose using Geant4 simulations. Our findings showed that the treatment has the potential to be the alternative to ^{90}Y, able to deliver a comparable tumour dose with added advantage of gamma radiation for imaging of *in vivo* distribution of the microparticles. The treatment is also reasonably safe since the dose to the normal organs never exceeded 1 Gy. Additionally, we have also successfully created a dose calculation spreadsheet for this treatment for the benefit of dose estimation for future clinical use.

CHAPTER 7: COMPARISON OF ORGAN DOSES FROM HEPATIC RADIOEMBOLIZATION WITH ^{90}Y, ^{153}SM, ^{166}HO, ^{177}LU and ^{188}RE

7.1 Introduction

In Chapter 6 the dosimetric aspects of transarterial radioembolization (TARE) with samarium-153 (^{153}Sm)-microparticles have been thoroughly investigated. As mentioned in Chapter 2, other than ^{153}Sm, there were several other radionuclides which have been suggested as alternative to yttrium-90 (^{90}Y) in TARE of hepatocellular carcinoma (HCC) (Poorbaygi et al., 2011; Hafeli et al., 1999; Mumper et al., 1991), which include holmium-166 (^{166}Ho), lutetium-177 (^{177}Lu), and rhenium (^{188}Re). The physical characteristics of these radionuclides along with ^{90}Y and ^{153}Sm are tabulated in **Table 7.1**. Since the half-lives, decay energies (both beta and gamma) and the corresponding decay yields differ largely between these radionuclides, the amount of administered activities required to deliver similar absorbed dose to the tumour will also be different. As highlighted in Chapter 5, the beta energies of the radionuclides will also affect the amount of energy being deposited in the normal liver tissue as a result of some beta particles that escaped from the tumour. Also, the amplitude of energy being deposited to the neighbouring organs will be of interest. Thus, these comparisons should be considered, in deciding the radionuclide of choice that provides the most ideal characteristics as alternative to ^{90}Y.

Table 7.1: Physical characteristics of theranostic radionuclides suggested for TARE of HCC as alternative to ^{90}Y. (LNHB (2014),*IAEA (1974)). Eγ: energy of gamma; E_β: energy of beta.

Radionuclide	**^{90}Y**	**^{153}Sm**	**^{166}Ho**	**^{177}Lu**	**^{188}Re**
Physical half-life, $t_{1/2}$ (h)	64.08	46.32	26.80	159.6	17.00
Principal Eγ (keV) [% yield]	None	103.2 [29.2]	80.6 [6.2]	208.4 [10.4]	155.0 [15.1]
Max E_β (keV) [% intensity]	2279.8 [99.98]	807.6 [19.5]	1854.5 [48.2]	498.3 [79.3]	2120.4 [71.7]
Mean β range in soft tissue (mm)	4.0	0.6	2.5	0.2	3.1
Max β range in soft tissue (mm)	11.3	2.5	8.0	1.8	10.4
Production method	^{89}Y(n,γ)^{90}Y ^{90}Sr/^{90}Y generator	^{152}Sm(n,γ)^{153}Sm	^{165}Ho(n,γ)^{166}Ho	^{176}Yb(n,γ,β-)^{177}Lu ^{176}Lu(n,γ)^{177}Lu	^{187}Re(n,γ)^{188}Re ^{188}W/^{188}Re generator
Daughter nuclide	^{90}Zr	^{153}Eu	^{166}Er	^{177}Hf	^{188}Os
***Thermal neutron activation cross section (barn)**	1.2 ± 0.1	210 ± 10.0	61.5 ± 2.0	5.5 ± 1.0 (^{176}Yb) 2050 ± 50 (^{176}Lu)	75 ± 4.0

In this chapter, the dosimetry between five radionuclides used for TARE; ^{90}Y, ^{153}Sm, ^{166}Ho, ^{177}Lu and ^{188}Re were assessed by simulating several treatment scenarios using the Geometry and Tracking 4 (Geant4) Monte Carlo (MC) code. The simulations were carried out for tumour involvements of 10, 30, 50, and 70 %; with 10 % lung shunting (LS) and tumour-to-normal liver uptake ratio (T/N) of 5. The tumours were aimed to receive 120 Gy, hence the radionuclides activities needed to deliver the tumour dose for each scenario were also estimated. The doses to normal liver tissue, lungs, and other organs for each radionuclide were recorded, and compared. Eventually, the pros and cons of the production and physical characteristics of each radionuclide intended for TARE were compared and discussed.

7.2 Objectives

The simulations were carried out to assess and compare the dosimetry between ^{90}Y, ^{153}Sm, ^{166}Ho, ^{177}Lu and ^{188}Re used in TARE of HCC, when the tumour was aimed to receive 120 Gy. The assessment will be completed by achieving these objectives:

i. To estimate and compare between the administered activities of each radionuclide required to achieve tumour dose of 120 Gy for various scenarios.
ii. To estimate and compare the absorbed dose to normal liver tissue, lungs and other organs, when 120 Gy of tumour dose is delivered for each radionuclide.
iii. To assess and compare the pros and cons of each radionuclide as alternative to ^{90}Y in TARE of HCC.

7.3 Methodology

7.3.1 Computational Phantom

The same mathematical hermaphrodite adult phantom as used in Chapter 6 (refer **Figure 6.1** p. 118) was adopted according to the Medical Internal Radiation Dose (MIRD) Pamphlet 5 consisting of complete anatomical organs (Snyder et al., 1978), with both female (ovaries and uterus) and male (testicles) reproductive organs. Female breasts were also incorporated into the phantom by adopting breasts from Cristy and Eckerman (1987). All the organs masses and the elemental composition of the tissues that made up the phantom are listed in **Table 6.1** (p. 118) and **Table 6.2** (p. 119), respectively.

7.3.2 Distribution of the Radionuclides Activities

After the administration of each radionuclide labelled microparticles into the tumour, a small fraction of the microparticles will be taken up by the normal liver tissue and both lungs. The amount of this extra-tumour uptakes were dependent on the LS and T/N, which can be calculated based on the partition model (PM) (Ho et al., 1996), used in TARE with ^{90}Y-microspheres. The model assumes that the radioactive microparticles are distributed only in the three compartments (tumour, normal liver and lungs), with no redistribution during the treatment. The distribution of the administered radionuclide labelled microparticles is determined using the method explained in **Section 6.3.2** (p. 119).

7.3.3 Geant4 Monte Carlo Simulations

This study was carried out using the Geant4 version 9.6.p03 (Allison et al., 2006; Agostinelli et al., 2003) with the computational phantom as provided in the Geant4 advanced example *human_phantom*. A similar tumour model as used in **Figure 6.2** (p. 121) was used to simulate the tumour with varying mass indirectly defined by the tumour

involvement as calculated using **Equation 6.6** (p. 121).

The Low Energy Electromagnetic Package (Chauvie et al., 2004), based on the Livermore Evaluated Data Libraries, was adopted to model the electromagnetic interactions of photons and electrons. The threshold of production of secondary particles was fixed to 1 mm. The Geant4 Radioactive Decay and General Particle Source components were used to model the decay of each radionuclide and its distribution in the main compartments (tumour, normal liver tissue and lungs), respectively. The radionuclide point sources were homogenously distributed within each compartment with activity uptake based on the selected T/N and LS, with randomised direction of emissions. The tumour, normal liver, lungs and other organs of interest were each set as a sensitive volume. The simulation output was set as mean energy (MeV) deposited to each volume.

Several patient scenarios consisting of combinations of different tumour involvements (10, 30, 50, 70 %), with 10 % LS and T/N of 5 were simulated for each radionuclide. 10^8 disintegrations corresponded to radionuclide activities as shown in **Table 7.2** (as calculated using **Equation 6.7** (p. 122)), were generated for each parameter combination and repeated three times to obtain a standard deviation of less than 1 %.

Table 7.2: Radionuclide activity corresponding to 1 x 10^8 events.

Radionuclides	Decay constant, λ (s^{-1})	Corresponding activity, A (Bq)
^{90}Y	3.00E-06	300.5
^{153}Sm	4.16E-06	415.7
^{166}Ho	7.18E-06	718.4
^{177}Lu	1.21E-06	120.6
^{188}Re	1.13E-05	1132.6

The mean energy (MeV) deposited within each compartment/organ was converted to joules, J and divided by the mass to obtain the absorbed dose (Gy) to each compartment/organ. The dose per activity ($Gy.GBq^{-1}$) of the tumour (obtained by

dividing tumour dose with activities in **Table 7.2**) for each scenario was used to estimate the total administered activity of each radionuclide required to achieve tumouricidal dose of 120 Gy. The absorbed doses for all compartments/organs were normalised to the tumour absorbed dose to obtain the corresponding normalised absorbed dose for each compartment/organ. The normalised value was used to obtain the corresponding absorbed dose to each organ when 120 Gy of tumour dose is being delivered. Using the normalised absorbed doses, the maximum limit allowed for treatment for each radionuclide was estimated by targeting the highest possible dose to the tumour without exceeding the maximum absorbed dose to normal liver and lungs of 70 and 30 Gy, respectively.

7.4 Results

7.4.1 Comparison of Administered Activity

The administered activities required to achieve 120 Gy of tumour dose for all tumour involvements (with 10 % LS and T/N of 5) and radionuclides are shown in **Table 7.3**. The conversion factor, when multiplied with ^{90}Y activities will result in the corresponding radionuclide activities required to achieve similar tumour dose. ^{153}Sm and ^{177}Lu require the highest and lowest activities, respectively, to achieve similar tumour dose as ^{90}Y.

Table 7.3: Total administered activity (GBq) required to achieve 120 Gy of tumour dose for 10 % lung shunting (LS) and tumour-to-normal liver uptake ratio (T/N) of 5. TI: tumour involvement.

TI	Administered Activity (GBq)					Conversion Factor			
(%)	^{90}Y	^{153}Sm	^{166}Ho	^{177}Lu	^{188}Re	^{153}Sm	^{166}Ho	^{177}Lu	^{188}Re
10	1.46	6.49	4.58	3.40	6.42	4.45	3.14	2.33	4.40
30	2.24	10.06	7.06	5.30	9.85	4.49	3.15	2.37	4.40
50	3.03	13.63	9.56	7.20	13.33	4.50	3.16	2.38	4.40
70	3.82	17.20	12.07	9.09	16.81	4.50	3.16	2.38	4.40
Mean Conversion Factor						4.48 ± 0.03	3.15 ± 0.01	2.36 ± 0.02	4.40 ± 0.00

7.4.2 Absorbed Dose to Source Organs

7.4.2.1 Normal Liver Tissue

The normal liver absorbed dose for tumour involvements of 10, 30, 50 and 70 % (with 10 % LS and T/N of 5), for ^{90}Y, ^{153}Sm, ^{166}Ho, ^{177}Lu and ^{188}Re when tumour dose of 120 Gy is delivered are shown in **Figure 7.1**. When the partition model is being used for ^{90}Y, the estimated normal liver absorbed dose is 24 Gy (for 120 Gy of tumour dose), as marked by the red dotted lines. As highlighted in Chapter 5, the actual normal liver dose (simulated by Geant4) was higher and increased with larger tumour involvement, which are also shown in **Figure 7.1**. This effect is also seen in the other radionuclides with ^{177}Lu recorded the lowest normal liver dose as compared to the others. Following ^{177}Lu, in the ascending order, ^{153}Sm, ^{166}Ho, ^{188}Re and ^{90}Y delivered increasing normal liver dose.

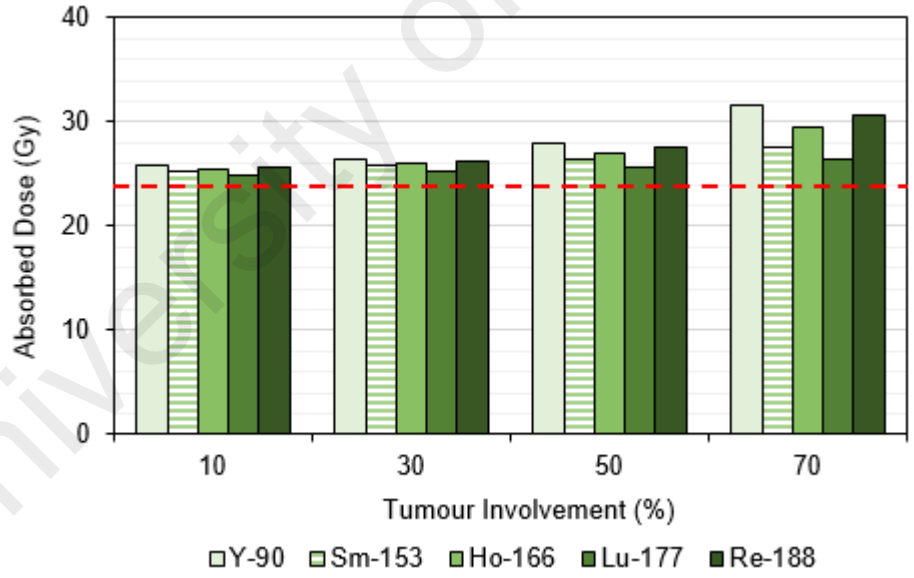

Figure 7.1: Absorbed dose to normal liver for all radionuclides and tumour involvements (for 10 % lung shunting (LS) and tumour-to-normal liver uptake ratio (T/N) of 5), when 120 Gy is delivered to the tumour. Red dotted line indicated the normal liver dose of 24 Gy as estimated by the partition model (PM).

7.4.2.2 Lungs

The absorbed dose to both lungs for tumour involvements of 10, 30, 50 and 70 % (with 10 % LS and T/N of 5), for ^{90}Y, ^{153}Sm, ^{166}Ho, ^{177}Lu and ^{188}Re when tumour dose of 120 Gy is delivered are shown in **Figure 7.2**. In general, the absorbed dose to lungs increase with increase tumour involvement. As shown in the figure, the right lung received slightly higher absorbed dose as compared to the left lung. Amongst the radionuclides, ^{177}Lu contribute to the highest lung dose, followed by ^{153}Sm, ^{166}Ho, ^{188}Re and ^{90}Y.

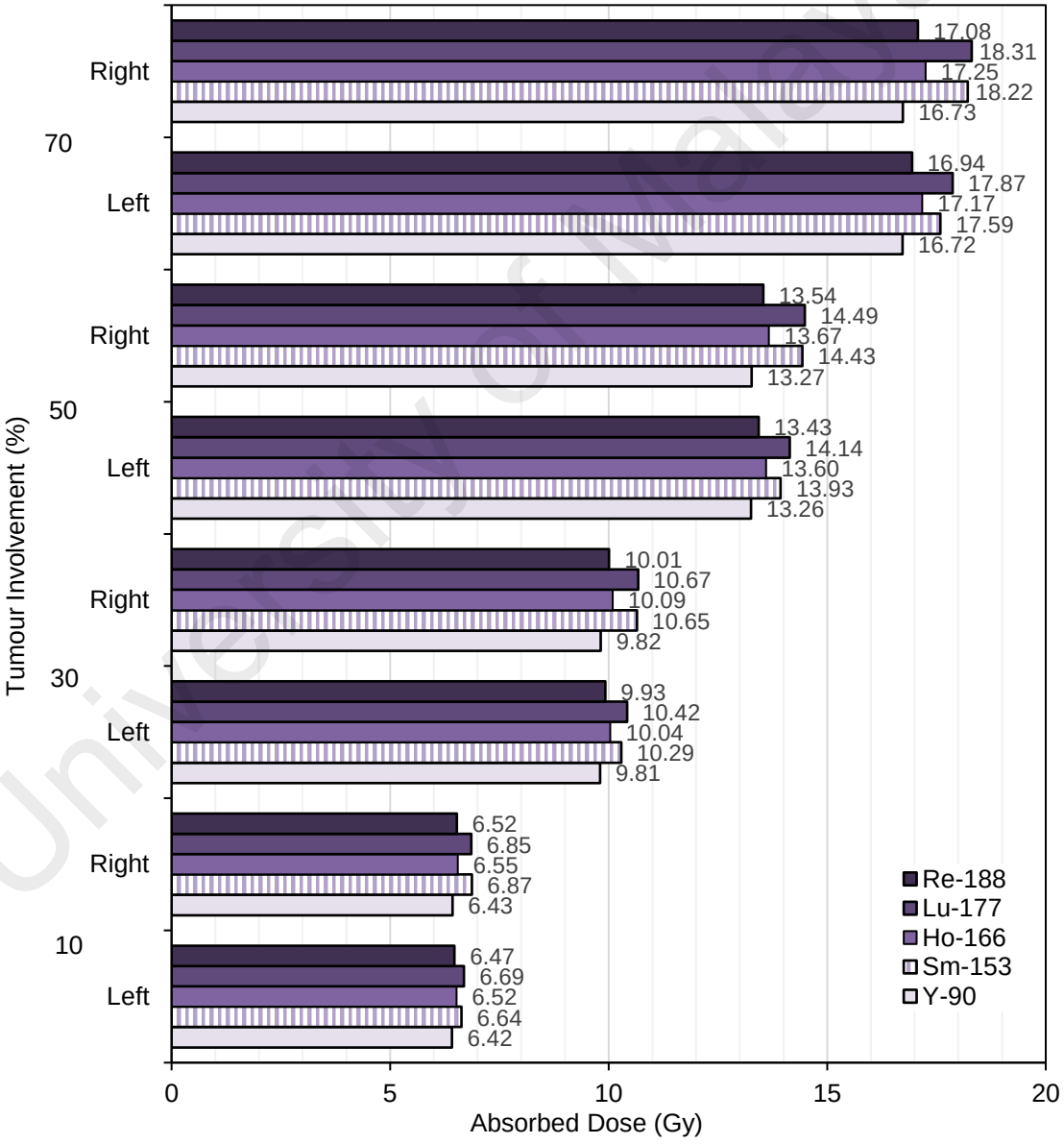

Figure 7.2: Absorbed dose to left and right lungs for all radionuclides and tumour involvements (for 10 % lung shunting (LS) and tumour-to-normal liver uptake ratio (T/N) of 5), when 120 Gy is delivered to the tumour.

7.4.3 Absorbed Dose to Other Organs

The absorbed dose to the other organs for tumour involvements of 10, 30, 50 and 70 % (with 10 % LS and T/N of 5), for ^{90}Y, ^{153}Sm, ^{166}Ho, ^{177}Lu and ^{188}Re when tumour dose of 120 Gy is delivered are shown in **Figure 7.3**. In general, the absorbed dose to these organs increase with increase tumour involvement. As shown in the figure, organs located at the right side of the phantom received higher absorbed doses, with right adrenal, right kidney and pancreas receiving the highest doses. For organs located close to the liver, ^{153}Sm contribute to the highest doses, followed by ^{177}Lu, ^{166}Ho, ^{188}Re and ^{90}Y. However, it can be observed that as the locations of the organs went further from the liver, absorbed doses from ^{177}Lu were higher than ^{153}Sm, followed by the other radionuclides. Although ^{153}Sm and ^{177}Lu obviously contribute to the highest organs doses than the other radionuclides, all organ doses were still far below 1 Gy.

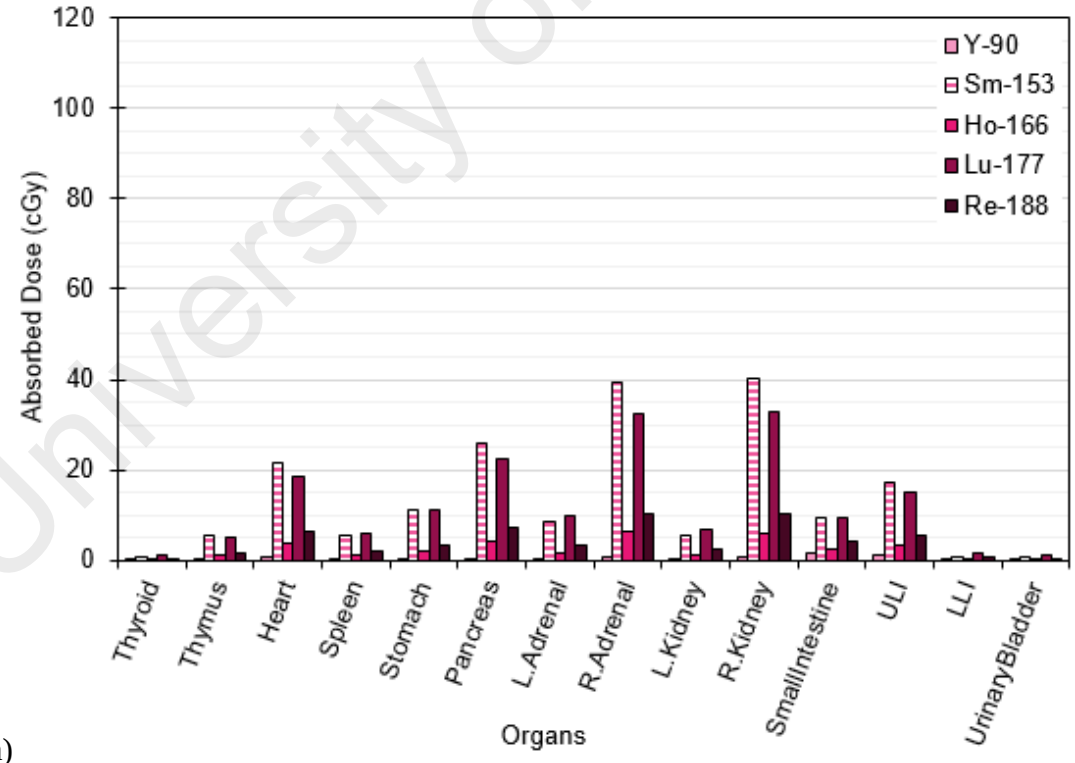

(a)

Figure 7.3: Absorbed dose to other organs for all radionuclides and tumour involvements of (a) 10, (b) 30, (c) 50, and (d) 70 (all for 10 % lung shunting (LS) and tumour-to-normal liver uptake ratio (T/N) of 5), when 120 Gy is delivered to the tumour. ULI: upper large intestine, LLI: lower large intestine.

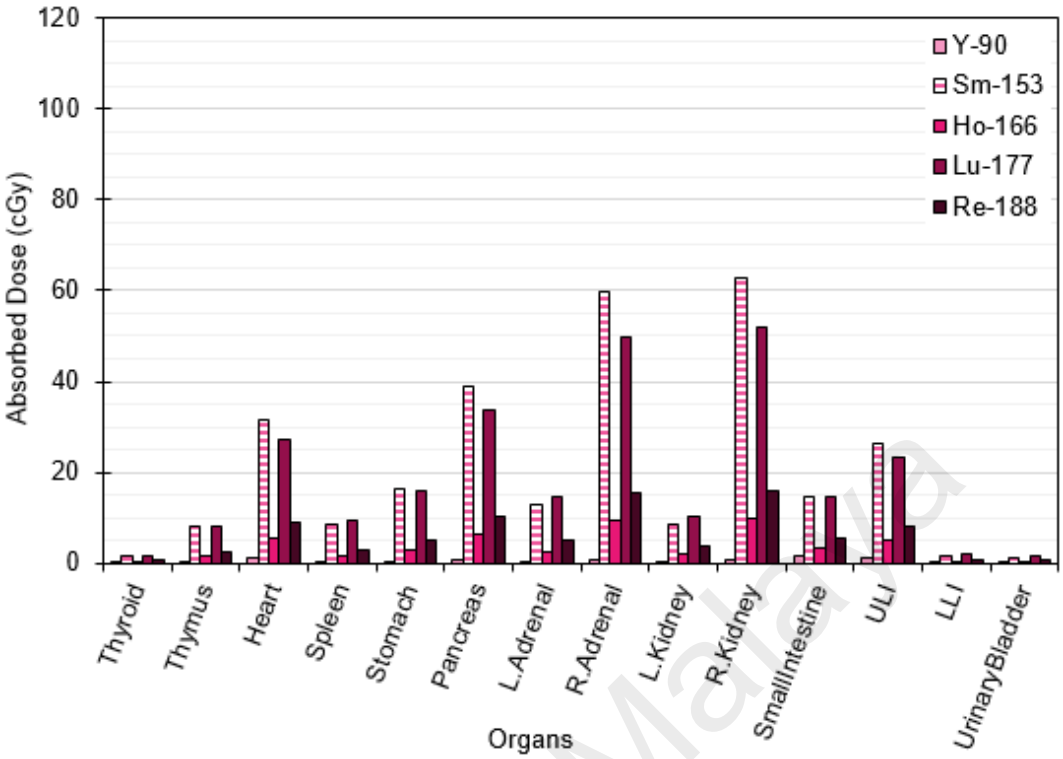

(b)

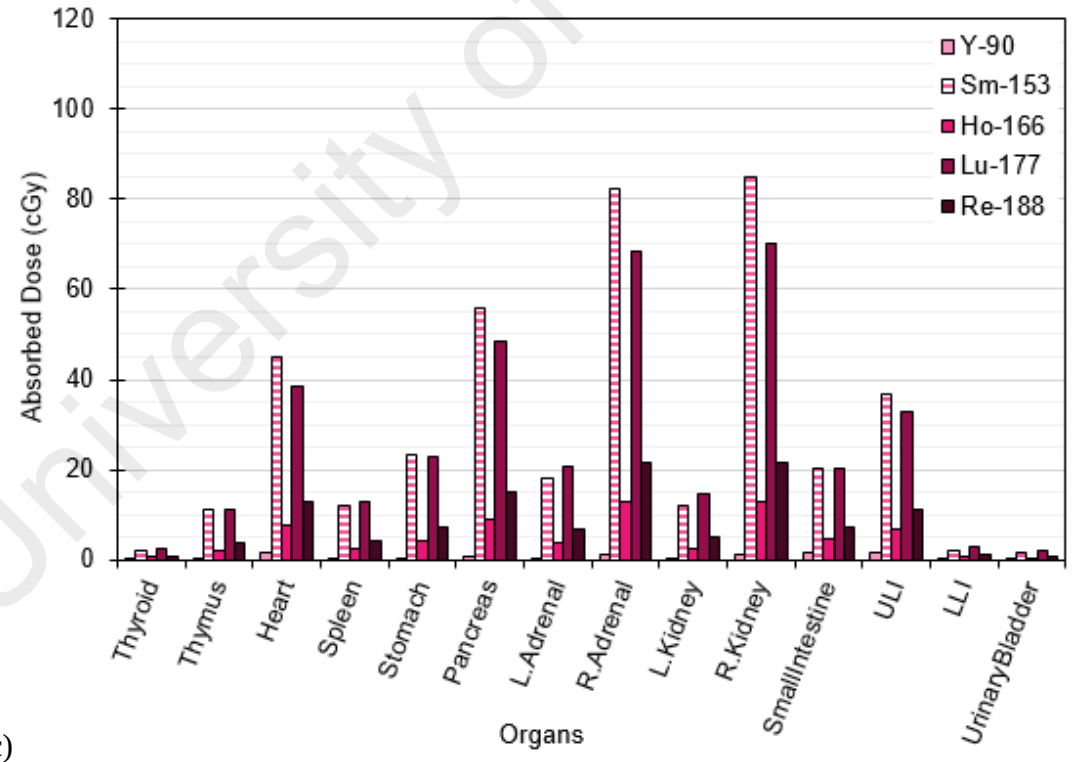

(c)

Figure 7.3: Continued.

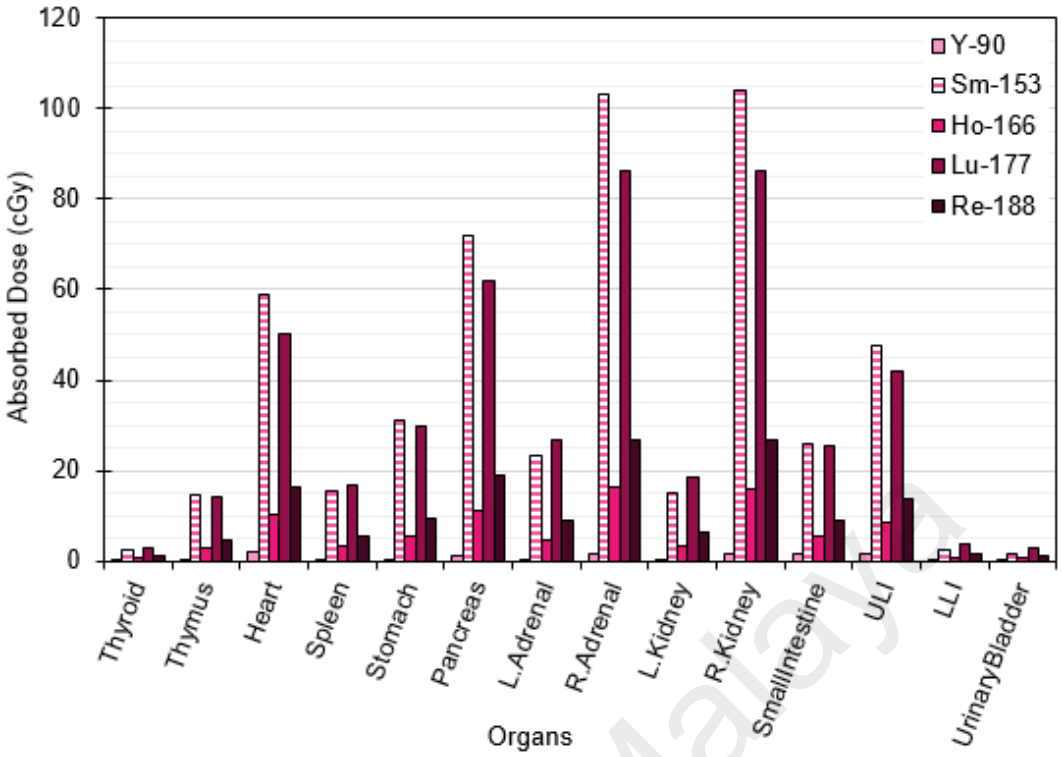

(d)

Figure 7.3: Continued.

7.4.4 Absorbed Dose to Male and Female Organs

The absorbed dose to both male and female gonads, breasts and uterus for tumour involvements of 10, 30, 50 and 70 % (with 10 % LS and T/N of 5), for all radionuclides when tumour dose of 120 Gy is delivered are shown in **Figure 7.4**. In general, the absorbed doses to these organs increase with increased tumour involvement. Again, the organs located at the right side of the phantom received higher absorbed doses. For breasts, ^{153}Sm contribute to the highest doses, followed by ^{177}Lu, ^{166}Ho, ^{188}Re and ^{90}Y. However, for ovaries, testicles and uterus, the absorbed doses from ^{177}Lu were higher than ^{153}Sm, followed by the other radionuclides. All doses to these organs were still far below 1 Gy.

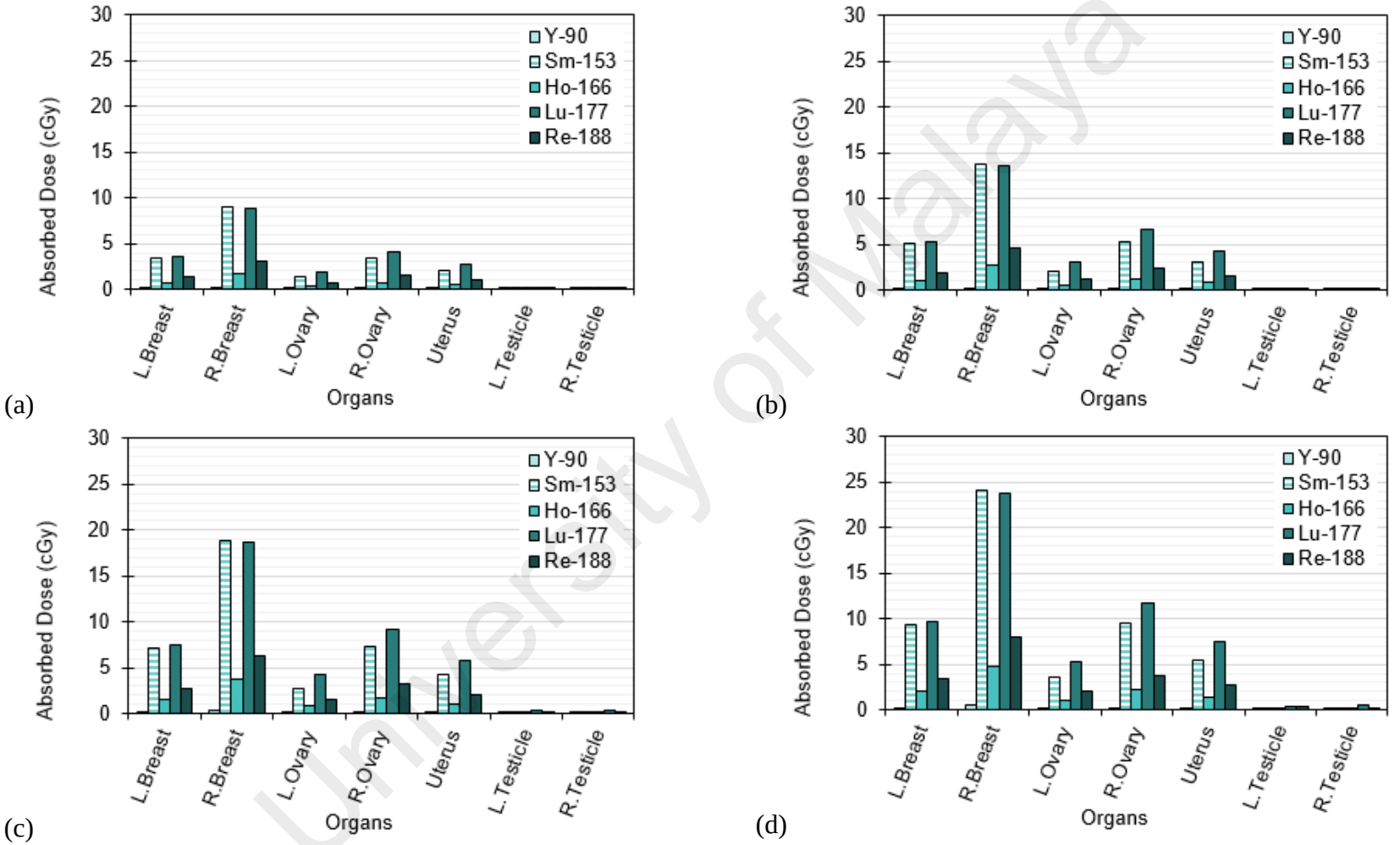

Figure 7.4: Absorbed dose to male and female organs for all radionuclides and tumour involvements of (a) 10, (b) 30, (c) 50, and (d) 70 (all for 10 % lung shunting (LS) and tumour-to-normal liver uptake ratio (T/N) of 5), when 120 Gy is delivered to the tumour.

7.4.5 Maximum Limit for Treatment

The maximum tumour dose allowed to be delivered without exceeding either 70 Gy to normal liver or 30 Gy to lungs for all radionuclides with tumour involvements of 10, 30, 50 and 70 % (all for 10 % LS and T/N of 5), are shown in **Table 7.4**.

Table 7.4: Estimated maximum absorbed dose allowed for treatment for all tumour involvements (TI) and radionuclides (for 10 % lung shunting (LS) and tumour-to-normal liver uptake ratio (T/N) of 5). A: activity.

TI (%)	Radionuclide	A (GBq)	Absorbed dose (Gy)			
			Tumour	Normal Liver	Left Lung	Right Lung
10	^{90}Y	4.0	324.7	**70.0**	17.4	17.4
	^{153}Sm	18.0	332.1	**70.0**	18.4	19.0
	^{166}Ho	12.6	330.9	**70.0**	18.0	18.1
	^{177}Lu	9.6	337.8	**70.0**	18.8	19.3
	^{188}Re	17.5	327.0	**70.0**	17.6	17.8
30	^{90}Y	5.9	318.4	**70.0**	26.0	26.1
	^{153}Sm	27.3	325.2	**70.0**	27.9	28.9
	^{166}Ho	19.0	323.7	**70.0**	27.1	27.2
	^{177}Lu	14.7	332.6	**70.0**	28.9	29.6
	^{188}Re	26.3	320.5	**70.0**	26.5	26.7
50	^{90}Y	6.8	271.3	63.3	30.0	**30.0**
	^{153}Sm	28.4	249.8	55.2	29.0	**30.0**
	^{166}Ho	21.0	263.4	59.1	29.9	**30.0**
	^{177}Lu	14.9	248.5	53.3	29.3	**30.0**
	^{188}Re	29.5	265.9	61.1	29.8	**30.0**
70	^{90}Y	6.8	215.2	56.9	30.0	**30.0**
	^{153}Sm	28.4	197.9	45.4	29.0	**30.0**
	^{166}Ho	21.0	208.7	51.4	29.9	**30.0**
	^{177}Lu	14.9	196.7	43.3	29.3	**30.0**
	^{188}Re	29.5	210.8	53.9	29.8	**30.0**

For all radionuclides, lower tumour involvement (10 and 30 %) were able to receive higher tumour dose, with both limited by the maximum dose to the normal liver of 70 Gy. For larger tumour involvement (50 and 70 %), the tumour doses were limited by the maximum dose to the right lung of 30 Gy, hence the tumour was only able to receive a smaller dose. For tumour involvements of 10 and 30 %, ^{177}Lu was able to deliver the highest tumour doses, followed by ^{153}Sm, ^{166}Ho, ^{188}Re and ^{90}Y. However, for larger tumour involvement, ^{90}Y was able to deliver the highest tumour dose, followed by ^{188}Re, ^{166}Ho, ^{153}Sm and ^{177}Lu, which were the opposite of the lower tumour involvement.

7.5 Discussions

^{90}Y-microspheres have been widely used in TARE of HCC. However since ^{90}Y decays almost fully via beta emission, imaging of the *in vivo* distribution of the microparticles following the treatment is rather difficult. Hence, various radionuclides have been suggested as alternative to ^{90}Y, which are able to possess both therapeutic beta alongside gamma radiation for *in vivo* imaging. These radionuclides include ^{153}Sm, ^{166}Ho, ^{177}Lu and ^{188}Re. As discussed earlier in Chapter 3 and 4, only ^{153}Sm, ^{166}Ho, and ^{177}Lu are ideal to be produced via neutron activation method, while ^{90}Y and ^{188}Re are more appropriately produced in Strontium-90 (^{90}Sr)/^{90}Y and tungsten-188 (^{188}W)/^{188}Re generators, respectively. Neutron activation method allows easier and cheaper radionuclide production and hence, is more advantageous than generators. Thus ^{153}Sm, ^{166}Ho, and ^{177}Lu are superior from the production perspective as compared to ^{90}Y and ^{188}Re. Based on **Table 7.1**, the beta energy of ^{166}Ho and ^{188}Re provide highest maximum beta energies, close to that of ^{90}Y. However, the gamma energy of ^{166}Ho is relatively low thus, high resolution images might still not able to be achieved. ^{177}Lu, which possesses the highest gamma energy is beneficial for imaging however, its beta energy is very low. The thermal

neutron activation cross-section of lutetium-176 (^{176}Lu) has the highest value of 2050 barn, while ^{165}Ho possesses the lowest cross-section value of only 61.5 barn. Thus, the production of ^{177}Lu is relatively much easier than ^{166}Ho and ^{153}Sm. For treatment practicality, ^{188}Re and ^{166}Ho are more difficult to handle due to their half-lives of about 1 day or less. This requires the treatment to be carried out quickly following the supply of the radionuclides, to avoid the fast radionuclide decay from affecting the treatment dosimetry. On the contrary, ^{177}Lu with the longest half-life of 6.65 days, will require longer hospital stays hence, contributing to added cost.

Between these radionuclides, ^{153}Sm and ^{188}Re require the highest activities to achieve 120 Gy of tumour dose, with approximately 4.44 times more activities that that of ^{90}Y. This is because ^{153}Sm needs to compensate for having lower beta energy and shorter half-life than ^{90}Y, while ^{188}Re needs to compensate for its very short half-life, even though its beta energy is the closest to the energy of ^{90}Y. ^{177}Lu requires the lowest activities with about 2.36 times higher than ^{90}Y. Although the beta energy of ^{177}Lu is relatively low, due to its long half-life, ^{177}Lu were able to deliver the absorbed dose with closest activities to that of ^{90}Y.

Between all the five radionuclides, ^{177}Lu delivers the lowest normal liver dose hence is the most beneficial for normal tissue sparing, followed by ^{153}Sm, ^{166}Ho, ^{188}Re and lastly, ^{90}Y. This was affected by the energy of the beta decay, with ^{177}Lu having the lowest beta energy with about 4.6 times lower than ^{90}Y. As shown in **Figure 7.1**, based on the partition model estimation of normal liver dose of 24 Gy, ^{90}Y shows the largest amount of escaped beta particles which increases with larger tumour involvement as compared to the other radionuclides, due to it having the most energetic beta radiation. For absorbed dose to the lungs, ^{177}Lu delivered the highest lung doses, followed slightly by ^{153}Sm as a

result of added dose from the higher energies of gamma radiation as compared to the other three radionuclides.

For the other organs located at the proximity of the liver i.e. right adrenal and kidney, pancreas, heart, and ULI, ^{153}Sm contributed to the highest absorbed doses, even though the gamma energy of ^{153}Sm is lower than ^{177}Lu. This can be explained as a result of contribution of dose from escaped beta particles from the liver and also from the consequent bremsstrahlung radiation, produced from the interactions of beta particles with the soft tissues. Since beta energy of ^{153}Sm is higher, thus this contribute to larger dose as compared to ^{177}Lu. On the other hand, for organs located further from the liver i.e. spleen, left adrenal and kidney, LLI, bladder and thyroid, the absorbed dose from ^{177}Lu were observed to be higher, as a result of higher gamma energy thus, able to penetrate further and deposit larger dose as compared to ^{153}Sm. The absorbed dose to the other organs from ^{90}Y was almost negligible, while doses from ^{188}Re and ^{166}Ho were relatively low and for some organs, were almost unnoticeable as compared to ^{177}Lu and ^{153}Sm. For the male and female organs, the absorbed doses to right breast were much higher for ^{153}Sm while for left breast, ^{177}Lu gave slightly higher doses, due to the effect of distance from the liver as explained earlier. This can also be observed in the doses to both ovaries, uterus and both testicles, with ^{177}Lu contributed to the highest absorbed doses. The absorbed dose to the testicles were almost negligible for all radionuclides, as a result of the longer distance from the liver.

For tumour involvements of 10 and 30 %, the tumour was able to receive higher dose due to relatively lower activity that goes to the lungs, as compared to the larger tumour involvement. ^{177}Lu was able to deliver the highest dose for lower tumour involvement amongst other radionuclides because, it possesses the lowest beta energy which consequently results in lesser amount of beta particles escaped from the tumour, hence

when the normal liver limit was reached, the tumour was able to receive a higher dose. For larger tumour involvement, ^{90}Y was able to deliver the highest tumour dose due to the absence of gamma radiation, hence a larger tumour dose can be achieved without exceeding the maximum dose limit to the lungs.

7.6 Conclusion

^{153}Sm, ^{166}Ho, ^{177}Lu and ^{188}Re have the potential to be used as substitute to ^{90}Y in TARE of HCC. Although each radionuclide has its own benefits and drawbacks in terms of the physical characteristics and the production methods, they are still able to deliver complementary absorbed dose to tumour with acceptable normal liver and lung doses, and other organ doses which were far from exceeding 1 Gy. However, significantly larger amount of administered activities will be needed for these radionuclides to deliver the same dose to that of ^{90}Y, which will require more effort in the shielding of the sources. Nonetheless, this opens up to a wider option for the treatment of HCC, with improved availability and thus the treatment costs could be further reduced.

CHAPTER 8: CONCLUSION AND FUTURE WORK

In this thesis, the potential theranostic application of samarium-153 (^{153}Sm) as an alternative radionuclide to yttrium-90 (^{90}Y) in transarterial radioembolization (TARE) of hepatocellular carcinoma (HCC) has been explored. ^{153}Sm-labelled microparticles has been produced, thoroughly characterised and the dosimetric aspects related to its application in TARE of HCC has been systematically investigated.

8.1 Production of ^{153}Sm-Labelled Microparticles

8.1.1 Conclusion

In Chapter 3, radioactive ^{153}Sm has been produced from the neutron activation of samarium-152 (^{152}Sm) in the TRIGA PUSPATI Nuclear Reactor, via ^{152}Sm(n,γ)^{153}Sm reaction. Two types of resin microparticles from commercially available options have been studied for their suitability as radioembolic agents in TARE of HCC. ^{152}Sm was labelled with each resin microparticle (20 – 40 μm) via ion exchange process of the resin with samarium chloride ($^{152}SmCl_3$) salt. The crucial properties of the resins have been studied which include, the suitability for neutron activation via gamma spectrometry; to ensure no radionuclide impurities produced following the process, and radiolabelling efficiency of the resins via prolong immersion in distilled water and human blood plasma over the course of 48 h. The Amberlite microparticles, which is a styrene-divinylbenzene (DVB) with sulphonic acid group resin type has been chosen as the ideal resin labelled with ^{153}Sm, for application in TARE of HCC. The microparticles did not result in any radionuclide impurities following neutron activation, and it also possesses excellent

labelling efficiency of >99 and 96% in distilled water and human blood plasma, respectively, as compared to the other resin type.

In Chapter 4, the chosen ^{153}Sm-labelled microparticles have been further characterised for its suitability for intra-arterial administration which includes, the analysis of chemical structures, surface morphology, elemental analysis, particle size distribution analysis, particle density measurements and suspension stability study. The microparticles show unaffected chemical structure by retaining the sulphonic group throughout the production stages. From the EDX analysis, the data supports the gamma spectrometry studies showing that the microparticles did not produce any radionuclide impurities following neutron activation. From the SEM, the microparticles were observed to be irregular in shape as a result of physical grinding, with increase smaller fragments following neutron activation, hence reducing the mean diameter from 32.6 ± 2.1 to 23.5 ± 2.3 μm. The microparticles produced have a density of 2.538 ± 0.012 g.cm^{-3}, close to that of SIR-Spheres®, resulting in low settling velocity thus avoiding the tendency for sedimentation during administration.

8.1.2 Limitations and Recommendations for Future Work

Due to the grinding process to reduce the microparticles to the desired size of 20 – 40 μm, the microparticles were not able to retain the spherical morphology they possess in the initial bead form. This consequently affects the mechanical strength of the microparticles which were observed by the increase of smaller fragments following neutron activation. Also, the sieving of the microparticles requires extensive time due to the irregular microparticles, which results in only a relatively smaller portion of microparticles able to be collected in the desired range during this study. These can be overcome with the production of an improved microparticles of the same type, but with spherical morphology. An effort to overcome this issue has been carried out by

spheroidising the microparticles via melt-spraying method, however the material was shown to be unsuitable for the process.

Despite the excellent properties the microparticles have to offer, we did not manage to further advance this study to a pre-clinical stage for animal studies, as a result of the microparticles morphology which may affect the administration of the microparticles during the treatment. The important aspects to be considered in the production of the ^{153}Sm-microparticles have been highlighted in this thesis, apart for the spherical morphology which were not able to be achieved. At the moment we are actively looking for methods to produce the microparticles from raw materials with multiple research collaborations. An alternative to produce the polystyrene microparticles are currently underway, which will then be proceed with radiolabelling, neutron activation, and other characterisation process (which has been shown in this study) for its suitability in TARE of HCC.

8.2 Related Dosimetric Studies

8.2.1 Conclusion

In Chapter 5, the accuracy of the dosimetry model commonly used in TARE with ^{90}Y-microspheres was systematically investigated. The significance of this study was to investigate how the assumption for the exclusion of cross-fire irradiation made in this model affect the absorbed dose estimations. The absorbed doses to tumour, normal liver and lungs for various cases with combinations of different tumour involvements, lung shunting (LS) and tumour-to-normal liver uptake ratio (T/N) were estimated via the partition model (PM) estimation, and the results were compared with the dose estimated via Geometry and Tracking 4 (Geant4) Monte Carlo (MC) simulations. From this study,

it was found that PM overestimated the absorbed dose to tumour by up to 8 % with larger overestimation for smaller tumour involvement. Also, the model constantly overestimated the absorbed dose to lungs by 12 %. For the absorbed dose to normal liver tissue, it was found that PM underestimated the dose by 'surprisingly' up to -78 %, especially for larger tumour involvement. For both tumour and normal liver, the inaccuracy of PM was due to the exclusion of the cross-fire irradiation at the tumour-normal liver boundary. However for lungs, the inaccuracy was due to the derivation of the PM formula, which assumed the same material density and composition for both soft tissue and lungs. A corrected formula has been suggested for the estimation of the absorbed dose to lungs, and the cases with parameters which contribute to large inaccuracy by PM were highlighted, so it will be useful to know when the model is safe to be used.

In Chapter 6, the dosimetry of ^{153}Sm-microparticles for application in TARE was systematically assessed by simulating various treatment scenarios using Geant4 MC simulations. The absorbed dose to tumour was aimed to be 120 Gy, and the corresponding absorbed doses to normal liver, lungs, and other organs were recorded. Also, the maximum treatment scenarios allowed for treatment were determined by targeting the absorbed dose to normal liver or lungs to the maximum dose limit of 70 and 30 Gy, respectively. From the simulations, it was found that for ^{153}Sm to deliver similar tumour dose to that of ^{90}Y, the administered activities of ^{153}Sm need to be increased to about 4.51 times higher than ^{90}Y. The treatment with ^{153}Sm-microparticles were found to be limited only by the absorbed dose to the normal liver and lungs, as the absorbed dose to the other organs were found to be far below 1 Gy (with each organ dose to be less than 1 % as compared to the dose delivered to the tumour). From this study, the dosimetric data has been provided and compiled into an interactive spreadsheet for future use. Thus, from the systematic dosimetric assessment, TARE with ^{153}Sm-microparticles have the potential to

be the alternative to ^{90}Y as it was shown to be a safe option, able to deliver tumour dose similar to ^{90}Y without overdosing the normal tissues and other organs, with added advantage for gamma imaging.

Finally, in Chapter 7 the dosimetric comparison between five radionuclides intended for TARE of HCC were carried out via Geant4 MC simulations. These radionuclides include ^{90}Y, ^{153}Sm, holmium-166 (^{166}Ho), lutetium-177 (^{177}Lu) and rhenium-188 (^{188}Re). Different tumour involvements (10, 30, 50 and 70 %) with fixed LS (10 %) and T/N (5) were simulated for each radionuclide by targeting a tumour dose of 120 Gy. Amongst the radionuclides, ^{153}Sm requires the highest administered activities followed by ^{188}Re, ^{166}Ho, ^{177}Lu and ^{90}Y. For similar tumour dose, ^{177}Lu delivered the lowest dose to normal liver and highest dose to lungs, followed by ^{153}Sm, ^{166}Ho, ^{188}Re and ^{90}Y. For the absorbed dose to the other organs, ^{177}Lu and ^{153}Sm contributed to the highest doses, for organs located at the distal and proximal to the liver, respectively. ^{153}Sm, ^{166}Ho, ^{177}Lu and ^{188}Re have the potential to be used as substitute to ^{90}Y in TARE of HCC. Although each radionuclide has its own benefits and drawbacks in terms of the physical characteristics and the production methods, they are still able to deliver complementary absorbed dose to tumour with acceptable absorbed dose to normal liver and lungs, and doses to other organs which were far from exceeding 1 Gy. Thus, this opens up to a wider option for the treatment of HCC, with improved availability and thus the treatment costs can be largely reduced.

8.2.2 Limitations and Recommendations for Future Work

In Chapter 5, even though a spherical tumour model is ideal, it was limited to a maximum of only 18 % tumour involvement. This is because in order for the dose deposition to be recorded accurately, the tumour model needs to be confined within the liver volume without intersection between the boundaries. Thus, the trapezoidal model was chosen to represent the tumour up to 70 % tumour involvement. An alternative of

using multiple spheres to represent the tumour volume has been considered, however this will result in a complicated findings as the cross-fire irradiation between the tumour and normal liver is largely affected by the distance between each tumour, its location within the liver, and the size and numbers of the spherical tumours used (which corresponds to different surface area-to-volume ratios (SA/V)). Also, in our study the distribution of ^{90}Y within the source organs were assumed to be homogenous, which is not exactly true in real patients as a result of tumour higher vascularity as compared to normal tissues. Thus, for these purposes, patient specific dosimetry using CT images can be considered. Various studies involving the use of ^{90}Y-microspheres for patient specific dosimetry have been carried out. However, most of these did not take into account the tissue inhomogeneity correction, but only assumed the density and composition of all tissues to be equivalent to water. Future works incorporating heterogeneity in both source distribution and tissue density and composition should be carried out.

In Chapter 6, a dose calculation spreadsheet has been successfully built for ease in future clinical use. However, since the simulations were only carried out in a discrete manner, the spreadsheet will not be directly available for certain treatment scenarios. Future work to obtain a trend curve (connecting the values for each parameter) for every organ and scenario should be carried out. However this effort may be relatively complex as collectively hundreds scenarios could be derived as a result of combinations of different tumour involvements, LS and T/N. A recommendation would be to interpolate the absorbed dose between the discrete values, however the accuracy of this method needs to be validated. Following this improvement, the data could be compiled into a standalone graphic user interface (GUI) or a web application for wider availability.

In Chapter 7, the dosimetric comparison between five radionuclides has been carried out. Although all radionuclides were targeted to deliver tumour dose of 120 Gy, due to

different physical characteristics (i.e. half-lives and energies), the therapeutic effect of each radionuclide will be different, as a result of different dose rate. Since it is well known that higher dose rate will be more damaging due to the inability for the cells to be repaired, the radionuclides with lower dose rate e.g. ^{177}Lu may require a higher dose to deliver comparable therapeutic effect as compare to radionuclides with higher dose rate i.e. ^{188}Re. Hence, for future work, a radiobiological studies to address this issue should be carried out.

8.3 Overall Conclusion

The ^{153}Sm-Amberlite microparticles are easy to be labelled and the procedure does not involve unnecessary radiation exposure. They are able to withstand prolonged irradiation, at the same time possesses excellent labelling efficiency with strong and prolong retention of ^{153}Sm, no radioactive impurities following neutron activation, low settling velocity and stable in suspension, lower production cost than that of ^{90}Y SIR-Spheres®, and ability to deliver comparable tumour dose to ^{90}Y, without exceeding the maximum organ dose limit. Following improvements to the physical morphology of the microparticles, it has been shown that the treatment with ^{153}Sm-microparticles has the potential to be used as an alternative to ^{90}Y-microspheres, with added advantage of gamma radiation for imaging of activity distribution following TARE of HCC.

REFERENCES

Agostinelli, S., Allison, J., Amako, K., Apostolakis, J., Araujo, H., Arce, P., . . . Zschiesche, D. (2003). Geant4—a simulation toolkit. *Nuclear Instruments and Methods in Physics Research Section A: Accelerators, Spectrometers, Detectors and Associated Equipment, 506*(3), 250-303.

Allison, J., Amako, K., Apostolakis, J., Araujo, H., Dubois, P. A., Asai, M., . . . Yoshida, H. (2006). Geant4 developments and applications. *IEEE Transactions on Nuclear Science, 53*(1), 270-278.

American Cancer Society (2016a). How is liver cancer staged? Retrieved March 24th, 2016, from http://www.cancer.org/cancer/livercancer/detailedguide/liver-cancer-staging

American Cancer Society (2016b). Tumor ablation for liver cancer. Retrieved March 24th, 2016, from http://www.cancer.org/cancer/livercancer/detailedguide/liver-cancer-treating-tumor-ablation

American Joint Committee on Cancer (2002). *Comparison Guide: Cancer Staging Manual, Fifth Versus Sixth Edition*. New York: Springer-Verlag.

Anthony, P. P. (2001). Hepatocellular carcinoma: an overview. *Histopathology, 39*(2), 109-118.

Awang, M. B., Hardy, J. G., Davis, S. S., Wilding, I. R., & Parry, S. J. (1993). Radiolabelling of pharmaceutical dosage forms by neutron activation of Samarium-152. *Journal of Labelled Compounds and Radiopharmaceuticals, 33*(10), 941-948.

Battistoni, G., Cerutti, F., Fasso, A., Ferrari, A., Muraroi, S., Ranft, J., . . . Sala, P. R. (2007). The FLUKA code: description and benchmarking. *AIP Conference Proceedings, 896*, 31-49.

Berger, M. J. (1963). Monte Carlo calculation of the penetration and diffusion of fast charged particles. In B. Alder, S. Fernbach & M. Rotenberg (Eds.). *Methods in computational physics*, 1, pp. 135-215. New york: Academic.

Bielajew, A. F. (2013). History of Monte Carlo. In J. Seco & F. Verhaegen (Eds.). *Monte Carlo Techniques in Radiation Therapy*, pp. 342. Boca Raton, FL: Taylor & Francis.

Bismuth, H., & Chiche, L. (1993). Comparison of hepatic resection and transplantation in the treatment of liver cancer. *Seminars in Surgical Oncology, 9*(4), 341-345.

Bouchet, L. G., Bolch, W. E., Blanco, H. P., Rajon, D. A., Clairand, I., Sgouros, G., & Wessels, B. W. (2003). MIRD Pamphlet No. 19: absorbed fractions and radionuclide S values for six age-dependent multi-region models of the kidney. *Journal of Nuclear Medicine, 44*, 1113-1147.

Bouchet, L. G., Bolch, W. E., Weber, D. A., Atkins, H. L., & Poston, J. W., Sr. (1999). MIRD Pamphlet No. 15: Radionuclide S values in a revised dosimetric model of the adult head and brain. *Journal of Nuclear Medicine, 40*(3), 62S-101S.

Brown, F. B. (2003). *MCNP - A general Monte Carlo N-particle transport code.* Los Alamos, NM: Los Alamos National Laboratory.

Bruix, J., Reig, M., & Sherman, M. (2016). Evidence-based diagnosis, staging, and treatment of patients with hepatocellular carcinoma. *Gastroenterology, 150*(4), 835-853.

Bruix, J., Sherman, M., Llovet, J. M., Beaugrand, M., Lencioni, R., Burroughs, A. K., . . . Rodes, J. (2001). Clinical management of hepatocellular carcinoma. Conclusions of the Barcelona-2000 EASL Conference. *Journal of Hepatology, 35(3),* 421-430.

BTG International, L. (2013). About TheraSphere® Retrieved April 26th, 2015, from http://www.therasphere.com/

Campbell, A. M., Bailey, I. H., & Burton, M. A. (2000). Analysis of the distribution of intra-arterial microspheres in human liver following hepatic yttrium-90 microsphere therapy. *Physics in Medicine and Biology, 45*(4), 1023-1033.

Campbell, A. M., Bailey, I. H., & Burton, M. A. (2001). Tumour dosimetry in human liver following hepatic yttrium-90 microsphere therapy. *Physics in Medicine and Biology, 46*(2), 487-498.

Canadian Cancer Society (2016). Anatomy and physiology of the liver. Retrieved June 12th, 2016, from http://www.cancer.ca/en/cancer-information/cancer-type/liver/anatomy-and-physiology/?region=on

Cancer Research UK (2016). More about the stages of primary liver cancer Retrieved June 19th, 2016, from http://www.cancerresearchuk.org/about-cancer/type/liver-cancer/treatment/more-about-the-stages-of-primary-liver-cancer#child

Caon, M. (2004). Voxel-based computational models of real human anatomy: a review. *Radiation and Environmental Biophysics, 42*(4), 229-235.

Cassola, V. F., Lima, V. J., Kramer, R., & Khoury, H. J. (2010). FASH and MASH: female and male adult human phantoms based on polygon mesh surfaces: I. Development of the anatomy. *Physics in Medicine and Biology, 55*(1), 133-162.

Chauvie, S., Guatelli, S., Ivanchenko, V., Longo, F., Mantero, A., Mascialino, B., . . . Tnndade, A. (2004). Geant4 low energy electromagnetic physics. Paper presented at the *IEEE Nuclear Science Symposium,* 16-22 Oct. 2004.

Chen, J. H., Chai, J. W., Huang, C. L., Hung, H. C., Shen, W. C., & Lee, S. K. (1999). Proximal arterioportal shunting associated with hepatocellular carcinoma: features revealed by dynamic helical CT. *American Journal of Roentgenology, 172*(2), 403-407.

Coldwell, D. M., Kennedy, A. S., & Nutting, C. W. (2007). Use of yttrium-90 microspheres in the treatment of unresectable hepatic metastases from breast

cancer. *International Journal of Radiation Oncology*Biology*Physics, 69*(3), 800-804.

Cristy, M., & Eckerman, K. F. (1987). Specific absorbed fractions of energy at various ages for internal photon sources. *ORNL/TM-8381. Oak Ridge, TN: Oak Ridge National Laboratory.*

Dancey, J. E., Shepherd, F. A., Paul, K., Sniderman, K. W., Houle, S., Gabrys, J., . . . Goin, J. E. (2000). Treatment of nonresectable hepatocellular carcinoma with intrahepatic 90Y-microspheres. *Journal of Nuclear Medicine, 41*(10), 1673-1681.

Das, U. (2002). A radical approach to cancer. *Medical Science Monitor, 8*(4), RA79-92.

DeSilva, F. J. (1999). *Essentials of Ion Exchange.* Paper presented at the 25th Annual Water Quality Association Conference.

Deutsch, E., & Huguet, F. (2005). Perspectives in biological modulation of radiotherapy. *Bulletin du Cancer, 92*(1), 90-96.

Dezarn, W. A., Cessna, J. T., DeWerd, L. A., Feng, W., Gates, V. L., Halama, J., . . . American Association of Physicists in Medicine. (2011). Recommendations of the American Association of Physicists in Medicine on dosimetry, imaging, and quality assurance procedures for 90Y microsphere brachytherapy in the treatment of hepatic malignancies. *Medical Physics, 38*(8), 4824-4845.

Dow (2015). Dow water and process solutions. Products. AMBERLITE™ IR120 H Retrieved April 28th, 2015, from http://www.dowwaterandprocess.com/en/Products/A/AMBERLITE_IR120_H

Dubois, D., & Dubois, E. (1916). A formula to estimate the approximate surface area if height and weight be known. *Archives of Internal Medicine, 17,* 863-871.

Edwards, A. A., & Lloyd, D. C. (1998). Risks from ionising radiation: deterministic effects. *Journal of Radiological Protection, 18*(3), 175-183.

Elder, D. P. (2005). Pharmaceutical Applications of Ion-Exchange Resins. *Journal of Chemical Education, 82*(4), 575.

Emsley, J. (2001). *Nature's building blocks: an A-Z guide to the elements.* Cambridge, UK.: Oxford University Press Inc.

Farah, J., Broggio, D., & Franck, D. (2010). Creation and use of adjustable 3D phantoms: application for the lung monitoring of female workers. *Health Physics, 99,* 649-661.

FDA, United States Food and Drug Administration (2002). Medical Devices. Products and Medical Procedures. Device Approvals and Clearance. *Recently-Approved Devices.* Retrieved April 26th, 2015, from http://www.fda.gov/MedicalDevices/ProductsandMedicalProcedures/DeviceApprovalsandClearances/Recently-ApprovedDevices/ucm083605.htm

Ferlay, J., Soerjomataram, I., Dikshit, R., Eser, S., Mathers, C., Rebelo, M., . . . Bray, F. (2015). Cancer incidence and mortality worldwide: sources, methods and major patterns in GLOBOCAN 2012. *International Journal of Cancer, 136(5),* E359-E386.

Fisher, H. L. J., & Snyder, W. S. (1966). Variation of dose delivered by 137Cs as a function of body size from infancy to adulthood. *Health Physics Division Annual Progress Report for Period Ending July 31, 1966.* pp. 221-228. Oak Ridge, TN: Oak Ridge National Laboratory.

Fisher, H. L. J., & Snyder, W. S. (1967). Distribution of dose in the body from a source of gamma rays distributed uniformly in an organ. *Health Physics Division Annual Progress Report for Period Ending July 31, 1967.* pp. 257. Oak Ridge, TN: Oak Ridge National Laboratory.

Flamen, P., Vanderlinden, B., Delatte, P., Ghanem, G., Ameye, L., Van Den Eynde, M., & Hendlisz, A. (2008). Multimodality imaging can predict the metabolic response of unresectable colorectal liver metastases to radioembolization therapy with Yttrium-90 labeled resin microspheres. *Physics in Medicine and Biology, 53*(22), 6591-6603.

Forner, A., Llovet, J. M., & Bruix, J. (2012). Hepatocellular carcinoma. *The Lancet, 379*(9822), 1245-1255.

Fox, R. A., Klemp, P. F., Egan, G., Mina, L. L., Burton, M. A., & Gray, B. N. (1991). Dose distribution following selective internal radiation therapy. *International Journal of Radiation Oncology*Biology*Physics, 21*(2), 463-467.

Furhang, E. E., Sgouros, G., & Chui, C. S. (1996). Radionuclide photon dose kernels for internal emitter dosimetry. *Medical Physics, 23*(5), 759-764.

Garin, E., Rolland, Y., Laffont, S., & Edeline, J. (2015). Clinical impact of Tc-MAA SPECT/CT-based dosimetry in the radioembolization of liver malignancies with Y-loaded microspheres. *European Journal of Nuclear Medicine and Molecular Imaging*.

Goddu, S. M., Howell, R. W., & Rao, D. V. (1994). Cellular dosimetry: absorbed fractions for monoenergetic electron and alpha particle sources and S-values for radionuclides uniformly distributed in different cell compartments. *Journal of Nuclear Medicine, 35*(2), 303-316.

Goin, J. E., Dancey, J. E., Roberts, C. A., Sickles, C. J., Leung, D. A., & Soulen, M. C. (2004). Comparison of post-embolization syndrome in the treatment of patients with unresectable hepatocellular carcinoma: trans-catheter arterial chemo-embolization versus yttrium-90 glass microspheres. *World Journal of Nuclear Medicine, 3*, 49-56.

Goin, J. E., Salem, R., Carr, B. I., Dancey, J. E., Soulen, M. C., Geschwind, J. F., . . . Thurston, K. (2005). Treatment of unresectable hepatocellular carcinoma with intrahepatic yttrium 90 microspheres: a risk-stratification analysis. *Journal of Vascular and Interventional Radiology, 16*(2 Pt 1), 195-203.

Gulec, S. A., Sztejnberg, M. L., Siegel, J. A., Jevremovic, T., & Stabin, M. (2010). Hepatic structural dosimetry in (90)Y microsphere treatment: a Monte Carlo modeling approach based on lobular microanatomy. *Journal of Nuclear Medicine, 51*(2), 301-310.

Gupta, T., Virmani, S., Neidt, T. M., Szolc-Kowalska, B., Sato, K. T., Ryu, R. K., . . . Larson, A. C. (2008). MR tracking of iron-labeled glass radioembolization microspheres during transcatheter delivery to rabbit VX2 liver tumors: feasibility study. *Radiology, 249(3)*, 845-854.

Hafeli, U. O., Casillas, S., Dietz, D. W., Pauer, G. J., Rybicki, L. A., Conzone, S. D., & Day, D. E. (1999). Hepatic tumor radioembolization in a rat model using radioactive rhenium (^{186}Re/^{188}Re) glass microspheres. *International Journal of Radiation Oncology*Biology*Physics, 44(1)*, 189-199.

Hafeli, U. O., Roberts, W. K., Pauer, G. J., Kraeft, S. K., & Macklis, R. M. (2001). Stability of biodegradable radioactive rhenium (Re-186 and Re-188) microspheres after neutron activation. *Applied Radiation Isotopes, 54*, 869-879.

Han, K. H., Kudo, M., Ye, S. L., Choi, J. Y., Poon, R. T. P., Seong, J., . . . Cheng, A. L. (2011). Asian consensus workshop report: expert consensus guideline for the management of intermediate and advanced hepatocellular carcinoma in Asia. *Oncology, 81*(Suppl. 1), 158-164.

Helfferich, F. G. (1964). *Ion Exchange*. McGraw-Hill Inc., USA.

Hilgard, P., Hamami, M., Fouly, A. E., Scherag, A., Muller, S., Ertle, J., . . . Antoch, G. (2010). Radioembolization with yttrium-90 glass microspheres in hepatocellular carcinoma: European experience on safety and long-term survival. *Hepatology, 52*(5), 1741-1749.

Ho, S., Lau, W. Y., Leung, T. W., Chan, M., Ngar, Y. K., Johnson, P. J., & Li, A. K. (1996). Partition model for estimating radiation doses from yttrium-90 microspheres in treating hepatic tumours. *European Journal of Nuclear Medicine, 23*(8), 947-952.

Ho, S., Lau, W. Y., Leung, T. W. T., Chan, M., Johnson, P. J., & Li, A. K. C. (1997). Clinical evaluation of the partition model for estimating radiation doses from yttrium-90 microspheres in the treatment of hepatic cancer. *European Journal of Nuclear Medicine, 24*(3), 293-298.

Hoefnagel, C. A. (1991). Radionuclide therapy revisited. *European Journal of Nuclear Medicine, 18*(6), 408-431.

Hruby, M., Skodova, M., Mackova, H., Skopal, J., Tomes, M., Kropacek, M., . . . Kucka, J. (2011). Lutetium-177 and Iodine-131 loaded chelating polymer microparticles intended for radioembolization of liver malignancies. *Reactive and Functional Polymers, 71(12)*, 1155-1159.

IAEA (1974). Handbook on nuclear activation cross-sections. *Technical Reports Series No. 156*. Vienna: International Atomic Energy Agency.

IAEA. (2015). Research Reactor Databases. Research Reactors Retrieved July 23rd, 2015, from http://nucleus.iaea.org/RRDB/RR/ReactorSearch.aspx?filter=0

Ibrahim, S. M., Mulcahy, M. F., Lewandowski, R. J., Sato, K. T., Ryu, R. K., Masterson, E. J., . . . Salem, R. (2008). Treatment of unresectable cholangiocarcinoma using yttrium-90 microspheres: results from a pilot study. *Cancer, 113*(8), 2119-2128.

ICRP. (1975). Publication 23: Report of the Task Group on Reference Man. New York: Pergamon Press.

ICRP. (2007). Publication 103: Recommendations of the International Commision on Radiological Protection. *Annals of the ICRP, 37*(2-4).

ICRP. (2009). Publication 110: Adult reference computational phantoms. *Annals of the ICRP, 39*(2).

ICRU. (1998). Fundamental quantities and units for ionizing radiation. Report No. 60. ICRU Publications: Bethesda.

ICRU. (2011). Fundamental quantities and units for ionizing radiation (revised). Report No. 85. *Journal of the ICRU, 11*(1).

Inarrairaegui, M., Pardo, F., Bilbao, J. I., Rotellar, F., Benito, A., D'Avola, D., . . . Sangro, B. (2012). Response to radioembolization with yttrium-90 resin microspheres may allow surgical treatment with curative intent and prolonged survival in previously unresectable hepatocellular carcinoma. *European Journal of Surgical Oncology, 38*(7), 594-601.

Kao, Y. H., Tan, E. H., Ng, C. E., & Goh, S. W. (2011). Clinical implications of the body surface area method versus partition model dosimetry for yttrium-90 radioembolization using resin microspheres: a technical review. *Annals of Nuclear Medicine, 25*(7), 455-461.

Kassis, A. I., & Adelstein, S. J. (2005). Radiobiologic principles in radionuclide therapy. *Journal of Nuclear Medicine, 46*(Suppl 1), 4S-12S.

Kennedy, A. S., Coldwell, D., Nutting, C., Murthy, R., Wertman, D. E. J., Loehr, S. P., . . . Sailer, S. (2006). Resin 90Y-microsphere brachytherapy for unresectable colorectal liver metastases: modern USA experience. *International Journal of Radiation Oncology*Biology*Physics, 65*(2), 412-425.

Kennedy, A. S., Nag, S., Salem, R., Murthy, R., McEwan, A. J., Nutting, C., . . . Coldwell, D. (2007). Recommendations for radioembolization of hepatic malignancies using yttrium-90 microsphere brachytherapy: a consensus panel report from the radioembolization brachytherapy oncology consortium. *International Journal of Radiation Oncology*Biology*Physics, 68*(1), 13-23.

Kennedy, A. S., Nutting, C., Coldwell, D., Gaiser, J., & Drachenberg, C. (2004). Pathologic response and microdosimetry of (90)Y microspheres in man: review of four explanted whole livers. *International Journal of Radiation Oncology*Biology*Physics, 60*(5), 1552-1563.

Kim, D. H., Chen, J., Omary, R. A., & Larson, A. C. (2015). MRI visible drug eluting magnetic microspheres for transcatheter intra-arterial delivery to liver tumors. *Theranostics, 5*(5), 477-488.

Koch, W., & Tatsch, K. (2008). Nuclear medicine procedures for treatment evaluation. In J. Bilbao & M. Reiser (Eds.). *Liver radioembolization with ^{90}Y microspheres.* pp. 75-91. Springer: Berlin Heidelberg.

Kolbert, K. S., Sgouros, G., Scott, A. M., Bronstein, J. E., Malane, R. A., Zhang, J., . . . Larson, S. M. (1997). Implementation and evaluation of patient-specific three-dimensional internal dosimetry. *Journal of Nuclear Medicine, 38*(2), 301-308.

Kooby, D. A., Egnatashvili, V., Srinivasan, S., Chamsuddin, A., Delman, K. A., Kauh, J., . . . Kim, H. S. (2010). Comparison of yttrium-90 radioembolization and transcatheter arterial chemoembolization for the treatment of unresectable hepatocellular carcinoma. *Journal of Vascular and Interventional Radiology, 21*(2), 224-230.

Koukourakis, M. I. (2001). Tumour angiogenesis and response to radiotherapy. *Anticancer Research, 21*(6B), 4285-4300.

Kramer, R., Zankl, M., Williams, G., & Drexler, G. (1982). The calculation of dose from external photon exposures using reference human phantoms and Monte Carlo methods: *Part I. The male (ADAM) and female (EVA) adult mathematical phantoms.* Neuherberg: Institut fuer Strahlenschutz, GSF-Forschungszentrum fuer Umwelt und Gesundheit.

Kwok, P. C.-H., Leung, K. C., Cheung, M. T., Lam, T. W., Szeto, L. T., Chou, S. Q.-H., . . . Law, C. K. (2014). Survival benefit of radioembolization for inoperable hepatocellular carcinoma using yttrium-90 microspheres. *Journal of Gastroenterology and Hepatology, 29*(11), 1897-1904.

Lau, W. Y., Ho, S., Leung, T. W., Chan, M., Ho, R., Johnson, P. J., & Li, A. K. (1998). Selective internal radiation therapy for nonresectable hepatocellular carcinoma with intraarterial infusion of 90yttrium microspheres. *International Journal of Radiation Oncology*Biology*Physics, 40*(3), 583-592.

Lau, W. Y., Kennedy, A. S., Kim, Y. H., Lai, H. K., Lee, R. C., Leung, T. W., . . . Wang, S. C. (2012). Patient selection and activity planning guide for selective internal radiotherapy with yttrium-90 resin microspheres. *International Journal of Radiation Oncology*Biology*Physics, 82*(1), 401-407.

Leyton, M. (2001). *A Generative Theory of Shape*. Berlin: Springer.

Liu, D. M., Salem, R., Bui, J. T., Courtney, A., Barakat, O., Sergie, Z., . . . Wong, C. Y. (2005). Angiographic considerations in patients undergoing liver-directed therapy. *Journal of Vascular and Interventional Radiology, 16*(7), 911-935.

LNHB, Laboratoire National Henri Becquerel (2014). Recommended data (by Z). Retrieved August 28th, 2014, from http://www.nucleide.org/DDEP_WG/DDEPdata_by_Z.htm

Mardirossian, G., Tagesson, M., Blanco, P., Bouchet, L. G., Stabin, M., Yoriyaz, H., . . . Brill, A. B. (1999). A new rectal model for dosimetry applications. *Journal of Nuclear Medicine, 40*(9), 1524-1531.

Mazzaferro, V., Regalia, E., Doci, R., Andreola, S., Pulvirenti, A., Bozzetti, F., . . . Gennari, L. (1996). Liver transplantation for the treatment of small hepatocellular carcinomas in patients with cirrhosis. The *New England Journal of Medicine, 334*(11), 693-699.

Meo, S. L., Cicoria, G., Montini, G., Bergamini, C., Campanella, F., Pancaldi, D., . . . Marengo, M. (2008). Radiation emission dose from patients administered 90Y-labelled radiopharmaceuticals: comparison of experimental measurements versus Monte Carlo simulation. *Nuclear Medicine Communications, 29*(12), 1100-1105.

Merck, K. (2015). Product information. 1.16890/ 1.16882 Fractogel® EMD SO_3^- (S), (M) pp. 1. Darmstadt, Germany.

Mohamed Takip, K. (2009). *Progress in the preparation of a decommissioning plan.* Paper presented at the Workshop on Research Reactor Decommisioning Activities: Cost Estimattes, March 30th - April 3rd, Manila, Philippines.

Morrison, E., Ham, J. M., Sasaki, A. W., Ruimy, R., Busch, A., McKenna, D., . . . Blum, M. (2013). Viral Hepatitis. *U.S. Department of Veteran Affairs.* Retrieved October 18th, 2013, from http://www.hepatitis.va.gov/patient/complications/transplant/listing-process.asp

Movva, S. (2013). Understanding Liver Cancer -- the Basics. *WebMD.com.* Retrieved October 15th, 2013, from http://www.webmd.com/cancer/understanding-liver-cancer-basic-information?page=2

Muller, J. H., & Rossier, P. H. (1951). A new method for the treatment of cancer of the lungs by means of artificial radioactivity: (Zn63 and Au198) first experimental and clinical studies. *Acta Radiologica, 35*(5-6), 449-468.

Mumper, R. J., Ryo, U. Y., & Jay, M. (1991). Neutron-activated Holmium-166-poly (L-lactic acid) microspheres: a potential agent for the internal radiation therapy of hepatic tumors. *Journal of Nuclear Medicine, 32(11)*, 2139-2143.

Nijsen, J. F. W., van Steenbergen, M. J., Kooijman, H., Talsma, H., Kroon-Batenburg, L. M. J., van de Weert, M., . . . Hennink, W. E. (2001). Characterization of poly(l-lactic acid) microspheres loaded with holmium acetylacetonate. *Biomaterials, 22*(22), 3073-3081.

Nordion. (2004). TheraSphere Yttrium-90 microspheres [package insert]. Kanata, ON, Canada: MDS Nordion.

NRC, National Research Council (2013). EGSnrc. Retrieved April 6th, 2016, from http://irs.inms.nrc.ca/software/egsnrc/

nucleonica.net (2013). File: Sm153 DS3.png Retrieved September 9th, 2013, from http://www.nucleonica.net/wiki/index.php?title=File%3ASm153_DS3.png

Okuda, K., Ohtsuki, T., Obata, H., Tomimatsu, M., Okazaki, N., Hasegawa, H., . . . Ohnishi, K. (1985). Natural history of hepatocellular carcinoma and prognosis in relation to treatment. Study of 850 patients. *Cancer, 56*(4), 918-928.

Palumbo, E. (2007). Immigration and hepatitis B virus in Italy. Current state and perspectives. *Recenti Progressi in Medicina, 98*(11), 548-552.

Pearson Education Inc. (2011). *Fundamentals of Anatomy & Physiology (9th Edition)*: Benjamin Cummings.

Poorbaygi, H., Reza Aghamiri, S. M., Sheibani, S., Kamali-Asl, A., & Mohagheghpoor, E. (2011). Production of glass microspheres comprising ^{90}Y and ^{177}Lu for treating of hepatic tumors with SPECT imaging capabilities. *Applied Radiation Isotopes, 69(10)*, 1407-1414.

Pretorius, P. H., Xia, W., King, M. A., Tsui, B. M., Pan, T. S., & Villegas, B. J. (1997). Evaluation of right and left ventricular volume and ejection fraction using mathematical cardiac torso phantom. *Journal of Nuclear Medicine, 38*, 1528-1535.

Pujol, A., & Gibbs, S. J. (1982). A Monte Carlo method for patient dosimetry from dental x-ray. *Dentomaxillofacial Radiology, 11*, 25-33.

Qaim, S. M. (2001). Therapeutic radionuclides and nuclear data. *Radiochimica Acta, 89*, 297-302.

Riaz, A., Awais, R., & Salem, R. (2014). Side effects of Yttrium-90 radioembolization. *Frontiers in Oncology, 4*, 198.

Rogers, D. W. O., & Bielajew, A. F. (1990). Monte carlo techniques of electron and photon transport for radiation dosimetry. In K. R. Kase, B. E. Bjarngard & F. H. Attix (Eds.), *The dosimetry of ionizing radiation.* Academic press.

Salem, R., Lewandowski, R., Roberts, C., Goin, J., Thurston, K., Abouljoud, M., & Courtney, A. (2004). Use of Yttrium-90 glass microspheres (TheraSphere) for the treatment of unresectable hepatocellular carcinoma in patients with portal vein thrombosis. *Journal of Vascular and Interventional Radiology, 15*(4), 335-345.

Salem, R., & Thurston, K. G. (2006). Radioembolization with 90Yttrium microspheres: a state-of-the-art brachytherapy treatment for primary and secondary liver malignancies. Part 1: Technical and methodologic considerations. *Journal of Vascular and Interventional Radiology, 17*(8), 1251-1278.

Salvat, F., Fernandez-Varea, J. M., & Sempau, J. (2006). *PENELOPE - a code system for Monte Carlo simulation of electron and photon transport*. Workshop Proceedings July 4th-7th, 2006. Barcelona, Spain.

Sangro, B., Bilbao, J. I., Boan, J., Martinez-Cuesta, A., Benito, A., Rodriguez, J., . . . Prieto, J. (2006). Radioembolization using 90Y-resin microspheres for patients with advanced hepatocellular carcinoma. *International Journal of Radiation Oncology*Biology*Physics, 66*(3), 792-800.

Sangro, B., Bilbao, J. I., Inarrairaegui, M., Rodriguez, M., Garrastachu, P., & Martinez-Cuesta, A. (2009). Treatment of hepatocellular carcinoma by radioembolization using 90Y microspheres. *Digestive Disease, 27*(2), 164-169.

Saraswat, V. A., Pandey, G., & Shetty, S. (2014). Treatment Algorithms for Managing Hepatocellular Carcinoma. *Journal of Clinical and Experimental Hepatology, 4*(Suppl 3), S80-S89.

Sarfaraz, M., Kennedy, A. S., Lodge, M. A., Li, X. A., Wu, X., & Yu, C. X. (2004). Radiation absorbed dose distribution in a patient treated with yttrium-90 microspheres for hepatocellular carcinoma. *Medical Physics, 31*(9), 2449-2453.

Sato, K., Lewandowski, R. J., Bui, J. T., Omary, R., Hunter, R. D., Kulik, L., . . . Salem, R. (2006). Treatment of unresectable primary and metastatic liver cancer with yttrium-90 microspheres (TheraSphere): assessment of hepatic arterial embolization. *Cardiovascular and Interventional Radiology, 29*(4), 522-529.

Segars, W. P., Bond, J., Frush, J., Hon, S., Eckersley, C., Williams, C. H., . . . Samei, E. (2013). Population of anatomically variable 4D XCAT adult phantoms for imaging research and optimization. *Medical Physics, 40*(4), 043701.

Segars, W. P., & Tsui, B. M. W. (2010). The MCAT, NCAT, XCAT, and MOBY computational human and mouse phantoms. In X. G. Xu & K. F. Eckerman (Eds.), *Handbook of Anatomical Models for Radiation Dosimetry*. pp. 105-134. Boca Raton, FL: Taylor & Francis.

Singare, P., Lokhande, R., & Madyal, R. (2011). Thermal degradation studies of some strongly acidic cation exchange resins. *Open Journal of Physical Chemistry, 1(2)*, 45-54.

Siriwardena, A. K., Mason, J. M., Mullamitha, S., Hancock, H. C., & Jegatheeswaran, S. (2014). Management of colorectal cancer presenting with synchronous liver metastases. *Nature Review Clinical Oncology, 11*(8), 446-459.

Sirtex. (2004). SIR-Spheres Yttrium-90 microspheres [package insert]. Lane Cove, Australia: Sirtex Medical.

Sirtex. (2015). Sirtex Medical Training Manual Vol. TRN-RW-04. *Training Program: Physicians and Institutions.* pp. 108. Retrieved September 23rd, 2015 from http://foxfireglobal.sirtex.com/sites/foxfireglobal.sirtex.com/files/user/trn-rw-04_for_eu_au_nz_and_asia.pdf

Smits, M. L. J., Nijsen, J. F. W., van den Bosch, M. A. A. J., Lam, M. G. E. H., Vente, M. A. D., Mali, W. P. T. M., . . . Zonnenberg, B. A. (2012). Holmium-166 radioembolisation in patients with unresectable, chemorefractory liver metastases (HEPAR trial): a phase 1, dose-escalation study. *The Lancet Oncology, 13*(10), 1025-1034.

SNMMI, Society of Nuclear Medicine and Molecular Imaging (2016). Clinical & Practice. *Committee on Medical Internal Radiation Dose (MIRD).* Retrieved June 18th, 2016, from http://www.snmmi.org/ClinicalPractice/content.aspx?ItemNumber=4212

Snyder, W. S., Ford, M. R., & Warner, G. G. (1978). Estimates of specific absorbed fractions for photon sources uniformly distributed in various organs of a heterogenous phantom. *Society of Nuclear Medicine, MIRD Pamplet No. 5* (revised).

Snyder, W. S., Ford, M. R., Warner, G. G., & Fisher, H. L. J. (1969). Estimated of absorbed fractions for monoenergetic photon sources uniformly distributed in various organs of a heteregenous phantom. *Journal of Nuclear Medicine, 10*(Suppl 3), 5-52.

Snyder, W. S., Ford, M. R., Warner, G. G., & Watson, S. B. (1975). "S" absorbed dose per unit cumulated activity for selected radionuclides and organs. *Society of Nuclear Medicine, MIRD Pamplet No. 11*.

Stabin, M. G. (1994). A model of the prostate gland for use in internal dosimetry. *Journal of Nuclear Medicine, 35*(3), 516-520.

Stabin, M. G. (1996). MIRDOSE: Personal Computer Software for Internal Dose Assessment in Nuclear Medicine. *Journal of Nuclear Medicine, 37*(3), 538-546.

Stabin, M. G., Watson, E. E., Cristy, M., Ryman, J. C., Eckerman, K. F., Davis, J. L., . . . Gehlen, M. K. (1995). Mathematical models and specific absorbed fractions of photon energy in the nonpregnant adult female and at the end of each trimester of pregnancy. Oak Ridge, TN: Oak Ridge National Laboratory.

Stroud, I. (2006). *Boundary Representation Modelling Techniques*. London: Springer.

Sun, V. C.-Y., & Sarna, L. (2008). Symptom Management in Hepatocellular Carcinoma. *Clinical Journal of Oncology Nursing, 12*(5), 759-766.

Taylor, T. (2012). Liver. *InnerBody.com* Retrieved October 14th, 2013, from http://www.innerbody.com/image_digeov/card10-new2.html

ThermoFisherScientific. (2009). Derivation of count per milliliter from percentage of solids. Technical Note: TN-017.04.

Tianwu, X., & Habib, Z. (2014). Evaluation of radiation dose to anthropomorphic paediatric models from positron-emitting labelled tracers. *Physics in Medicine and Biology, 59*(5), 1165.

Tipton, I. H., Snyder, W. S., & Cook, M. J. (1966). Elemental Composition of Standard Man. pp. 241. *Health Physics Divison Annual Progress Report.* ORNL-4007.

Tsougos, I., Loudos, G., Georgoulias, P., Theodorou, K., & Kappas, C. (2010). Patient-specific internal radionuclide dosimetry. *Nuclear Medicine Communications, 31*(2), 97-106.

Turner, J. H., Claringbold, P. G., Klemp, P. F. B., Cameron, P. J., Martindale, A. A., Glancy, R. J., . . . Lambrecht, R. M. (1994). ^{166}Ho-microsphere liver radiotherapy: a preclinical SPECT dosimetry study in the pig. *Nuclear Medicine Communications, 15*(7), 545-553.

UMMC, University of Malaya Medical Centre (2014). Department of Transfusion Medicine (Jabatan Perubatan Transfusi). Introduction: Blood Donation. Retrieved May 19th, 2015, from http://www2.ummc.edu.my/view/departments.php?deptID=16&page=1

UMMC, University of Malaya Medical Centre (2015a). Researcher. Research ethics: UMMC Medical Ethics Committee Retrieved May 19th, 2015, from http://www2.ummc.edu.my/view/content.php?ID=VGxSWlBRPT0=

UMMC, University of Malaya Medical Centre (2015b). Medical Ethics Application Standard Operating Procedure (SOP) *(Prosedur Kualiti Permohonan Kelulusan Etika Perubatan)*. Document No.: PK-7.1-QSU-011-E02 pp. 1-19. Kuala Lumpur, Malaysia.

Vanzi, E., Genovesi, D., & Di Martino, F. (2009). Evaluation of a method for activity estimation in Sm-153 EDTMP imaging. *Medical Physics, 36*(4), 1219-1229.

Vente, M. A. D., de Wit, T. C., van den Bosch, M. A., Bult, W., Seevinck, P. R., Zonnenberg, B. A., . . . Nijsen, J. F. W. (2010). Holmium-166 poly(L-lactic acid) microsphere radioembolisation of the liver: technical aspects studied in a large animal model. *European Radiology, 20*(4), 862-869.

Vente, M. A. D., Nijsen, J. F. W., de Roos, R., van Steenbergen, M. J., Kaaijk, C. N., Koster-Ammerlaan, M. J., . . . Krijger, G. C. (2009b). Neutron activation of holmium poly(L-lactic acid) microspheres for hepatic arterial radio-embolization: a validation study. *Biomedical Microdevices, 11*(4), 763-772.

Vente, M. A. D., Wondergem, M., van der Tweel, I., van den Bosch, M. A., Zonnenberg, B. A., Lam, M. G., . . . Nijsen, J. F. W. (2009a). Yttrium-90 microsphere radioembolization for the treatment of liver malignancies: a structured meta-analysis. *European Radiology, 19*(4), 951-959.

Watson, E. E., Stabin, M. G., Davis, J. L., & Eckerman, K. F. (1989). A model of the peritoneal cavity for use in internal dosimetry. *Journal of Nuclear Medicine, 30*(12), 2002-2011.

Wheaton, R. M., & Lefevre, L. J. (2000) Dow Liquid Separations: DOWEX ion exchange resins. Fundamentals of ion exchange. *Form No. 177-01837-600QRP*: The Dow Chemical Company.

Xu, X. G. (2014). An exponential growth of computational phantom research in radiation protection, imaging, and radiotherapy: a review of the fifty-year history. *Physics in Medicine and Biology, 59*(18), R233.

Yeong, C. H., Abdullah, B. J., Ng, K. H., Chung, L. Y., Goh, K. L., Sarji, S. A., & Perkins, A. C. (2011). Neutron-activated ^{153}Sm-ion-exchange resin as a tracer for gastrointestinal scintigraphy. *Nuclear Medicine Communications, 32(12)*, 1256-1260.

Yeong, C. H., Abdullah, B. J., Ng, K. H., Chung, L. Y., Goh, K. L., Sarji, S. A., & Perkins, A. C. (2012). Production and first use of $^{153}SmCl_3$-ion exchange resin capsule

formulation for assessing gastrointestinal motility. *Applied Radiation Isotopes, 70(3)*, 450-455.

Yeong, C. H., Cheng, M. H., & Ng, K. H. (2014). Therapeutic radionuclides in nuclear medicine: current and future prospects. *Journal of Zhejiang University: Science B, 15*(10), 845-863.

Yong Hum, N., Binquan, Z., Juying, Z., Peter, F. C., & Xu, G. (2010). Deformable adult human phantoms for radiation protection dosimetry: anthropometric data representing size distributions of adult worker populations and software algorithms. *Physics in Medicine and Biology, 55*(13), 3789.

Zaidi, H., & Xu, X. G. (2007). Computational anthropomorphic models of the human anatomy: the path to realistic Monte Carlo modeling in radiological sciences. *Annual Review of Biomedical Engineering, 9*(1), 471-500.

Zhang, J., Na, Y. H., Caracappa, P. F., & Xu, X. G. (2009). RPI-AM and RPI-AF, a pair of mesh-based, size-adjustable adult male and female computational phantoms using ICRP-89 parameters and their calculations for organ doses from monoenergetic photon beams. *Physics in Medicine and Biology, 54*(19), 5885-5908.

Ziaur, R., Shakeel ur, R., Waheed, A., Nasir, M. M., Abdul, R., & Jahan, Z. (2012). Absorbed dose estimations of 131 I for critical organs using the GEANT4 Monte Carlo simulation code. *Chinese Physics C, 36*(11), 1150.

Zubal, I. G., Harrell, C. R., Smith, E. O., Rattner, Z., Gindi, G., & Hoffer, P. B. (1994). Computerized three-dimensional segmented human anatomy. *Medical Physics, 21*, 299-302.

LIST OF PUBLICATIONS

Peer-reviewed Article

Hashikin, NAA, Yeong, CH, Abdullah, BJJ, Ng, KH, Chung, LY, Dahalan, R, & Perkins, AC. (2015). Neutron activated Samarium-153 microparticles for transarterial radioembolization of liver tumour with post-procedure imaging capabilities. *PLoS ONE, 10*(9), e0138106. (ISI-indexed)

Proceedings

Hashikin, NAA, Yeong, CH, Guatelli, S, Abdullah, BJJ, Ng, KH, Malaroda, A, Rosenfeld, AB, & Perkins, AC. (2016). Organ doses from hepatic radioembolization with ^{90}Y, ^{153}Sm, ^{166}Ho and ^{177}Lu: a Monte Carlo simulation study using Geant4. *Journal of Physics: Conference Series,* 694(1), 012059. (ISI-indexed)

Hashikin, NAA, Yeong, CH, Abdullah, BJJ, Ng, KH, Chung, LY, Dahalan, R, & Perkins, AC. (2015). Samarium-153 labelled microparticles for targeted radionuclide therapy of liver tumor. In DA Jaffray (Ed.), *World Congress on Medical Physics and Biomedical Engineering, June 7-12, 2015, Toronto, Canada*. Vol. 51, pp. 471-474: Springer International Publishing. (ISI-indexed)